May 2020

Development and Control of a 3-DoF Exoskeleton Robot for Forearm and Wrist Rehabilitation

Tanvir Ahmed
University of Wisconsin-Milwaukee

DEVELOPMENT AND CONTROL OF A 3-DOF EXOSKELETON ROBOT FOR FOREARM AND WRIST REHABILITATION

by

Tanvir Ahmed

A Thesis Submitted in

Partial Fulfillment of the

Requirements for the Degree of

Master of Science

in Engineering

at

The University of Wisconsin-Milwaukee

May 2020

ABSTRACT

DEVELOPMENT AND CONTROL OF A 3-DOF EXOSKELETON ROBOT FOR FOREARM AND WRIST REHABILITATION

by

Tanvir Ahmed

The University of Wisconsin-Milwaukee, 2020
Under the Supervision of Professor Mohammad Habibur Rahman

The research conducted under this project directly contributes to the development of a forearm and wrist rehabilitation robot (UWM-FWRR). Upper extremity impairment following stroke, trauma, sports injuries, occupational injuries, spinal cord injuries, and orthopaedic injuries results in significant deficits in hand manipulation and the performance of everyday tasks. Strokes affect nearly 800,000 people in the United States each year. Rehabilitation programs are the main method of promoting functional recovery in individuals with finger impairment. The conventional therapeutic approach requiring a long commitment by both the clinician and the patient. Robotic devices (RDs) are novel and rapidly expanding technologies in hand rehabilitation. However, existing RDs have not been able to fully restore hand functionality as they cannot provide the independent joint control and levels of velocity and torque required. Our customer discovery [1] reveals that therapists often prescribe therapeutic devices for passive arm/leg movement assistance but no therapeutic devices exist for combined hand, wrist, and forearm movements that can be used at home/clinic. Regaining hand strength and mobility plays an important role in supporting essential activities of daily living, such as eating, and thus has the potential to

improve the physical and mental status of both stroke patients and their family caregivers. Therefore, through this research author has develop UWM-FWRR that can provide rehabilitative exercises for forearm and, wrist movements. In contrast to existing RDs, developed UWM-FWRR is a portable, light weight, low cost, and novel powered rehabilitation device that will be developed to provide therapeutic exercises to a wide group of patients with different degrees of impairments. This innovation provides an opportunity for the patients to perform exercises not only with the guidance of a therapist at clinic but also be used at home as a telerehabilitation device through smartphone application (Future works).

Keywords: Exoskeleton, Robot, Rehabilitation, Forearm, Wrist, 3-DoF, Forearm Pronation, Forearm Supination, Wrist Radial Deviation, Wrist Ulnar Deviation, Wrist Flexion, Wrist Extension.

TABLE OF CONTENTS

LIST OF FIGURES

LIST OF TABLES

ACKNOWLEDGMENTS

Tanvir Ahmed would like to convey his endless gratitude to Professor Dr. M. Habibur Rahman of UWM, and Dr. Bhahim Brahmi for their relentless guidance and motivation during his thesis works. Dr. Rahman, without a doubt, can bring out the best in his pupils, and Tanvir feels lucky to have him as his supervisor.

Tanvir Ahmed would also like to acknowledge his colleagues from Biorobotics Lab, UWM, for extending their support and providing encouragement during this endeavour. Tanvir Ahmed is thankful to his lab-mates from the Biorobotics Lab, UWM, specially Asif-Al-Zubayer Swapnil, Md. Assad-Uz-Zaman and Md. Rasedul Islam Shihab for their immense support during every phase of this endeavour. A special thanks to John, Bob from EMS workshop, UWM, for their help during the manufacturing phases.

Finally, yet importantly, Tanvir wishes to convey heartiest thanks to his wife Fouzia Kamal Emon and his other family members for their enormous patience, sacrifice, support, and encouragement during this project. Furthermore, Tanvir is grateful to his seniors at Milwaukee, USA, for rendering their support.

CHAPTER 1

INTRODUCTION

Upper extremity impairment such as full or partial loss of function in the hand, wrist, and forearm following a stroke, trauma, sports injuries, occupational injuries, spinal cord injuries, and orthopedic injuries results in significant deficits in hand manipulation and the performance of everyday tasks. Stroke remains an important cause of morbidity and mortality, and the most common cause of disability. According to the World Health Organization, stroke affects more than 15 million people worldwide each year [2], and nearly 800,000 people in the *United States*. Within this population, 85% of stroke survivors will incur acute arm impairment, and 40% will be chronically impaired or permanently disabled [3]. It is estimated, more than 3 million people in the USA have a disability in their hands and/or forearms, including analyzations, orthopedic impairments, either congenital or injury related. On other statistics [4], it is revealed that hand injuries count for a 1/3 of all injuries at work, 1/3 of chronic injuries, 1/4 of lost working time, 1/5 of permanent disability. This results in a burden on their families, communities and to the country as well. According to the statistics found in 'Atlas of Heart Disease and Stroke' [2], "stroke burden is projected to rise from around 38 million disability-adjusted life years (DALYs) globally in 1990 to 61 million DALYs in 2020". Most stroke survivors live with long-term disabilities leading to serious social and economic impacts: it is estimated that stroke costs Canada more than $22.2 billion annually [5]. This cost burden is triple in the United States, estimated $65.5 billion annually including direct and indirect costs [6]. On the other hand, in the twenty seven European Union countries, the total annual cost of strokes is estimated at US$30.5 billion [6]. These numbers will

continue to rise as the population continues to age. Rehabilitation programs are the main method to promote functional recovery in these individuals [7]. The conventional therapeutic approach requires a long commitment by a therapist or clinician. Unfortunately, there is a consistent shortage of qualified therapists/clinicians both in developing countries and the developed countries as well. In addition, the treatment duration is usually very long, requiring many hours of the therapist's time for each individual patient. The problem is further compounded by the constantly growing number of such cases. Therefore, an alternative to conventional treatments is essential.

To solve this excruciating issue, researchers have invested their knowledge into developing robotic devices that can aid rehabilitation [8]. More on this can be found from CHAPTER 2. However, most of the research on robotic devices are in the development phase, and a few of them are available commercially. Among the commercial exoskeleton type robots for rehabilitation, most of them can only be used in clinical settings and costly. There are few devices that are somewhat portable, but most of them are either passive rehabilitation devices or simply CPM (Continuous passive motion) devices that do not provide force feedback.

Therefore, to contribute in this field, this research focuses on the development of a 3DoFs exoskeleton type robot named *UWM-FWRR* (Forearm and Wrist Rehabilitation Robot) to effective rehabilitation therapy to the individual with impairment in their forearm and wrist and in need of rehabilitation therapy, so that they would be able to receive required therapies while being at home resulting faster recovery. The UWM-FWRR is comprised of a forearm motion support part and a wrist motion support part. It is designed to be worn by the patient as an exoskeleton and for providing forearm (i.e., pronation/supination), and wrist joint (i.e., radial/ulnar deviation, and flexion/extension) motions to the wearer.

This thesis focuses on the modeling, design, development, and control of the FWRR. The kinematic model of the *FWRR* was developed based on modified Denavit-Hartenberg (DH) notations [9]. In dynamic modeling and control, robot parameters such as robot arm link lengths, masses of different link segments, upper-limb masses, and inertia, were estimated according to the upper limb properties of a typical adult [10].

This research concentrated only on the passive form of rehabilitation. Passive arm movements and exercises are usually performed slow [11] compared to the natural speed of arm movement. Therefore, as a first step, we implemented a computationally inexpensive PID controller, rather than complex model-based control algorithms. Most industrial robots nowadays use this control technique because of problems with the estimation of dynamic parameters [12]. Later, to realize better tracking performance of the *FWRR,* the dynamic models of human forearm and wrist (APPENDIX – B) and *UWM-FWRR* were considered in the nonlinear control techniques. Note that the dynamic modeling of human arm movement is nonlinear in nature; therefore, a nonlinear control technique namely modified computed torque control (CTC) was used for the dynamic simulation of the developed model. Furthermore, a robust controller, Sliding Mode Control with Time Delay Estimation (SMC-TDE) has been evaluated through simulation using dynamic model of a 2-DoF serial manipulator robot to implement on UWM-FWRR in near future. In the experiments, a PID, and CTC were implemented to control the developed robot, where trajectory tracking (i.e., pre-programmed trajectory tracking approach) that corresponds to typical rehabilitation (passive) exercises forearm and wrist joint movements were carried out to evaluate performances of the *FWRR* and the controllers.

In experiments, typical rehabilitation exercises for single and multi-joint movements (e.g., reaching) were performed. Experiments were carried out with healthy human subjects (n=3) where trajectories (i.e., pre-programmed trajectories recommended by a therapist/clinician) tracking the form of passive rehabilitation exercises were carried out. Experimental results show that the *FWRR* can efficiently perform passive rehabilitation therapy. This thesis is organized as follows:

CHAPTER 2: Literature Review

This chapter is a critical overview of research work conducted in the fields of development of orthoses and/or robotic exoskeletons, methods adopted to control such robots, and their real-world applications are presented.

CHAPTER 3 Exoskeleton Robot for Rehabilitation - Market Opportunity

A brief overview of the current market trends of the exoskeleton-based rehabilitation robot industry has been given in this chapter. Moreover, the potential commercialization opportunity of the developed robot has been briefly discussed.

CHAPTER 4: Design Thinking & Objectives

Initial design thinking for the development of UWM-FWRR based on customer discovery and literature review has been discussed in this chapter. Through vigorous brainstorming, the objectives of this research have been solidified.

CHAPTER 5: Forearm and Wrist Rehabilitation Robot (UWM-FWRR)

This chapter outlines the overall design of the proposed *UWM-FWRR*. It describes the motivation for the major design choices and gives the reader an overall sense of the complete hardware package and the components that comprise it.

CHAPTER 6: Kinematics and Dynamics

Chapter 3 describes the kinematics and the dynamics of the *UWM-FWRR*. The modified DH notations were used to develop the kinematic modeling, whereas, in dynamic modeling, the iterative Newton-Euler formulation was used.

CHAPTER 7: Control and Simulation

This chapter presents the theoretical structure of the different control techniques (such as PID, Computed Torque Control) that were applied to maneuver the *UWM-FWRR* to follow a reference trajectory. This chapter also presents simulation results to validate the *UWM-FWRR* model developed in Chapter 6, and to evaluate the performance of the different control techniques about trajectory tracking.

CHAPTER 8: Experiments and Results

To evaluate the performance of the *UWM-FWRR* and the control techniques, this chapter describes experimental set-up and the procedure carried out during the experiments. The chapter presents all the test results, discusses the test results in detail, and gives some specific comments on the test results.

Conclusions, Recommendations and Future Scopes

Finally, the Conclusions section of the paper summarizes the research outcomes and suggests directions for further research in section Recommendations. The future scopes section presents the potential of this research through further development.

CHAPTER 2

LITERATURE REVIEW

Evident from the importance of rehabilitation through robotic devices in this current era, many researches have been conducted, and few of them have already been commercialized. For the development of a robotic device for Forearm and Wrist rehabilitation, these research works (from 2014 until today) have been reviewed, and in this chapter, those scientific researches and current products in the market aimed for wrist and forearm rehabilitation have been discussed briefly. This literature review excludes the Continuous passive movement (CPM) devices available in the market, such as 6000 Hand CPM, QAL medical, Vector1 | Hand CPM, Lantz medical, Kinetec Maestra Hand & Wrist Tabletop CPM, Kinetec, etc. as they do not provide feedback. Also, other passive therapeutic devices are also excluded from the scope of this review.

2.1 **Wrist Rotation Rehabilitation Robot (Kim et al., 2014):**

This 1-DoF end-effector type robot was developed by Kim et al. [13] around 2014 for providing pronation/supination motion to the human wrist for rehabilitation purposes. This robotic device intended for setting up beside the bed at the hospital or home, and the patient will have to lie down to receive the wrist pronation/ supination therapy. A 6-axis force sensor has been used for force feedback, and when the patient pulls the handle towards themselves, that acts as a trigger for the patient's discomfort resulting in the device to stop. The structure is bulky (430 mm X 320 mm X 800 mm) in nature and suitable for stationary usage. The clinical trial is yet to be done. The motion to the forearm (pronation/ supination) is provided to the patient's hand by a wrist handle that is actuated by an electric motor connected directly with the wrist handle.

Figure 2.1 Experimental setup of Wrist Rotation Rehabilitation Robot [13]

2.2 **Wearable Wrist Rehabilitation device (Kato et al., 2016):**

This rehabilitation device based on parallel robotics was developed by Kato et al. [14] around 2016 for providing wrist radial/ ulnar deviation and flexion/ extension motion to the human wrist for rehabilitation purposes. This robotic device consists of three flexible pneumatic cylinders, an accelerometer, an embedded controller (Renesas Co. Ltd., SH7125), and six quasi-servo valves. The robot needs to be mounted vertically, having the human forearm facing upwards for usage. Along with power cable, this device required compressed air supply. This end effector-based robot has a fixed base through which the subject must pass his/her forearm to grab the wrist handle. PID control strategy has been used for this robot. The device has a latency of 1 second due to its pneumatic actuation system.

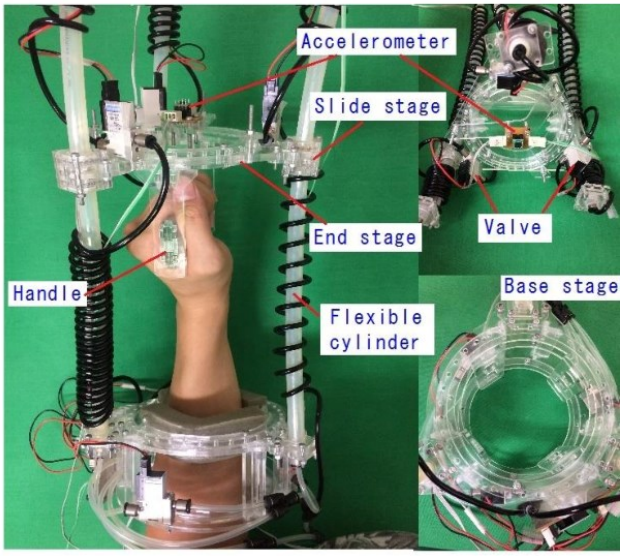

Figure 2.2 Experimental setup of Wearable Wrist Rehabilitation device [14]

2.3 **Assistive Wrist Orthosis (Sutton et al., 2016):**

This wearable device (1-DoF) based on direct actuation of joints through artificial muscle was developed by Sutton et al. [15] around 2016 for providing wrist flexion/ extension motion to the human wrist for assistive purpose. The main contribution of this research is to show the efficacy of conductive nylon-based actuation in rehabilitation purposes. This robotic device consists of modified 16 nylon strings to actuate a single degree of freedom in the human wrist. The authors have yet to test the device using human subjects. For the control of this device, a PID control technique had been implemented.

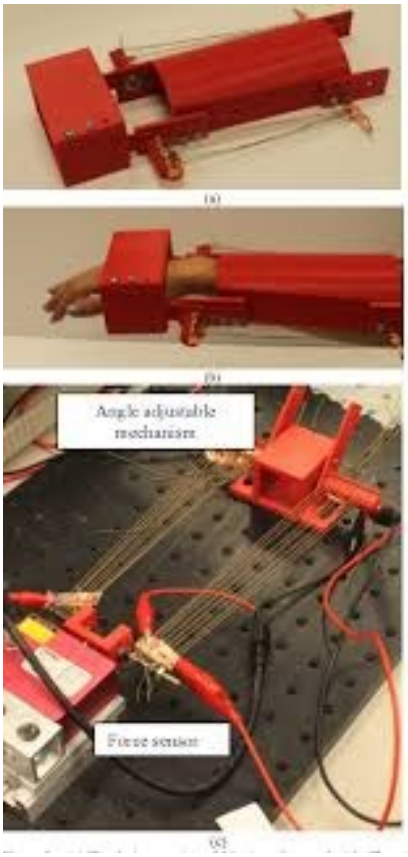

Figure 2.3 Experimental setup of Assistive Wrist Orthosis [15]

2.4 **NU-Wrist (Omarkulov et al., 2016):**

This self-aligning rehabilitation device (3-DoF) based on direct actuation of joints through DC servo motors was developed by Omarkulov et al. [16] around 2016 for providing forearm Pronation/ Supination, wrist flexion/ extension, and wrist Radial/ Ulnar Deviation motion to the human forearm and wrist for rehabilitation purposes. This robot provides all three joint movements using the wrist handle which is to be grabbed by the patient. However, when the patient needs only pronation/ supination motion to the forearm, the patient's wrist will need to transmit rotation to the forearm generating torque at the wrist joint. The authors have implemented a compliance mechanism in the wrist handle to compensate the forearm and wrist misalignment and this feature

has been achieved with parallelogram linkages with three compression springs. However, this alignment requires a change of the springs with different stiffness coefficients. The range of motion associated with this robot are as follows: forearm Pronation/ Supination (90°/85°), wrist flexion/ extension (85°/85°), and wrist Radial/ Ulnar Deviation (15°/45°). The NU-Wrist was tested with healthy individuals with a pre-programmed trajectory.

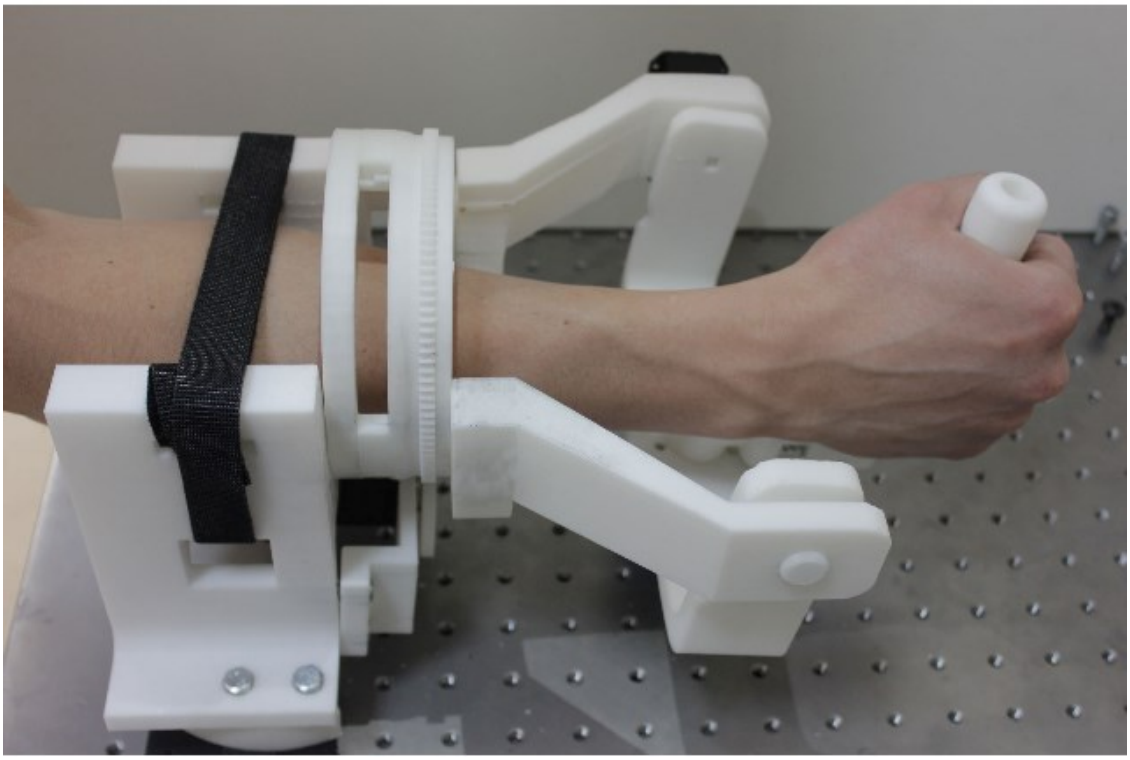

Figure 2.4 Experimental setup of NU-Wrist [16]

2.5 **OpenWrist (Pezent et al., 2017):**

This wrist rehabilitation device (3-DoF) was developed by Pezent et al. [17] around 2017 for providing forearm Pronation/ Supination, wrist flexion/ extension, and wrist Radial/ Ulnar Deviation motion to the human forearm and wrist for rehabilitation purposes. This end-effector

based robot provides all three joint movements using the wrist handle, which acts as the end-effector. Same as NU-Wrist, when the patient needs only pronation/ supination motion to the forearm, the patient will go through rotary motion in the wrist joint, causing generating unnecessary torque there. OpenWrist is the successor to its earlier design RiceWrist-S [18], and has been modified to be used along with Maestro Hand developed by ReNeu Lab. OpenWrist uses a capstan cable drive to ensure backlash-free operation. However, cable-driven power transmission requires redundant cable routing causing the setup to become bulky. This device is intended to be used in a desk-mounted setup while the forearm remains in the horizontal position. The range of motion associated with this robot are as follows: forearm Pronation/ Supination (85°/85°), wrist flexion/extension (70°/65°), and wrist Radial/ Ulnar Deviation (35°/40°). The OpenWrist was tested with healthy individuals with a pre-programmed trajectory through PD (proportional derivative) control technique.

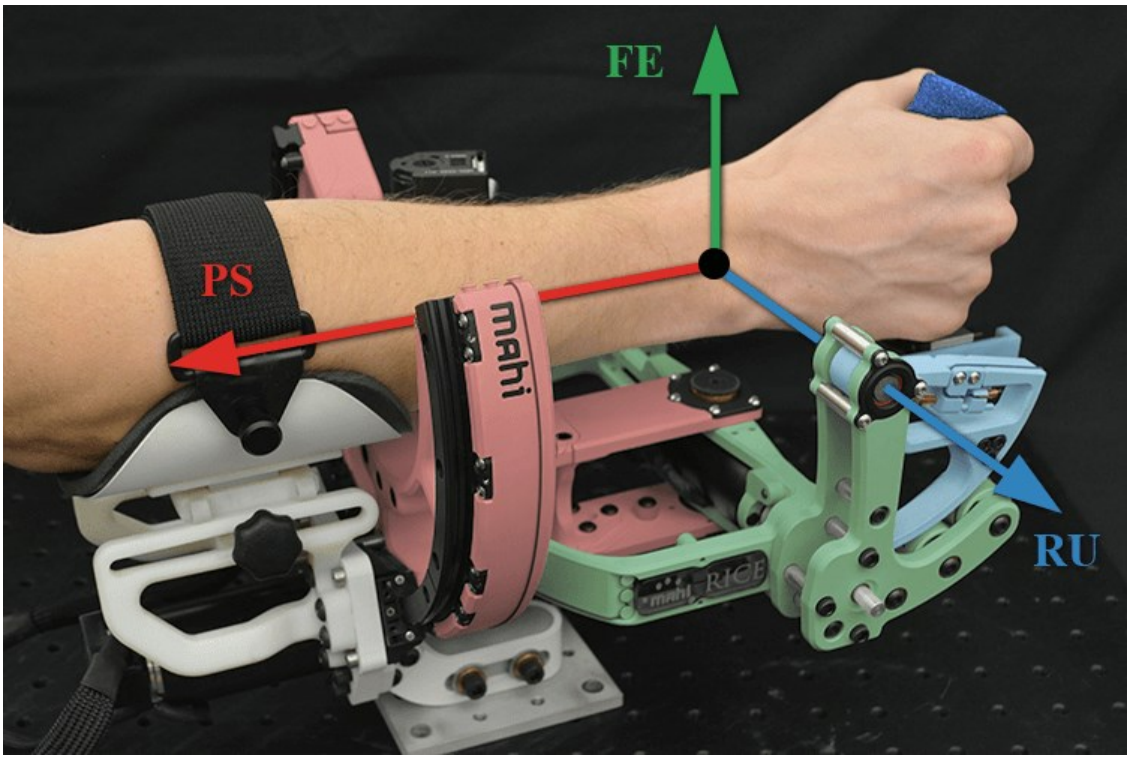

Figure 2.5 Experimental setup of OpenWrist [17]

2.6 **EFW Exo II (Bian et al., 2017):**

This elbow, forearm, and wrist rehabilitation device (4-DoF) was developed by Bian et al. [19] around 2017 for providing elbow Flexion/ Extension, forearm Pronation/ Supination, wrist flexion/ extension, and wrist Radial/ Ulnar Deviation motion to the human elbow, forearm, and wrist for rehabilitation purposes. This end-effector based robot provides all four joint movements using the wrist handle, which acts as the end-effector. EFW Exo II is based on a 3DoF parallel 2-URR/RRS mechanism and a serial R mechanism producing a 4DoF hybrid mechanism for all four movements. Due to the nature of the parallel mechanism, the structure of EFW Exo II is bulky. This robot setup is mounted in a wheeled base for portability. The range of motion associated with

this robot are as follows: Elbow Flexion/ Extension forearm (140°), Pronation/ Supination (>270°), wrist flexion/ extension (90°), and wrist Radial/ Ulnar Deviation (90°). The authors have put mechanical limits in the joints of EFW Exo II. As the EFW Exo II joints' range of motion is more than the nominal range of motion of Forearm Pronation/ Supination in humans.

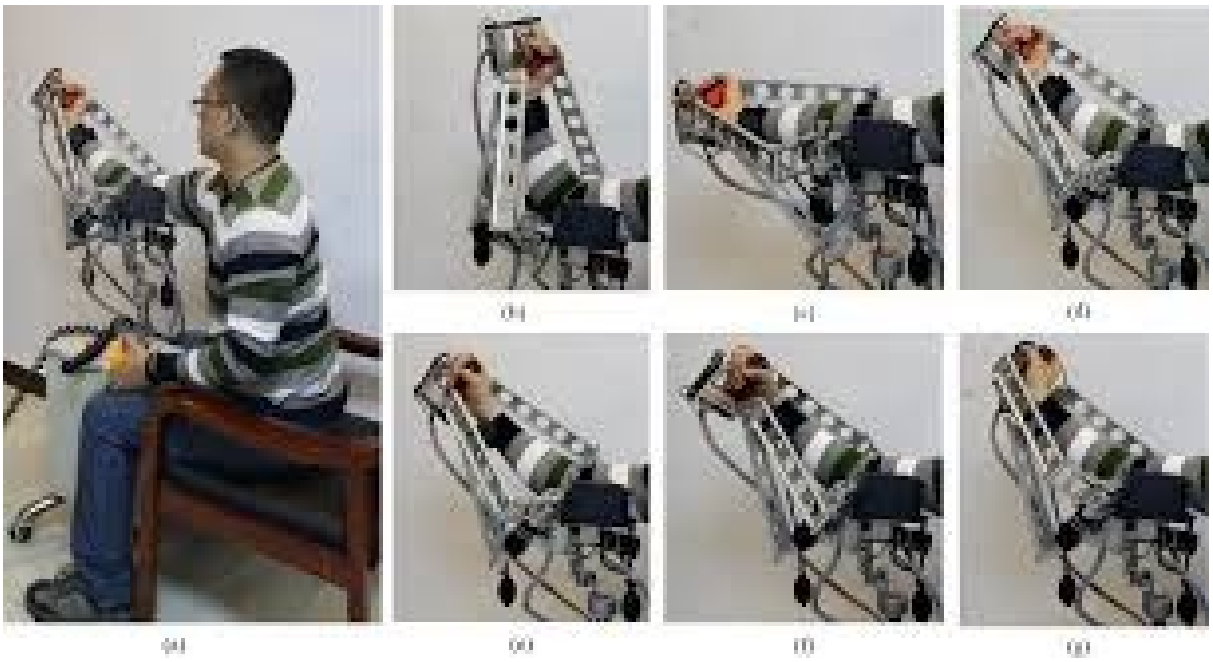

Figure 2.6 Experimental setup of EFW Exo II [19]

2.7 **Physiotherabot/WF (Atlihan et al., 2014):**

This forearm and wrist rehabilitation device (3-DoF) was developed by Atlihan et al. [20] around 2014 for providing forearm pronation/ supination, wrist flexion/ extension, and wrist radial/ ulnar deviation motion to the human forearm and wrist as therapeutic exercises. This robot provides all three joint movements using the wrist handle. Again, like OpenWrist [17], this robot causes torque generation at the wrist joint in the event of providing individual pronation and supination motion. Physiotherabot/WF is driven by direct actuation provided by electric motors. This robot is

equipped with a force sensor for force control mode. In this device, there are two control modes, which are position control mode and force control mode. For these two modes, A hybrid impedance control (HIC) was used. The robot structure is quite bulky, and the resulting weight is around 11 kilograms. The range of motion associated with this robot are as follows: Forearm Pronation/ Supination (85°/85°), wrist flexion/ extension (80°/ 80°), and wrist Radial/ Ulnar Deviation (30°/ 45°).

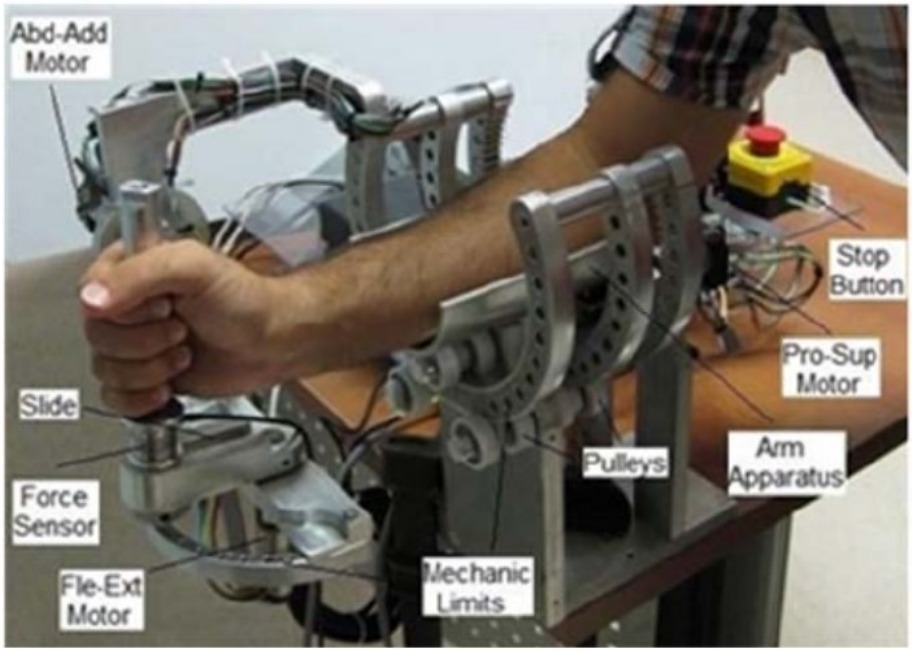

Figure 2.7 Experimental setup of Physiotherabot/WF [20]

2.8 **Wrist Rehabilitation Exoskeleton Robot (Al-Fahaam et al., 2016):**

This exoskeleton type wrist rehabilitation robot (2-DoF) was developed by Al-Fahaam et al. [21] around 2016 for providing wrist flexion/ extension, and wrist Radial/ Ulnar Deviation motion to the human wrist for rehabilitation. This robot provides joint movements by making the patient wear the robot as a glove. This is driven by five soft pneumatic actuators which act as artificial

muscle, and the actuation is controlled by four channels MATRIX 3/3 750 solenoid valves. This robot is equipped with a vacuum absolute pressure sensor, MD-PS002 (700kPa), for control and feedback. To achieve therapeutic motion to human wrist, this device requires up to 5 bar air pressure for providing actuation.

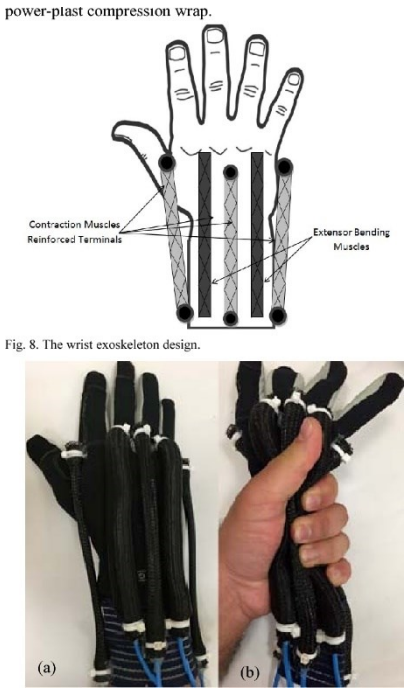

Figure 2.8 Wrist Rehabilitation Exoskeleton Robot [21]

2.9 **WRES (Buogiorno et al., 2018):**

This exoskeleton type forearm and wrist rehabilitation robot (3-DoF) was developed by Al-Buogiorno et al. [22] around 2017 for providing Forearm Pronation/ Supination, wrist flexion/ extension, and wrist Radial/ Ulnar Deviation motion to the human forearm and wrist for rehabilitation. This serial kinematics-based tendon driven robot provides joint movements by making the patient wear the robot as an exoskeleton. This is driven by BLDC gear motors and uses differential transmission for power transmission for the forearm and wrist joint movements. The

range of motion associated with this robot is as follows: Forearm Pronation/ Supination (146°), wrist flexion/ extension (75°), and wrist Radial/ Ulnar Deviation (40°). Due usage of differential transmission mechanism, the WRES weights around 2.9 kg as it requires quite a few moving parts. All the joint movements are provided by the wrist handle that acts as an end-effector.

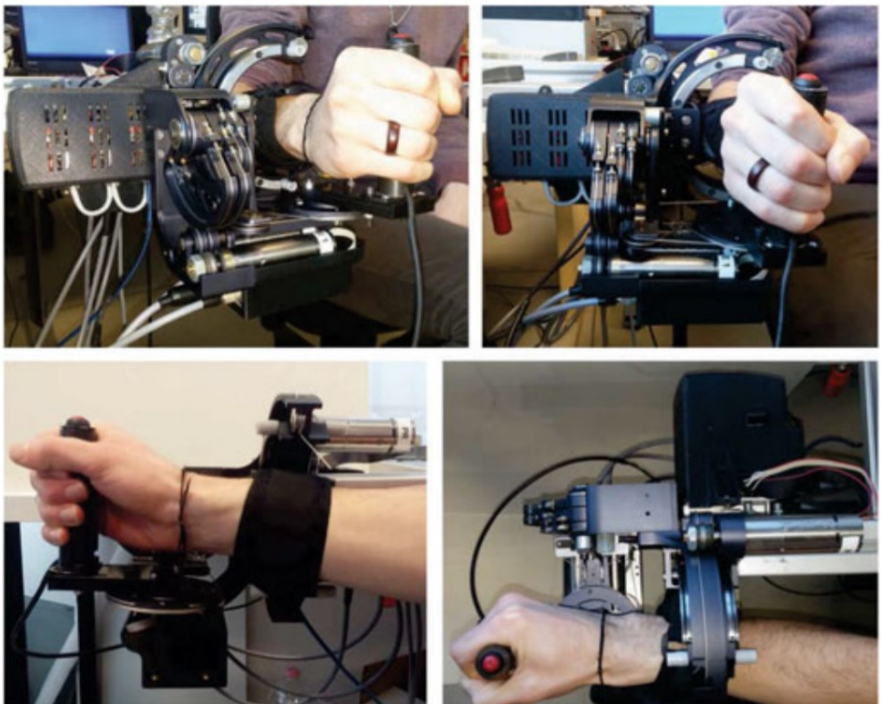

Figure 2.9 Experimental setup of WRES [22]

2.10 **Wrist Robot (Su et al., 2019):**

This exoskeleton type forearm and wrist rehabilitation robot (3-DoF) was developed by Su et al. [23] around 2018 for providing Forearm Pronation/ Supination (PS), wrist flexion/ extension (FE), and wrist Radial/ Ulnar Deviation (RU) motion to the human forearm and wrist for rehabilitation. This serial kinematics-based robot provides joint movements by making the patient wear the robot as an exoskeleton. This is driven by stepper motors and generates series elastic actuation through planar spring attachment for transmitting power to the forearm and wrist joint movements. The

range of motion associated with this robot is as follows: Forearm Pronation/ Supination (150°), wrist flexion/ extension (100°), and wrist Radial/ Ulnar Deviation (100°). The elastic actuation provides adaptability regards to the active and passive joint misalignments of FE and RU joint to the PS joint. This robot uses an impedance control technique for force/ torque control. The total reported weight of this robot is 1.5 kg. Wrist Robot shows promise in its application; however, to use this robot, the patient must pass his/ her forearm through closed-loop, reducing ease of donning/ doffing.

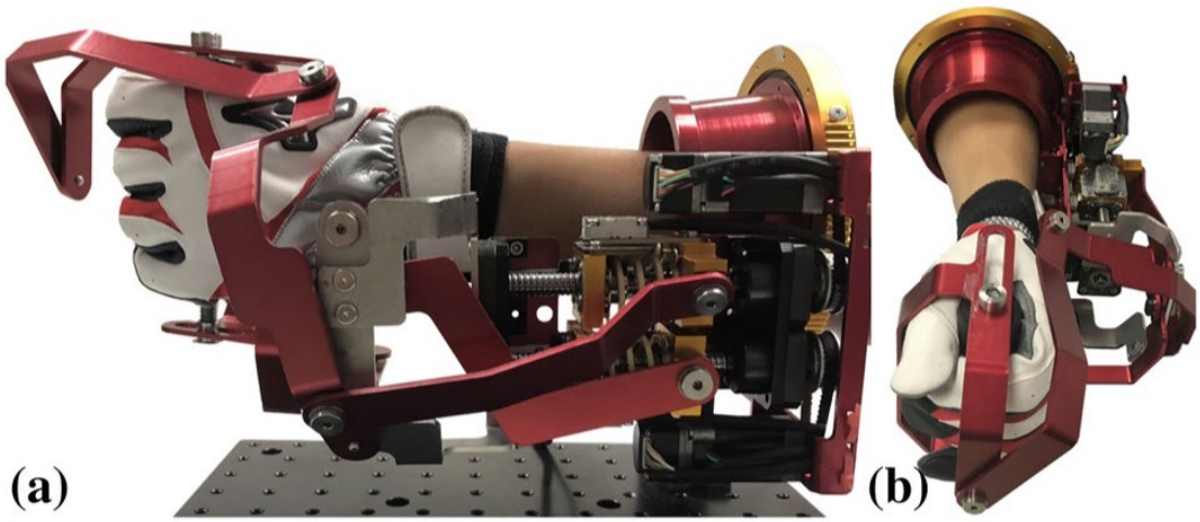

Figure 2.10 Experimental setup of Wrist Robot [23]

2.11 **InMotionWRIST™ (Bionik Laboratories Corp.):**

This commercially available exoskeleton type forearm and wrist rehabilitation robot (3-DoF) was developed Bionik Laboratories Corp. for providing Forearm Pronation/ Supination (PS), wrist

flexion/ extension (FE), and wrist Radial/ Ulnar Deviation (RU) motion to the human forearm and wrist for rehabilitation purposes. All three joints the produced by the wrist handle, which acts as an end-effector. As bulky in structure, the total setup of InMotionWRIST is suitable for clinical application yet to be used for the in-house environment.

Figure 2.11 InMotionWRIST ™ (Bionik Laboratories Corp.)

CHAPTER 3

EXOSKELETON ROBOT FOR REHABILITATION MARKET OPPORTUNITY

The increasing dominance of nervous system trauma is one of the crucial factors that are expected to drive the application of exoskeletons in the healthcare industry. Patients suffering from SCI are one of the principal end-users of these products. The significant market growth is also due to the increasing prevalence of degenerative diseases such as Parkinson's, and the growing number of CVA, ALS, multiple sclerosis, and cerebral palsy patients who require rehabilitation therapy. The elderly and disabled assistive devices' global market was valued at $18.7 B in 2017 and is expected to surpass $30.82B (growing at a CAGR of around 7.40%) by 2024, according to Zion Market Research (Coherent Market Insights) [24], and Rehabilitation robot market size at $641M in 2018 is expected to grow dramatically to reach $6.4B by 2025. Exoskeleton markets will be separate and additive to this market *Figure 3.1*.

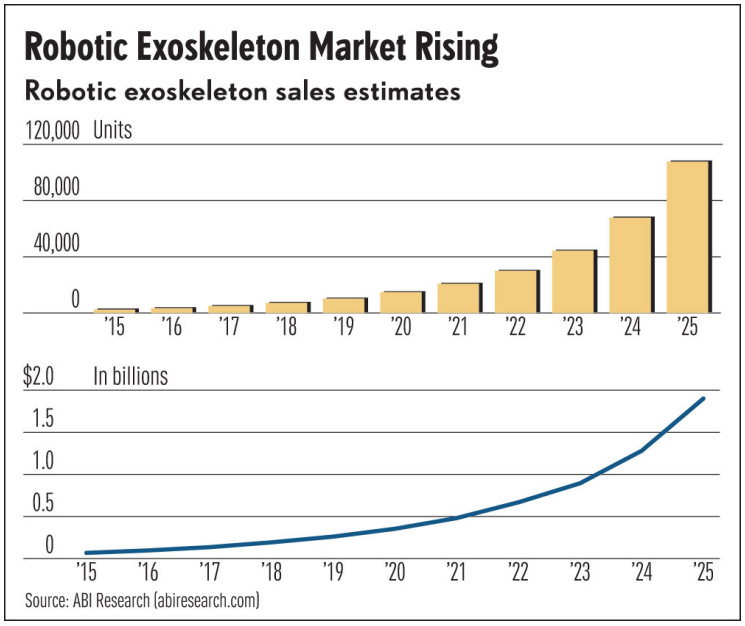

Figure 3.1 Robotic Exoskeleton Market Forecast (2015-2025)

Wintergreen research reports [25], US Exoskeleton Wearable Robot Markets (EWRM) at $130M in 2018 are anticipated to reach $5.2B (at a CAGR of 43.4%**)** by 2025. Powered exoskeleton type is expected to grow at the highest rate of 43.4% during the forecast period. From another report [26], The Global Extremities (Shoulder and Small Joint Implants) Market was $1954.1M (2018) and is expected to reach $3310.9M by 2026, at a CAGR of 6.8%. It can be interpolated that, Hand and Wrist rehabilitative and motion assist products market size (for individuals who needed Hand & Wrist implants) in the US is expected to be $288.64M (Global $662.18M) by 2026. Based on our market research/survey, we summarized our findings, as shown in *Figure 3.2*.

Figure 3.2 SOM, SAM, TAM, and PAM of UWM-FWRR

SOM – Serviceable Obtainable Market,
SAM – Served Available/ Addressable Market,
TAM – Total Addressable Market, and
PAM – Potential Addressable Market

Although the actual market for Hand and wrist rehabilitative and motion assist products in the US would be much larger (based on the previously mentioned data), at this moment, we are focusing on the specific market that considers individuals who had implants in their hands and/ or wrist.

Our pilot customer discovery (Milwaukee I-Corps site) [1] revealed that: (a) unaffordability (cost of rehabilitation therapy) increases patient's early dropout from rehab; (b) Occupational therapists (OTs) are the key stakeholders, they can suggest anything suitable for rehabilitation; (c) any rehab device might be covered by insurance, having suggested and justified by the OTs; (d) any devices valued below $2,000 have a greater chance of being covered by an insurance provider; (e) OTs

below 35 years of age are interested to adopt new technology in rehab; (f) elderly individuals who have lost hand mobility are much more interested in assistive devices than in rehab devices because they think the recovery chances for them are limited; (g) individuals with an orthopedic injury would also benefit; (h) travel and transportation is always problematic for patients, therefore home based rehab therapy is a top preference for the patients, (i) OTs often prescribe therapeutic devices for passive arm/leg movement assistance but no therapeutic devices exist for hand, wrist and forearm movements that can be used at home and are portable, (j) a therapeutic device needs to be customizable, etc.

Significance and Societal Impacts: The research(UWM-FWRR) will **(i)** reduce dependence on caregivers; **(ii)** decrease dropout rate from rehab; **(iii)** speed up rehab process; **(iv)** lower cost burden for the patients; **(v)** lower insurance provider costs; and **(v)** provide more service per day to patients at outpatients' clinics with the help of the proposed device.

From the market analysis, it can be inferred that a robotic device that is able to provide forearm and wrist rehabilitation at home has a great potential of becoming a profitable commercial product in the future market not only in the USA but also worldwide.

CHAPTER 4

DESIGN THINKING & OBJECTIVES

This chapter focuses on the design thinking behind the development of UWM-FWRR and refinement of objectives of this research based on the literature review conducted in CHAPTER 2 and customer discovery during NSF I-Corps [1] Development of UWM-FWRR leverages the pain point of customers in need of ease of access to therapeutic devices which can effectively provide rehabilitative exercises.

Our pilot customer discovery [1] funded by NSF I-Corps with 120+ interviewees comprised of Occupational Therapists, Physical Therapists, Patients, caregivers, family members of the patients, Insurance providers, revealed that: (a) unaffordability (cost of rehabilitation therapy) increases patient's early dropout from rehab; (b) Occupational therapists (OTs) are the key stakeholders, they can suggest anything suitable for rehabilitation; (c) any rehab device might be covered by insurance, having suggested and justified by the OTs; (d) any devices valued below $2,000 have a greater chance of being covered by an insurance provider; (e) OTs below 35 years of age are interested to adopt new technology in rehab; (f) elderly individuals who have lost hand mobility are much more interested in assistive devices than in rehab devices because they think the recovery chances for them are limited; (g) individuals with an orthopedic injury would also benefit; (h) travel and transportation is always problematic for patients, therefore home based rehab therapy is a top preference for the patients, (i) OTs often prescribe therapeutic devices for passive arm/leg movement assistance but no therapeutic devices exist for hand, wrist and forearm movements that

can be used at home and are portable, (j) a therapeutic device needs to be customizable. The **key customer segments** we found through this process are:

- patients with impaired hand functions from neurological disorders and orthopedic injury,
- Occupational therapists (OTs),
- Hospital inpatient, and outpatient care units,
- Outpatient centers, and
- Rehab centers.

Moreover, during another customer discovery funded by NSF I-Corps (Site: Milwaukee) [27] we conducted interviews with 43 numbers of Occupational Therapists, Physical Therapists, Patients, Caregivers, Family members of the patients and some interesting facts were discovered.

- Patients often refer to the Continuous Passive Motion (CPM) Devices as torture machines – as these machines do not know if the patient is getting hurt or not. Therefore, close monitoring by therapists is required.
- Therapists do not know whether patients are doing in-home exercises properly. They can only rely on patients' word of mouth. Many times, it is seen that some patients do not follow through the prescribed in-home exercises, and some do extra exercises, causing a burden to their muscles, and the result is worse in both cases.
- Therapists are looking for a way to ensure that their patients are going through the rehabilitation process as prescribed as that will allow them to do proper evaluation of patients;' condition. The health insurance companies are keen on having the progress measure of the patients from the therapists.

The findings of the above two customer discoveries are summarized as follows:

- A therapeutic device should be portable that can be used at home,
- The device should be able to store or transmit accurate data regarding patients' in-home exercises,
- The robotic device should be of low cost,
- The device should be able to provide effective therapy (i.e., range of motion, variable motion speeds),
- The stored data should be accessible to healthcare providers so that they can optimize patients' rehabilitation programs more effectively.

As an initiative to soothe customers' pain points, our customer discovery reveals the unmet needs of the individuals with hand/wrist impairments; a need of a robotic therapeutic device for forearm/wrist rehabilitation that can:

- Provide effective therapeutic movements to the patients at the level of forearm pronation/supination; wrist joint radial/ ulnar deviation; and wrist flexion/ extension motion.
- The device should be able to prove the full range of motion (RoM) of the above-mentioned joints. The RoM of forearm and wrist have been discussed in section 5.1.1.
- The device should have portability (i.e., lower mass, lower inertia, compact in size)
- Donning/ Doffing of this device should be easy.
- The device should provide joint torque feedback for analysis.

Note that, the telerehabilitation feature has been kept for future works.

Objectives:

Aim-1: Development of a 3-DoF wearable therapeutic robot that includes design, modeling, fabrication, electrical & electronic instrumentation.

Aim -2: Validation of the developed robot for rehabilitation by providing passive therapeutic motions.to healthy subjects using established control algorithms.

To accomplish the Aim-1 and Aim-2, the steps that were followed are given below:

1. Development of kinematics
2. Development of dynamics
3. Joint torque requirement calculation through simulation
4. Actuator selection based on torque requirements
5. Design of the mechanism so that easier donning/ doffing can be ensured while ensuring ease of manufacture. Moreover, compact design for portability needed to be ensured while keeping the loss of power during transmission to a minimum.
6. Fabrication of the device.
7. Assembly and instrumentation
8. Prove that the device is indeed able to prove effective passive rehabilitation therapy through experiments.

CHAPTER 5

FOREARM AND WRIST REHABILITATION ROBOT (UWM-FWRR)

This chapter outlines the overall design of the developed UWM-FWRR. The design is based on the concept of human forearm and wrist articulations and joint movements. It is conceptualized from the design thinking process to address the users' needs found through I-Corps aided customer discovery. The robotic exoskeleton for this study was designed to provide rehabilitation for:

I. Forearm pronation/supination (1-DoF),

II. Wrist flexion/ extension (1-DoF), and

III. Wrist radial ulnar deviation (1-DoF)

In the first section of this chapter, design considerations through analysis of human biomechanics for required movements, associated range of motion are highlighted for the motivation of major design choices. At the end of each subsection, the adapted design criteria used for the development of UWM-FWRR has been explained.

The second section of this chapter gives the overall view of the complete hardware package and the components that comprise UWM-FWRR.

5.1 General Design Considerations

To develop the exoskeleton type rehabilitation devices for rehabilitation of human forearm and wrist the following design criteria [28] have been considered:

5.1.1 Range of Motion (RoM) and associated Degrees of Freedom (DoF):

For providing rehabilitation therapies to forearm and wrist using exoskeleton type robot, the natural range of motion of humans must be accounted. The robot must be such that it is able to

produce the natural RoM to the human body. The main reason behind this is, the exoskeleton type robot is worn by the human. Human has 3 degrees of freedom in their forearm and wrist. The forearm motion is known as pronation/supination, which acts like a revolute joint. Forearm pronation/ supination can be seen from (*Figure 5.1*), and this motion comes from the twist of Radius and Ulnar bones of the human forearm.

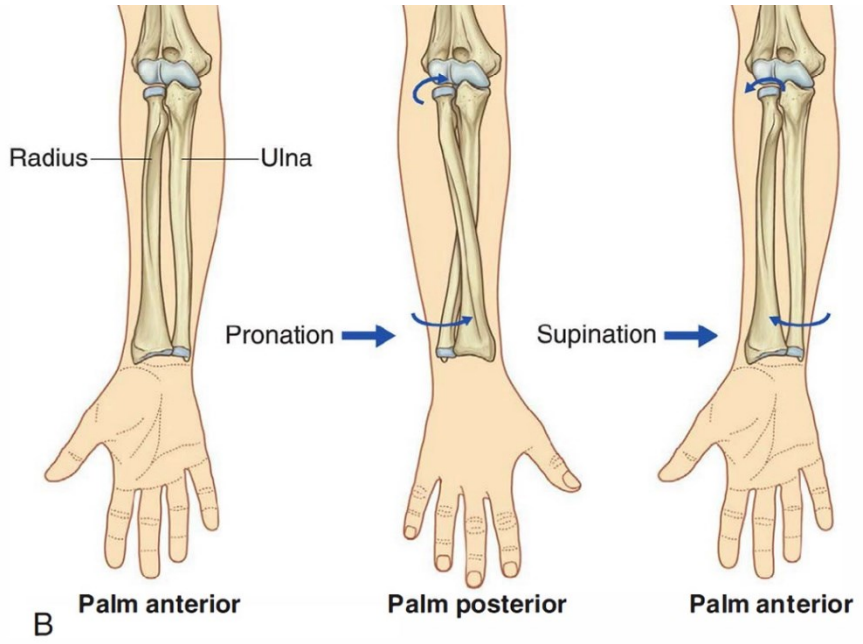

Figure 5.1 Forearm Pronation/ Supination movement [29]

The human wrist has 2 degrees of freedom. One is wrist Flexion/ Extension, and the other is wrist radial-ulnar deviation. Flexion/ Extension of the wrist can be seen from (Figure 5.2). And the other movement of the wrist, radial-ulnar deviation can be seen from (Figure 5.3).

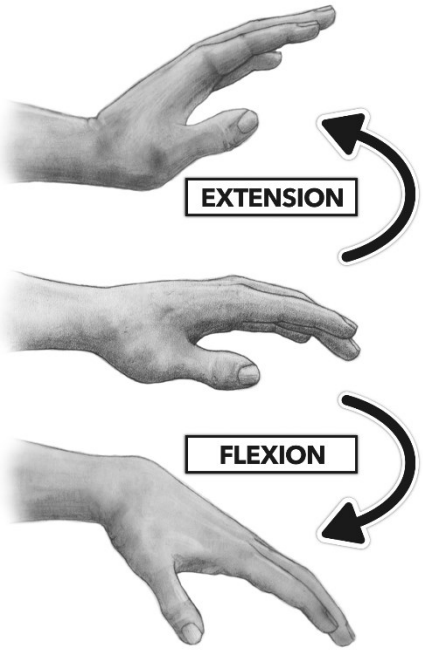

Figure 5.2 Wrist Flexion/ Extension [30]

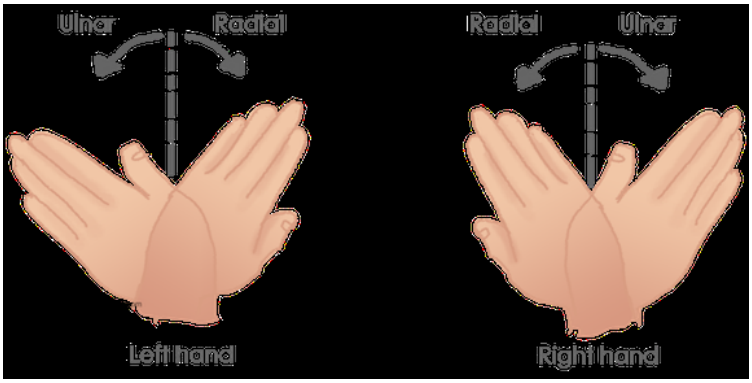

Figure 5.3 Wrist Radial Ulnar Deviation [31]

The nominal range of motion of all these movements of the forearm and wrist of the human body mentioned above can be found from [32] and shown in Table 5.1.

Table 5.1 Wrist joint range of movements

°**Types of motion**	**Anatomical Range of Human Forearm and Wrist** [32]		
	Source 1	Source 2	Source 3
Forearm Pronation	80°	90°	80°
Forearm Supination	80°	85°	90°
Wrist Flexion	60°	90°	60°
Wrist Extension	60°	70°	50°
Wrist Radial Deviation	20°	20°	20°
Wrist Ulnar Deviation	30°	30°	30°

The rehabilitative robot should be able to produce and allow the wearer to have a full range of motions for rehabilitation purposes.

To provide effective rehab therapy to the forearm and wrist, the UWM-FWRR developed in this research comprises 3DoFs such that it can provide a full range of motion to wearers' forearm and wrist joint when required. The anatomical range of forearm and wrist motions were carried out [33] to choose the suitable range for the UWM-FWRR while avoiding design complexity. The selected range of motion of the UWM-FWRR is given in *Table 5.2*.

Table 5.2 UWM-FWRR's Range of Motion

Types of Motion		*UWM-FWRR's* Workspace
Joint 1	Forearm Pronation	- 90°
	Forearm Supination	+90°
Joint 2	Wrist Flexion	+ 90°
	Wrist Extension	- 80°
Joint 3	Wrist Radial Deviation	+ 20°
	Wrist Ulnar Deviation	- 25°

5.1.2 **Lightweight design with low mass/inertia**

Exoskeleton types robots should be lighter while having structural rigidity to support the human bodies and provide the required movements at the same time. This type of device is worn by the user, and often the practical usage may require the user to wear the device on his/her body. A lighter structure can be actuated with the lower-powered motor. Having low mass lowers the effects of gravity and inertia.

All links of UWM-FWRR have been fabricated using Aluminum 6061 except the motors and gears. Aluminum has a very high strength to weight ratio, making it a suitable choice for developing a lightweight, rigid, yet easily manufacturable structure. In this research, brushless DC motors (Maxon EC45) have been used. Detailed specifications of these motors can be found in

APPENDIX – I .The design choice of the UWM-FWRR's actuator selection came from simulation results, which gives the joint torques required for providing movements to the specific user. These results can be seen from. From the joint torques found through simulation while considering human forearm and wrist mass, the torques required for actuator was calculated. Then suitable brushless DC motors were selected. Afterward, the CAD model was generated using links design that give effective structural integrity while serving the purpose of rehabilitation.

5.1.3 **Safety**

Exoskeleton type rehabilitative devices are attached to the human limb; therefore, the safety of the user one of the primary concerns when designing such devices. The device must not harm the user in any way. Precaution while designing such a structure must be taken. Such devices should have fail-safe measures integrated into the software used to control as well as the mechanical limits should be placed in the structure. Mechanical limits are crucial because in the events of software failure, the mechanical limits must prevent the robot from going beyond the range of motion, thus keeping the user safe.

To satisfy this requirement, mechanical stoppers have been used in UWM-FWRR's all three joints (Table 5.2). In the event of software failure, the mechanical stopper will prevent the mechanism from going beyond the nominal human range of motion keeping the user safe. In Joint 1 and Joint 3 soft stopper have been used to prevent the actuators from facing hard stop. Furthermore, an adjustable mechanical stopper has been integrated so that users with limited joint movements can also use this device without any worry. The actuators are covered so that no rotating parts will

come in contact with the user. These safety features will be elaborated while describing the design of UWM-FWRR in section *5.3.1 CAD Modeling*. The emergency switch is placed near the user during the experiment so that in the event of any difficulty user can press the switch, which cuts for power to all the actuators. On the software side, limits have been placed in the ranges of movements depending on patient requirements, joint speed, joint torques, and voltage supply values. The supply voltage is the final output of the controller used to control the motors.

5.1.4 **Comfort in wearing the exoskeleton robot**

Prescribed by the therapists and depending on the patients' requirements, the patient may undergo 30 to 90 minutes rehab therapy session. To facilitate this, exoskeleton type robotic rehabilitative devices should be such that user feels no discomfort while using the device. The device must be able to be fitted easily, adjustable to the user's forearm length, and should have the option to be removed easily. The user should not feel fatigued while using this type of device.

The UWJM-FWRR's joint used for producing forearm pronation/ supination motion to the human body gets attached to the forearm with the use of soft cuff. Provision has been made, so the metal parts of exoskeleton will not touch the user in any way. The user will hold a wrist handle for wrist Flexion/ Extension, and Radial/ Ulnar Deviation movement, and that handle is covered with soft cushioned foam. Moreover, UWM-FWRR has option for adjustability. This device was designed for typical adults [34]. Men and women with height range 5ft-6.2ft have been considered while designing UWM-FWRR. The links have the option to adjust depending on the user's forearm and

wrist dimensions. For easier mount and dismount of the device open type cuff has been used in the forearm cuff. Further description of the design will be provided in the section 5.3.1.

5.1.5 **Reduction of complexity**

To ensure mass acceptance of the device by wide variety of users, reduction of manufacturing cost is essential. Complex parts will require extensive manufacturing processes which result in increase in product price. Furthermore, simplicity in design will encourage industries to adopt to this device and commercialization of such devices will be hastened.

Throughout UWM-FWRR's development, a key design factor was the reduction of the design complexity so that the manufacturing can be done comparatively easily. Moreover, complex cable routing [35] in design has been avoided in UWM-FWRR rather, integrated actuated cuff has been designed for forearm pronation/ supination motion.

5.1.6 **Gravity force compensation**

While providing rehabilitation through an external device such as exoskeleton type robots, it is important that the mass of the device does not cause a burden to the user. Moreover, the device should be able to bear the load of user's arm as well. Otherwise, the user, while undergoing therapy, may incur extra load burden, which may have adverse effects.

UWM-FWRR's can compensate for the gravity in real-time. The non-linear controller "Computed Torque Control" used in controlling UWM-FWRR includes the mass/ inertia of the device itself

as well as the mass of the human forearm and wrist. This makes sure that during rehabilitation, the user will not have to bear any load of the device and his/ her arm segments.

5.2 **Development of *UWM-FWRR***

The development and control of UWM-FWRR can be divided into two major phases. One is hardware development, and the other is controller development. Steps and progression of these two phases are shown in *Figure 5.4* and *Figure 5.5*.

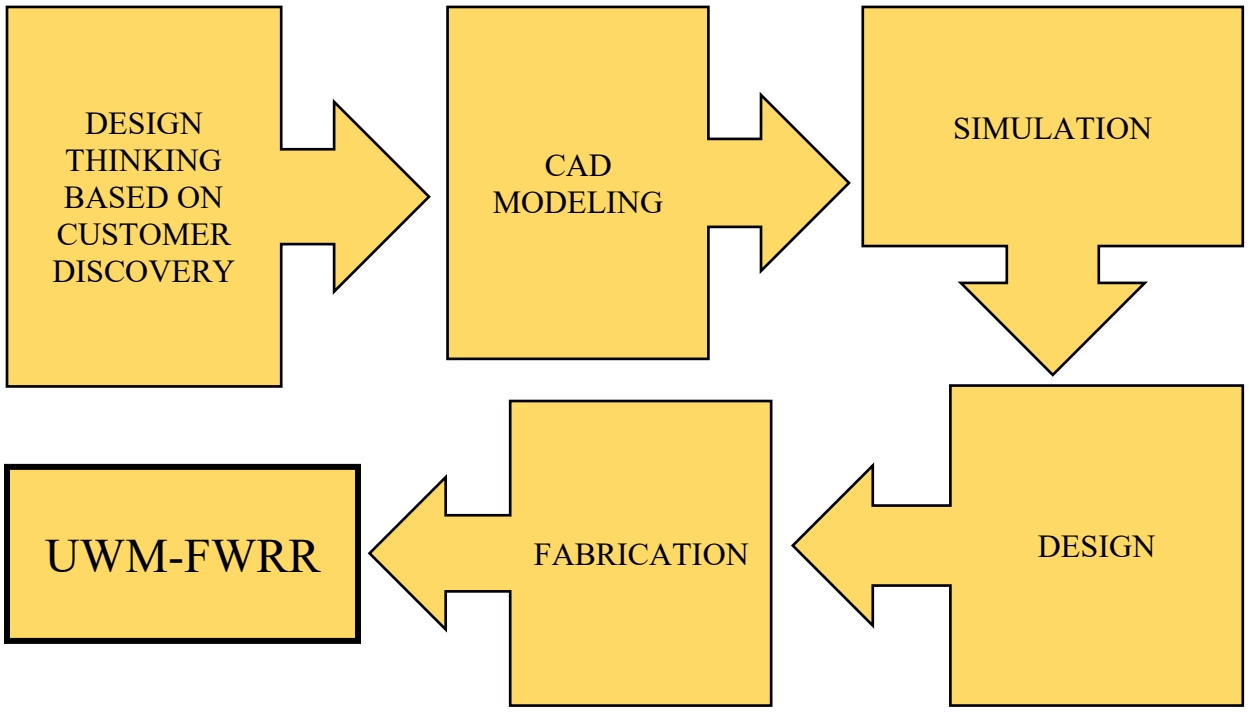

Figure 5.4 Hardware development phase of UWM-FWRR

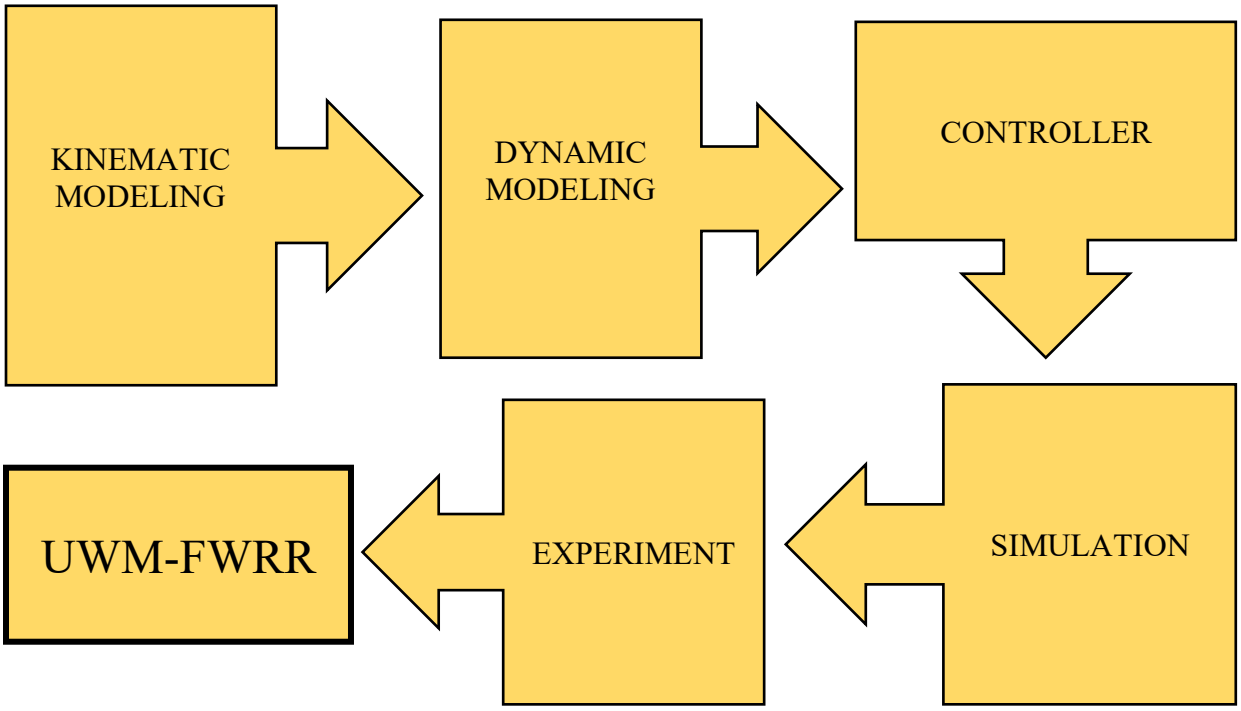

Figure 5.5 Control development phase of UWM-FWRR

5.3 **Hardware implementation of *UWM-FWRR***

5.3.1 **CAD Modeling**

To develop the CAD model of UWM-FWRR, detailed study of the biomechanics of human upper extremities was done beforehand to estimate the user parameters such as human forearm, hand length, mass of limb segments (APPENDIX – B), joint articulations and range of movements. Based on the design consideration, CAD modeling of the proposed exoskeleton type robot was done using *PTC-CREO software*. The mass and inertial parameters of the UWM-FWRR were calculated using PTC-CREO software with accurate mass property assignment of the elements. The mass and inertia properties used for simulation and design in shown in

5.3.2 **Simulation**

Simulation for development of UWM-FWRR was carried out in two phases. In the first phase, the kinematic and dynamics of the proposed mechanism was developed. Then the mass and inertia properties of initially modelled UWM-FWRR skeleton and mass of human limb segments were incorporated. The mass and dimension of human forearm and hand was obtained from [34] [10]. Then the parameters: Segment Length/ Stature, Segment Weight/Body Weight, Centre of Mass / Segment length and Radius of Gyration / Segment length, APPENDIX - A-II, and APPENDIX – B), was incorporated in PTC-CREO environment and mass and inertia properties were derived for simulation (APPENDIX – B to APPENDIX – H). Through simulation, the joint torques required for selection actuators were determined. For simulation MATLAB SIMULINK module was used. This method was used for optimizing the design for achieving greater power/ weight ratio. The simulated results have been shown in CHAPTER 7. After completion of design of UWM-FWRR, the second phase simulation was done to validate the joint torques with respect updated mass/ inertia properties and the range of motion allowed by the mechanism.

5.3.3 **Mechanical Design**

The UWM-FWRR comprises of 3 joints responsible for providing three different movements to the human forearm and wrist. *Figure 5.6* shows the rendered model of UWM-FWRR. The first part is the forearm motion support part, which gives the pronation/ supination movement to the forearm; the second one is responsible for providing radial/ ulnar deviation motion to the wrist,

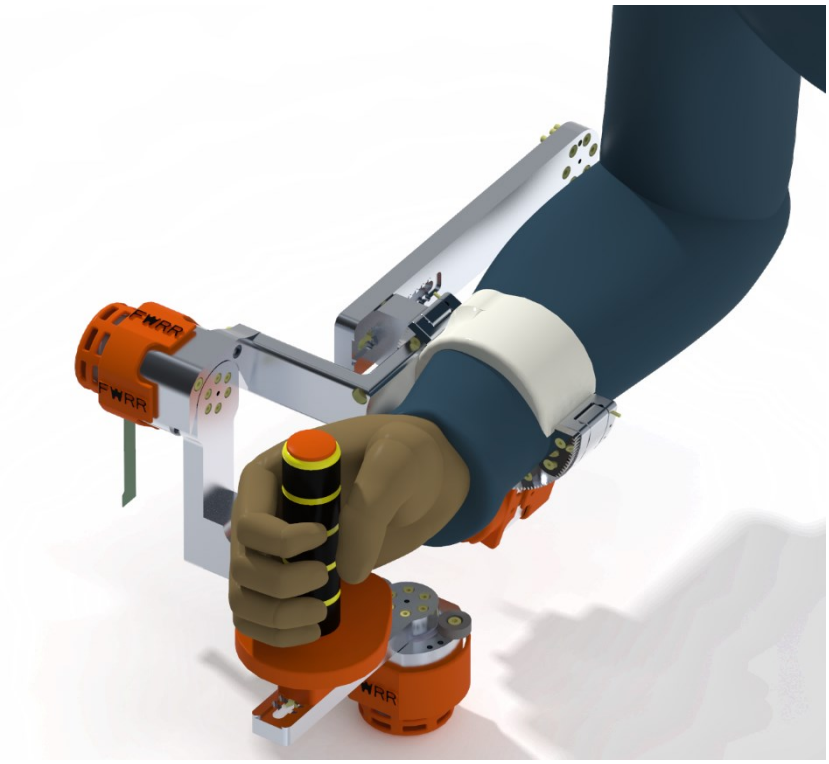

Figure 5.6 CAD Rendering of modelled UWM-FWRR in PTC-CREO

and finally, the third part with the wrist handle gives the wrist Flexion/ extension movement. *Figure 5.7* shows that the forearm motion support part includes a sliding link (link-I), motor-I (Maxon EC-45 30W), harmonic drive, and gear mechanism consisting a custom-made open type bearing (210°), an open ring gear (210°), and an anti-backlash gear mounted on the motor. The

forearm link depicted in *Figure 5.7* is connected to a stationary base through point-A and is set to be in parallel to the human forearm.

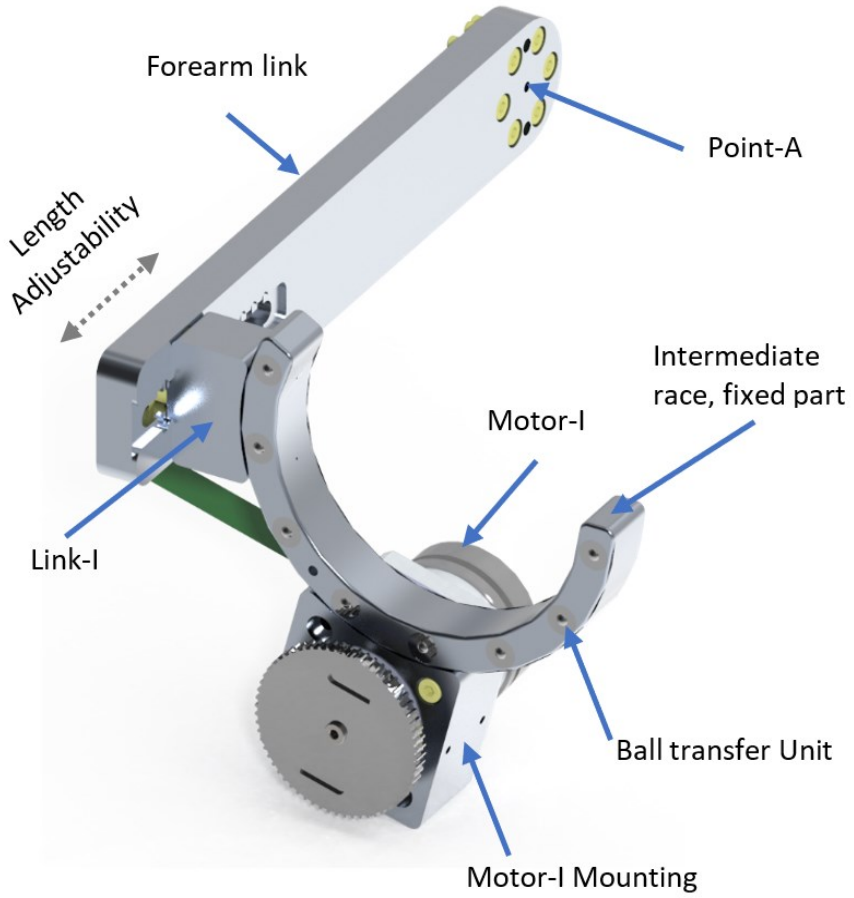

Figure 5.7 Forearm motion support part (forearm cuff is not assembled)

The outer circular ring/ intermediate race is rigidly connected to the forearm link via a sliding link (Link-I) which can be adjusted at 6mm increment and decrement to change the distance between the forearm cuff and the fixed base as well as to adjust the distance between the forearm cuff and wrist joints.

The open structure of the forearm cuff is designed for users' ease of placing their forearm, alleviating the need for inserting the forearm through a closed circular structure. The motor

(Maxon-EC45) is mounted on the back of the fixed outer circular ring through motor-I mounting *Figure 5.8* shows the anti-backlash gear, which is connected to the motor's shaft to transmit the rotary motion to the ring gear. The ring gear (open type) is attached to the forearm arm cuff (*Figure 5.8*) and produces rotation to the outer ring, which is connected to the forearm strap (*Figure 5.9*).

Finally, human upper arm/forearm is set in a proper position through the soft arm straps (*Figure 5.9*), as to when the motor drives the anti-backlash gear the rotation is transmitted to the human forearm thus creating 1st joint of FWRR and producing the "pronation-supination" movement to the forearm.

The custom open type bearing consists of intermediate race and outer ring (*Figure 5.8*). To reduce friction, several ball transfer units (BTU) have been fixed into both sides of the intermediate race. For creating a sliding path for the BTUs, grooves have been made into the insides of the outer ring. The unique installation technique for the outer race onto the intermediate race creates a lock that

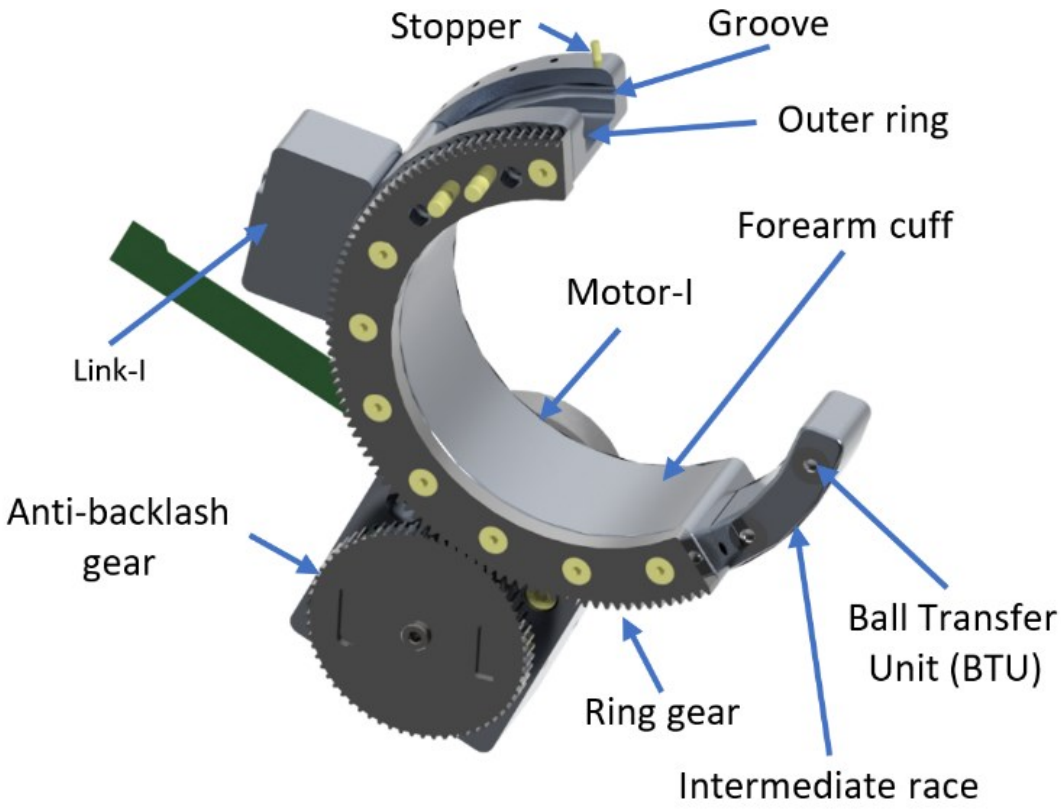

Figure 5.8 Forearm motion support part, showing the gear arrangement and forearm cup assembly to the fixed intermediate race

allows the outer race to be always mounted on the intermediate race. The wrist motion support part (as shown in *Figure 5.9*) has two degrees of freedom. One produces "radial/ulnar deviation" and the other gives 'flexion/extension' motion to the human wrist. To assist in the movement of radial/ulnar deviation (at wrist joint), the FWRR is comprised of an L type fixed link (link-II),

motor-II (Maxon EC-45 30W). Link-II (as shown in *Figure 5.9*) is fixed with the forearm cuff and houses the motor-II, which corresponds to 2nd joint (radial/ulnar deviation) of the FWRR.

The "radial/ulnar deviation" motion produced by motor-II is transmitted through Link- III and Link- IV to the motor-III mounting. Motor-III mounting houses the motor-III (Maxon EC45 30W), which gives the 'flexion/extension' motion to the human wrist through fixed Link-V and sliding

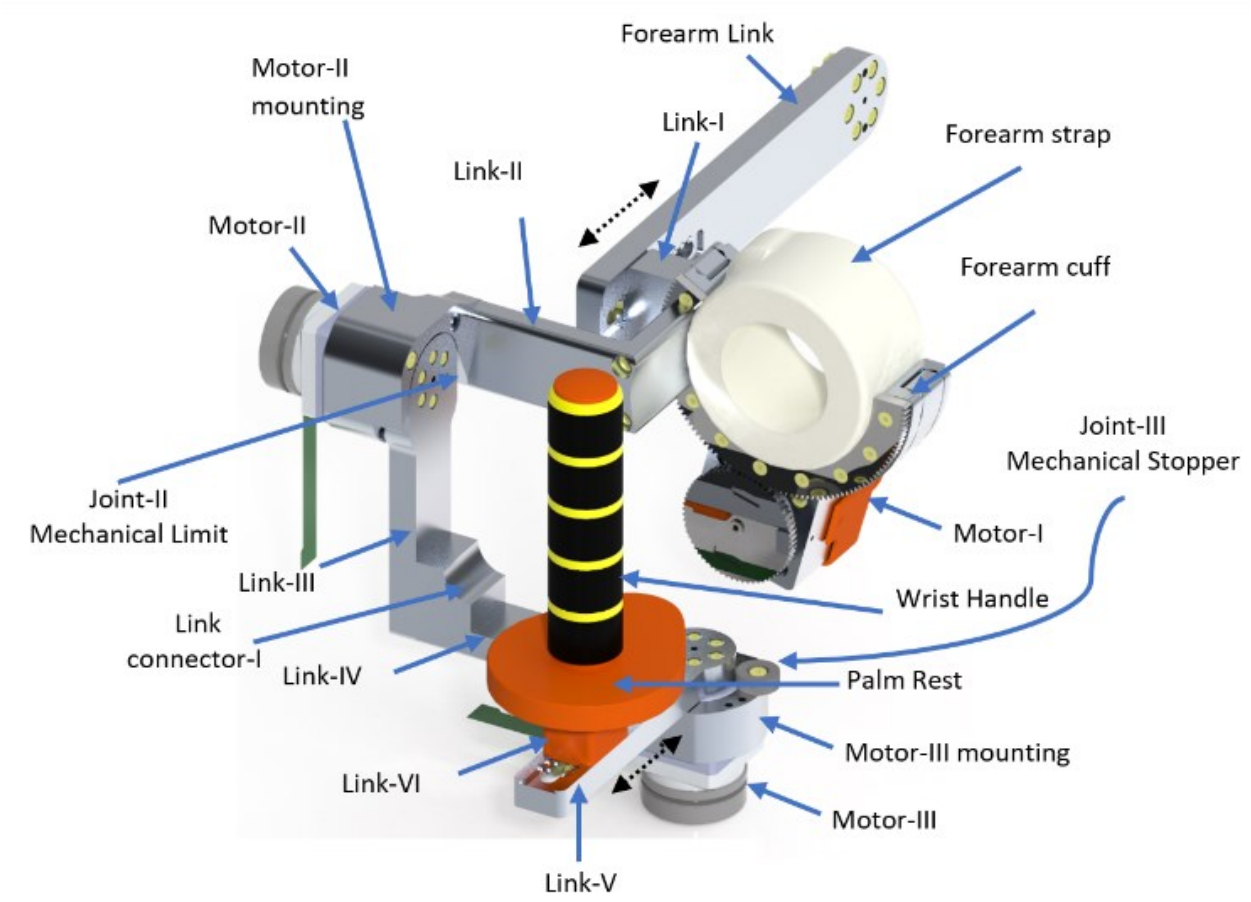

Figure 5.9 Wrist motion support part (2DoFs)

wrist handle (*Figure 5.9*). The sliding wrist handle can be positioned at 6mm increment or decrement distance from the center of rotation of the human wrist according to users' length of the

hand. The wrist handle acts as an end-effector producing both “radial/ulnar deviation” and ‘flexion/extension’ motion for the human wrist. Link connector-I connects Link-III and Link-IV.

5.3.4 **Electrical and Electronic Design of UWM-FWRR Instrumentation**

The electrical and electronic configuration for the UWM-FWRR system is depicted in *Figure 5.10*. It consists of a Host PC, a PXI Real-Time Target consisting of a NI PXIe-8135 real-time controller with a PXI Reconfigurable IO card with an embedded FPGA housed in a PXIe-1078 chassis, a main board, multiple motor driver cards, and actuators.

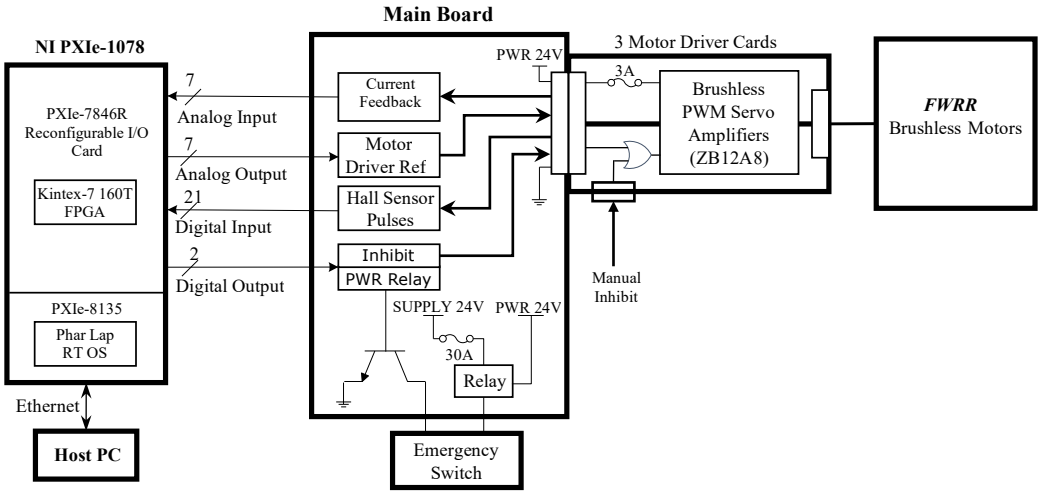

Figure 5.10 Electrical and electronic configuration for UWM-FWRR

5.3.4.1 **PXI Real-Time Target**

The PXI Real-Time Target consists of a National Instruments PXIe-8135 Real-Time Controller and a PXIe-7846R Reconfigurable IO card housed in a PXIe-1078 chassis. The PXIe-8135 Real-

Time Controller module includes a 3.3 GHz quad-core Intel Core i7-3610QE processor, 4GB dual-channel DDR3, 1600 MHz memory controller, and an integrated hard drive. The standard I/O on the module includes two DisplayPort video ports, one RS-232 serial port, a parallel port, four high-speed USB 2.0 ports, two high-speed USB 3.0 ports, a PCI-based GPIB controller, and two Gigabit Ethernet connectors. The module runs Phar Lap real-time OS provided by National Instruments that can execute the real-time portions of the LabVIEW code. It is connected to the PXIe-7846R card through National Instrument's PXI Express bus through the back panel of the PXIe-1078 Chassis. The module communicates with the Host PC via one of the two Gigabit Ethernet connectors. The PXIe-7846R reconfigurable IO Device with 8 Analog Inputs (±10V 16bit SAR ADCs), 8 Analog Outputs (±10V 16bit ER2R DACs), and 48 Digital I/O (3.3v LVTTL/LVCMOS Compatible) pins arranged across two connectors. The PXIe-7846R includes a Kinetix-7 FPGA processor that executes at a default clock speed of 40MHz and communicates with the RT OS by DMA through PXI Express bus. The FPGA unit reads and keeps track of joint positions by reading hall sensor pulses through digital inputs in a 100µs cycle. It also reads the current feedback from the motor drivers through analog inputs, applies a second-order filter before passing it to the controller running in RT OS. And finally, it gets the current signal from the controller in RT OS and executes a PI controller running at 50 µs frequency before outputting it through analog output pins.

5.3.4.2 **Main board**

The main board as shown in *Figure 5.10*, acts as a connection hub for all motor drivers and control units, and is powered by a 24V 42A switch mode DC power supply. The motherboard routes

various analog and digital signals from/to the PXI Real-Time Target from/to the FWRR system. For instance, it routes the current feedback of the motor drivers to the PXIe-7846R module's analog input; motor driver reference voltage signals from analog outputs of the PXIe-7846R module; and digital outputs (e.g., to activate the motors, relay switch control, etc.) from the PXIe-7846R module to the FWRR system. The board, as shown, was designed to have slots for motor driver cards, only one of which is depicted in *Figure 5.10*. Note that as a safety feature, an emergency stop switch was installed with the board to cut off the power in case of an emergency. In addition, a 30A quick blow fuse was also used to protect the whole system from short circuits.

5.3.4.3 **Motor driver cards**

Several identical slide-in cards carrying motor driver units are used for each motor in the FWRR system. The drivers used are Zilvertron-ZB12A8 type PWM servo amplifiers, industrial standard units for driving brushless DC motors at high switching frequency (33 kHz) (spec: reference voltage: ± 15 VDC; analog output: ± 10 VDC; maximum continuous current: ± 6 A). Note that, to double the safety features, a 3A slow blow fuses were installed in each of the motor driver cards. The cards contain circuitry to connect the motor driver's current reference and feedback signals to the PXI Real-Time Target as well as motor phases and hall sensor feedback signals to the motor through the motherboard. The cards also include circuitry to enable the motor driver unit's inhibit state depending on individual physical switches or inhibit signal from the motherboard.

5.3.4.4 **The Host PC**

The host PC, as depicted in the schematic (*Figure 5.10*), is used for user interface purposes. It is connected to the PXI Real-Time Target through ethernet and runs a non-real time portion of the LabVIEW code, and communicates to the Real-Time Target partially via Network Variables Various and via File Transfer Protocol (FTP). Commands including the activation and deactivation of the motor systems, setting and resetting the initial position of the robot joints, controller selection, trajectory selection, etc. are input via the user interface in the Host PC that is sent to the PXI Real-Time Target, and after completion of each trajectory run, the data recorded in the PXI Real-Time Target is sent back to the Host PC via FTP for storage.

5.3.4.5 **Actuators**

The motors used for the UWM-FWRR are brushless DC motors (APPENDIX – I) manufactured by Maxon Motor AG. The motors are three-phase brushless motor configuration with integrated hall sensors. Harmonic drives are incorporated into the motors in order to increase the torque and to reduce the speed of rotation. Detailed specifications of the HD can be found in APPENDIX – J.

5.3.5 **Safety**

Pronation/ Supination movement (Joint-1): Provision for mechanical limit has been introduced in the outer ring (*Figure 5.8*) at 10° interval that allows setting the device in a way that prevents the rotation of 1st Joint beyond the human range of motion or specific to the user. The total range of motion of this joint is +90° and -90°. A patient may be suggested by the therapists, not to rotate

his/ her forearm beyond +60° and -60°. Then mechanical limit can be adjusted so that the robot will not exceed this range of motion.

Radial/ Ulnar deviation (Joint-2): Mechanical limit is introduced to the motor mounting-II at +20° and -25° (*Figure 5.9*) to prevent the robot from going beyond the intended range of motion.

Flexion/ Extension (Joint-3): Adjustable soft Joint-III mechanical stopper has been introduced in the motor-III mounting (*Figure 5.9*) at 15° interval that allows setting the device in a way that prevents the rotation of 3rd Joint beyond the human range of motion or specific to the user.

If any motion reaches the set limit, then the mechanical current exceeding the programmed limit will flow through the current, and the control signal is sent to power down all actuators.

5.3.6 **Fabrication**

UWM-FWRR has been fabricated using machined aluminum with the use of traditional 3-axis CNC milling and CNC lathe machines. The spur gears (Anti-backlash drive gear of first joint and the open type spur gear) have been made using Stainless Steel (Grade SS-303).

5.3.7 **UWM-FWRR Overview**

The mass major mass inertia properties and adjustability of UWM-FWRR are shown in *Table 5.3 Mass and Inertia Properties of UWM-FWRR*. The mass and inertia properties of UWM-FWRR has been generated by material assignment to every component using PTC-CREO software. The mass of UWM-FWRR has been validated by taking the actual weight measurement of the robot components. The details of mass and inertia properties are given in APPENDIX – C, APPENDIX – D, APPENDIX – F, and APPENDIX – G.

Table 5.3 Mass and Inertia Properties of UWM-FWRR

Segment (*Figure 5.9*)	Segment length (mm)	Segment weight (kg)	Centre of gravity *CG (*mm)			Moment of Inertia *I at CG* (kg.mm^2)		
			CG_X	CG_Y	CG_Z	*Ixx*	*Iyy*	*Izz*
Base to Forearm cuff (Joint-1)	171.8 ± 24	0.974	-44.2	-131.9	41.7	368.5	2863.9	3910.3
Forearm cuff to wrist (Joint-2)	97.82	0.819	-7.35	94.1	-36.16	5711.20	1806.5	4635.9
Wrist (Joint-2) to Wrist (Joint-3)	121.5	0.696	0.27	-106.0	46.85	3554.18	2442.51	1353.3
Wrist (Joint-3) to Wrist handle (End-effector)	75±30	0.325	84.65	0.03	-52.28	754.06	1212.42	551.4

The design specs of the developed UWM-FWRR is summarized in *Table 5.4*.

Table 5.4 UWM-FWRR at a Glance

Material: Aluminum 6061 and SS 303		**Degrees of Freedom: 3**
	Range of movements (degrees)	
Joint-1	Joint-2	Joint-3
-90° to 90°	-25° to 20°	-80° to 90°
	Actuators (Brushless DC Servomotor)	
Specification	Maxon EC 45, Flat 30W (Joint-1)	
Nominal Voltage (V)	24	
Nominal Speed (rpm)	2940	
Torque Constant (mNm/A)	51	
Weight (g)	75	
	Harmonic Drives	
Specification:		CSF-11-100-2XH-F (Joint 1,2,3)
Torque at 2000 rpm (Nm)		5
Momentary Peak Torque, Nm		25
Repeated Peak Torque (Nm)		11
Gear Ratio		100
	Anti-Backlash Gear and Ring Gear (Pressure angle: 20^0 Pitch: 32)	
Specification	Anti-Backlash Spur Gear, S1A86A-C032A062 (Joint-1)	Open-type Ring Spur Gear Joint-1
Number of teeth	62	143
Bore Diameter (mm)	6.35	85

All links of UWM-FWRR have been fabricated using Aluminum 6061 except the motors and gears. Aluminum has a very high strength to weight ratio, making it a suitable choice for developing a lightweight, rigid, yet easily manufacturable structure. In this research, brushless DC motors (Maxon EC45) have been used. Detailed specifications of these motors can be found in

CHAPTER 6

KINEMATICS AND DYNAMICS

This chapter presents the details of the kinematic modeling and dynamic modeling done for design-optimization, simulation, and development of UWM-FWRR. For kinematic analysis, modified Denavit-Hartenberg (DH) notations were used. Iterative Newton-Euler methods were used for dynamic modeling. At first, the DH notation has been introduced. Then kinematic modeling has been explained. Secondly, equations used for dynamic modeling have been shown, and finally, singularity analysis has been shown using Jacobian.

6.1 **Kinematics**

In order to develop a functional and effective exoskeleton type robot for rehabilitation, the UWM-FWRR was modeled based on the anatomy and biomechanics of the human upper limb. The procedure of link frame attachment and the definition of modified DH parameters are briefly described in the following subsection.

6.1.1 **Coordinate Frame Assignment Procedure**

There are various ways to assign coordinate frames to the serial type manipulator links. For the Kinematic modeling of UWM-FWRR, the modified Denavit-Hartenberg method has been used [12]. The notations steps are as follows [9]:

- Assume each joint is 1DoF revolute joint;

- Identify and locate the axes of rotation;

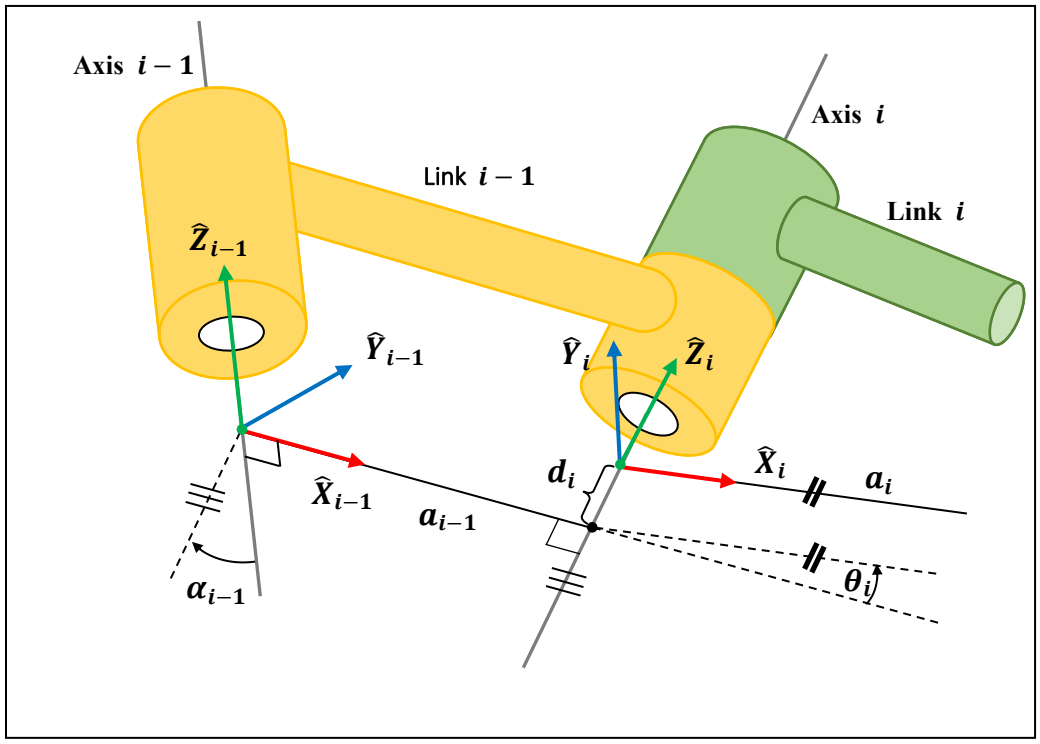

Figure 6.1 Coordinate frame assignment, Adapted from Craig (2005)

- Label the joint axes $Z_0, \ldots\ldots, Z_n$;
- Locate the origin of each link-frame (O_i) where the common perpendicular line between the successive joint axes (i.e., Z_{i-1} and Z_i) intersects. If the joint axes are not parallel, locate the link-frame origin at the point of intersection between the axes;
- Locate the X_i axis (at link frame origin O_i) as pointing along the common normal line between the axes Z_{i-1} and Z_i. If the joint axes intersect, establish X_i in a direction *normal* to the plane containing both axes (Z_{i-1} and Z_i);
- Establish the Y_i axis through the origin O_i to complete a right-hand coordinate system.

6.1.2 **Definition of D-H Parameters**

A serial link manipulator robot can be defined using four parameters (two parameters for describing the link itself and other two for describing the link's relation to a neighboring link) if we assign the co-ordinate frames as described above [9] . These parameters are defined as Denavit-Hartenberg (DH) parameters. The definitions of the DH parameters are as follows [36]:

- Link Length (a_i): the length measured along X_i, from axis Z_i to axis $Z_{i+1;}$
- Link Twist (α_i): the angle measured about X_i, from axis Z_i to axis $Z_{i+1;}$
- Link Offset (d_i): the distance measured along the axis $Z_{i;}$ from X_{i-1} *to* X_i, and
- Joint Angle (θ_i): the angle measured about Z_i, from X_{i-1} *to* $X_{i.}$

In order to do the kinematic and dynamic analysis of this serial link exoskeleton robot, modified

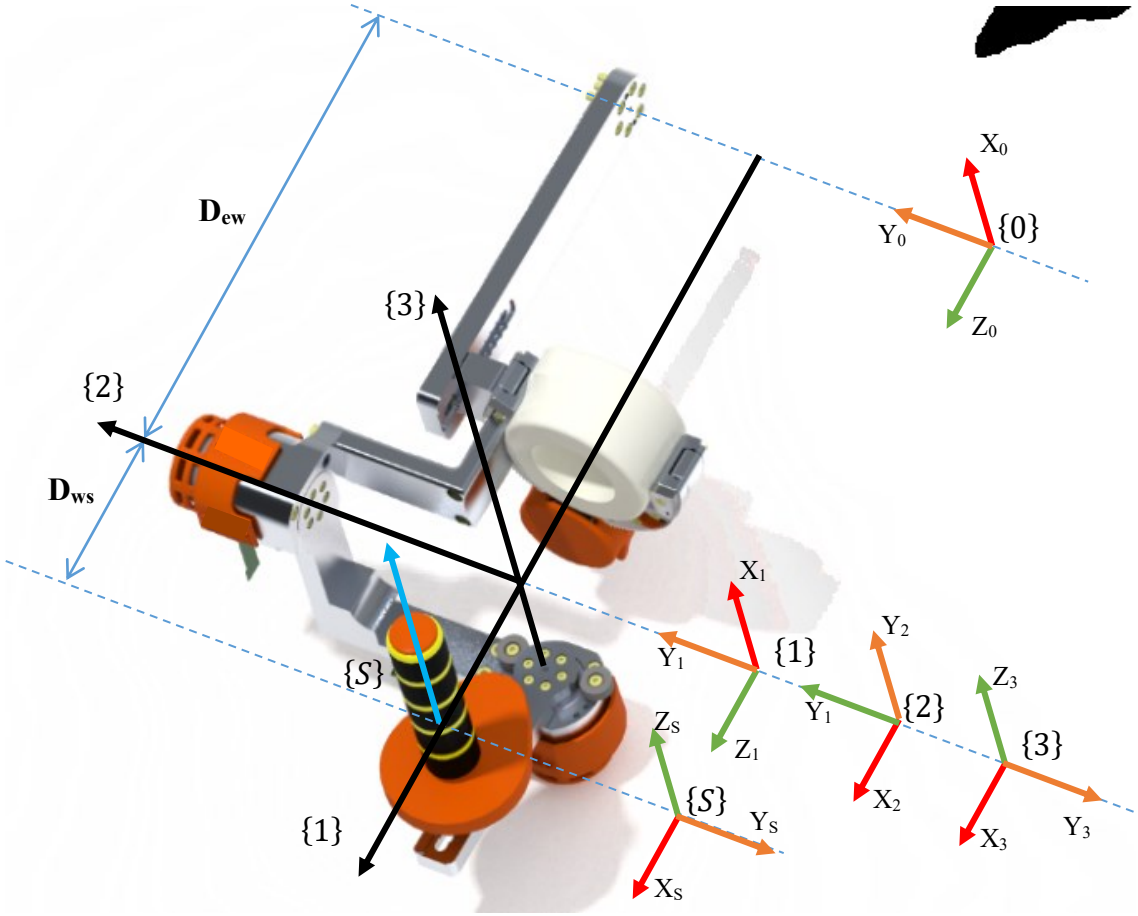

Figure 6.2 DH frames assignment of UWM-FWRR

Denavit-Hartenberg (DH) parameters have been used. The link frame assignment for FWRR can be seen in *Figure 6.2*.

To obtain the DH parameters, it has been assumed that the co-ordinate frames (i.e., the link-frames which map between the successive axes of rotation) coincide with the joint axes of rotation and have the same order, i.e., frame {1} coincides with joint 1 (forearm pronation-supination), frame

{2} with joint 2 (radial/ulnar deviation), and finally, frame {3} with joint 3 (wrist flexion/extension).

As shown in *Figure 6.2*, the joint axes of rotation of the FWRR corresponding to that of the human upper limb are indicated by dark black arrow heads (i.e., Zi). In this model, joints 1, 2, and 3 coincide together. We know that the general form of a link transformation that relates frame {i} relative to the frame {i-1} (Craig, 2005) is:

$$ {}^{i-1}_{i}T = \begin{bmatrix} {}^{i-1}_{i}R^{3\times3} & {}^{i-1}_{i}P^{3\times1} \\ 0^{1\times3} & 1 \end{bmatrix} \tag{6.1} $$

where, ${}^{i-1}_{i}R$ is the rotation matrix that represents the frame $\{i\}$ relative to frame $\{i-1\}$ and can be articulated as follows:

$$ {}^{i-1}_{i}R = \begin{bmatrix} \cos\theta_i & -\sin\theta_i & 0 \\ \sin\theta_i \cos\alpha_{i-1} & \cos\theta_i \cos\alpha_{i-1} & -\sin\alpha_{i-1} \\ \sin\theta_i \sin\alpha_{i-1} & \cos\theta_i \sin\alpha_{i-1} & \cos\alpha_{i-1} \end{bmatrix} \tag{6.2} $$

Table 6.1 Modified Denavit-Hartenberg parameters

Joint *(i)*	α_{i-1}	d_i	a_{i-1}	θ_i
1	0	*0*	D_{ew}	θ_1
2	-π/2	0	0	θ_2-π/2
3	-π/2	*0*	0	θ_3

where, α_{i-1} is the link twist, a_{i-1} corresponds to link length, d_i stands for link offset, and θ_i is the joint angle of the FWRR.

and, ${}^{i-1}_{i}P$ is the vector that locates the origin of frame $\{i\}$ relative to frame $\{i-1\}$ and can be expressed as the following:

$$ {}^{i-1}_{i}P = [a_{i-1} \quad -s\,\alpha_{i-1}\,d_i \quad c\,\alpha_{i-1}\,d_i]^T \tag{6.3} $$

Using Equations (6.1), (6.2), and (6.3), the individual homogeneous transfer matrix that relates two successive frames *Figure 6.2* can be found as:

$$ {}^{0}_{1}T = \begin{bmatrix} C_1 & -S_1 & 0 & 0 \\ S_1 & C_1 & 0 & 0 \\ 0 & 0 & 1 & D_{ew} \\ 0 & 0 & 0 & 1 \end{bmatrix} \tag{6.4} $$

$$ {}^{1}_{2}T = \begin{bmatrix} C_2 & -S_2 & 0 & 0 \\ 0 & 0 & 1 & 0 \\ -S_2 & -C_2 & 0 & 0 \\ 0 & 0 & 0 & 1 \end{bmatrix} \tag{6.5} $$

$$ {}^{2}_{3}T = \begin{bmatrix} C_3 & -S_3 & 0 & 0 \\ 0 & 0 & 1 & 0 \\ -S_3 & -C_3 & 0 & 0 \\ 0 & 0 & 0 & 1 \end{bmatrix} \tag{6.6} $$

The homogenous transformation matrix that relates frame {3} to frame {0} can be obtained by multiplying individual transformation matrices that result in the generic form (6.7).

$$ {}^{0}_{3}T = [{}^{0}_{1}T.{}^{1}_{2}T.{}^{2}_{3}T] \tag{6.7} $$

For FWRR the Equation (6.7) becomes Equation (6.8), where D_{ew} is the distance (see *Figure 6.2*) from base frame {0} to joint frames {1},{2}, and {3},

$$ {}^{0}_{3}T = \begin{bmatrix} S_1 S_3 + C_1 C_2 C_3 & C_3 S_1 - C_1 C_2 S_3 & -C_1 S_2 & 0 \\ C_2 C_3 S_1 - C_1 S_3 & -C_1 C_3 - C_2 S_1 S_3 & -S_1 S_2 & 0 \\ -C_3 S_2 & S_2 S_3 & -C_2 & D_{ew} \\ 0 & 0 & 0 & 1 \end{bmatrix} \tag{6.8} $$

The single transformation matrix thus found from Equation (6.8), represents the positions and orientations of the reference frame attached to the wrist joint (axis 3) with respect to the fixed reference frame {0}.

The distance from the wrist joint to the wrist handle (see *Figure 6.2*) is denoted as D_{ws}. Finally, the transformation matrix which relates the end effector (Wrist handle) frame {S} with the base frame {0} can be obtained through Equation (6.9).

$$ {}^{0}_{s}T = {}^{0}_{3}T . {}^{3}_{s}P \tag{6.9} $$

Upon usage of Equation (6.9), the transformation matrix Equation (6.10) is formed, which gives the position and orientation of the wrist handle frame {S} with the fixed base frame {0}.

$$ {}^{0}_{S}T = \begin{bmatrix} R_{xx} & R_{yx} & R_{zx} & P_x \\ R_{xy} & R_{yy} & R_{zy} & P_y \\ R_{xz} & R_{yz} & R_{zz} & P_z \\ 0 & 0 & 0 & 1 \end{bmatrix} \tag{6.10} $$

Where,

$R_{xx}= \quad S_1 S_3 + C_1 C_2 C_3;$ $\qquad R_{yx}= \quad C_3 S_1 - C_1 C_2 S_3;$

$R_{zx}= \quad -C_1 S_2;$

$R_{xy}= \quad C_2 C_3 S_1 - C_1 S_3;$ $\qquad R_{yy}= \quad -C_1 C_3 - C_2 S_1 S_3;$

$R_{zy}= \quad -S_1 S_2;$

$R_{xz}= \quad -C_3 S_2;$ $\qquad R_{yz}= \quad S_2 S_3;$

$R_{zz}= \quad -C_2;$

$P_x= \quad D_{ws}(S_1 S_3 + C_1 C_2 C_3);$ $\quad P_y= \quad D_{ws}(C_2 C_3 S_1 - C_1 S_3);$

$P_z= \quad D_{ew} - D_{ws} C_3 S_2;$

The vector that gives the position of the wrist handle with respect to frame {0} (*Figure 6.2*) is denoted by Equation (6.11) and (6.12).

$$ {}^{3}_{s}P = [S_x \quad 0 \quad 0]^T \tag{6.11} $$

$$ {}^{0}_{S}P = \begin{bmatrix} D_{ws}(S_1\, S_3 + C_1 C_2 C_3) \\ D_{ws}(C_2\, C_3\, S_1 - C_1 S_3) \\ D_{ew} - D_{ws} C_3 S_2 \end{bmatrix} \tag{6.12} $$

The above equations are used to define the workspace of the developed FWRR and, finally, the application of various control approaches.

6.2 **Dynamics**

To simulate the joint movements of UWM-FWRR and for experimentation using nonlinear control such as Computed Torque control, the dynamics of UWM-FWRR have been analyzed. Dynamics calculates the motion of bodies under the action of external forces. Among the different established methods found in literature, the iterative Newton-Euler formulation and the Lagrangian formulation are used widely for the development of the dynamic model of manipulators. The Newton-Euler approach is 100 times (computationally) more efficient compared to the Lagrangian approach [12] for 3 DoF robots such as UWM-FWRR. Therefore, the iterative Newton-Euler method [37] has been used to develop a dynamic model for this robot. A brief overview of this method is as such:

Iterative Newton-Euler Formulation:

In this approach, the manipulator's joint torque is computed iteratively using Newton's and Euler's equations. For a rigid body manipulator, Newton's and Euler's equations can be expressed as follows:

Newton's Equation:

$$F = m\dot{v}_C \tag{6.13}$$

where F is the force acting at the center of mass, m, of a rigid body, therefore moving the mass at acceleration $\dot{v}_C$.

Euler's Equation:

$$N = {}^{C}I\dot{\omega} + \omega \times {}^{C}I\omega \tag{6.14}$$

where N is the moment acting on a rigid body having inertia tensor ${}^{C}I$ at its center of mass, causing the motion of the rigid body with angular velocity and acceleration, ω, $\dot{\omega}$ respectively.

The algorithm to compute joint torques (τ_i) as well as to derive the dynamic model of a manipulator includes the following steps:

- Outward iterations:

  First step: Interactively compute the link angular velocities and linear and angular accelerations from the first link out to the n_{th} link.

  Second step: Computation of inertial force and torque of each link acting at the center of mass, using Newton-Euler equations.

- Inward iterations:

  Third step: Computation of forces and torques of interaction and joint, recursively from the n_{th} link back to the first link. A complete derivation of Newton-Euler formulation can be found in [12].

The dynamic equation of a manipulator (considering rigid body) derived from the Newton-Euler formulation can be found using equation (6.15):

$$\tau = M(\theta)\ddot{\theta} + V\left(\theta, \dot{\theta}\right) + G(\theta) \tag{6.15}$$

where $M(\theta)$ is the $n \times n$ mass matrix,

$V\left(\theta, \dot{\theta}\right)$ is an $n \times 1$ vector of centrifugal and Coriolis terms, and

$G(\theta)$ is an $n \times 1$ vector of gravity terms.

By adding friction to the model, the dynamic equation (6.15) results in equation (6.16):

$$\tau = M(\theta)\ddot{\theta} + V\left(\theta, \dot{\theta}\right) + G(\theta) + F\left(\theta, \dot{\theta}\right) \tag{6.16}$$

where $F\left(\theta, \dot{\theta}\right) \in \mathbb{R}^3$ is the vector of nonlinear Coulomb friction and can be expressed by equation (6.17).

$$F\left(\theta, \dot{\theta}\right) = c.sgn\left(\dot{\theta}\right). \tag{6.17}$$

UWM-FWRR Parameters:

The mass terms $M(\theta)$, centrifugal & Coriolis terms $V\left(\theta, \dot{\theta}\right)$, and gravity terms $G(\theta)$ in Equation (6.15) were computed both symbolically and numerically in MATLAB (The MathWorks, USA). The center of mass of the robot, UWM-FWRR, was generated using PTC-CREO software (see APPENDIX – C to H). The human masses used for the simulation and experiments were used from [32] (see APPENDIX – B).

6.3 **Jacobians**

In robotics, Jacobians $J(\theta)$ are used to relate joints' velocities to the Cartesian velocities of end-effector [12]. General equation of Jacobian in a robot manipulator,

$$^{0}v = {}^{0}J(\theta)\dot{\theta} \tag{6.18}$$

For a 3 DoFs robot,

the Jacobian is 6×3 matrix, $\dot{\theta}$ is 3×1 vector, and ^{0}v is 6×1 vector.

This 6×1 Cartesian velocity vector is comprised of a 3×1 linear velocity vector (v) and 3×1 rotational velocity vector (ω).

$$^{0}v = \begin{bmatrix} {}^{0}v \\ {}^{0}\omega \end{bmatrix} \tag{6.19}$$

The Jacobian of *UWM-FWRR* was computed using MATLAB/Simulink (The MathWorks, USA). The Jacobian of any dimension can be defined. The number of rows equals the number of Doffs in the Cartesian space and number of columns in a Jacobian is equal to the number of joints for the robotic manipulator.

CHAPTER 7

CONTROL AND SIMULATION

7.1 PID Control

For initial testing and control of the developed UWM-FWRR, PID control technique has been used [12]. The general layout of the PID control approach used for FWRR is depicted in Figure 7.1. The joint torque commands are expressed by the equation (7.1):

$$\tau = K_P(\theta_d - \theta) + K_V\left(\dot{\theta}_d - \dot{\theta}\right) + K_I \int (\theta_d - \theta)\, dt \tag{7.1}$$

Where,

$\theta_d, \theta \in \mathbb{R}^3$ are the vectors of desired and measured joint angles,

$\dot{\theta_d}$, $\dot{\theta} \in \mathbb{R}^3$ are the vectors of desired and measured joint velocities,

K_P, K_V, K_I are the diagonal positive definite gain matrices,

$\tau \in \mathbb{R}^3$ is the generalized torque vector.

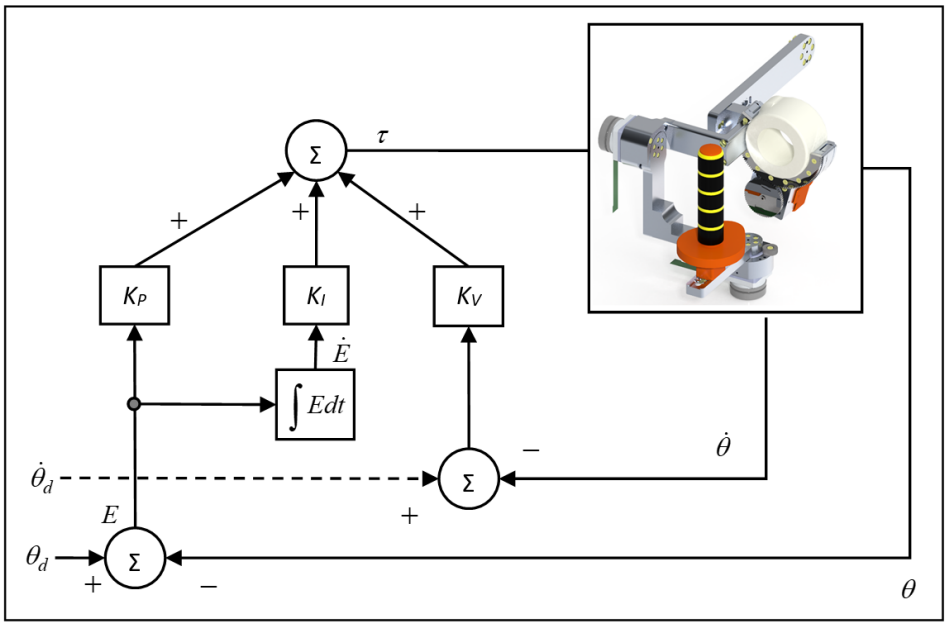

Figure 7.1 Schematic of PID control

E is an error vector and its derivative $\dot{E}$ given by equation (7.2)(7.3):

$$E = \theta_d - \theta \tag{7.2}$$

$$\dot{E} = \dot{\theta_d} - \dot{\theta} \tag{7.3}$$

Therefore, this equation (7.1) has been re-formulated as an error equation (7.4):

$$\tau = K_P E + K_V \dot{E} + K_I \int E\, dt \tag{7.4}$$

By decoupling relation (7.4), individual torque command for each joint is given by Equation (7.5).

$$\tau_i = K_{P_i} e_i + K_{V_i} \dot{e}_i + K_{I_i} \int e_i \, dt \tag{7.5}$$

7.1.1 **Simulation with PID control**

With the SIMULINK (MathWorks, USA) software, the simulations for UWM-FWRR with PID control have been done. A brief description of the trajectories used in the simulations (throughout this CHAPTER 7) are presented below:

Forearm Pronation/ Supination (Joint-1) trajectory:

After 0.5s this joint starts from 0° then completes +85° to -85° and returns to 0° within 6s, and then there's a 0.5s delay. Afterward the same trajectory is run within 4s, and after the same delay, then trajectory is run within 3s. The generated trajectory for Forearm Pronation/ Supination, associated velocity and acceleration profile can be seen from *Figure 7.2*.

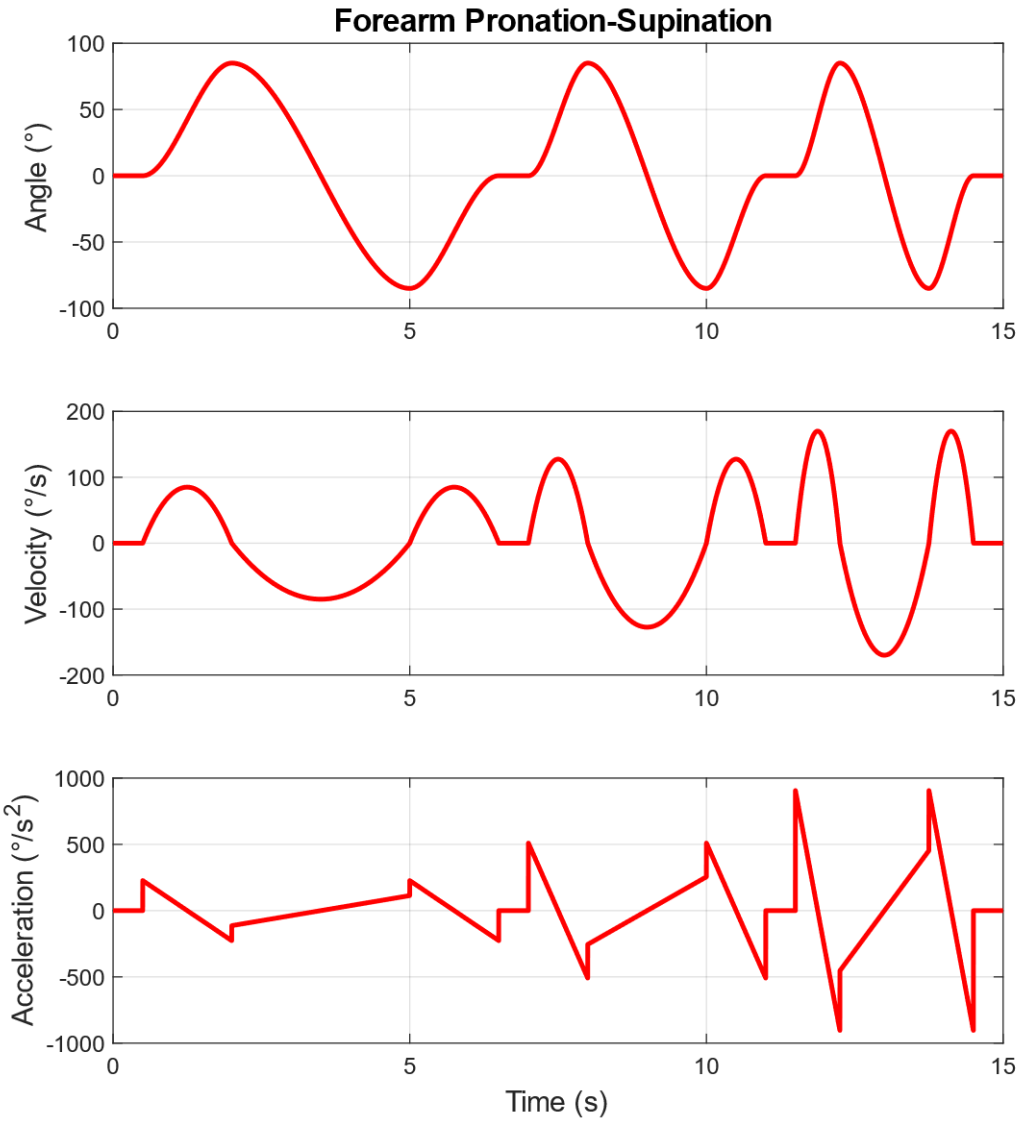

Figure 7.2 Generated trajectory for Forearm Pronation/ Supination movement

Wrist Radial/ Ulnar Deviation (Joint-2) trajectory:

After 0.5s this joint starts from 0° then completes +20° to -25° and returns to 0° within 6s, and then there's a 0.5s delay. Afterward the same trajectory is run within 4s, and after the same delay,

then trajectory is run within 3s. The generated trajectory for Wrist Radial/ Ulnar Deviation movement, associated velocity and acceleration profile can be seen from *Figure 7.3*.

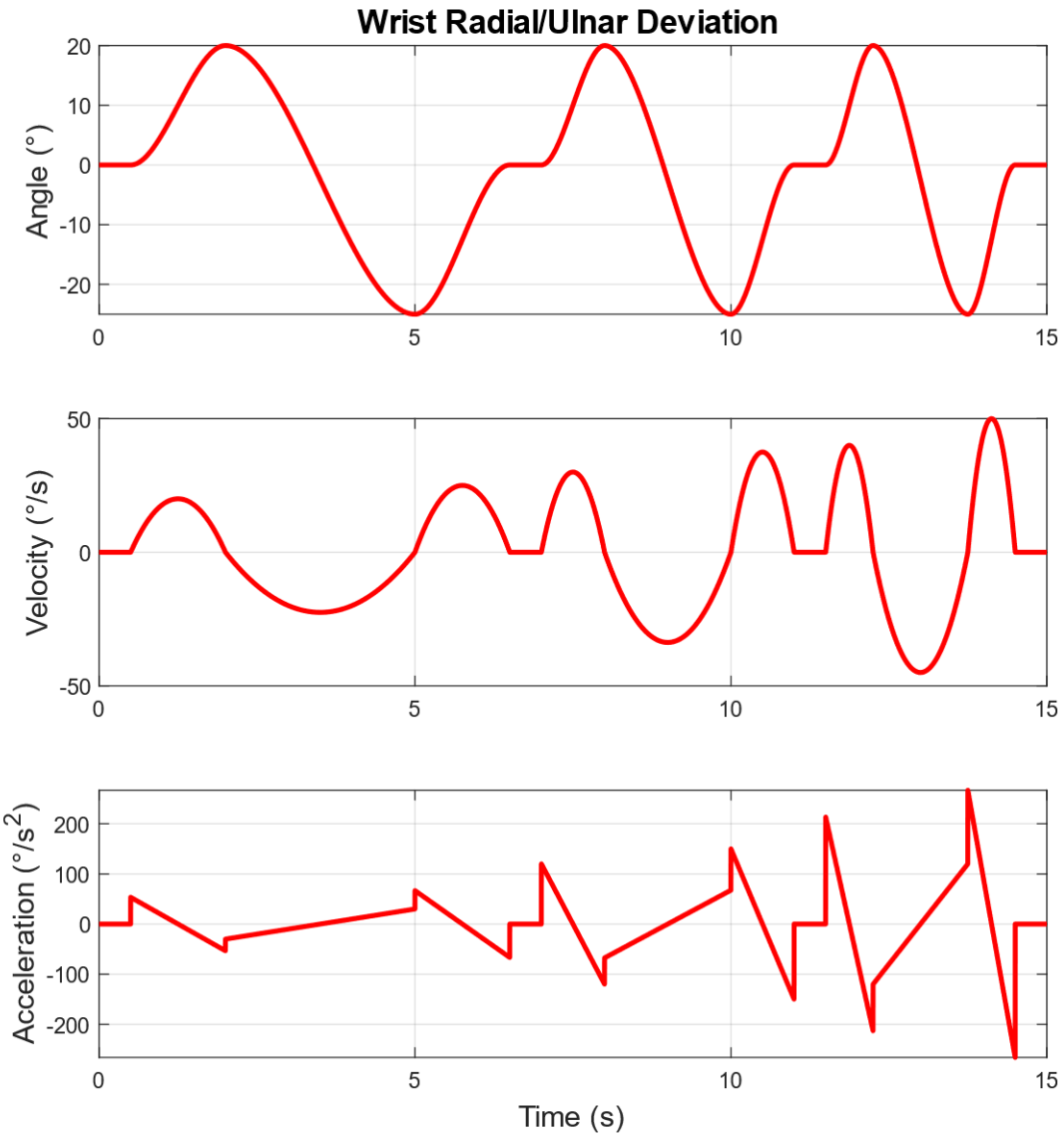

Figure 7.3 Generated trajectory for Wrist Radial/ Ulnar Deviation movement

Wrist Flexion/ Extension (Joint-3) trajectory:

After 0.5s this joint starts from 0 ° then completes +60° to -60° and returns to 0° within 6s, and then there's a 0.5s delay. Afterward the same trajectory is run within 4s, and after the same delay, then trajectory is run within 3s. The generated trajectory for Wrist Flexion/ Extension movement, associated velocity and acceleration profile can be seen from *Figure 7.4*.

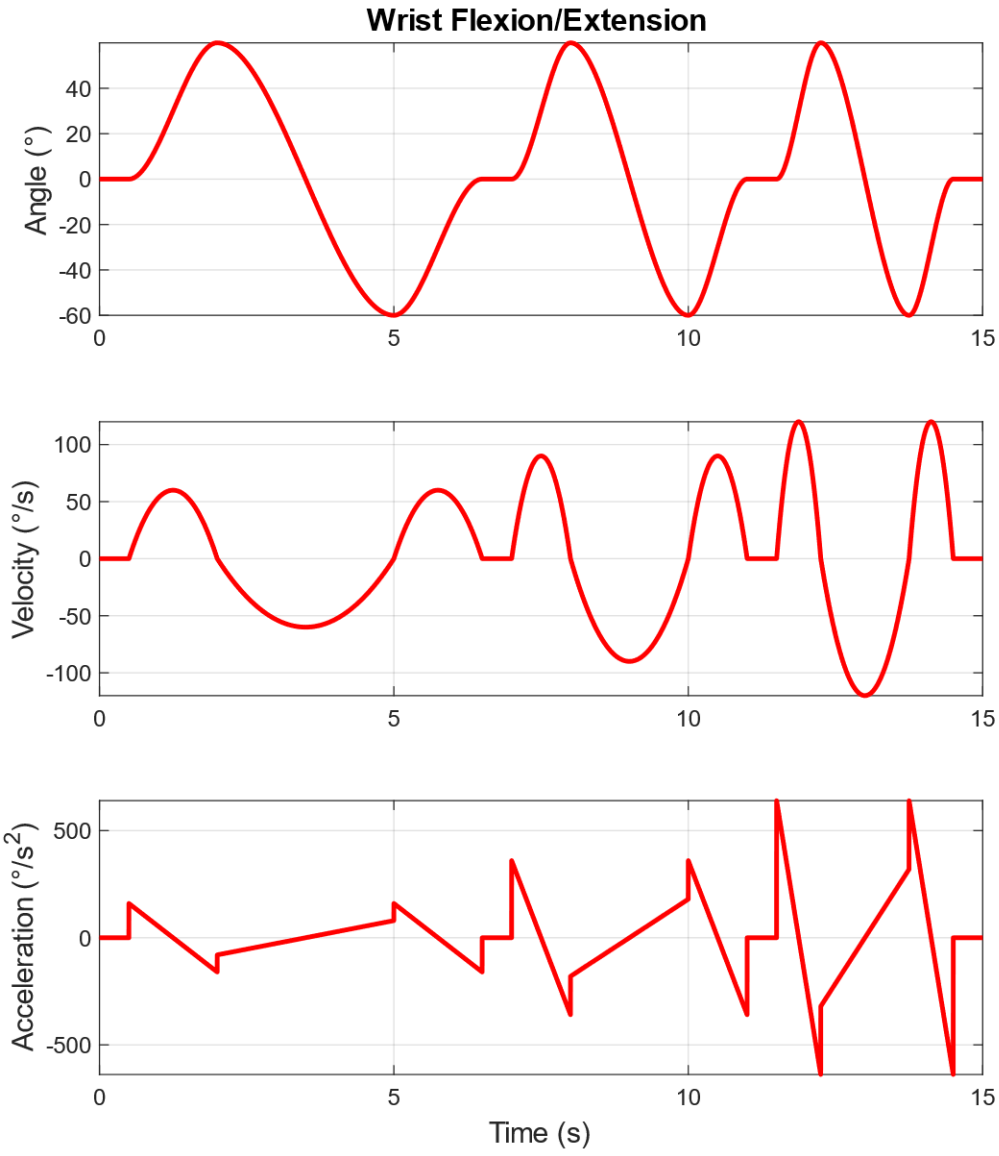

Figure 7.4 Generated trajectory for Wrist Flexion/ Extension movement

In all cases, initial velocities and acceleration are given as zero. Note that the desired trajectories and associated velocities were generated using the cubic polynomial approach [12]. The control gains used for the simulation were found by trial and error, and are as follows:

$$K_P = diag[300 \quad 200 \quad 200],$$

$$K_V = diag[10 \quad 10 \quad 1.5], \text{ and}$$

$$K_I = diag[0.5 \quad 0.1 \quad 0.1].$$

7.1.1.1 **Simultaneous Joint movements without disturbance (PID)**

All three joints (Joint-1 – range: +85° -85°, Joint-2 – range: +20° -25°, & Joint-3 – range: +60° -60°) move at the same time period (15s) and follows the trajectory mentioned above. The simulated results can be seen in *Figure 7.5*, *Figure 7.6*, *Figure 7.7*, and *Figure 7.8*. The tracking performance of all three joints' simultaneous movement can be seen from *Figure 7.5*, where 1st column corresponds to Joint-1, and the 2nd and 3rd column corresponds to Joint-2 and Joint-3, respectively. The first row shows the trajectory comparison (Given joint angles – red dotted line, Measured joint angles – solid blue line) for three joints. The second row shows the tracking error, and the third row shows the measured torque from the simulation. Here the maximum tracking error found to be less than 0.5° (0.7%), which proves that the tracking performance is quite good. *Figure 7.6*, Figure 7.7, and *Figure 7.8* shows the plots of the joints separately. Here, the given velocities (third row) are denoted with the red dotted line, and the measured trajectory from the simulation is shown with a solid blue line. Throughout subsection 7.1.1, 7.2.1, and 7.2.2, the notations for figures are kept consistent. Maximum joint torque (using robot mass only) for Joint-1 found to be -2 Nm and

+1 Nm, for Joint-2, the maximum joint torque is -0.3 Nm and +0.5 Nm, and for Joint-3 it is -0.2 Nm and +0.2 Nm. The positive and negative signs denoted the direction of the joint torques.

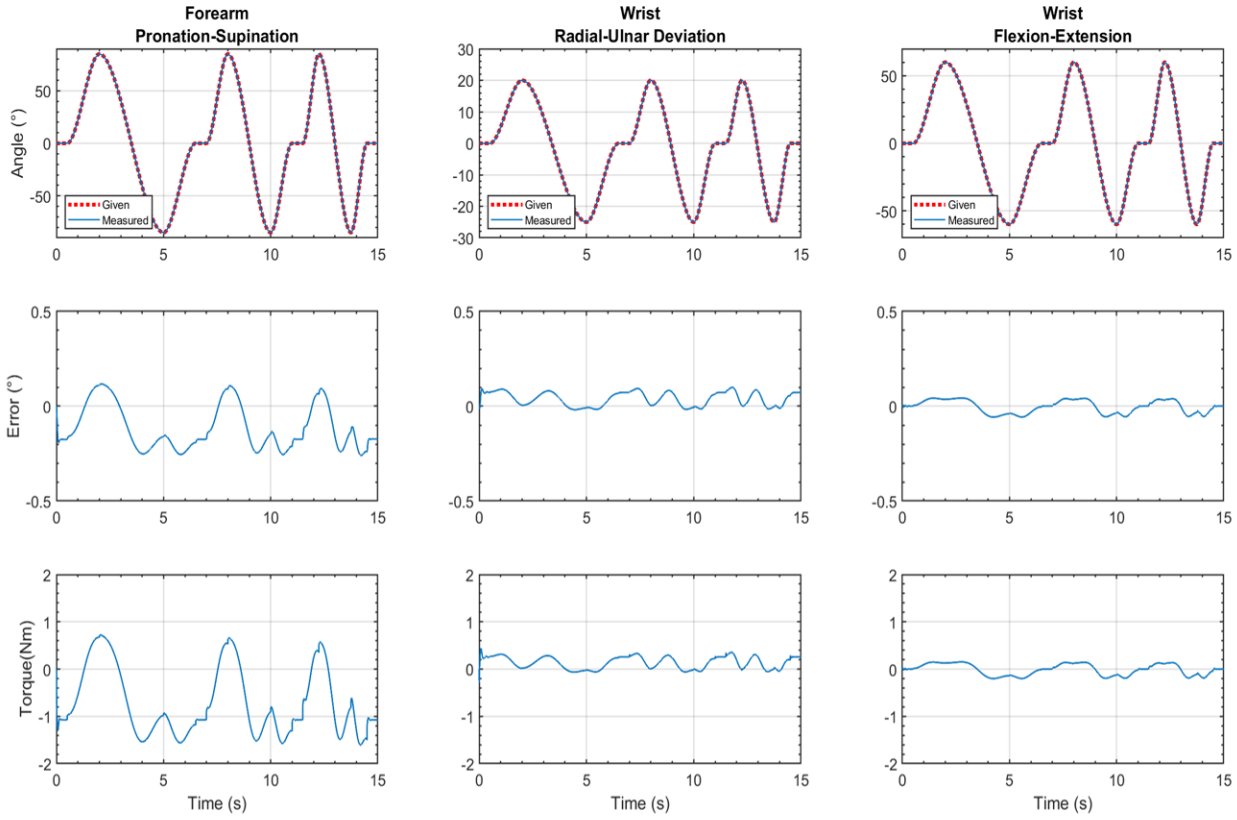

Figure 7.5 All three joints *simultaneous motion w/o disturbance (PID)*

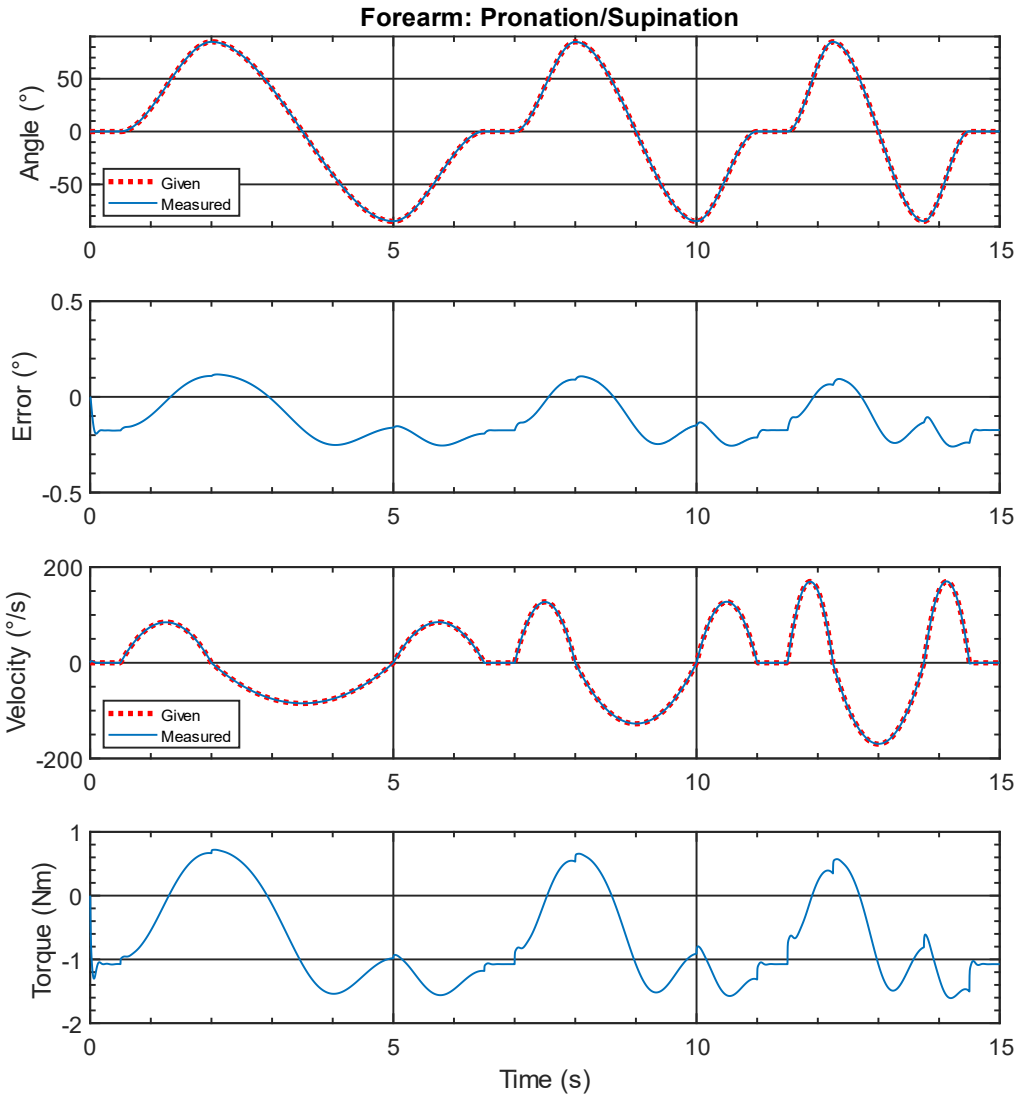

Figure 7.6 All three joints simultaneous movement (detail of Joint-1 movement with velocity comparison w/o disturbance (PID)

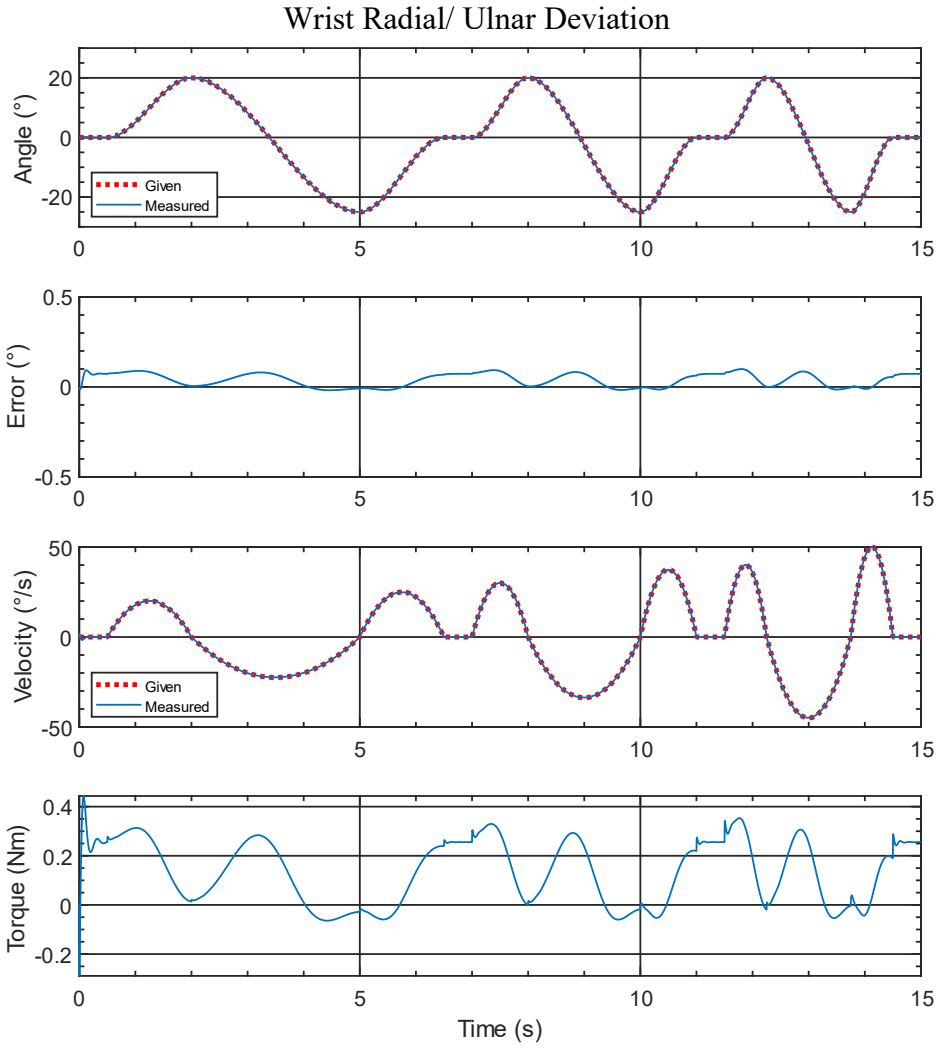

Figure 7.7 All three joints simultaneous movement (detail of Joint-2 movement with velocity comparison) w/o disturbance (PID)

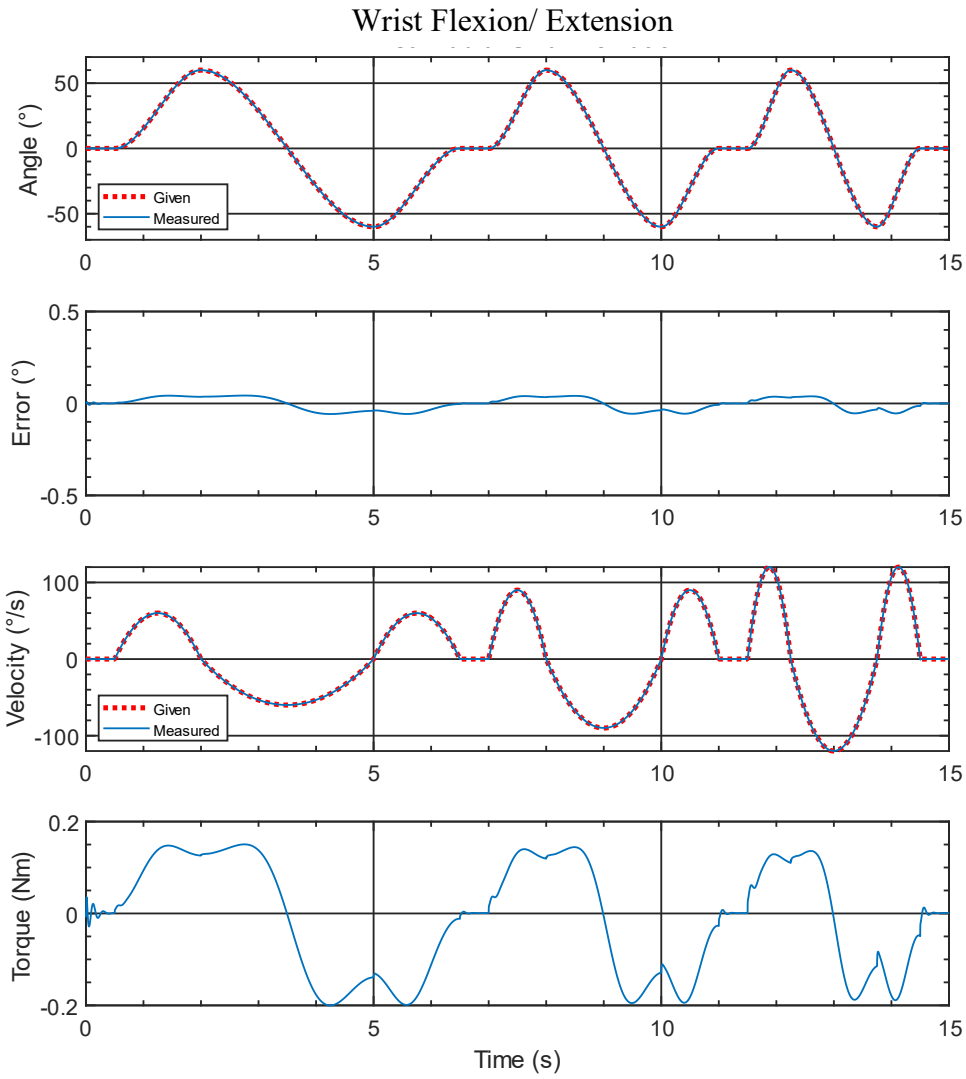

Figure 7.8 All three joints simultaneous movement (detail of Joint-3 movement with velocity comparison) w/o disturbance (PID)

7.1.1.2 **Individual Joint -1 movement without disturbance (PID)**

Only Joint-1 moves (range: +85° -85°) at the period of 15s and Joint-2 & Joint-3 stays at 0° angular position. The simulated results can be seen from *Figure 7.9*, *Figure 7.10*, *Figure 7.11*, and, *Figure 7.12*. Tracking performance of all three joints can be seen from *Figure 7.9* where, 1st column corresponds to Joint-1, and 2nd and 3rd column corresponds to Joint-2 and Joint-3 respectively. First row shows the trajectory comparison (Given joint angles – red dotted line, Measured joint

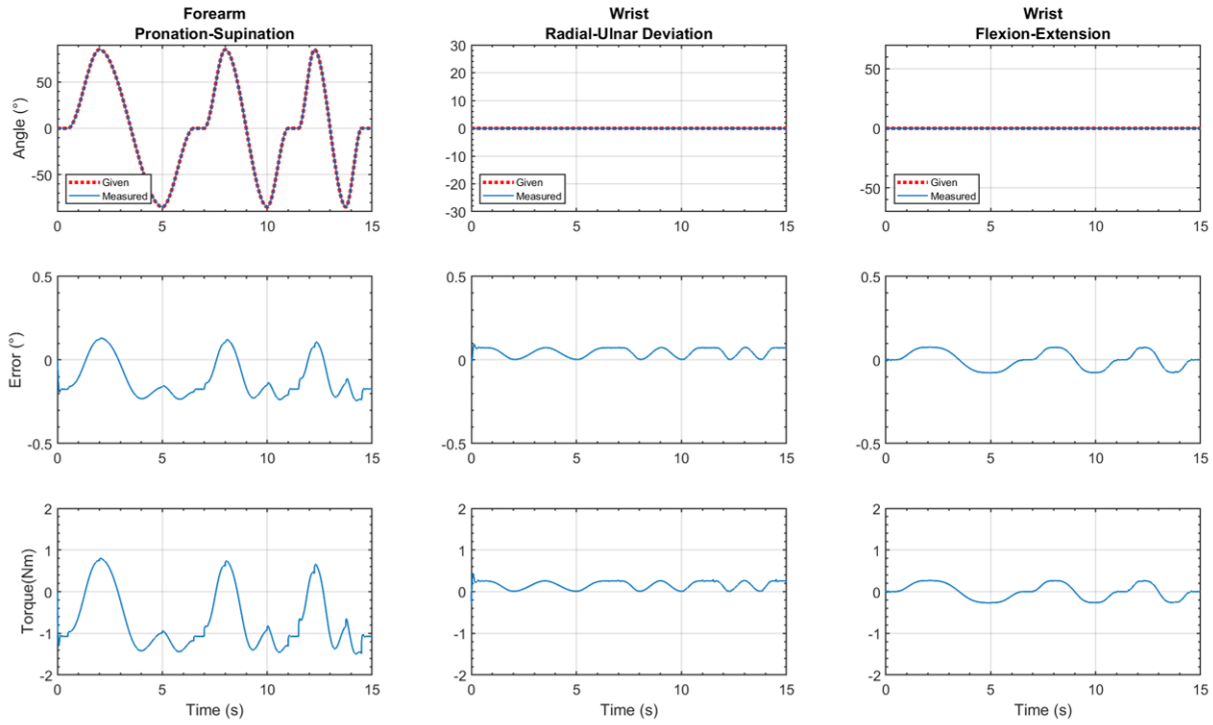

Figure 7.9 Plots of all three joints during Individual Joint-1 movement w/o disturbance (PID)

angles – solid blue line) for three joints. The second row shows the tracking error, and the third row shows the measured torque from the simulation.

Here the maximum tracking error found to be less than 0.5° (0.7%), which proves that the tracking performance is quite good. *Figure 7.10*, *Figure 7.11*, and *Figure 7.12* shows the plots of the joints separately. Maximum joint torque (using robot mass only) for Joint-1 found to be -1.5 Nm and +1 Nm, for Joint-2, the maximum joint torque is -0.3 Nm and +0.5 Nm, and for Joint-3 it is -0.3 Nm and +0.3 Nm. The positive and negative signs denoted the direction of the joint torques.

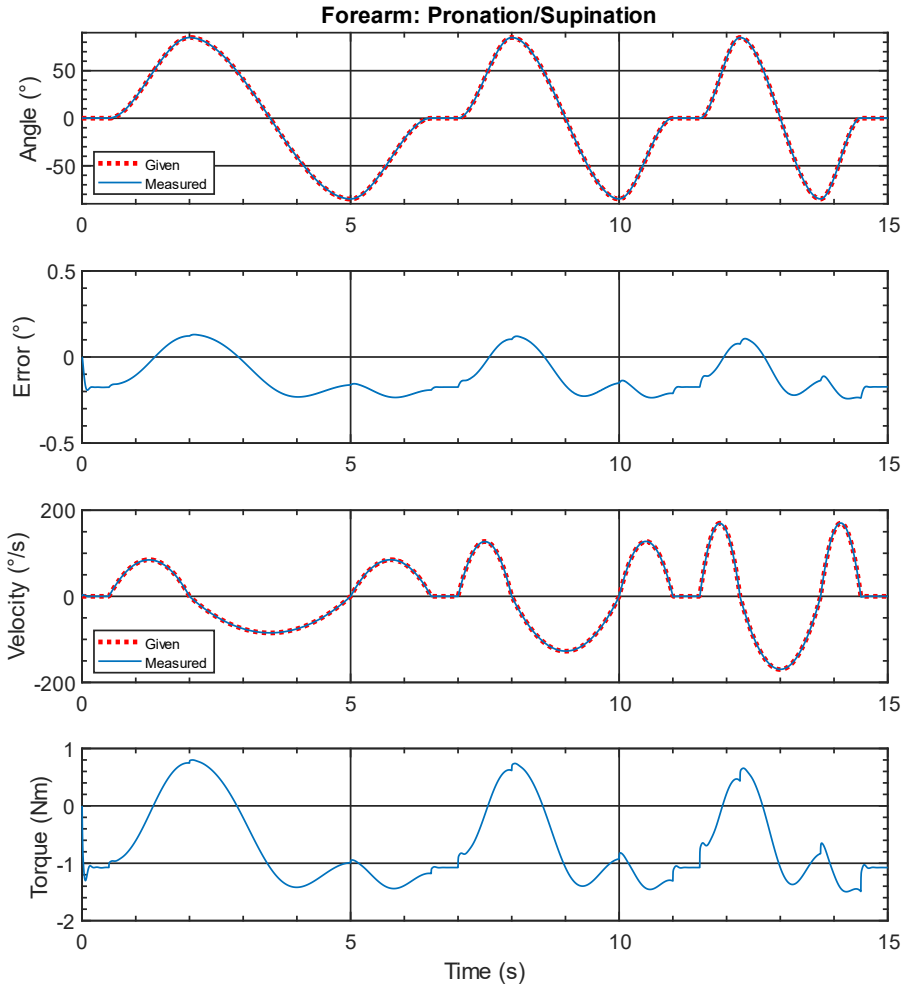

Figure 7.10 Individual Joint-1 movement with velocity comparison w/o disturbance (PID)

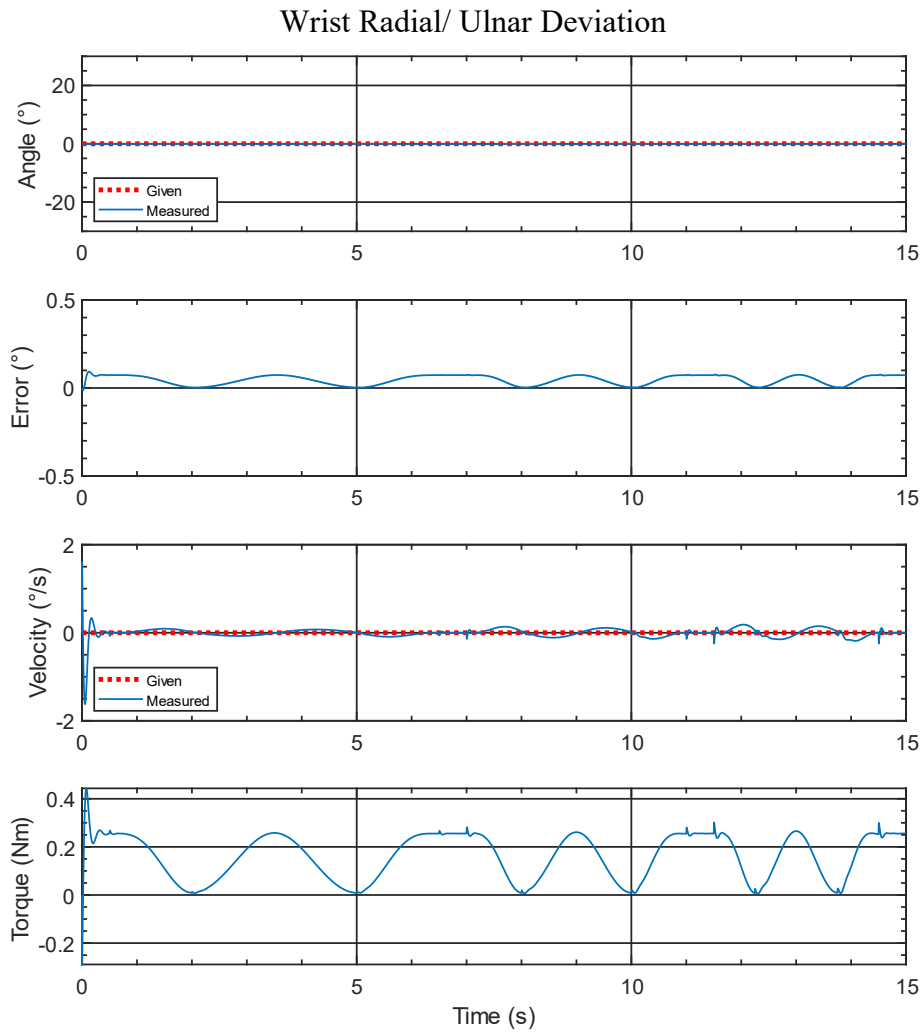

Figure 7.11 Joint-2 plot with velocity comparison during individual Joint-1 movement w/o disturbance (PID)

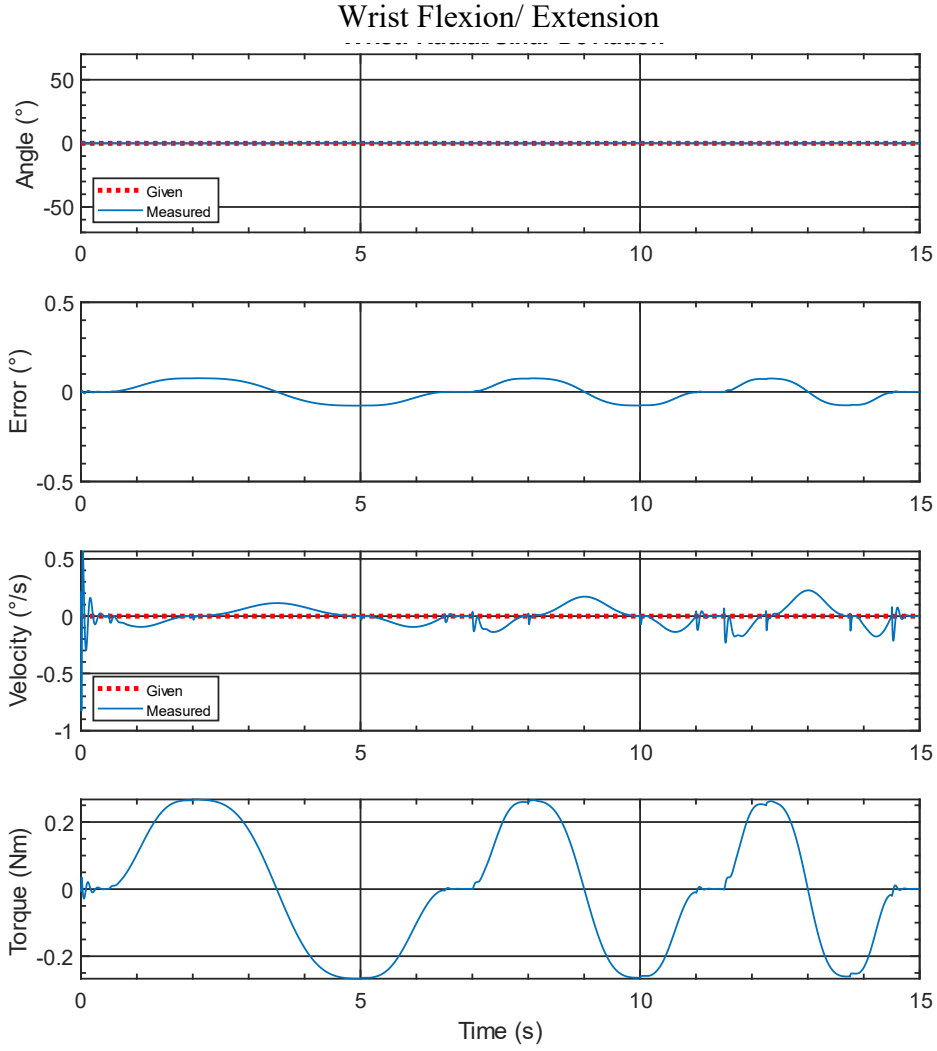

Figure 7.12 Joint-3 plot with velocity comparison during individual Joint-1 movement w/o disturbance (PID)

7.1.1.3 **Individual Joint -2 movement without disturbance (PID)**

Only Joint-2 (range: +20° -25°) moves at the period of 15s, and Joint-1 & Joint-3 stays at 0° angular position during the same period. The simulated results can be seen from *Figure 7.13*, *Figure 7.14*, *Figure 7.15*, and *Figure 7.16*. The tracking performance of all three joints can be seen from *Figure 7.13*.

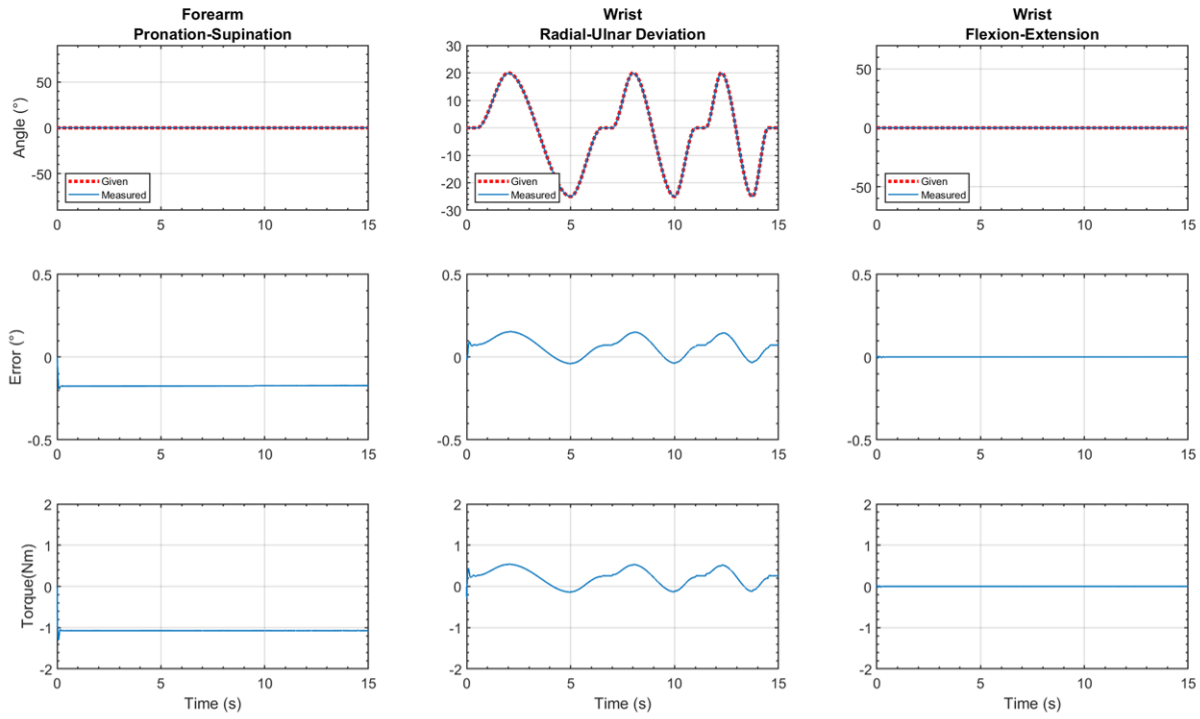

Figure 7.13 Plots of all three joints during Individual Joint-2 movement w/o disturbance (PID)

Here, the maximum tracking error found to be less than 0.5° (0.7%), which proves that the tracking performance is quite good. *Figure 7.14*, *Figure 7.15*, and *Figure 7.16* show the plots of the joints separately. Here, the given velocities (3rd row) are denoted with a red dotted line, and the measured trajectory from the simulation is shown with a solid blue line. Maximum joint torque (using robot

mass only) for Joint-1 found to be -1 Nm and +1 Nm; for Joint-2, the maximum joint torque is -0.3 Nm and +0.6 Nm, and for Joint-3 it is -0.03 Nm and +0.04 Nm.

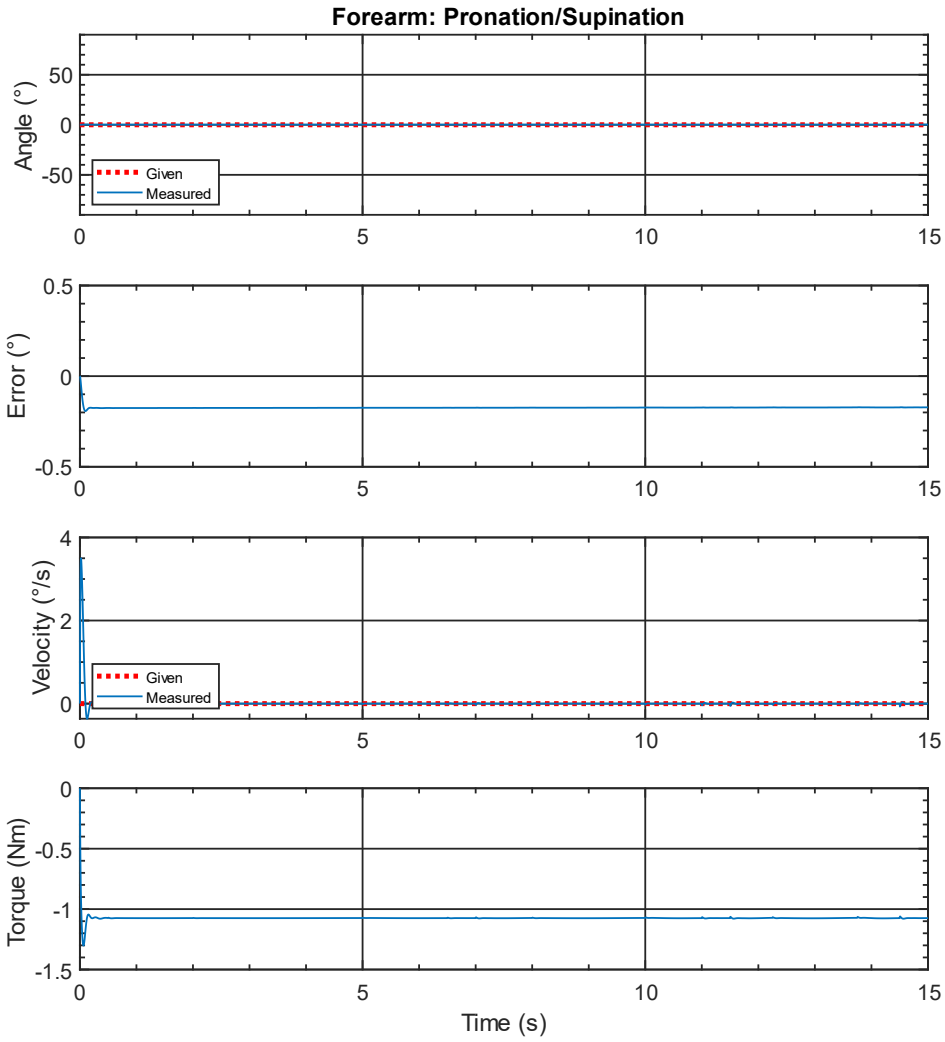

Figure 7.14 Joint-1 plot with velocity comparison during individual Joint-2 movement w/o disturbance (PID)

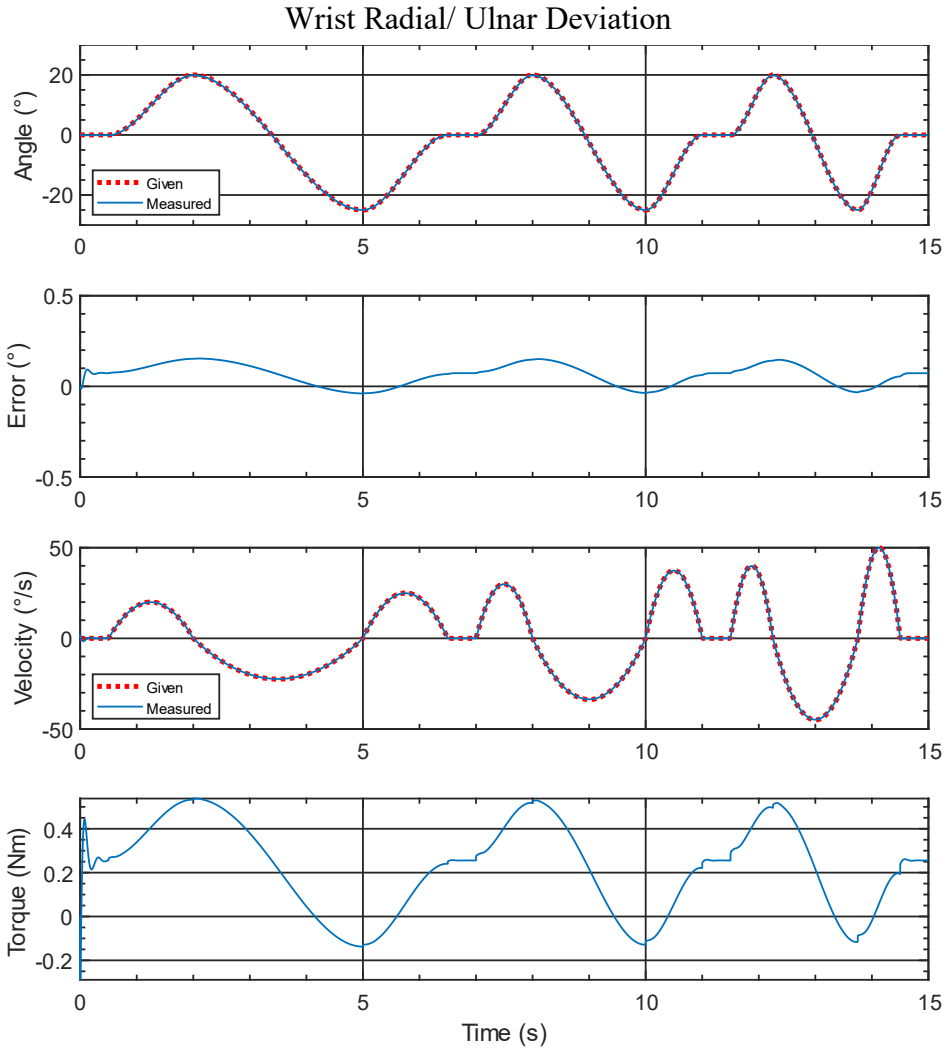

Figure 7.15 Individual Joint-2 movement with velocity comparison w/o disturbance (PID)

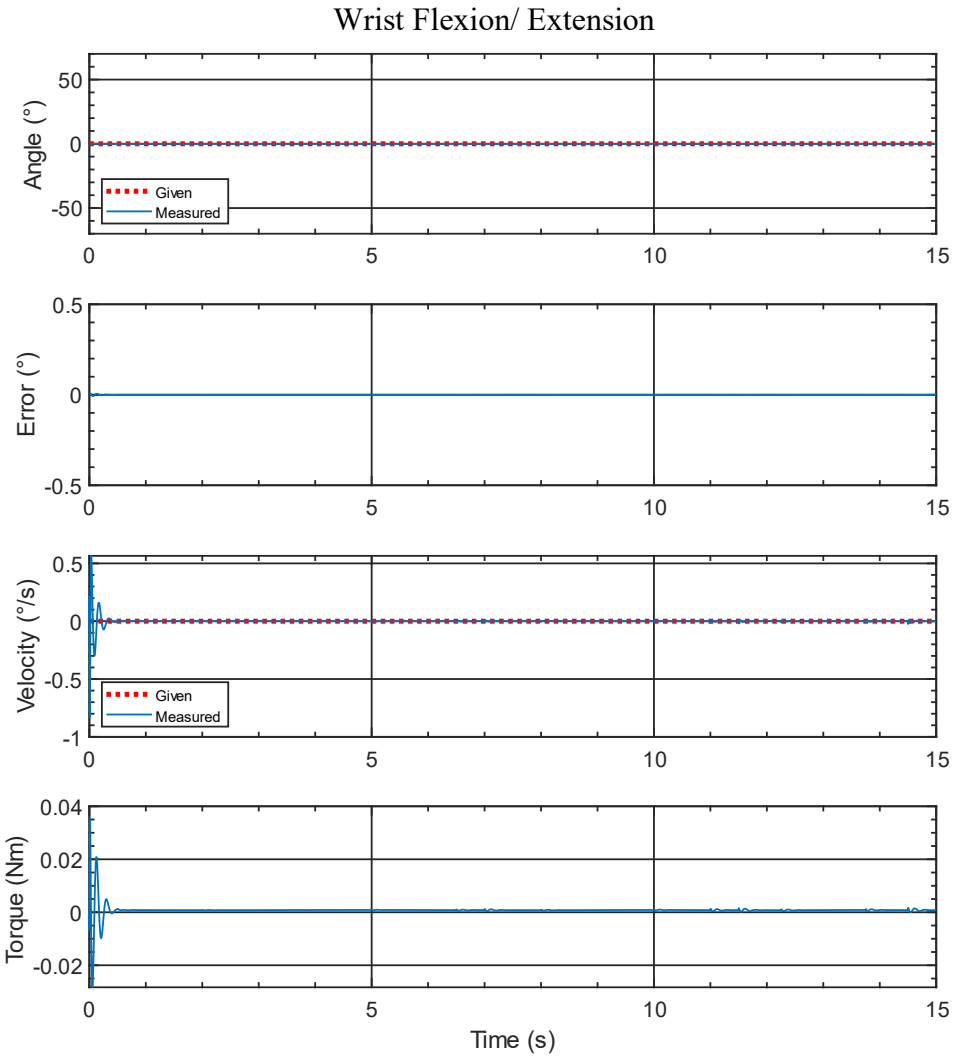

Figure 7.16 Joint-3 plot with velocity comparison during individual Joint-2 movement w/o disturbance (PID)

7.1.1.4 **Individual Joint -3 movement without disturbance (PID)**

Only Joint-3 moves (range: +60° -60°) at the period of 15s, and Joint-1 & Joint-3 stays at 0° angular position during the same period. The simulated results can be seen from *Figure 7.17*, *Figure 7.18*, *Figure 7.19*, and *Figure 7.20*. The tracking performance of all three joints can be seen from *Figure 7.17*. Here, the maximum tracking error found to be less than 0.5° (0.7%), which proves that the

tracking performance is quite good. *Figure 7.18*, *Figure 7.19*, and *Figure 7.20* show the plots of the joints separately.

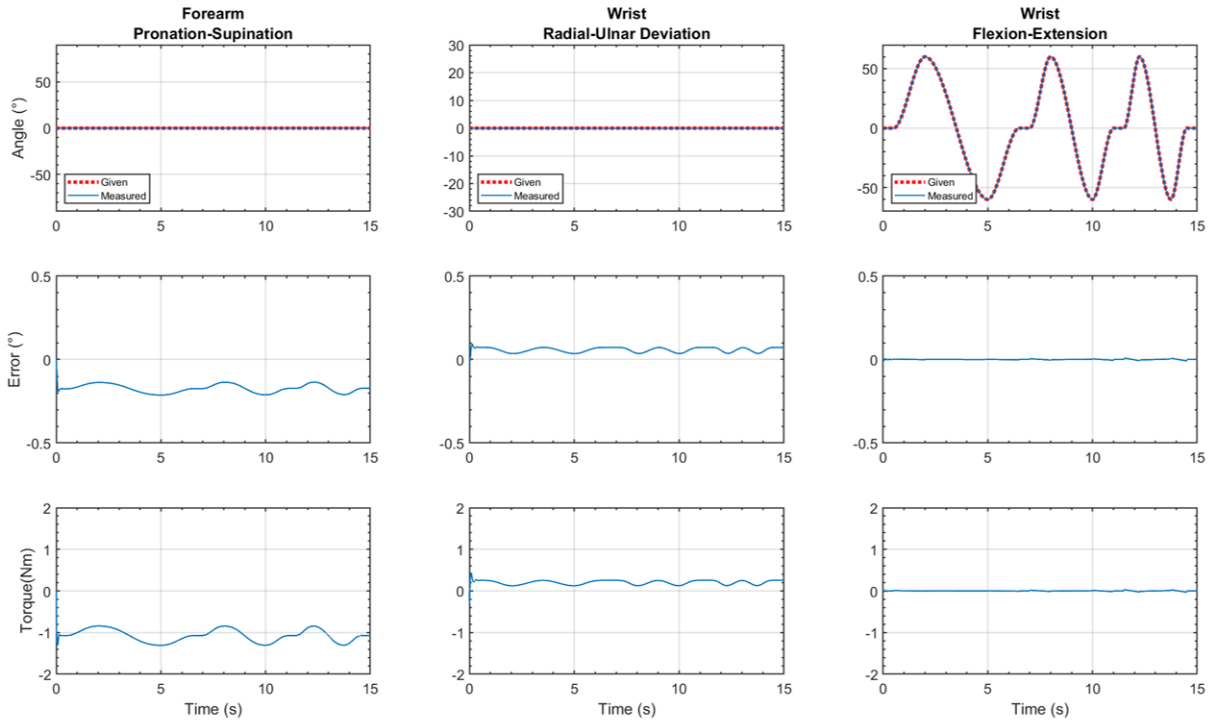

Figure 7.17 Plots of all three joints during Individual Joint-3 movement w/o disturbance (PID)

Maximum joint torque (using robot mass only) for Joint-1 found to be -1 Nm and +1 Nm; for Joint-2, the maximum joint torque is -0.3 Nm and +0.5 Nm, and for Joint-3 it is -0.04 Nm and +0.04 Nm.

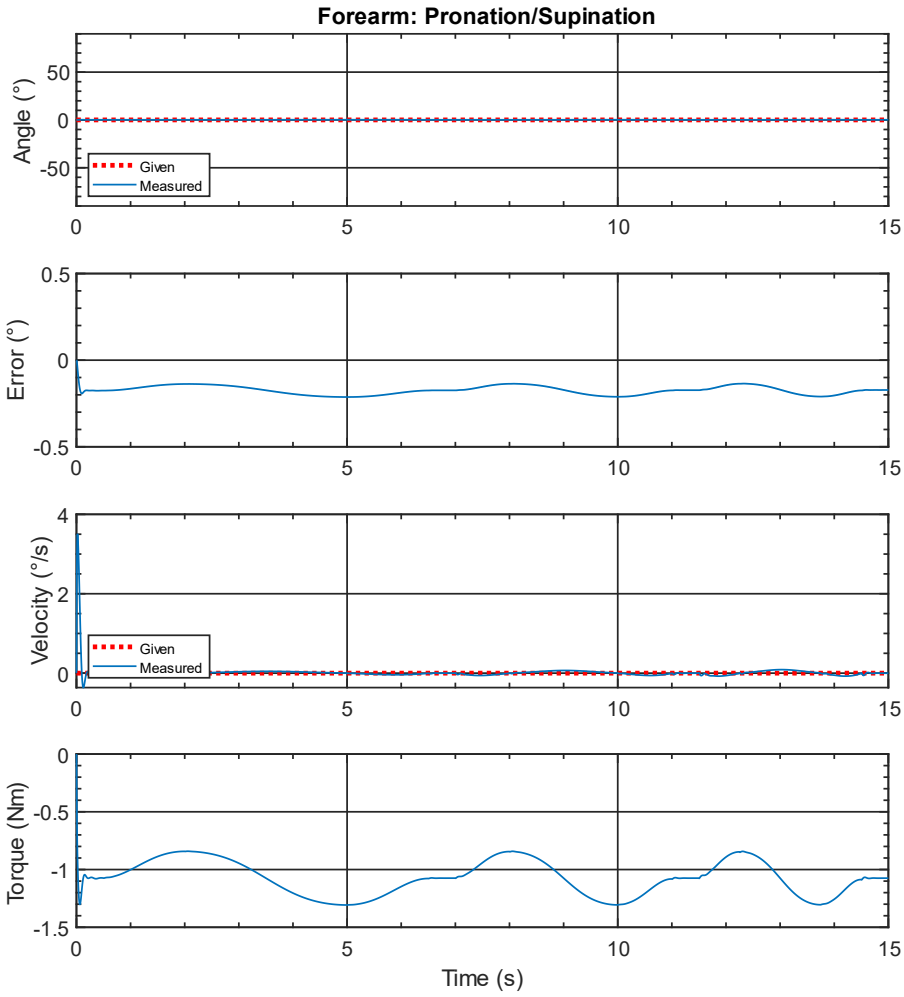

Figure 7.18 Joint-1 plot with velocity comparison during individual Joint-3 movement w/o disturbance (PID)

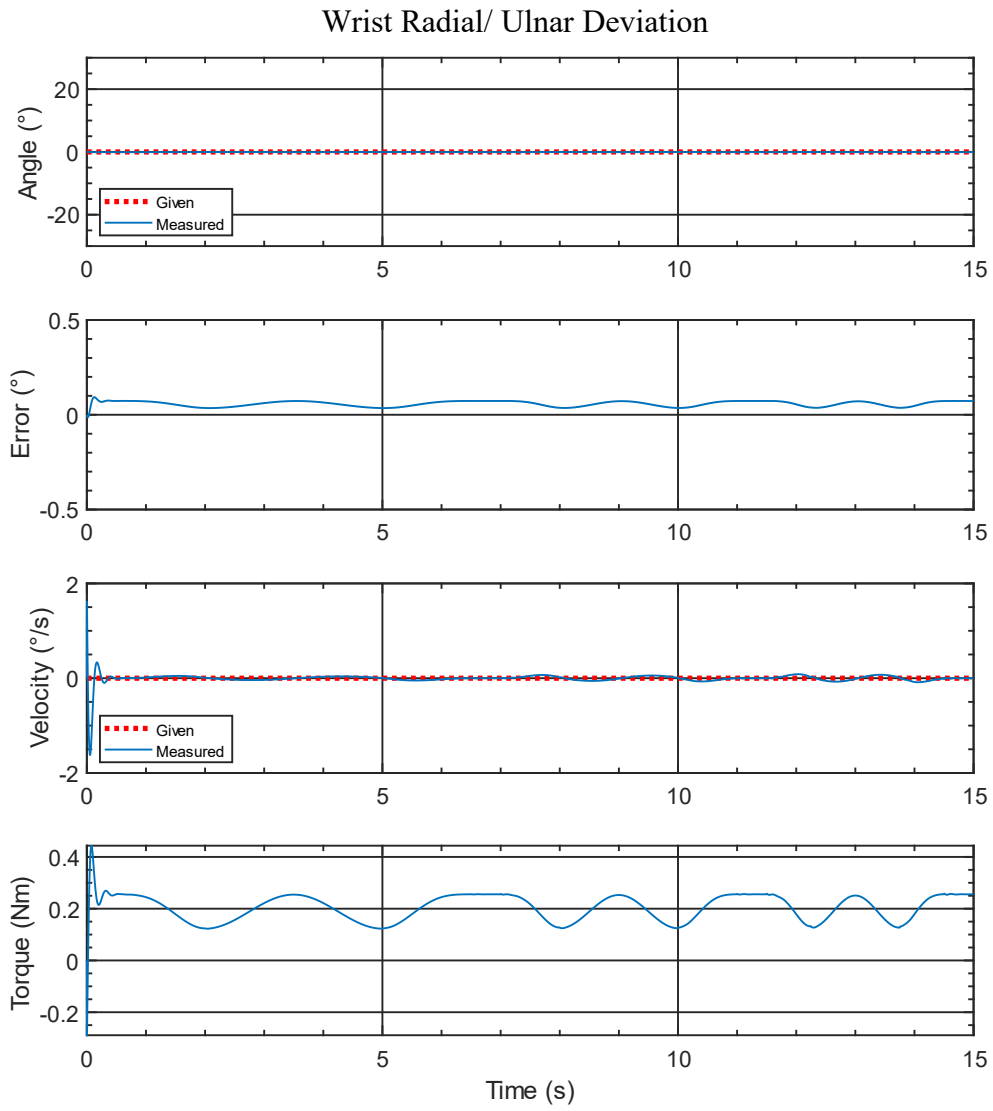

Figure 7.19 Joint-2 plot with velocity comparison during individual Joint-3 movement w/o disturbance (PID)

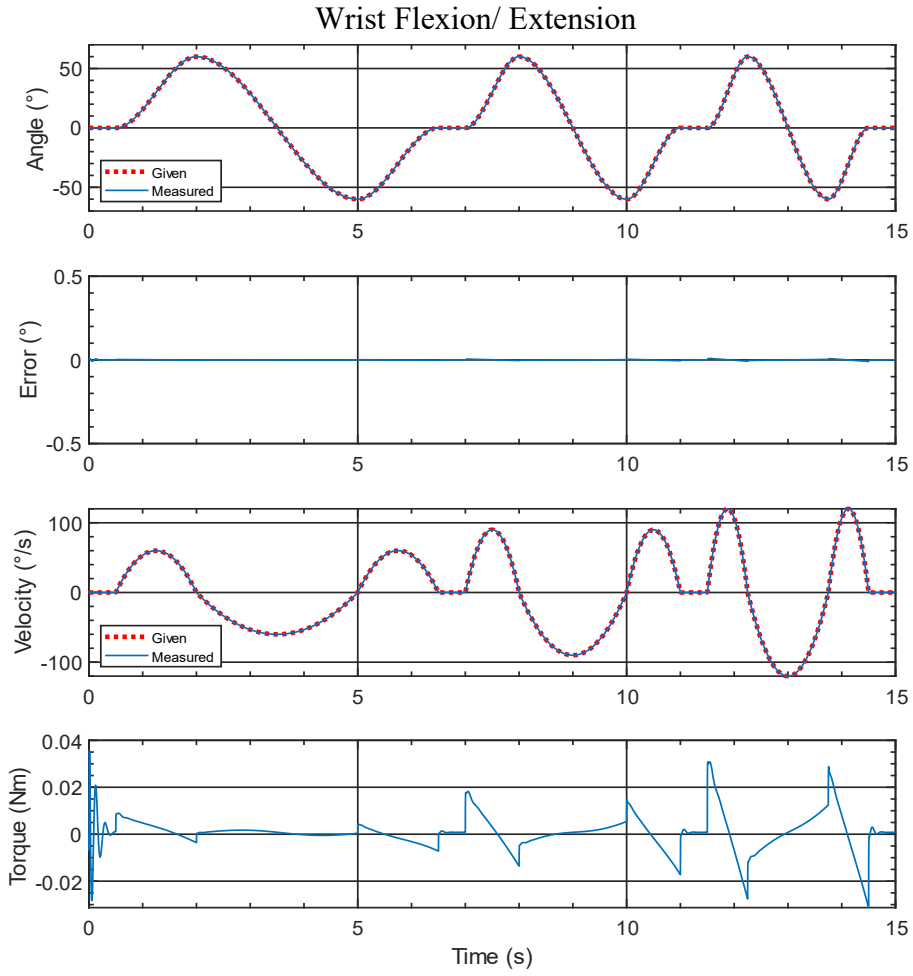

Figure 7.20 Individual Joint-3 movement with velocity comparison w/o disturbance (PID)

7.2 **Modified Computed Torque Control (mCTC)**

To realize better tracking performance of the FWRR, the dynamic model of the FWRR including human forearm and wrist mass properties (APPENDIX – C, APPENDIX – E, APPENDIX – F, and APPENDIX – H), has been implemented using a nonlinear computed torque control (CTC) technique.

The dynamic behavior of the FWRR is expressed by the well-known rigid body dynamic equation (7.6):

$$M(\theta)\ddot{\theta} + V\left(\theta, \dot{\theta}\right) + G(\theta) + F\left(\theta, \dot{\theta}\right) = \tau \tag{7.6}$$

Where,

$\theta \in \mathbb{R}^3$ is the joint variables vector,

τ is the generalized torque vector,

$M(\theta) \in \mathbb{R}^{3\times3}$ is the inertia matrix,

$V\left(\theta, \dot{\theta}\right) \in \mathbb{R}^3$ is the Coriolis/ centrifugal vector,

$G(\theta) \in \mathbb{R}^3$ is the gravity vector,

$F\left(\theta, \dot{\theta}\right) \in \mathbb{R}^3$ is the friction vector.

The friction vector is modeled as a nonlinear Coulomb friction formulated by Equation (7.7):

$$\tau_{friction} = F\left(\theta, \dot{\theta}\right) = c.sgn\left(\dot{\theta}\right) \tag{7.7}$$

Where,

c is the Coulomb-friction constant.

Equation (7.6) can be written as (7.8) for controller implementation:

$$\ddot{\theta} = -M^{-1}(\theta)\left[V\left(\theta,\dot{\theta}\right) + G(\theta) + F\left(\theta,\dot{\theta}\right)\right] + M^{-1}(\theta)\tau \tag{7.8}$$

$M^{-1}(\theta)$ always exists since $M(\theta)$ is symmetrical and positive definite.

The schematic of the used modified computed torque control technique is shown in *Figure 7.21*. As a modification to the conventional computed torque control approach, an integral term has been added to have a better tracking performance and to compensate the trajectory tracking error that can result from imperfect parameter estimation namely friction, and other external disturbances.

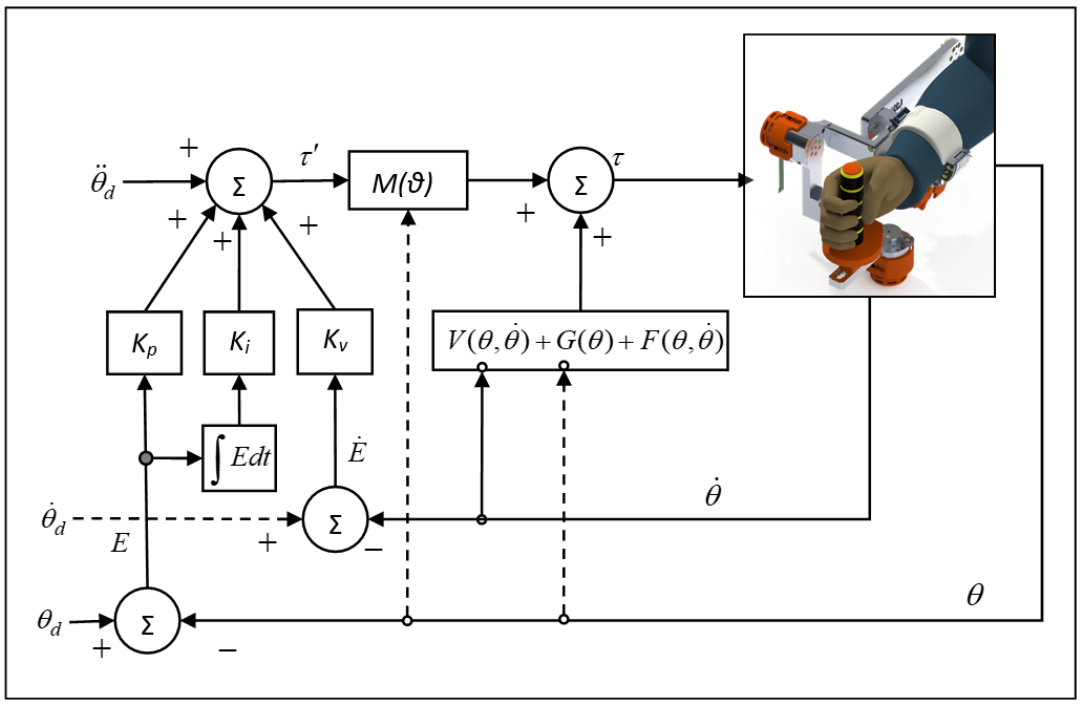

Figure 7.21 Schematic of Modified Computed Torque Control (mCTC)

The control torque in *Figure 7.21* is expressed by:

$$\tau = M(\theta)\left[\ddot{\theta_d} + K_v\left(\dot{\theta}_d - \dot{\theta}\right) + K_p(\theta_d - \theta) + K_i \int (\theta_d - \theta)\, dt\right] + V\left(\theta, \dot{\theta}\right) + G(\theta) + F\left(\theta, \dot{\theta}\right) \tag{7.9}$$

From relations (7.6) and (7.9), equation (7.10) is found:

$$\ddot{\theta} = \ddot{\theta_d} + K_v\left(\dot{\theta}_d - \dot{\theta}\right) + K_p(\theta_d - \theta) + K_i \int (\theta_d - \theta)\, dt \tag{7.10}$$

Where,

$\theta_d, \dot{\theta}_d,$ and $\ddot{\theta}_d$ are the desired position, velocity, and acceleration, respectively,

K_p, K_v, and K_i diagonal positive definite matrices.

The error vector E and its derivatives are given by Equation (7.11), (7.12) & (7.13):

$$E = \theta_d - \theta \tag{7.11}$$

$$\dot{E} = \dot{\theta_d} - \dot{\theta} \tag{7.12}$$

$$\ddot{E} = \ddot{\theta_d} - \ddot{\theta} \tag{7.13}$$

Therefore, equation (7.10) is rewritten in the following equation (7.14):

$$\ddot{E} + K_v\dot{E} + K_pE + K_i \int E\, dt = 0 \tag{7.14}$$

Where, K_p, K_v, and K_i control gains are positive definite matrices.

7.2.1 **Simulation with modified Computed Torque control (mCTC) without disturbance**

The simulations for UWM-FWRR with mCTC has been done in SIMULINK software. For this nonlinear control implementation robot mass as well as the human segments' masses were incorporated in the mass terms $M(\theta)$, centrifugal & Coriolis terms $V(\theta, \dot{\theta})$, and gravity terms $G(\theta)$. The same trajectories as the PID controller simulation were used. The control gains used for the simulation were found by trial and error, and are as follows:

$$K_P = diag[15 \quad 15 \quad 15],$$

$$K_V = diag[5 \quad 5 \quad 5], \text{ and}$$

$$K_I = diag[2 \quad 2 \quad 2].$$

7.2.1.1 **Simultaneous Joint movements without disturbance (mCTC)**

The simulated results using the mCTC for all three joints' movements (Joint-1 – range: +85° -85°, Joint-2 – range: +20° -25°, & Joint-3 – range: +60° -60°), can be seen from *Figure 7.22*, *Figure 7.23*, *Figure 7.24*, and *Figure 7.25*. The tracking performance of all three joints' simultaneous movement can be seen from *Figure 7.22* where 1st column corresponds to Joint-1, and the 2nd and 3rd column corresponds to Joint-2 and Joint-3, respectively. The first row shows the trajectory comparison (Given joint angles – red dotted line, Measured joint angles – solid blue line) for three joints. The second row shows the tracking error, and the third row shows the measured torque from the simulation. Here the maximum tracking error found to be less than 0.1° (0.1%), which proves that the tracking performance is excellent. *Figure 7.23*, *Figure 7.24*, and *Figure 7.25* show the plots of the joints separately. Here, the given velocities (third row) are denoted with a red dotted line, and the measured trajectory from the simulation is shown with a solid blue line. Maximum joint torque (using robot mass only) for Joint-1 found to be -2 Nm and +1 Nm; for Joint-2, the maximum joint torque is -0.8 Nm and +0.6 Nm, and for Joint-3 it is -0.3 Nm and +0.3 Nm. The positive and negative signs denoted the direction of the joint torques.

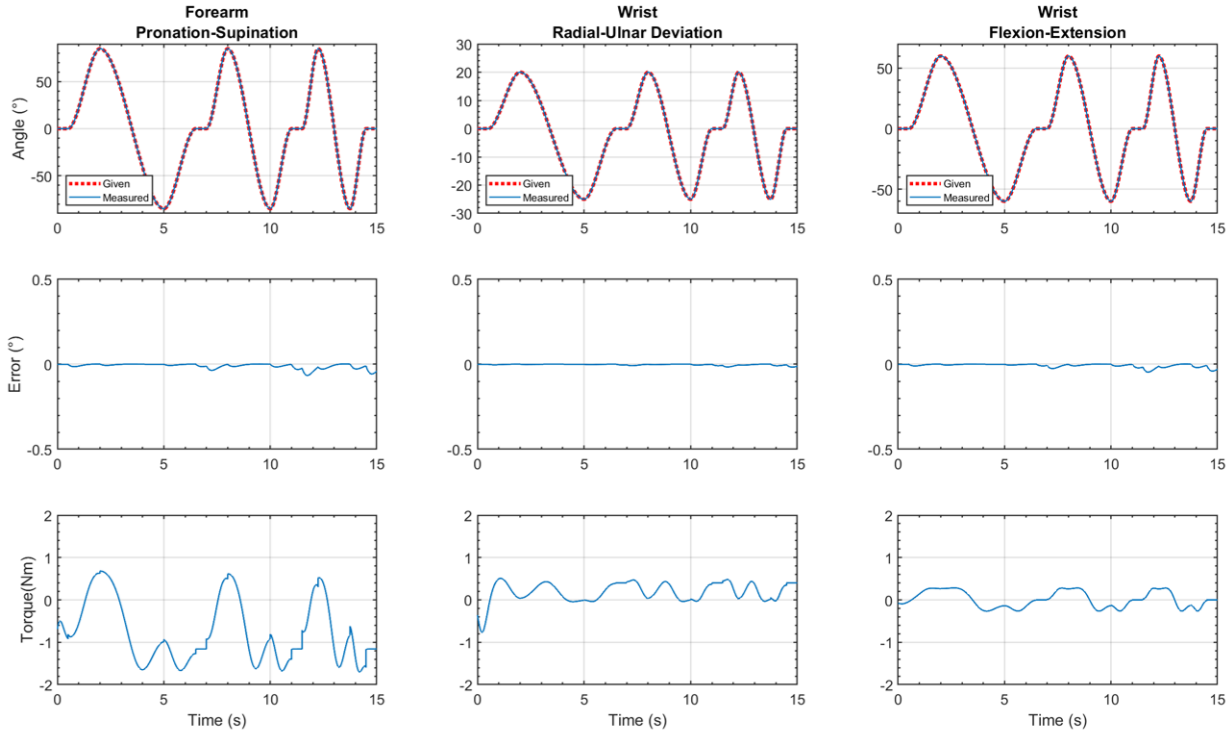

Figure 7.22 All three joints simultaneous motion w/o disturbance (mCTC)

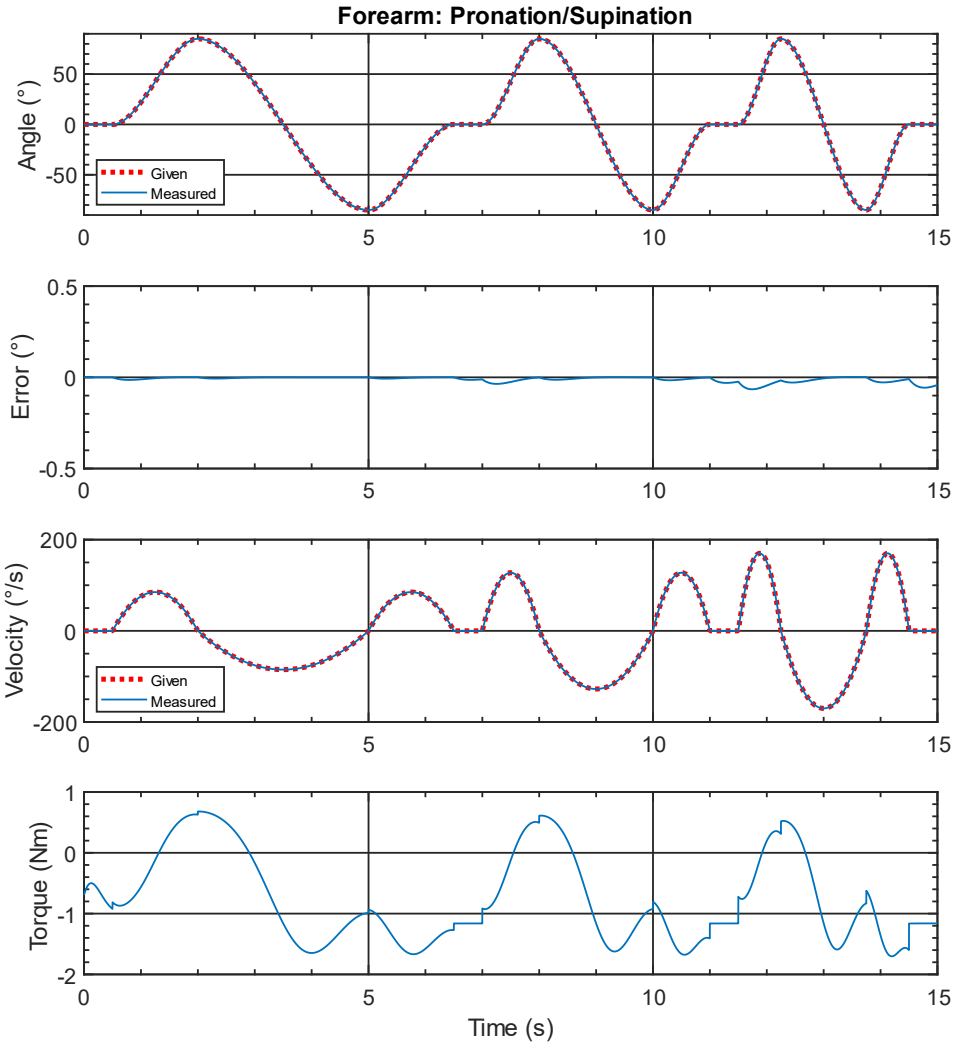

Figure 7.23 All three joints simultaneous movement (detail of Joint-1 movement with velocity comparison w/o disturbance) (mCTC)

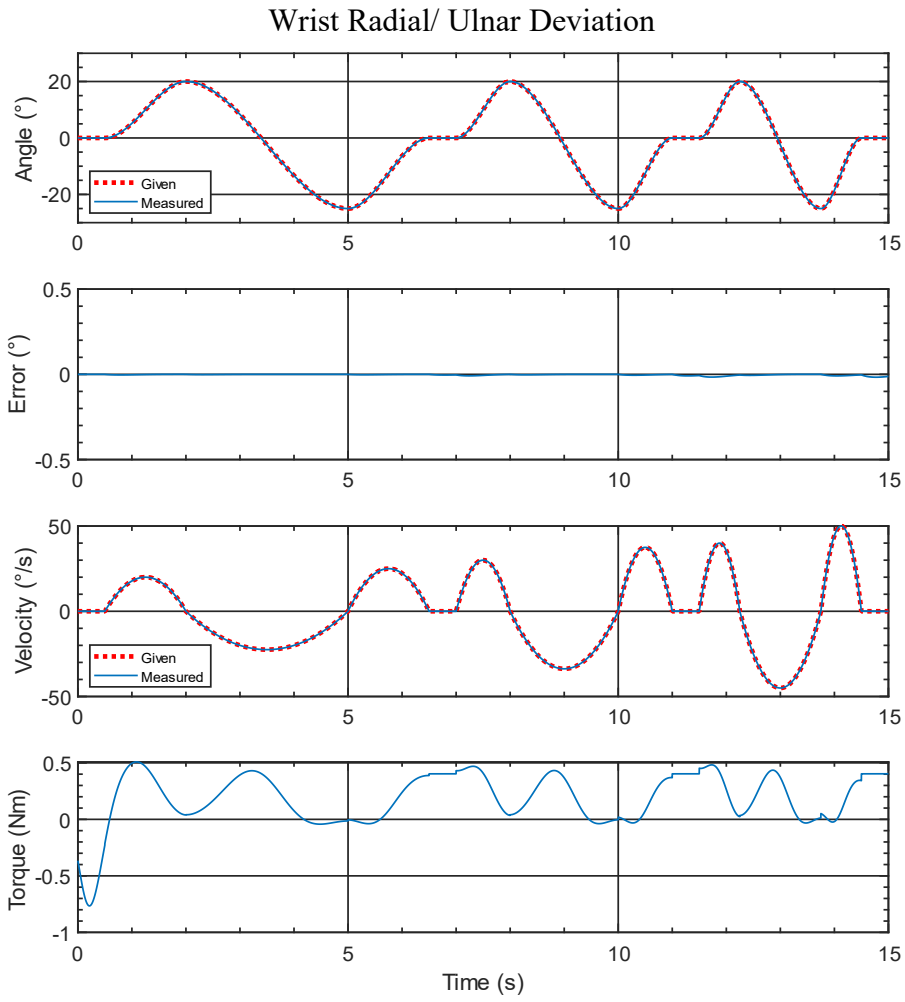

Figure 7.24 All three joints simultaneous movement (detail of Joint-2 movement with velocity comparison) w/o disturbance (mCTC)

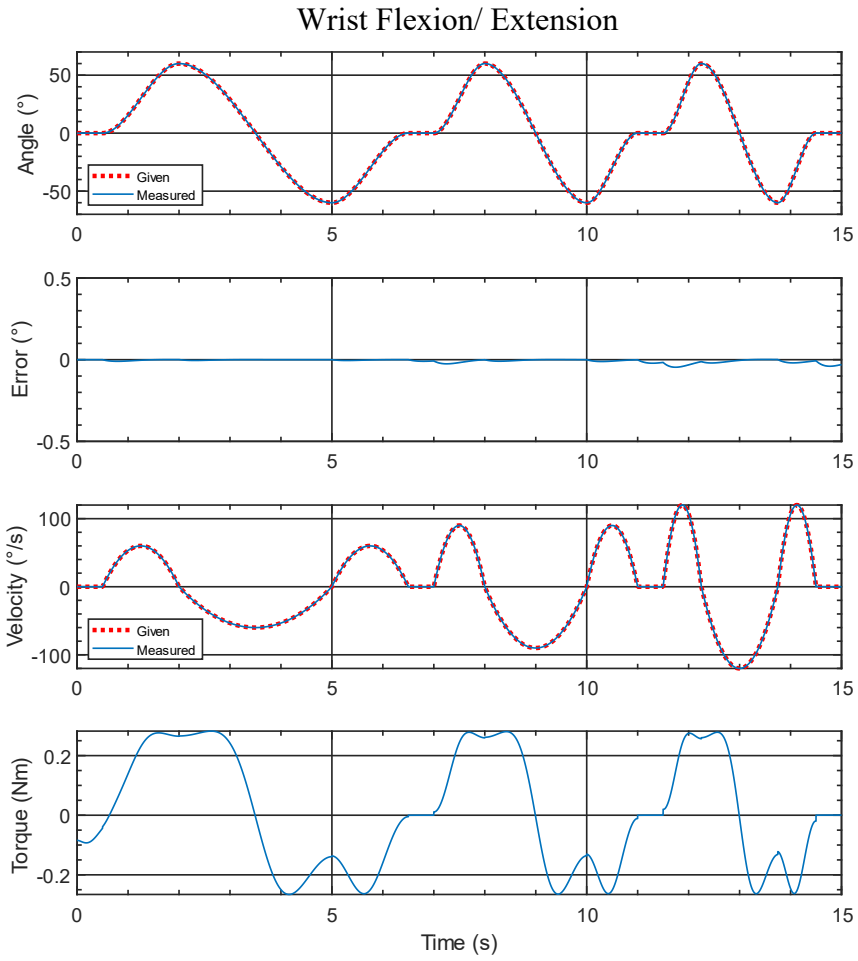

Figure 7.25 All three joints simultaneous movement (detail of Joint-3 movement with velocity comparison) w/o disturbance (mCTC)

7.2.1.2 **Individual Joint -1 movement without disturbance (mCTC)**

The simulated results using the mCTC, for only the Joint-1 movement (range: +85° -85°) at the period of 15s while Joint-2 & Joint-3 stays at 0° angular position, can be seen from *Figure 7.26*,

Figure 7.27, *Figure 7.28*, and *Figure 7.29*. Tracking performance of all three joints' can be seen from *Figure 7.26*.

Here the maximum tracking error for Joint-1 found to be less than 0.08° (0.1%), and for other joints, it's close to zero (10^{-14}), which proves that the tracking performance is excellent. *Figure 7.27*, *Figure 7.28*, and *Figure 7.29* show the plots of the joints separately. Here, the given velocities (third row) are denoted with a red dotted line, and the measured trajectory from the simulation is shown with a solid blue line. Maximum joint torque (using robot mass only) for Joint-1 found to be -2 Nm and +1 Nm; for Joint-2, the maximum joint torque is -0.8 Nm and +0.6 Nm, and for Joint-3 it is -0.4 Nm and +0.4 Nm. The positive and negative signs denoted the direction of the joint torques.

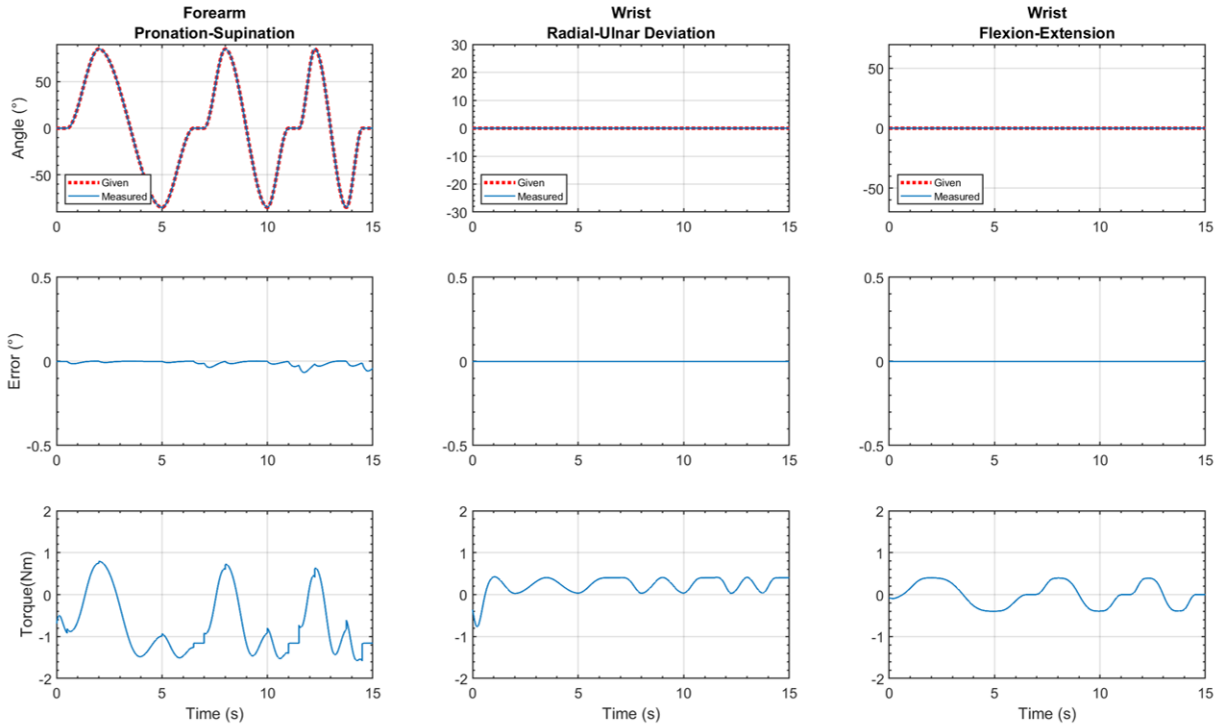

Figure 7.26 Plots of all three joints during Individual Joint-1 movement w/o disturbance (mCTC)

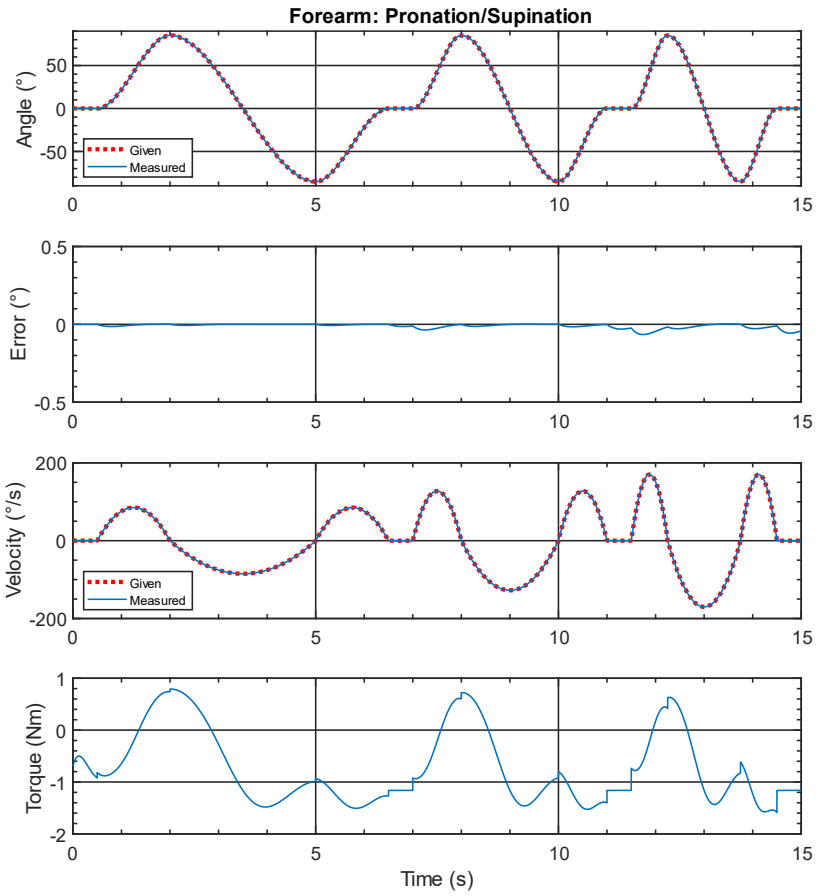

Figure 7.27 Individual Joint-1 movement with velocity comparison w/o disturbance (mCTC)

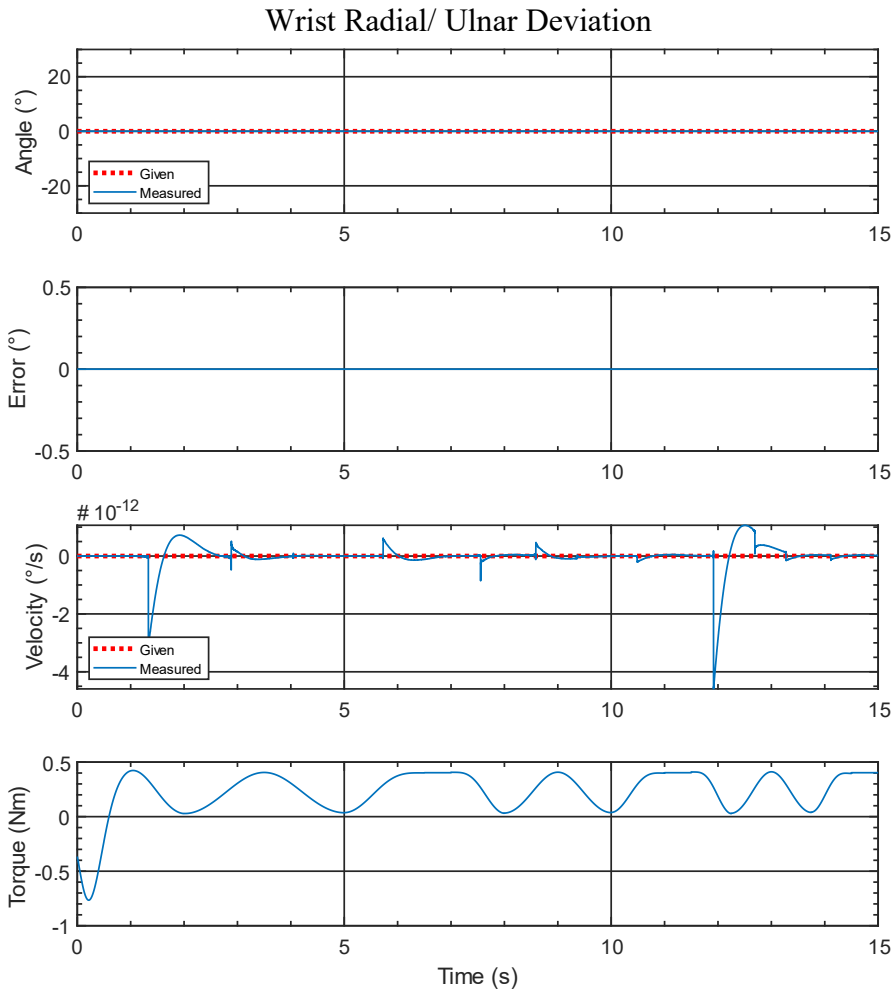

Figure 7.28 Joint-2 plot with velocity comparison during individual Joint-1 movement w/o disturbance (mCTC)

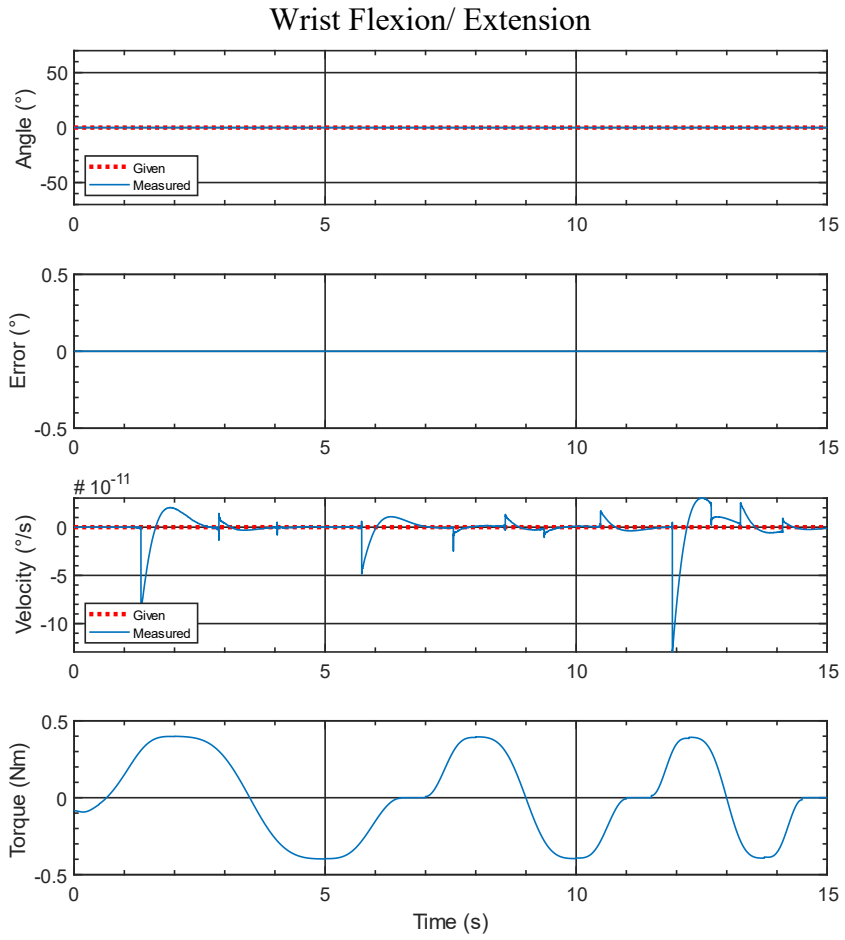

Figure 7.29 Joint-3 plot with velocity comparison during individual Joint-1 movement w/o disturbance (mCTC)

7.2.1.3 **Individual Joint -2 movement without disturbance (mCTC)**

The simulated results using mCTC, for only the Joint-2 movement (range: +20° -25°) at the period of 15s while Joint-1 & Joint-3 stays at 0° angular position, can be seen from *Figure 7.30*, *Figure 7.31*, *Figure 7.32*, and *Figure 7.33*. The tracking performance of all three joints' can be seen from *Figure 7.26*. Here the maximum tracking error for Joint-2 found to be less than 0.02° (0.08%), and for other joints, it's close to zero (10^{-14}), which proves that the tracking performance is excellent. *Figure 7.31*, *Figure 7.32*, and *Figure 7.33*, shows the plots of the joints separately. Maximum joint torque (using robot mass only) for Joint-1 found to be -1.2 Nm and -0.4 Nm, for Joint-2, the maximum joint torque is -0.8 Nm and +0.8 Nm, and for Joint-3 it is -0.1 Nm and +0.04 Nm.

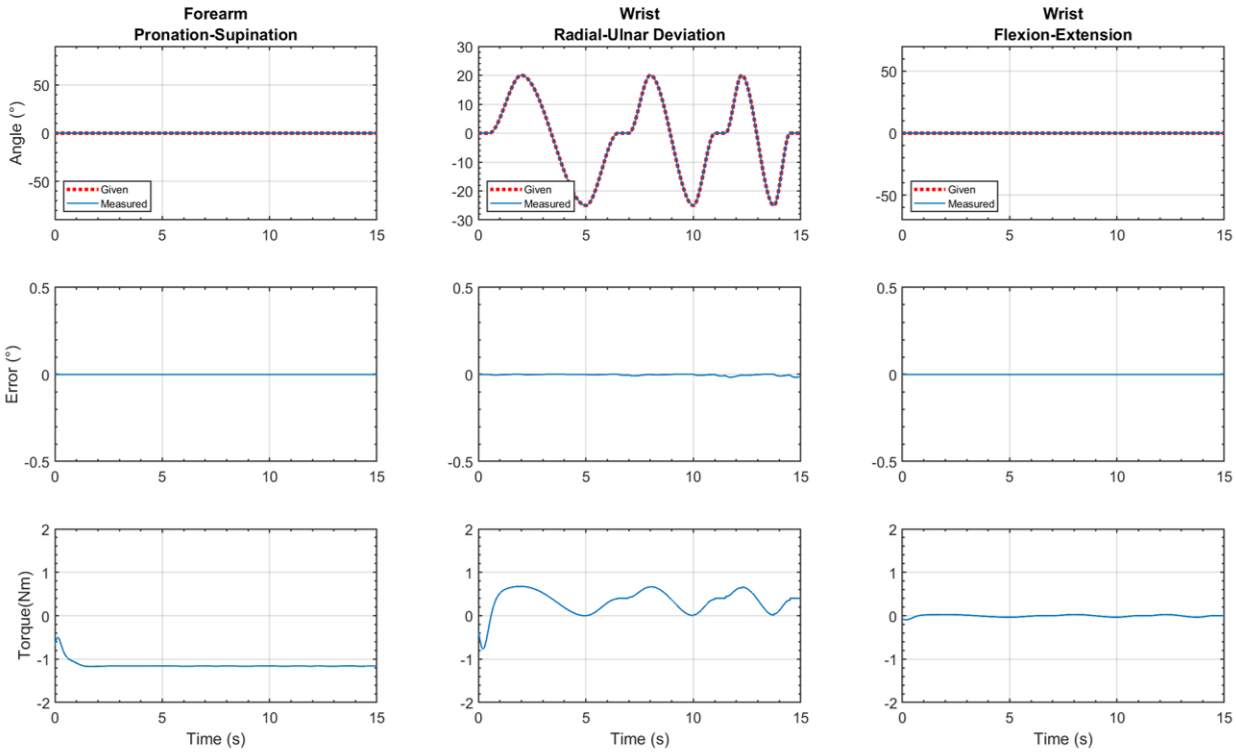

Figure 7.30 Plots of all three joints during Individual Joint-2 movement w/o disturbance (mCTC)

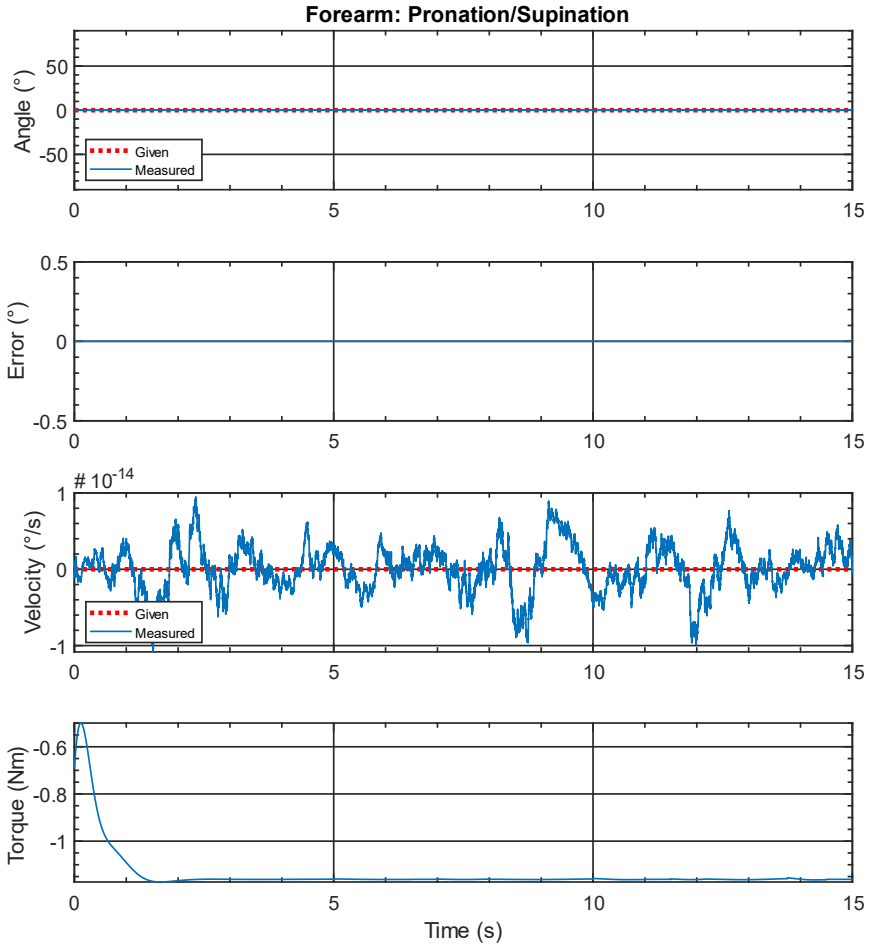

Figure 7.31 Joint-1 plot with velocity comparison during individual Joint-2 movement w/o disturbance (mCTC)

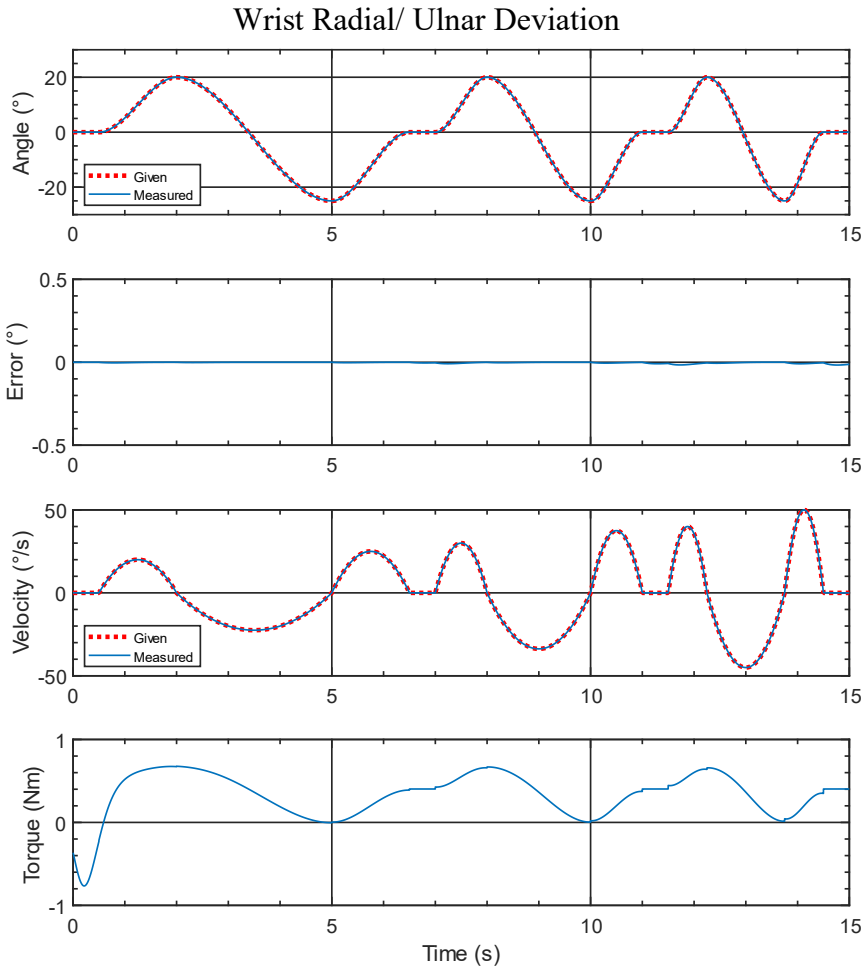

Figure 7.32 Individual Joint-2 movement with velocity comparison w/o disturbance (mCTC)

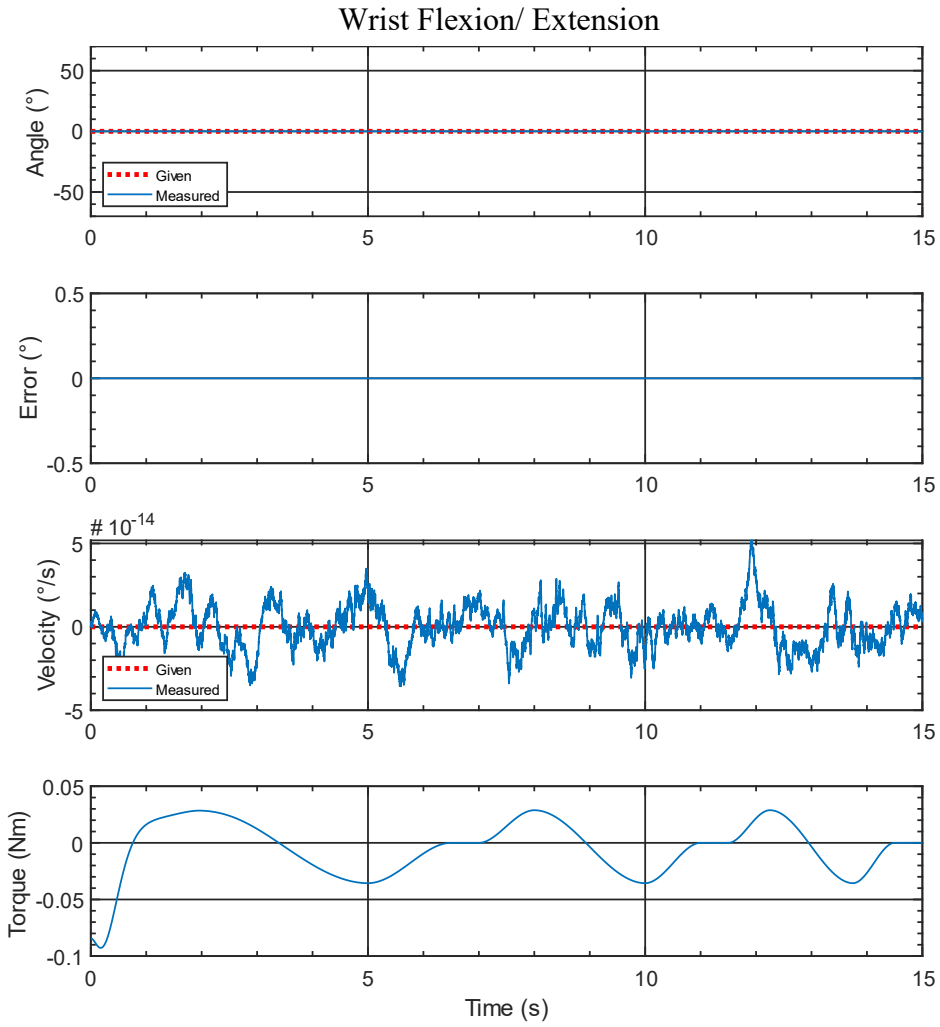

Figure 7.33 Joint-3 plot with velocity comparison during individual Joint-2 movement w/o disturbance (mCTC)

7.2.1.4 **Individual Joint -3 movement without disturbance (mCTC)**

The simulated results using the mCTC, for only the Joint-3 movement (range: +60° -60°) at the period of 15s while Joint-1 & Joint-2 stays at 0° angular position, can be seen from *Figure 7.34*, *Figure 7.35*, *Figure 7.36*, and *Figure 7.37*. The tracking performance of all three joints' simultaneous movement can be seen from *Figure 7.34*. Here the maximum tracking error for Joint-3 found to be less than 0.06° (0.1%), and for other joints, it's close to zero (10^{-14}), which proves that the tracking performance is excellent. *Figure 7.35*, *Figure 7.36*, and *Figure 7.37* show the plots of the joints separately. Maximum joint torque (using robot mass only) for Joint-1 found to be -0.015 Nm and -0.015 Nm; for Joint-2, the maximum joint torque is -0.9 Nm and -0.9 Nm, and for Joint-3 it is -0.4 Nm and +0.4 Nm. The positive and negative signs denoted the direction of the joint torques.

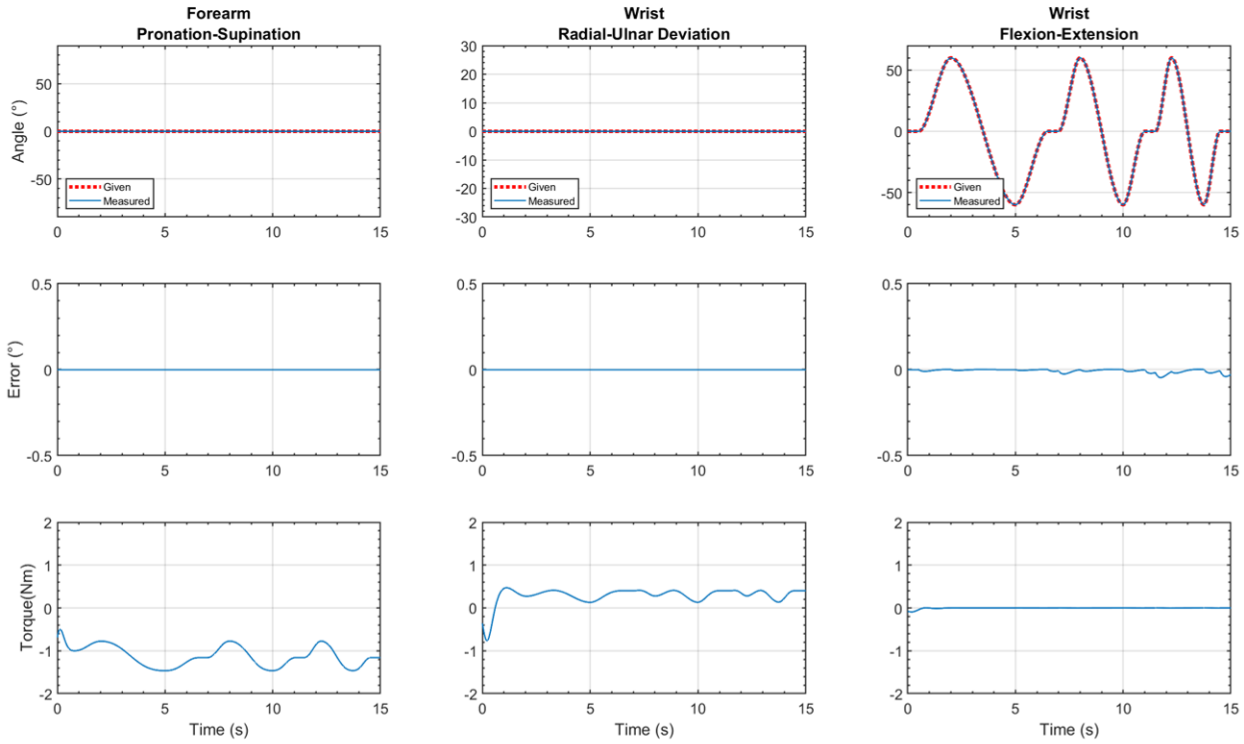

Figure 7.34 Joint-3 plot with velocity comparison during individual Joint-2 movement w/o disturbance (mCTC)

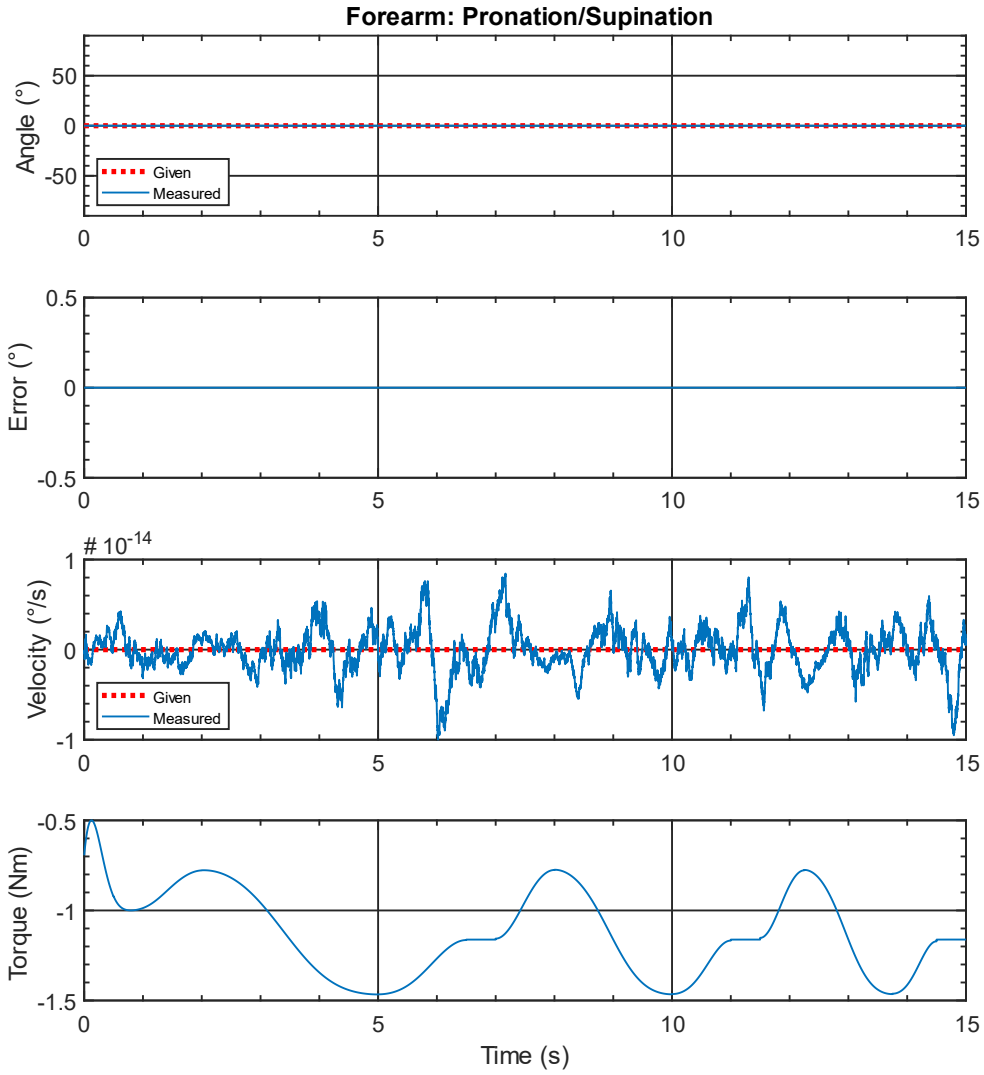

Figure 7.35 Joint-1 plot with velocity comparison during individual Joint-3 movement w/o disturbance (mCTC)

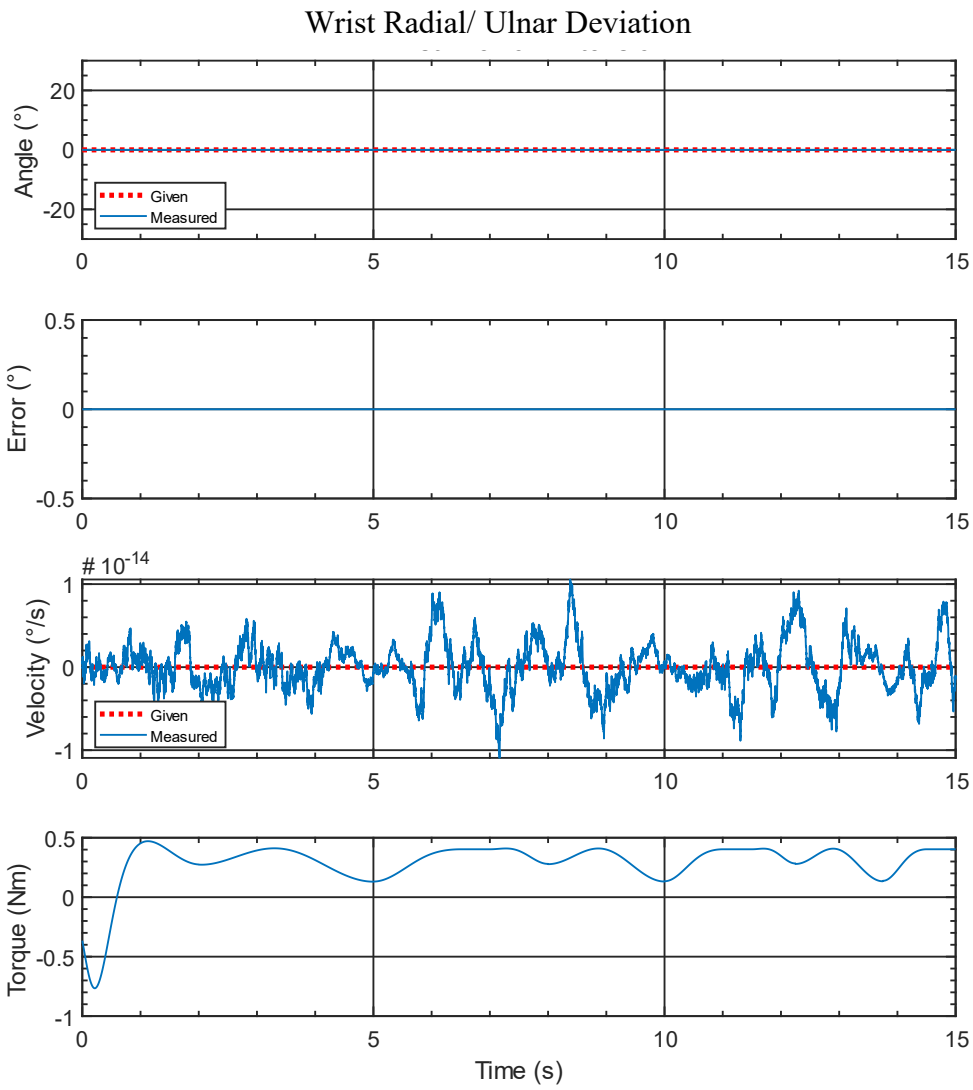

Figure 7.36 Joint-2 plot with velocity comparison during individual Joint-3 movement w/o disturbance (mCTC)

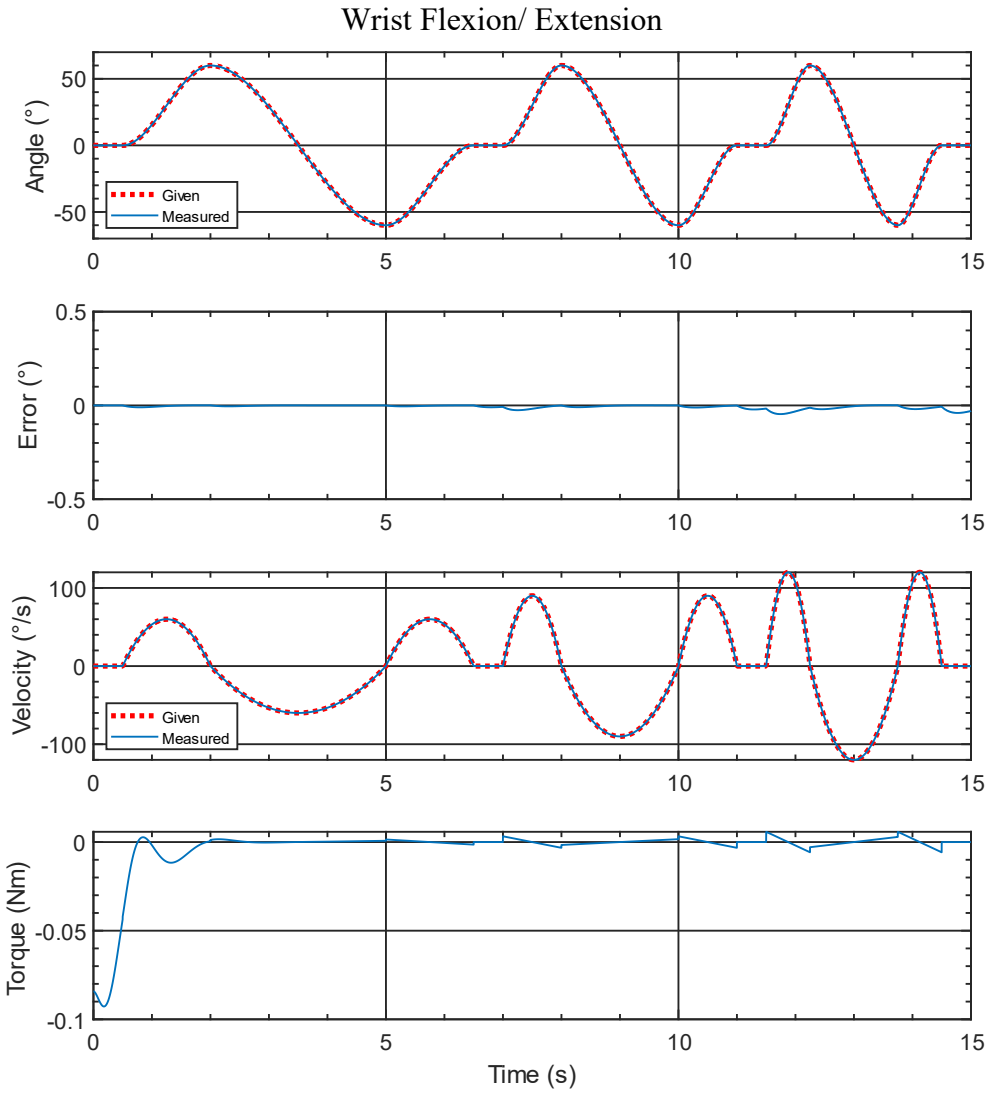

Figure 7.37 Individual Joint-3 movement with velocity comparison w/o disturbance (mCTC)

7.2.2 **Simulation with modified Computed Torque control (mCTC) with disturbances**

The simulated results using the mCTC for all three joints' movements (Joint-1 – range: +85° -85°, Joint-2 – range: +20° -25°, & Joint-3 – range: +60° -60°) with the addition of 10% resistive torque and random noise (±0.01) and the tracking performance of all three joints' simultaneous movement can be seen from *Figure 7.38*. Here the maximum tracking error found to be less than 1° (1.42%), which proves that even while under disturbances, the tracking performance is excellent. Maximum joint torque for Joint-1 found to be -2 Nm and +1 Nm; for Joint-2, the maximum joint torque is -0.8 Nm and +0.6 Nm, and for Joint-3, it is -0.3 Nm and +0.3 Nm. This proves that with even external disturbances, the controller is able to keep trajectory tracking error to a minimum just by tuning the gain parameters. The control gains used for the simulation were found by trial and error, and are as follows:

$$K_P = diag[500 \quad 1250 \quad 10000],$$

$$K_V = diag[15 \quad 15 \quad 120], \text{ and}$$

$$K_I = diag[8 \quad 15 \quad 20].$$

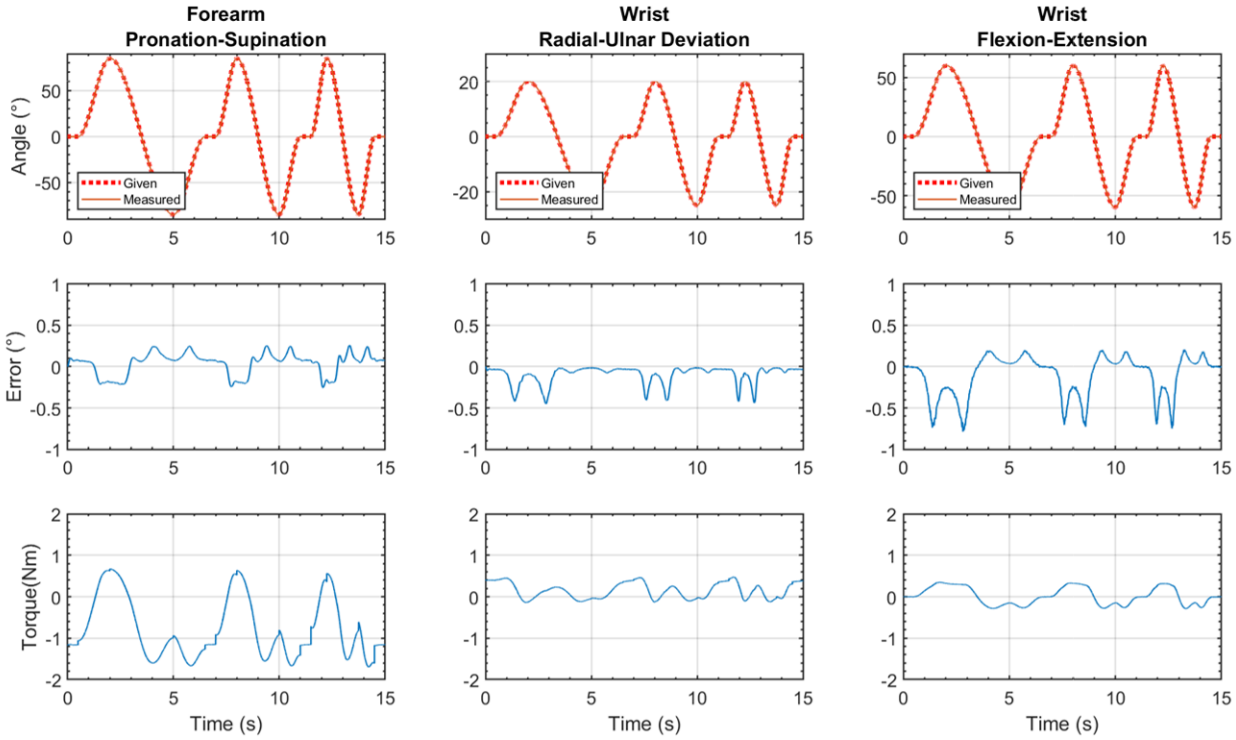

Figure 7.38 All three joints simultaneous motion with disturbance (mCTC)

7.3 **Sliding Mode Control with Time Delay Estimation (SMC-TDE)**

To alleviate the effect the uncertain nonlinear dynamics and external disturbances which influence a robot's performance, a robust sliding mode control controller combined with time delay estimation (SMC-TDE) has been evaluated. Here, a robot with 3 degrees of freedom (n=3) has been considered for dimensional notation purpose.

The dynamic behavior of the a 3 DoF robot can be expressed in joint space by the rigid body dynamic equation (7.15):

$$M(\theta)\ddot{\theta} + C\left(\theta, \dot{\theta}\right)\dot{\theta} + B_0\dot{\theta} + G(\theta) + d(t) = \tau \tag{7.15}$$

Where,

$\theta \in \mathbb{R}^3$ is the joint variables vector,

τ is the generalized torque vector,

$M(\theta) \in \mathbb{R}^{3\times3}$ is the symmetric positive-definite inertia matrix,

$G(\theta) \in \mathbb{R}^3$ is the gravity vector,

$C(q, \dot{q}) \in R^{3X3}$ is the Coriolis/centrifugal matrix,

$B_0 \in R^{3x3}$ is the diagonal viscous friction matrix,

$d(t) \in R^3$ is the unknown bounded disturbance caused by the patient muscular activity.

Equation (7.15) can be written separating the uncertainties in dynamic of the robot as:

$$M(q)\ddot{q} + H(\delta, \ddot{q}, \dot{q}, q, t) = \tau(t) \tag{7.16}$$

Where,

$H(\delta, \ddot{q}, \dot{q}, q, t) = C(q, \dot{q})\dot{q} + B_0\dot{q} + G(q) + d(t)$ is the total unknown nonlinear uncertain dynamic of the robot, and

δ are the uncertain parameters of the dynamic model.

Let us denote $H(\delta, \ddot{q}, \dot{q}, q, t) = H(t)$

$$M(q)\ddot{q} + H(t) = \tau(t) \tag{7.17}$$

The error vector E and its derivatives are given by Equation (7.18), (7.19), & (7.20):

$$E = \theta_d - \theta \tag{7.18}$$

$$\dot{E} = \dot{\theta_d} - \dot{\theta} \tag{7.19}$$

$$\ddot{E} = \ddot{\theta_d} - \ddot{\theta} \tag{7.20}$$

For the SMC-TDE technique, the sliding surface can be defined using the dynamic of the errors from eequation (7.18), (7.19), & (7.20) as following:

$$s = \dot{e} + \lambda e \tag{7.21}$$

$$s = \dot{\theta} - \dot{\theta}_d + \lambda e \tag{7.22}$$

$$s = \dot{\theta} - \dot{\theta}_r \tag{7.23}$$

Where,

$\ddot{\theta}_r = \ddot{\theta}_d - \lambda\dot{\theta}$,

$\theta_d \in R^3$ is the desired trajectory for all joints,

$\theta \in R^3$ is the measured position trajectory, and

λ is a 3x3 diagonal positive-definite matrix.

Using equation (7.23) the control law for SMC-TDE can be written as:

$$\tau = M[-k_1.\text{Sign(s)} + \ddot{\theta}_d - \lambda\dot{e}] + \widehat{H}(t) \tag{7.24}$$

Where,

$k_1 \in R^{3\times3}$ is the diagonal positive matrix,

$sign(s)$ is discontinuous function definite as follows:

$$sign(S) = \begin{cases} 1 \ \ for\ S > 0 \\ 0 \ \ for\ S = 0 \\ -1 \ \ for\ S < 0 \end{cases} \tag{7.25}$$

And,

$$\widehat{H}(t) \cong H(t - t_d) = \tau(t - t_d) - M\ddot{\theta}(t - t_d) \tag{7.26}$$

In equation (7.26), $\ddot{\theta}(t - t_d)$ is the delayed acceleration input computed by using the following approximation:

$$\ddot{\theta}(t - t_d) \cong \frac{\dot{\theta}(t - t_d) - \dot{\theta}(t - 2t_d)}{t_d} \tag{7.27}$$

Where, t_d is sampling time.

7.3.1 **Simulation using Sliding Mode Control with Time delay Estimation (SMC-TDE):**

To validate the control theory mentioned earlier in 7.3, a simple 2 link manipulator (2 DoF, n=2) has been tested in simulated environment using SIMULINK, MathWorks Inc. Here, Joint 1 starts from 0° (initial position), and after a 2 seconds delay, the trajectory reaches 90° in 8 seconds and then returns to its initial position over another 8 seconds. Afterward, the joint 1 stays at its initial position for a 2 seconds period. Simultaneously, Joint 2 starts from 0° (Initial position) and after 1 second delay goes to 55° over 8 seconds period and then stays at 55° for a 2 seconds period. Afterward, Joint 2 returns to its initial position over another 8 seconds and stays there for 1 second period. The generated desired trajectories for both joints can be seen from *Figure 7.39*, where the first column corresponds to Joint 1, and the 2nd column corresponds to Joint 2 of the 2-DoF manipulator robot.

In the simulation only robot's mass inertia, $M(\theta) \in \mathbb{R}^{2\times2}$ was fed into the controller. Whereas, gravity vector and Coriolis/centrifugal terms were kept unknown to the controller. Furthermore, viscous friction and unknown bounded disturbance caused by the patient's muscular activity were introduced by random noise being fed into the system.

It is noticeable from *Figure 7.39* that the trajectory tracking error less than 0.2° proving the SMC-TDE controller's robustness. However, oscillation in the torque output can be seen from the 3rd

row of *Figure 7.39*, which shows measured torque from the dynamic model. This chattering phenomenon is provoked by "$sign$" function used in the control model.

The control gains used for the simulation were found by trial and error, and are as follows:

$$\lambda = diag[25 \quad 25], and$$

$$K_1 = diag[90 \quad 90]$$

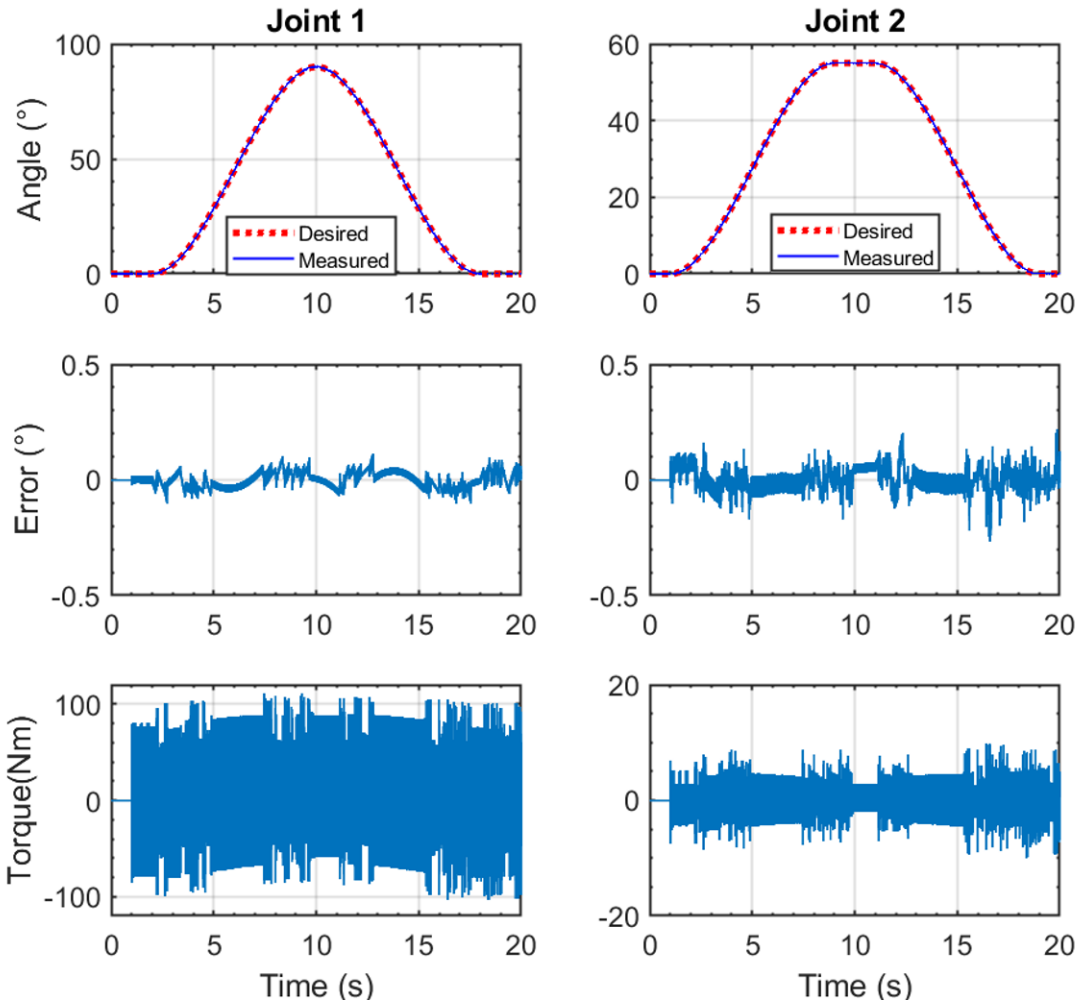

Figure 7.39 Simulation with Joint 1 and Joint 2 simultaneous motion using SMC-TDE

CHAPTER 8

EXPERIMENTS AND RESULTS

This chapter covers the experimentation of UWM-FWRR with human subjects. The experimental setup and the implementation of the control techniques have been described at the beginning of Chapter 7. Afterward, experimental results with two different control techniques (e.g., PID, CTC) are shown. During the experiments, the UWM-FWRR was maneuvered to follow a pre-programmed trajectory [38] that corresponds to the recommended passive rehabilitation protocol. The quantitative measure of passive arm movement therapy is evaluated by measuring tracking errors as a function of time (i.e., the deviation between desired and measured trajectories). The chapter ends with a brief discussion on the experimental results.

8.1 Experimental Setup and Control Implementation

The experimental set-up for the UWM-*FWRR* system is depicted in *Figure 8.1*. Hall sensors, which are embedded with each joint motor of the UWM-*FWRR,* are sampled at 100μs. The signals are then processed to increment and decrement the joint angle in the memory and passed over to the controller.

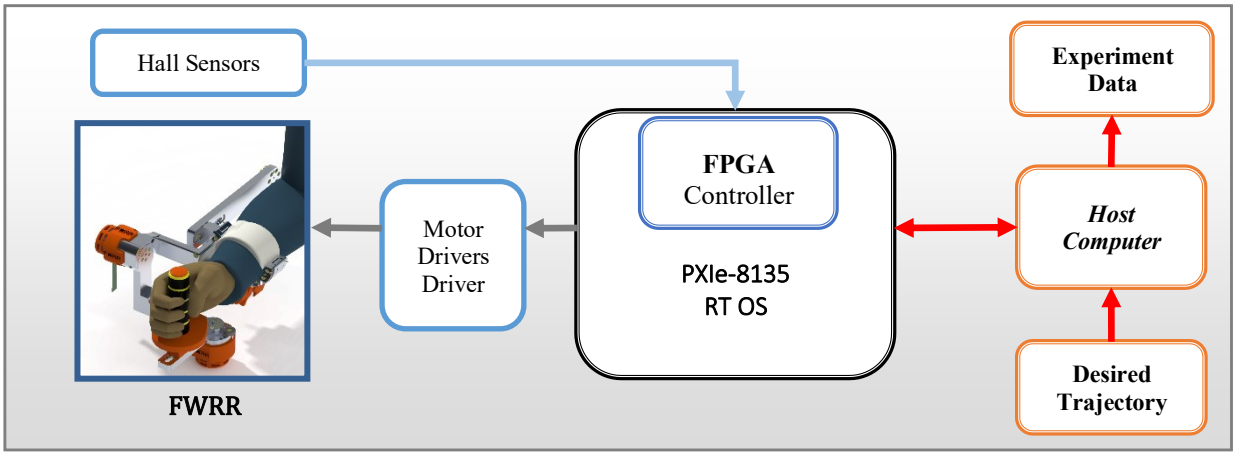

Figure 8.1 Experimental setup

The parameters of the filter were set by trial and error to $\omega_0 = 30$ rad/s, and $\zeta = 0.9$.

Control architecture for the *FWRR* system is depicted in *Figure 8.2*.

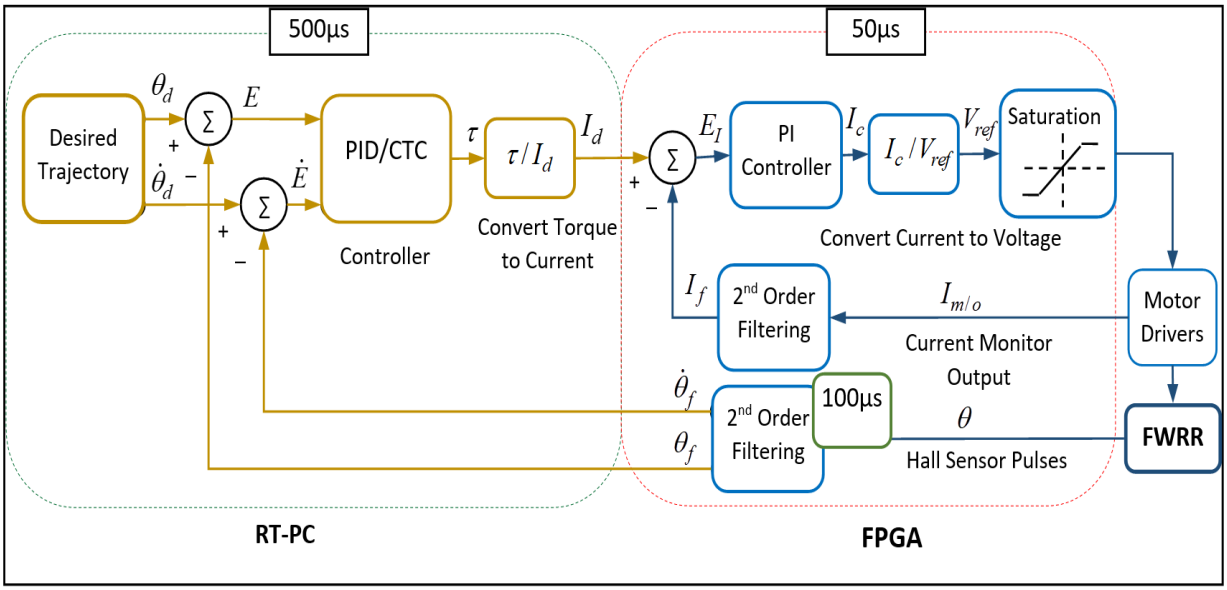

Figure 8.2 Control Architecture of UWM-FWRR

The joints' torque commands are the output of the controller. However, the torque commands are converted to motor currents, and finally, to reference voltage as voltage value is the drive command

for the motor drivers. Note that the controller (PID and CTC) updates the torque commands every 500μs and is executed in RT OS (left dotted circle, *Figure 8.2*).

Furthermore, to realize the real-time control of the *FWRR,* and also to ensure the right control torque commands were sent to the joints (as well as the reference voltage commands for the drivers), we have also added a PI controller (right dotted circle, *Figure 8.2*) to minimize the differences between desired and measured currents (i.e., the error command to PI controller). The PI controller runs ten times faster than the torque control loop and is executed in FPGA. The current signals measured from the current monitor output of motor drivers are sampled at 50 μs and are then filtered with a 2nd order filter (*Figure 8.3*) with a damping factor ζ=0.90 and natural frequency ω_0=1000 rad/s prior to being sent to the PI controller.

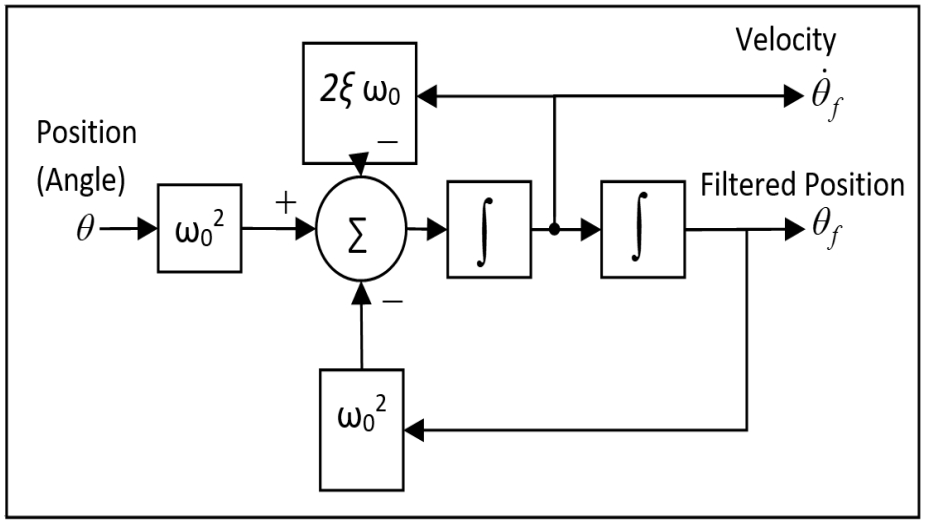

Figure 8.3 Second Order Filtering Scheme

8.2 **Rehabilitative Exercises with UWM-FWRR**

The aim of this experiment was to provide therapeutic movements to healthy Individuals in order to prove the functionality of the developed UWM-FWRR. The movements introduced during experiments were adapted from a library of passive rehabilitation exercises, which was formed according to recommended passive therapy [38]. Experiments were carried out with healthy male human subjects (age: 28-29 years; height: 5ft 4 in - 6 ft 1 in; Weight: 125-198 lbs.; the number of subjects: 3) to conduct passive rehab therapy sessions. This includes passive exercises of both simultaneous movements of all three wrist joints and individual wrist joint movement. For the experiments, the following passive movements were provided to the human participants.

- **Forearm Pronation/ Supination Exercise:**

The forearm cuff of UWM-FWRR starts from the initial position (0°) (see *Figure 8.4*), then provides supination movement to the human forearm until it reaches +70°(see *Figure 8.4*) then the joint rotates to -70° (see *Figure 8.4*) providing the supination motion and finally returns to the initial position. The first cycle completes within 6s, and then there's a 0.5s delay. Afterward, the same movement is provided within 12s period, and after another 0.5s delay it runs within 16s. The generated trajectory for conducting an experiment with subjects for Forearm Pronation/ Supination motion can be seen from *Figure 8.5*. For the first cycle, the maximum velocity is 44.5°/s; 29.5°/s and 22.5°/s for the 2nd and 3rd cycle, respectively.

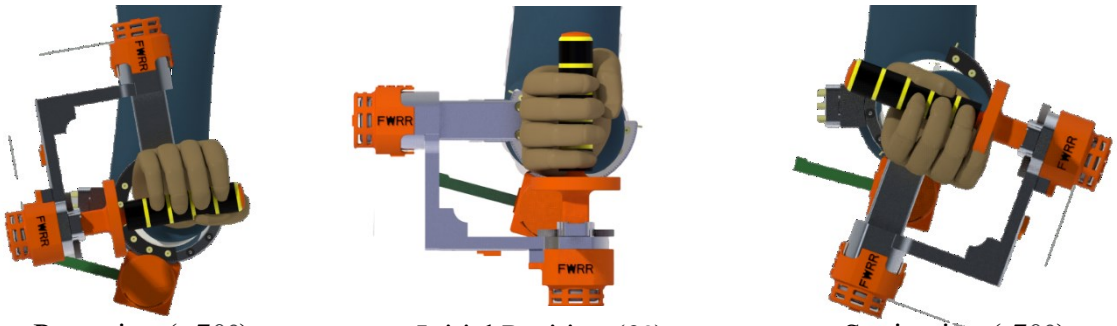

Figure 8.4 Passive Exercise (Forearm Pronation/ Supination)

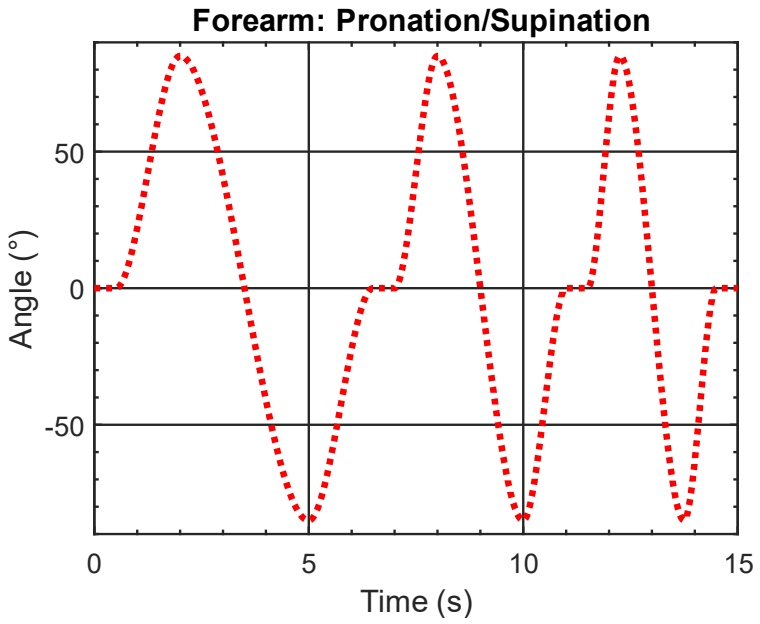

Figure 8.5 Generated trajectory for Forearm Pronation/ Supination exercise

- **<u>Wrist Radial/ Ulnar Deviation Exercise:</u>**

The wrist handle of UWM-FWRR starts from the initial position (0°) (see *Figure 8.6*), then provides radial deviation movement to the human wrist until it reaches +20° (see *Figure 8.6*) then the joint rotates to -25° (see *Figure 8.6*) providing the ulnar deviation motion and finally returns to the initial position. The first cycle completes within 6s, and then there's a 0.5s delay. Afterward,

the same movement is provided within 12s period, and then after another 0.5s delay it runs within 16 s. The generated trajectory for conducting an experiment with subjects for Wrist Radial/ Ulnar Deviation motion can be seen from *Figure 8.7*. For the first cycle, the maximum velocity is 18°/s; 12.5°/s and 9°/s for 2nd and 3rd cycle, respectively.

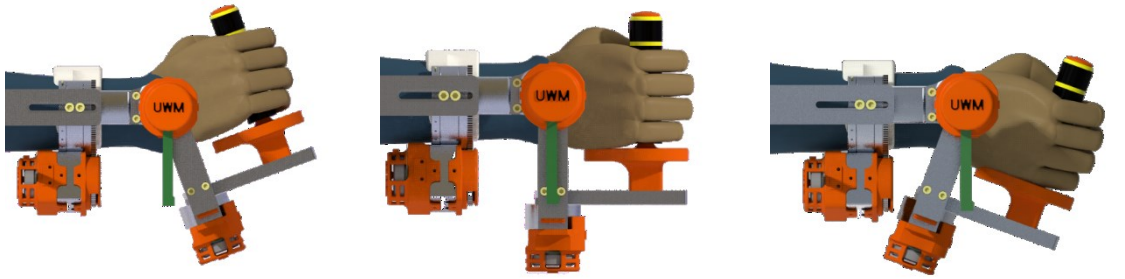

Radial Deviation (+20°) Initial Position (0°) Ulnar deviation (-25°)

Figure 8.6 Passive Exercise (Wrist Radial/ Ulnar Deviation)

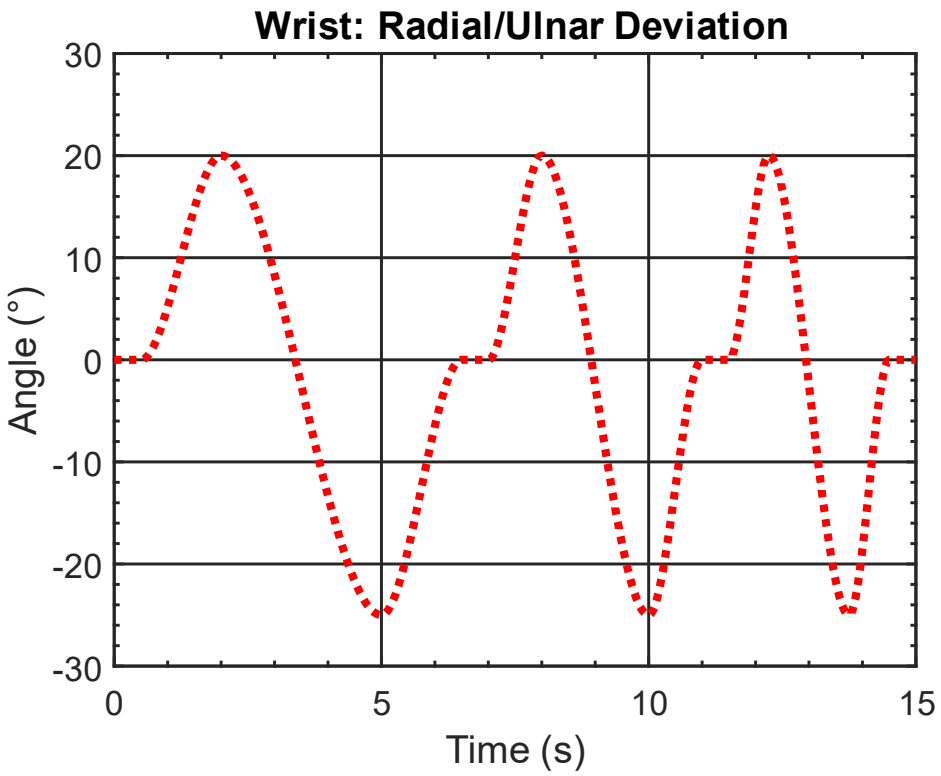

Figure 8.7 Generated trajectory for Wrist Radial/ Ulnar Deviation exercise

- **Wrist Flexion/ Extension exercise:**

The wrist handle of UWM-FWRR starts from the initial position (+30° which corresponds to human wrist nominal position 0°) (see *Figure 8.8*), then provides flexion movement to the human wrist until it reaches +60° which corresponds to human wrist position 30° (see *Figure 8.8*) then the joint rotates to -30° which corresponds to human wrist position -60° (see *Figure 8.8*) providing the wrist extension motion and finally returns to the initial position. The first cycle completes within 6s, and then there's a 0.5s delay. Afterward, the same movement is provided within the 12s period, and then after another 0.5s delay it runs within 16 s. The generated trajectory for conducting an experiment with subjects for Wrist Flexion/ Extension motion can be seen from *Figure 8.9*. For the first cycle, the maximum velocity is 33°/s; 20.5°/s and 17.5°/s for the 2^{nd} and 3^{rd} cycle, respectively.

Wrist Extension (-30°) Initial Position (+30°) Wrist Flexion (+60°)

Figure 8.8 Passive Exercise (Wrist Flexion/ Extension)

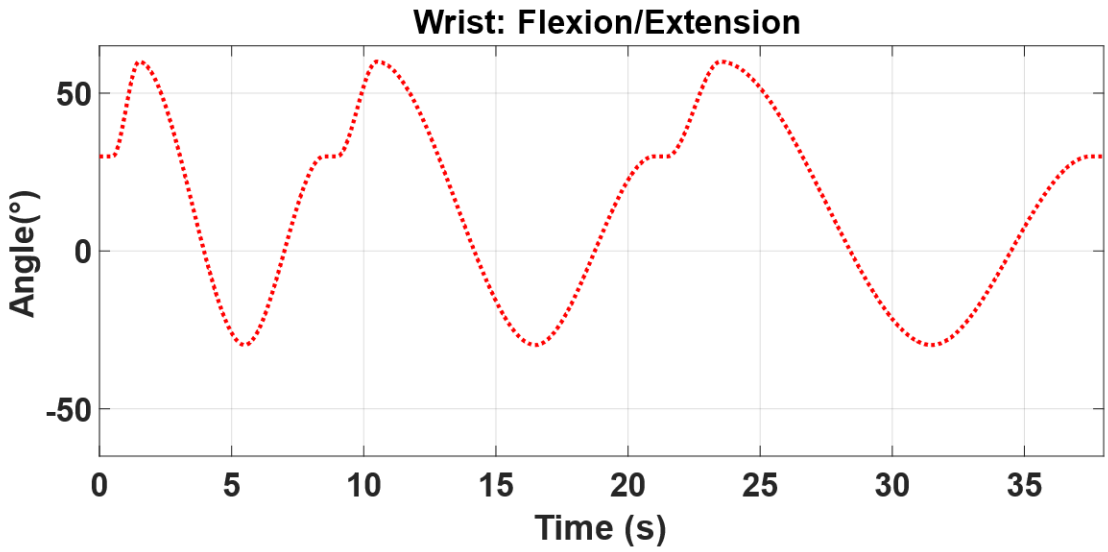

Figure 8.9 Generated trajectory for Wrist Flexion/ Extension exercise

In all cases, initial velocities and acceleration are given as zero. Note that the desired trajectories and associated velocities were generated using the cubic polynomial approach [12].

8.2.1 **Experimental Results with PID Control**

In this section experimental results can be seen for passive exercises of forearm and wrist joints of subjects, provided by UWM-FWRR on PID control mode.

8.2.1.1 **Simultaneous Joint movements of Subject-A with PID control**

Subject-A (age: 28 years; height: 5ft 4 in; Weight: 125 lbs.) wore the UWM-FWRR and all three joints (Forearm Pronation/ Supination (Joint-1) – range: +70° -70°, Wrist Radial/ Ulnar Deviation (Joint-2) – range: +20° -25°, & Wrist Flexion/ Extension (Joint-3) – range: +60° -30°) simultaneously move over the same time period (38s) and follows the trajectory mentioned in the previous section (see 8.2). The experimental results can be seen in *Figure 8.10*, *Figure 8.11*, *Figure 8.12*, and *Figure 8.13*. The tracking performance of all three joints' simultaneous movement can be seen from *Figure 8.10*, where the 1st column corresponds to Joint-1, and the 2nd and 3rd column corresponds to Joint-2 and Joint-3, respectively. The first row shows the trajectory comparison (desired joint angles – red dotted line, Measured joint angles – solid blue line) for three joints. The second row shows the tracking error, and the third row shows the measured torque from during the exercises. These notations are consistent throughout this CHAPTER 8 for all figures (*Figure 8.10* - *Figure 8.69*). Here the maximum tracking error found to be less than 0.5° (0.2%), which proves that the tracking performance is quite good. *Figure 8.11*, *Figure 8.12*, and *Figure 8.13* shows the plots of the joints separately. Here, the reference velocities (third row) are denoted with a red dotted line, and the measured velocities from the experiment are shown with a solid blue line. Maximum joint torque for Joint-1 found to be -3.9 Nm and +4.2 Nm; for Joint-2, the maximum joint torque is -1.72 Nm and +1.73 Nm, and for Joint-3 it is -1.92 Nm and +1.93 Nm. The positive

and negative signs denoted the direction of the joint torques. In all experiments with PID controller from section 8.2.1.1 to section 8.2.1.12 the controller gains used were same, and are as follows:

$$K_P = diag[5000 \quad 600 \quad 600],$$

$$K_I = diag[30 \quad 2 \quad 2], \text{ and}$$

$$K_V = diag[600 \quad 300 \quad 300].$$

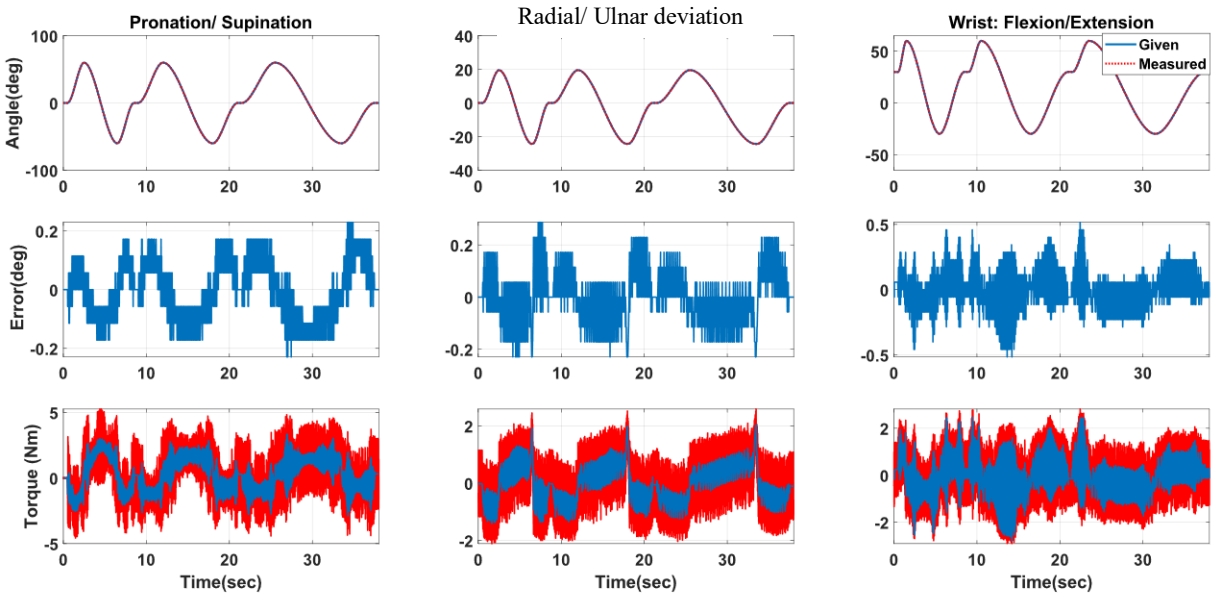

Figure 8.10 All three joints *simultaneous motion (PID) – Subject-A*

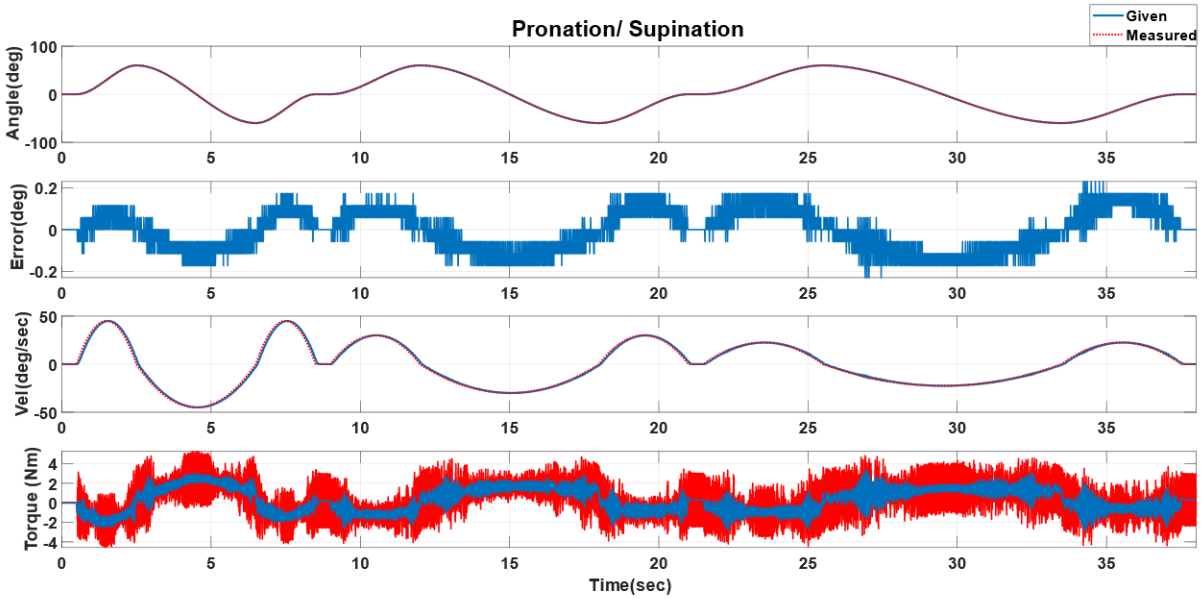

Figure 8.11 All three joints simultaneous movement (detail of Joint-1 movement with velocity comparison (PID) – Subject-A

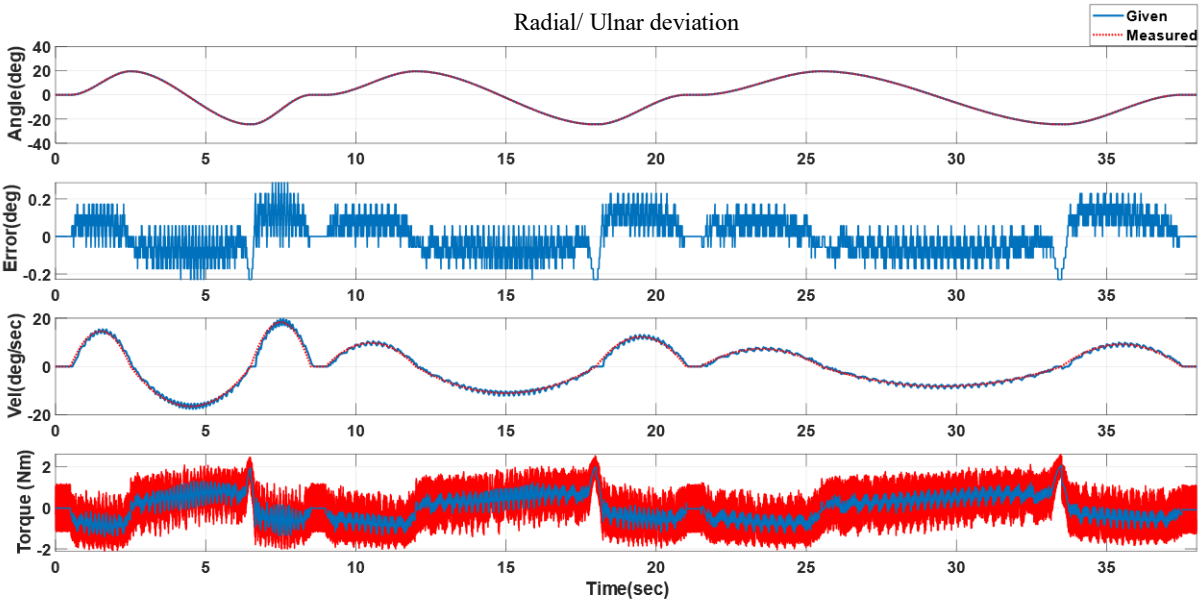

Figure 8.12 All three joints simultaneous movement (detail of Joint-2 movement with velocity comparison) (PID) – Subject-A

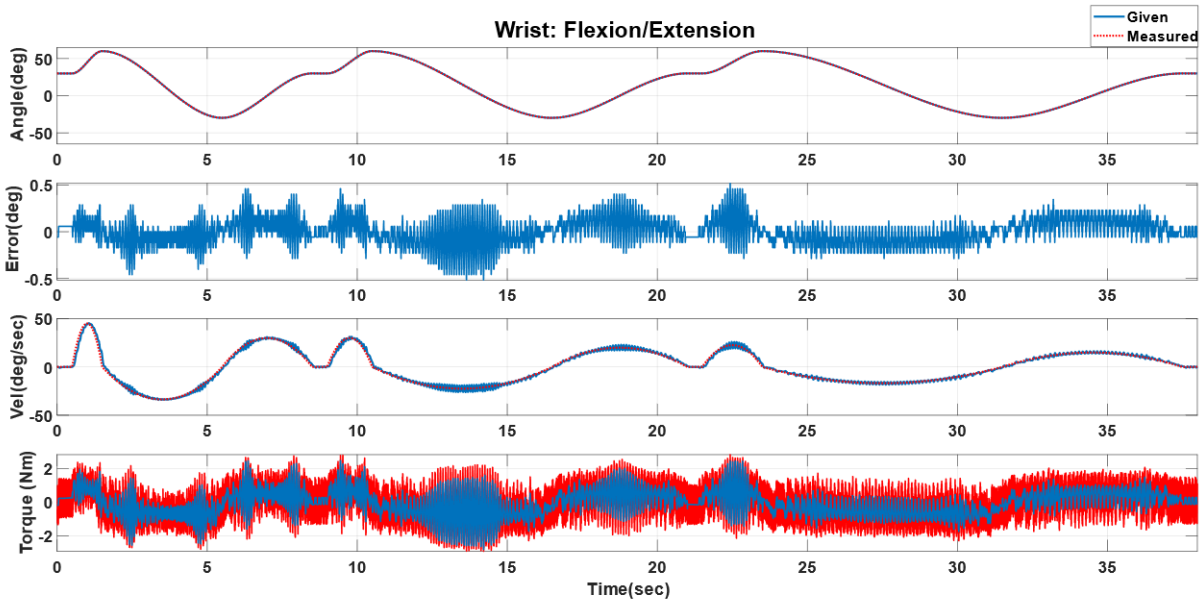

Figure 8.13 All three joints simultaneous movement (detail of Joint-3 movement with velocity comparison) (PID) – Subject-A

8.2.1.2 Individual Joint-1 (Forearm Pronation/ Supination) movement of Subject-A with PID control

Only forearm pronation and supination movement (range: +70° -70°) was provided at the period of 38s while Joint-2 (0°) & Joint-3 (+30°) stays at their initial positions. The results can be seen in *Figure 8.14* and *Figure 8.15*. The tracking performance of all three joints can be seen in *Figure 8.14*. whereas *Figure 8.15* shows velocity tracking, i.e., the reference velocity (solid blue line) during the exercise versus the measured velocity (red dotted line).

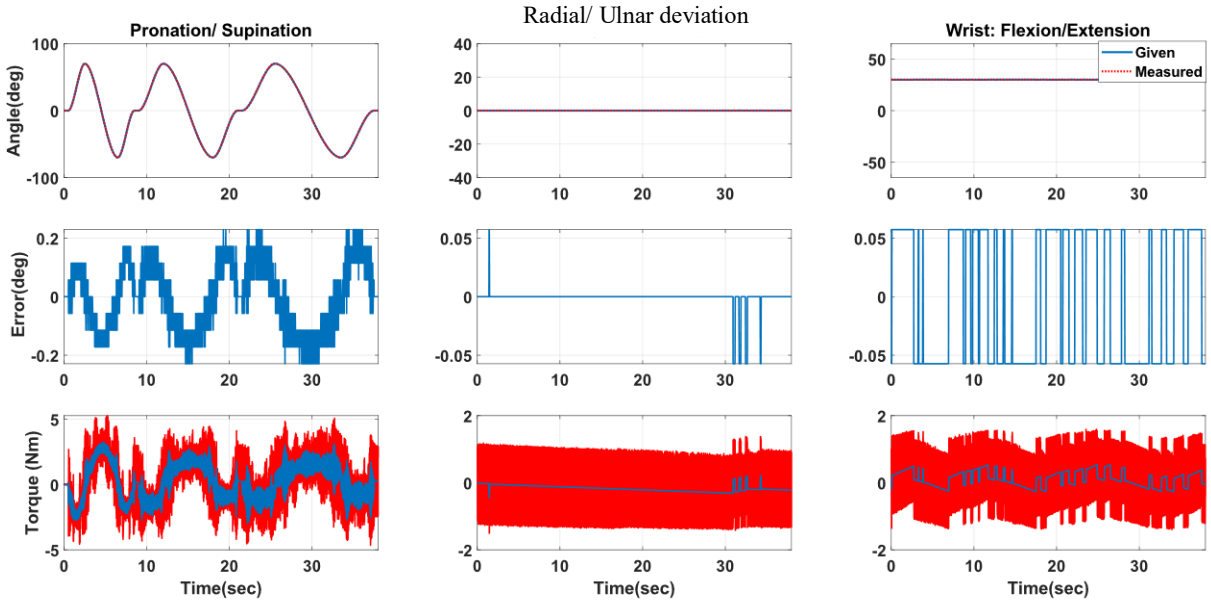

Figure 8.14 Plots of all three joints during Individual Joint-1 movement (PID) – Subject-A

1st column corresponds to Joint-1, and the 2nd and 3rd column corresponds to Joint-2 and Joint-3, respectively. The first row shows the trajectory comparison (given joint angles – red dotted line, Measured joint angles – solid blue line) for three joints. The second row shows the tracking error, and the third row shows the measured torque during the experiments.

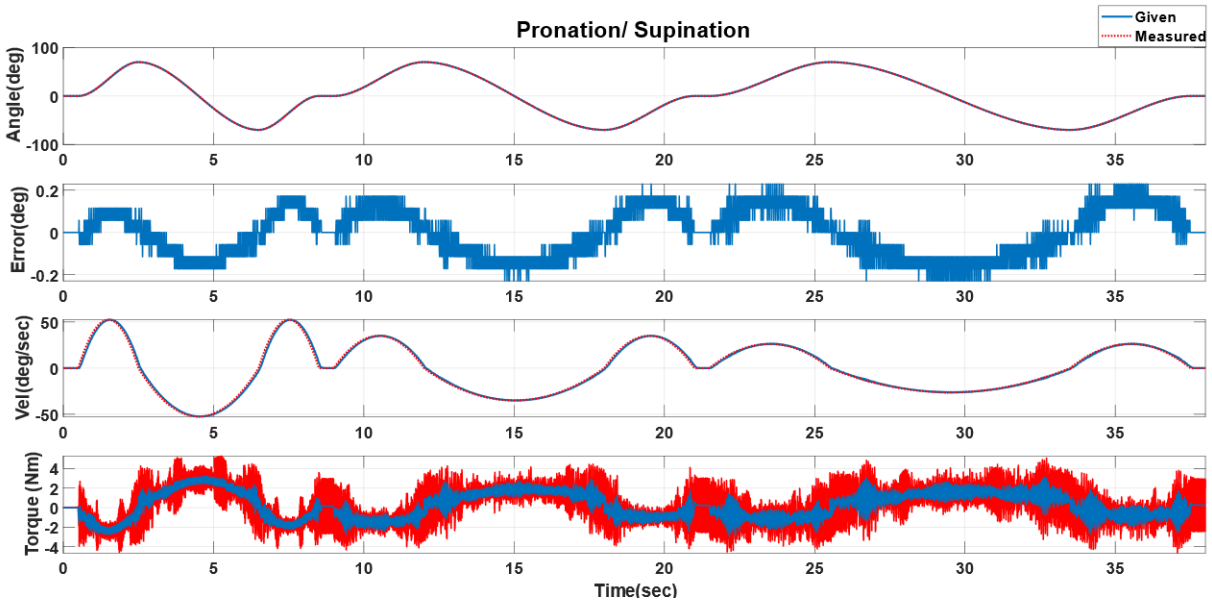

Figure 8.15 Individual Joint-1 movement with velocity comparison (PID) – Subject-A

8.2.1.3 Individual Joint-2 (Wrist Radial/ Ulnar Deviation) movement of Subject-A with PID control

Only wrist Radial/ Ulnar deviation movement (range: +20° -25°) was provided over the period of 38s while Joint-1 (0°) and Joint-3 (+30°) stayed at their initial positions. The results can be seen in *Figure 8.16* and *Figure 8.17*. The tracking performance of all three joints can be seen in *Figure*

8.16. *Figure 8.17* shows the referenced velocity (solid blue line) during the exercise and measured velocity (red dotted line).

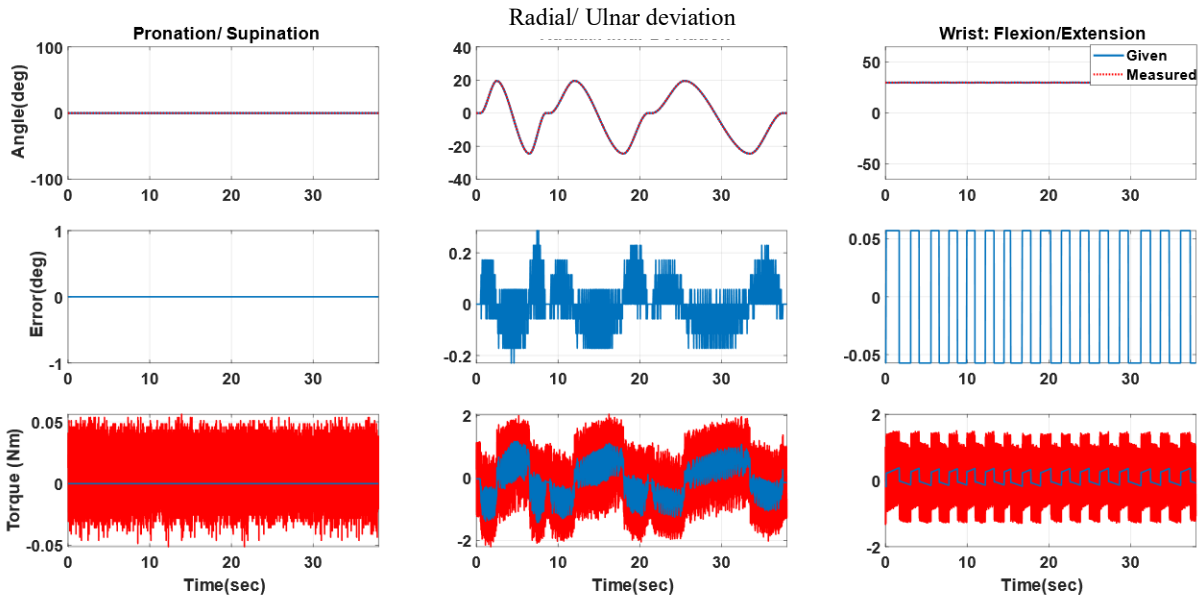

Figure 8.16 Plots of all three joints during Individual Joint-2 movement (PID) – Subject-A

1st column corresponds to Joint-1, and the 2nd and 3rd column corresponds to Joint-2 and Joint-3, respectively. The first row shows the trajectory comparison (given joint angles – red dotted line, Measured joint angles – solid blue line) for three joints. The second row shows the tracking error, and the third row shows the measured torque during the experiments.

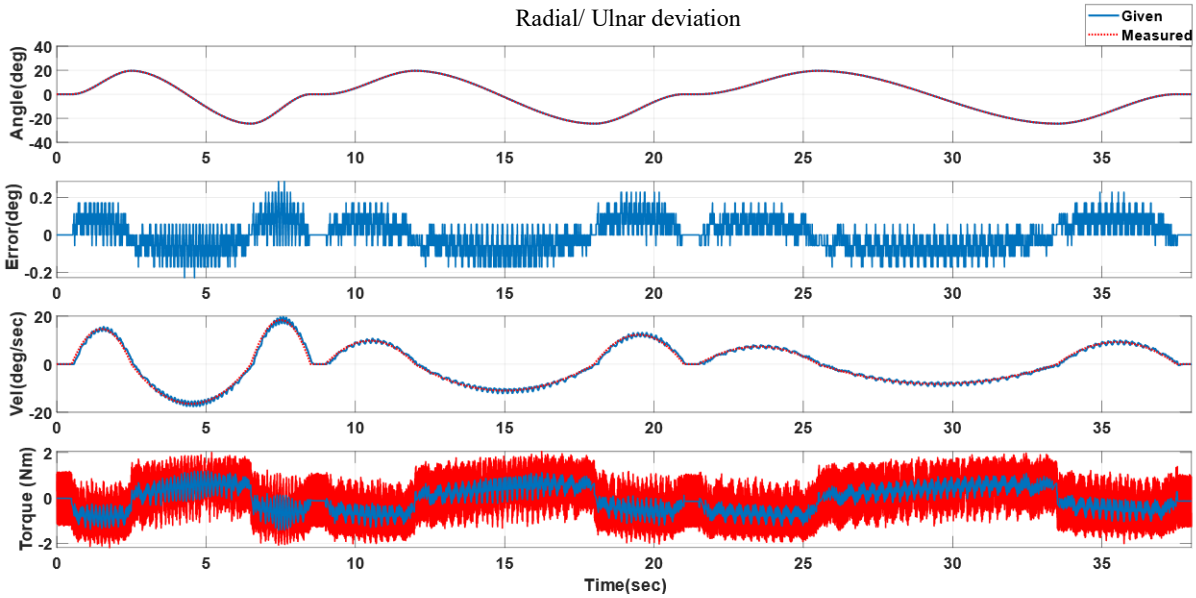

Figure 8.17 Individual Joint-2 movement with velocity comparison (PID) – Subject-A

8.2.1.4 Individual Joint-3 (Wrist Flexion/ Extension) movement of Subject-A with PID control

Only wrist flexion/extension movement (range: +60° -30°) was provided from the initial position (+30°) over the period of 38s while Joint-1 (0°) & Joint-2 (0°) stayed at their initial positions. The results can be seen in *Figure 8.18* and *Figure 8.19*. The tracking performance of all three joints can be seen from *Figure 8.18*, where the 1st column corresponds to Joint-1; and the 2nd and 3rd column corresponds to Joint-2 and Joint-3, respectively. The first row shows the trajectory comparison (Given joint angles – red dotted line, Measured joint angles – solid blue line) for three joints. The second row shows the tracking error, and third row shows the measured torque during

the experiments. *Figure 8.19* shows the reference velocity (solid blue line) during the exercise and measured velocity (red dotted line).

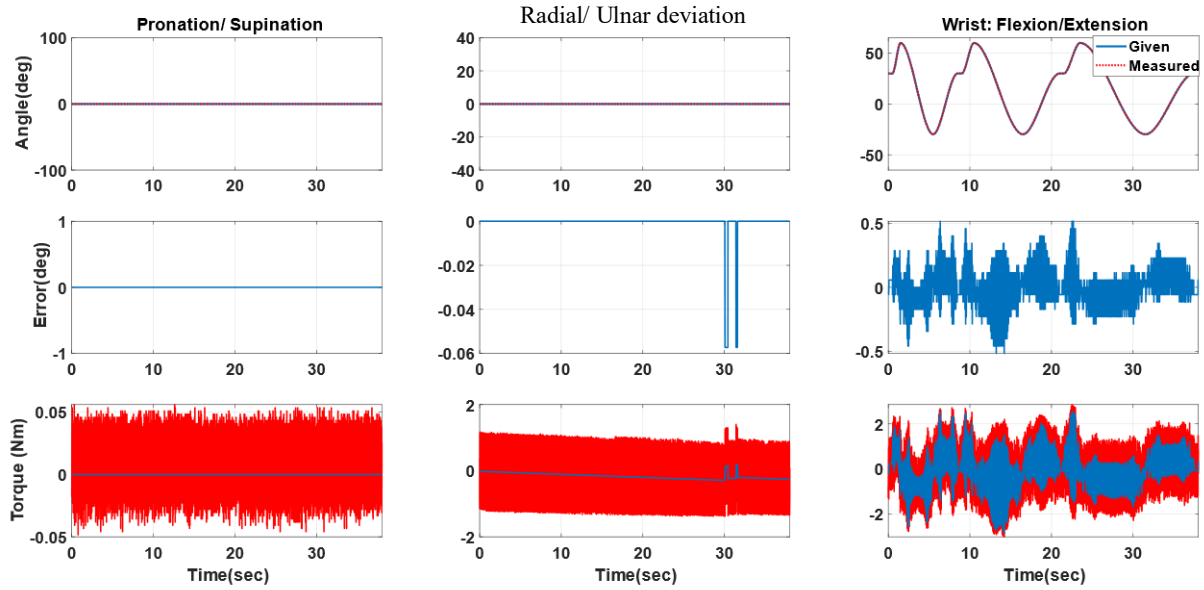

Figure 8.18 Plots of all three joints during Individual Joint-3 movement (PID) – Subject-A

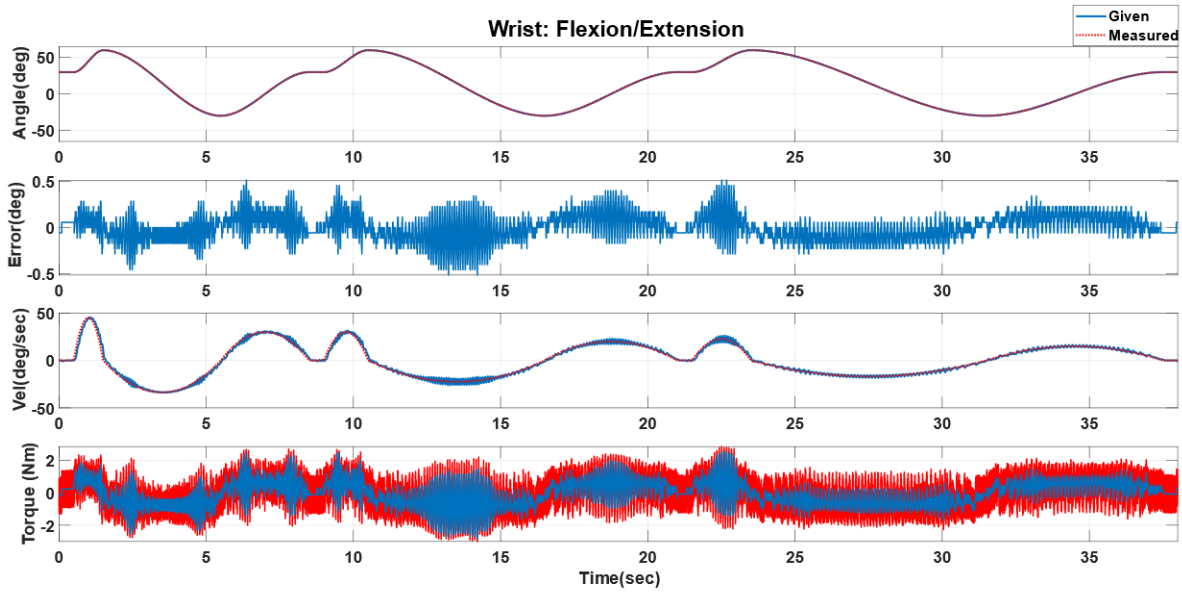

Figure 8.19 Individual Joint-3 movement with velocity comparison (PID) – Subject-A

8.2.1.5 **Simultaneous Joint movements of Subject-B with PID control**

Subject-B (age: 29 years; height: 5ft 4 in; Weight: 160 lbs.) wore the UWM-FWRR and all three joints (Forearm Pronation/ Supination (Joint-1) – range: +70° -70°, Wrist Radial/ Ulnar Deviation (Joint-2) – range: +20° -25°, & Wrist Flexion/ Extension (Joint-3) – range: +60° -30°) simultaneously move over the same time period (38s) and follows the trajectory mentioned in the section 8.2). The experimental results can be seen in *Figure 8.20*, *Figure 8.21*, *Figure 8.22*, and *Figure 8.23*. The tracking performance of all three joints' simultaneous movement can be seen in *Figure 8.20*. Here the maximum tracking error found to be less than 0.5° (0.7%), which proves that the tracking performance is quite good. *Figure 8.21*, *Figure 8.22*, and *Figure 8.23* show the plots of the joints separately. Maximum joint torque for Joint-1 found to be -4.23 Nm and +5.1

Nm; for Joint-2, the maximum joint torque is -1.84 Nm and +1.7 Nm, and for Joint-3 it is -2.9 Nm and +1.9 Nm. The positive and negative signs denoted the direction of the joint torques.

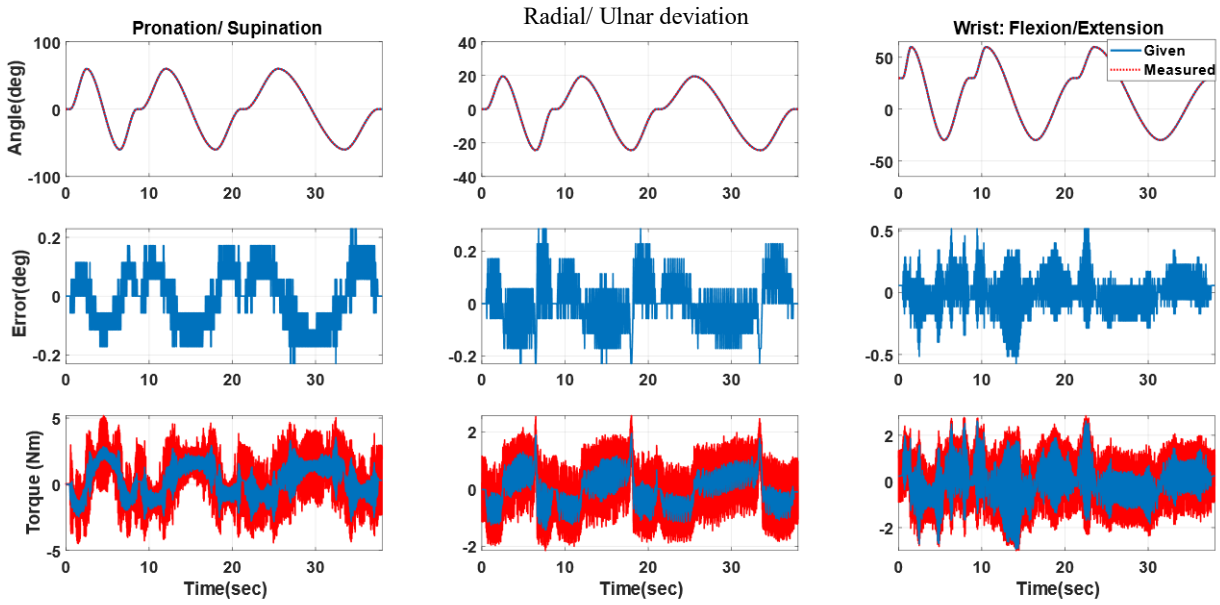

Figure 8.20 All three joints simultaneous motion (PID) – Subject-B

1st column corresponds to Joint-1, and the 2nd and 3rd column corresponds to Joint-2 and Joint-3, respectively. The first row shows the trajectory comparison (given joint angles – red dotted line, Measured joint angles – solid blue line) for three joints. The second row shows the tracking error, and the third row shows the measured torque during the experiments.

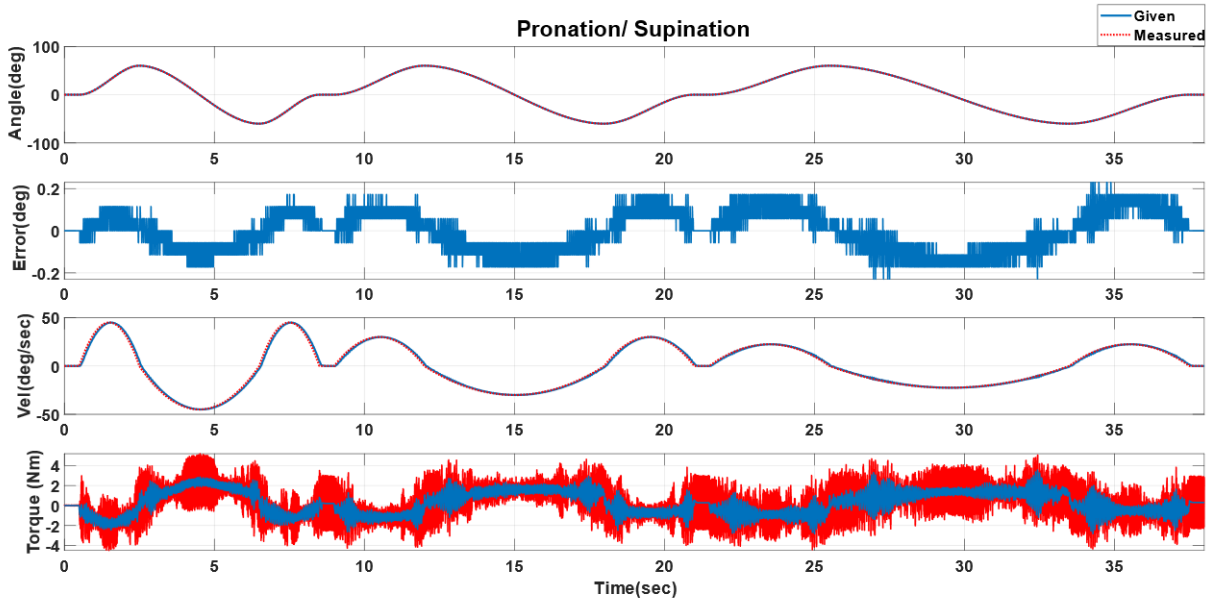

Figure 8.21 All three joints simultaneous movement (detail of Joint-1 movement with velocity comparison (PID) – Subject-B

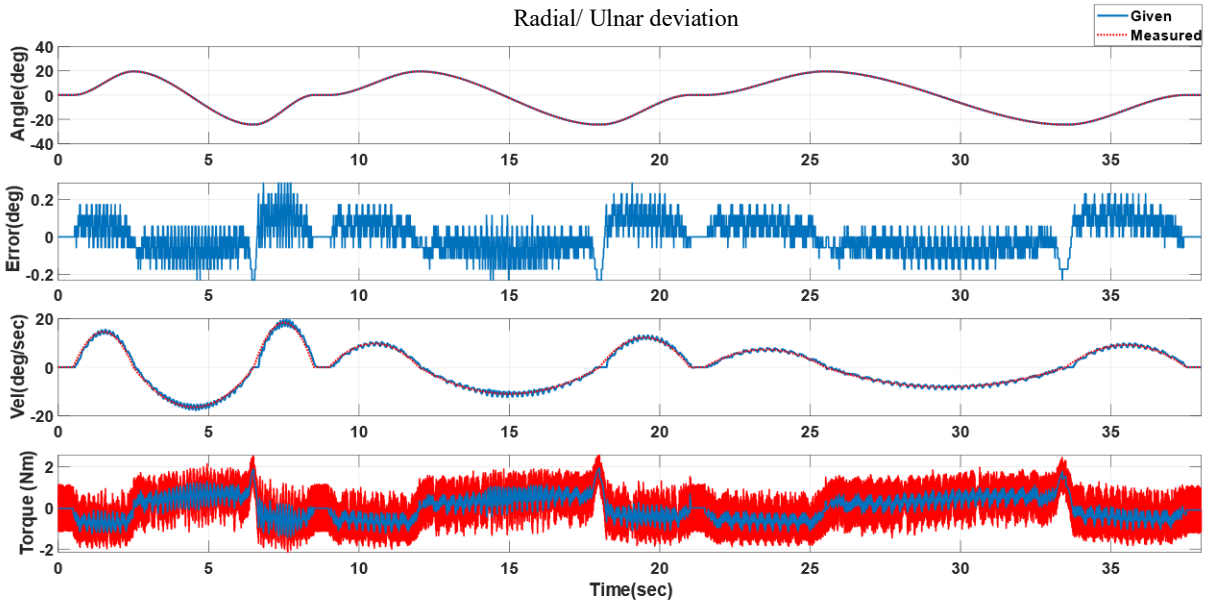

Figure 8.22 All three joints simultaneous movement (detail of Joint-2 movement with velocity comparison) (PID) – Subject-B

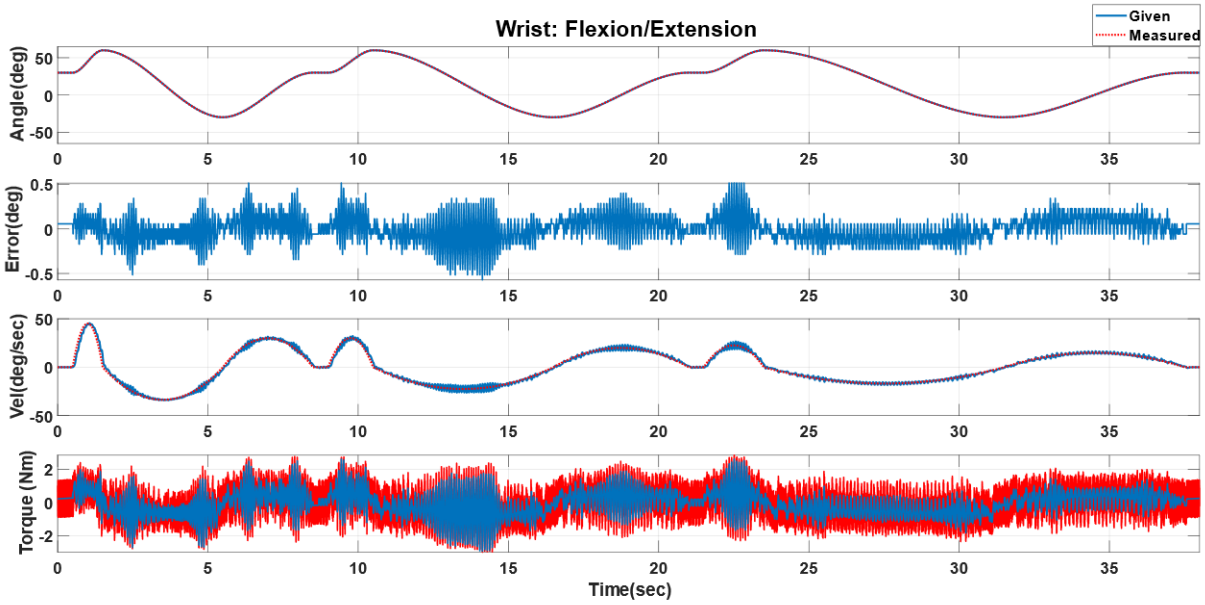

Figure 8.23 All three joints simultaneous movement (detail of Joint-3 movement with velocity comparison) (PID) – Subject-B

8.2.1.6 Individual Joint-1 (Forearm Pronation/ Supination) movement of Subject-B with PID control

Only forearm pronation and supination movement (range: +70° -70°) was provided at the period of 38s while Joint-2 (0°) & Joint-3 (+30°) stays at their initial positions. The results can be seen from *Figure 8.24*, and *Figure 8.25*. The tracking performance of all three joints can be seen in *Figure 8.24*. *Figure 8.25* shows the computed velocity (solid blue line) during the exercise and measured velocity (red dotted line).

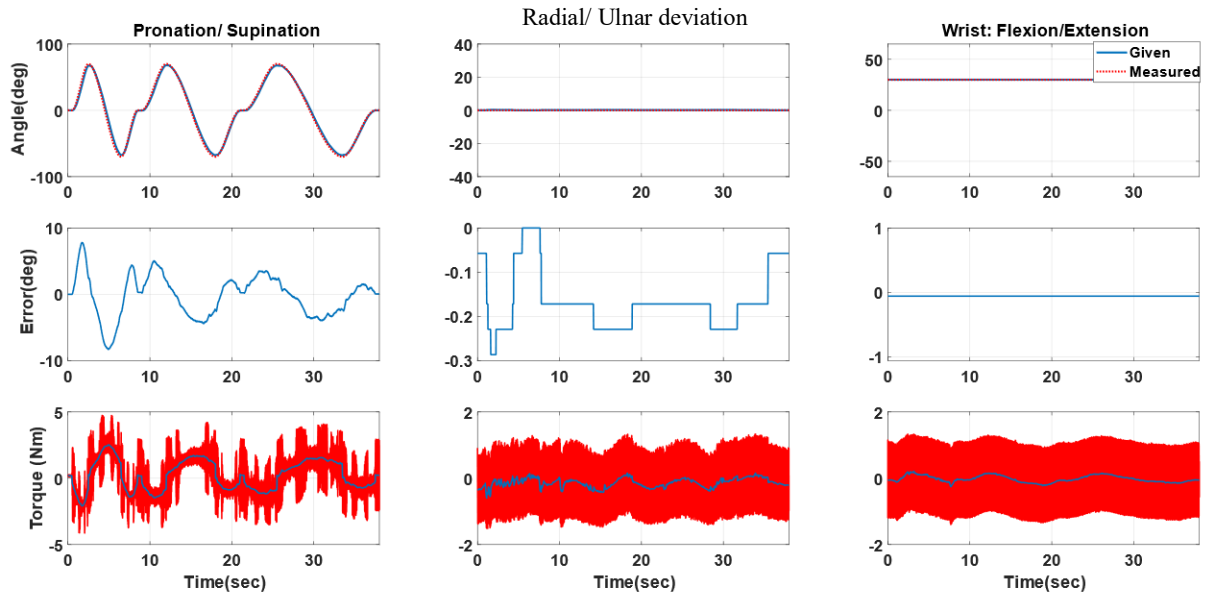

Figure 8.24 Plots of all three joints during Individual Joint-1 movement (PID) – Subject-B

1st column corresponds to Joint-1, and the 2nd and 3rd column corresponds to Joint-2 and Joint-3, respectively. The first row shows the trajectory comparison (given joint angles – red dotted line, Measured joint angles – solid blue line) for three joints. The second row shows the tracking error, and the third row shows the measured torque during the experiments.

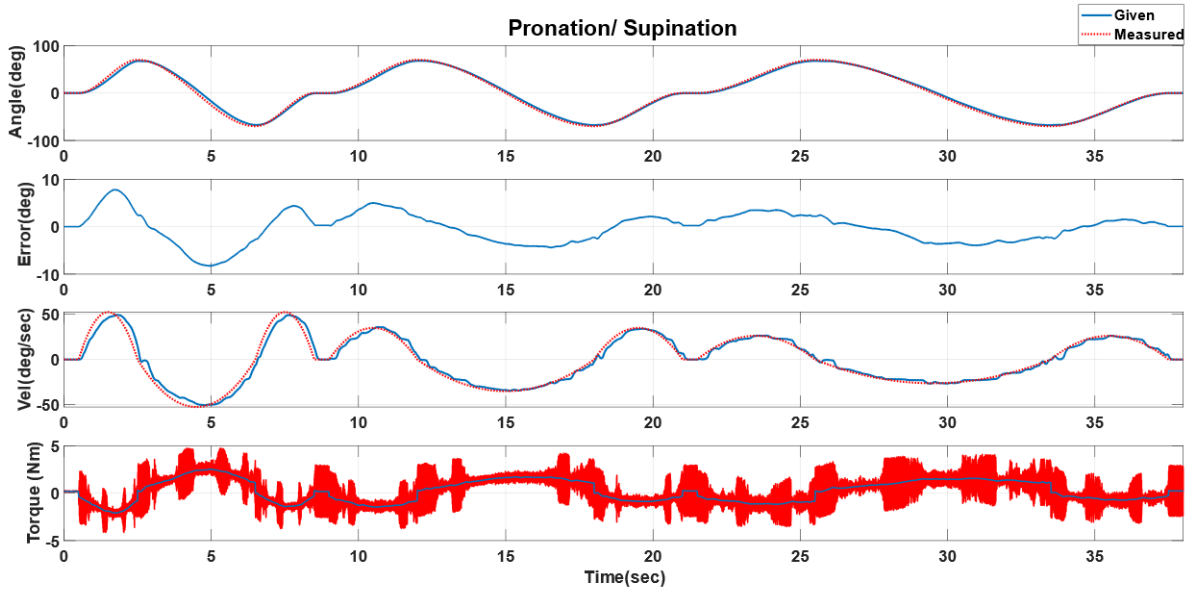

Figure 8.25 Individual Joint-1 movement with velocity comparison (PID) – Subject-B

8.2.1.7 Individual Joint-2 (Wrist Radial/ Ulnar Deviation) movement of Subject-B with PID control

Only wrist Radial/ Ulnar deviation movement (range: +20° -25°) was provided over the period of 38s while Joint-1 (0°) & Joint-3 (+30°) stayed at their initial positions. The results can be seen from *Figure 8.26*, and *Figure 8.27*. The tracking performance of all three joints can be seen in

Figure 8.26. *Figure 8.27* shows the reference velocity (solid blue line) during the exercise and measured velocity (red dotted line).

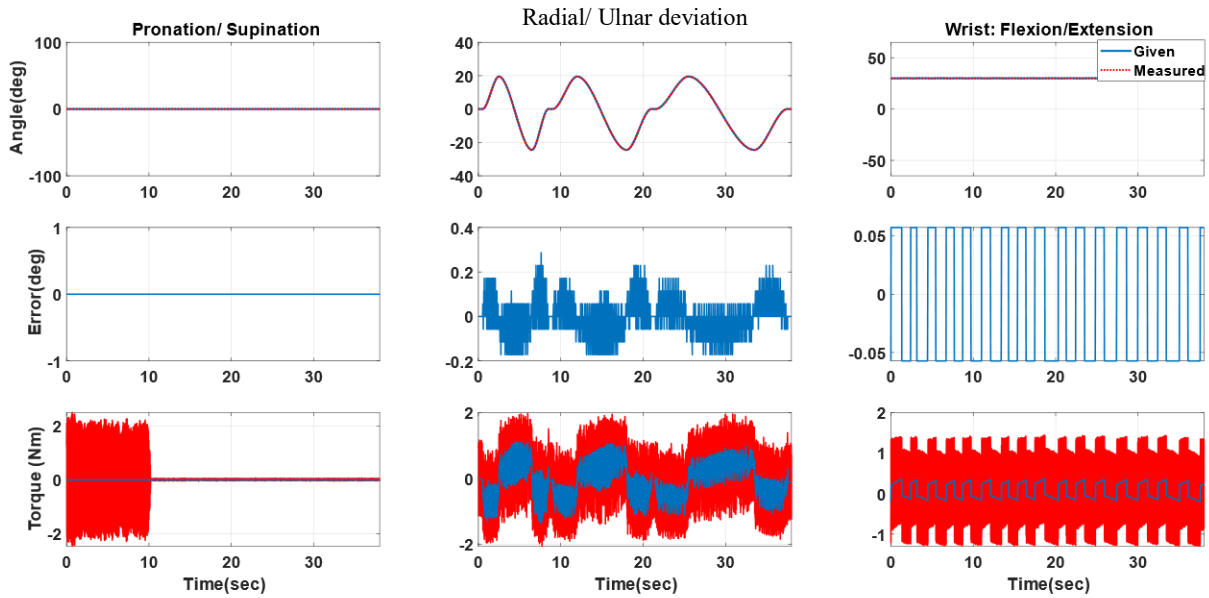

Figure 8.26 Plots of all three joints during Individual Joint-2 movement (PID) – Subject-B

1st column corresponds to Joint-1, and the 2nd and 3rd column corresponds to Joint-2 and Joint-3, respectively. The first row shows the trajectory comparison (given joint angles – red dotted line, Measured joint angles – solid blue line) for three joints. The second row shows the tracking error, and the third row shows the measured torque during the experiments.

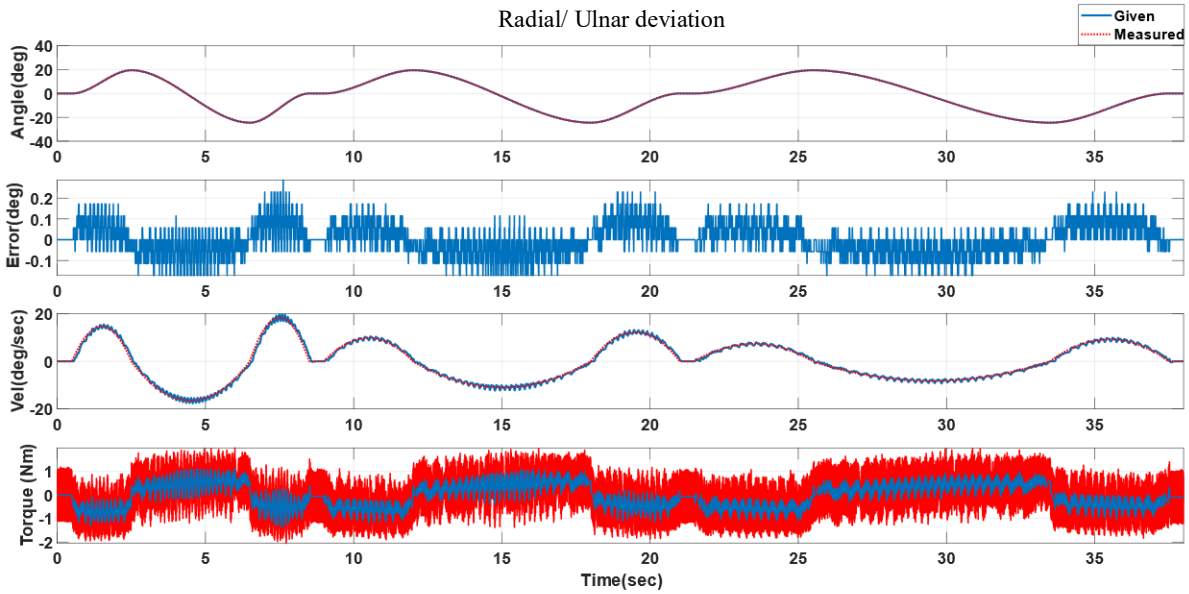

Figure 8.27 Individual Joint-2 movement with velocity comparison (PID) – Subject-B

8.2.1.8 **Individual Joint-3 (Wrist Flexion/ Extension) movement of Subject-B with PID control**

Only wrist flexion/ Extension movement (range: +60° -30°) was provided from an initial position (+30°) over the period of 38s while Joint-1 (0°) & Joint-2 (0°) stayed at their initial positions. The results can be seen from *Figure 8.28*, and *Figure 8.29*. The tracking performance of all three joints

can be seen in *Figure 8.28*. *Figure 8.29* shows the reference velocity (solid blue line) during the exercise and measured velocity (red dotted line).

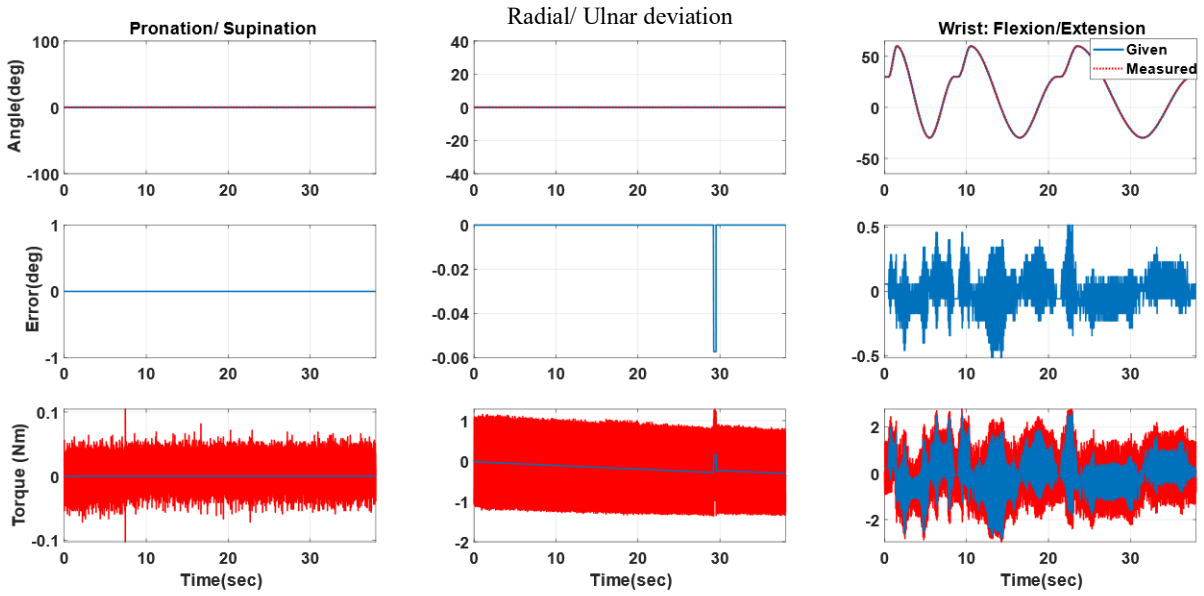

Figure 8.28 Plots of all three joints during Individual Joint-3 movement (PID) – Subject-B

1st column corresponds to Joint-1, and the 2nd and 3rd column corresponds to Joint-2 and Joint-3, respectively. The first row shows the trajectory comparison (given joint angles – red dotted line, Measured joint angles – solid blue line) for three joints. The second row shows the tracking error, and the third row shows the measured torque during the experiments.

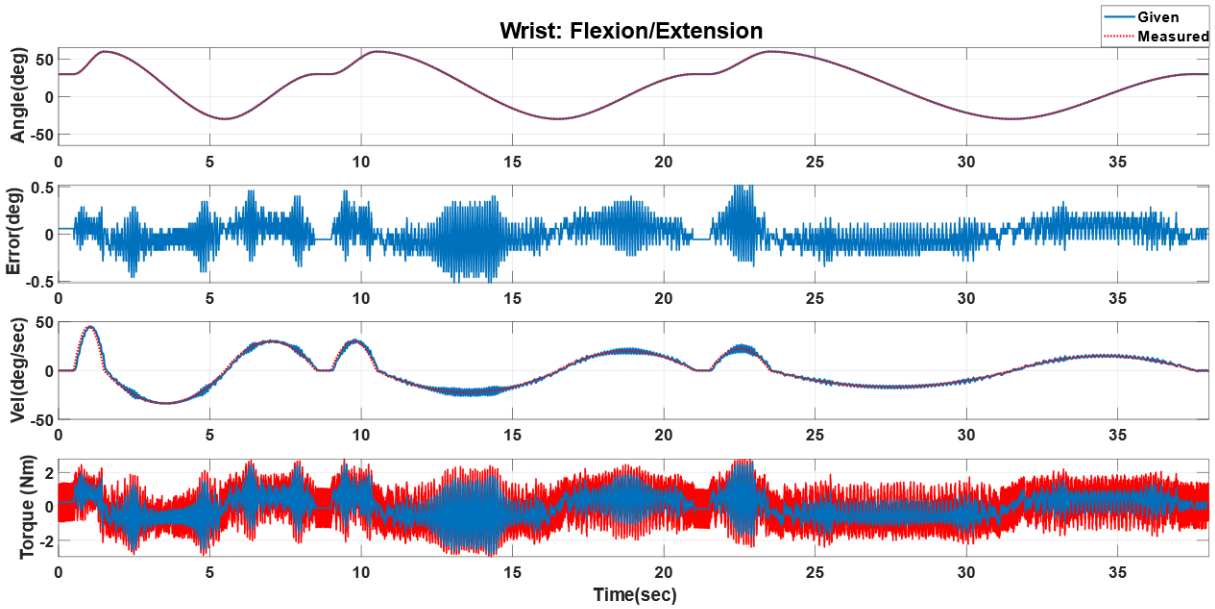

Figure 8.29 Individual Joint-3 movement with velocity comparison (PID) – Subject-B

8.2.1.9 **Simultaneous Joint movements of Subject-C with PID control**

Subject-C (age: 29 years; height: 6ft 1 in; Weight: 198 lbs.) wore the UWM-FWRR and all three joints (Forearm Pronation/ Supination (Joint-1) – range: +70° -70°, Wrist Radial/ Ulnar Deviation (Joint-2) – range: +20° -25°, & Wrist Flexion/ Extension (Joint-3) – range: +60° -30°) simultaneously move over the same time period (38s) and follows the trajectory mentioned in the section 8.2). The experimental results can be seen from *Figure 8.30*, *Figure 8.31*, *Figure 8.32*, and *Figure 8.33*. The tracking performance of all three joints' simultaneous movement can be seen from *Figure 8.30*. Here the maximum tracking error found to be less than 0.5° (0.7%), which proves that the tracking performance is quite good. *Figure 8.31*, *Figure 8.32*, and *Figure 8.33* show the plots of the joints separately. Here, the reference velocities (third row) are denoted with a red dotted line, and the measured velocities from the experiment are shown with a solid blue line.

Maximum joint torque for Joint-1 found to be -3.7 Nm and +4.8 Nm; for Joint-2 the maximum joint torque is -2.2 Nm and +1.57 Nm; and for Joint-3 it is -2.6 Nm and +2.6 Nm. The positive and negative signs denoted the direction of the joint torques.

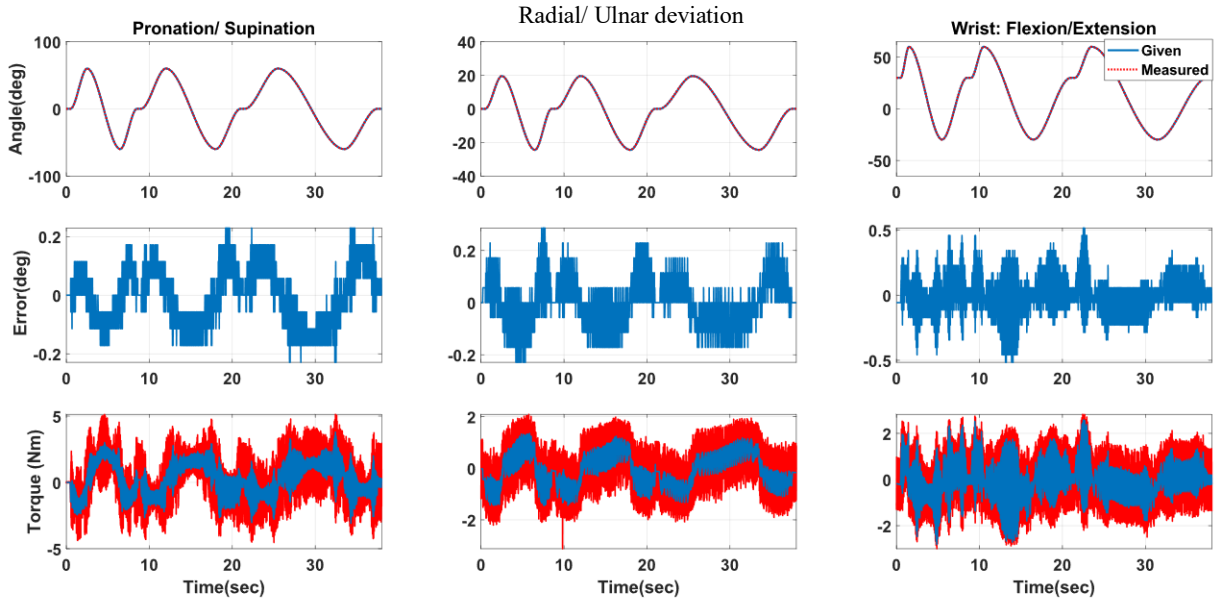

Figure 8.30 All three joints simultaneous motion (PID) – Subject-C

1st column corresponds to Joint-1, and the 2nd and 3rd column corresponds to Joint-2 and Joint-3, respectively. The first row shows the trajectory comparison (given joint angles – red dotted line, Measured joint angles – solid blue line) for three joints. The second row shows the tracking error, and the third row shows the measured torque during the experiments.

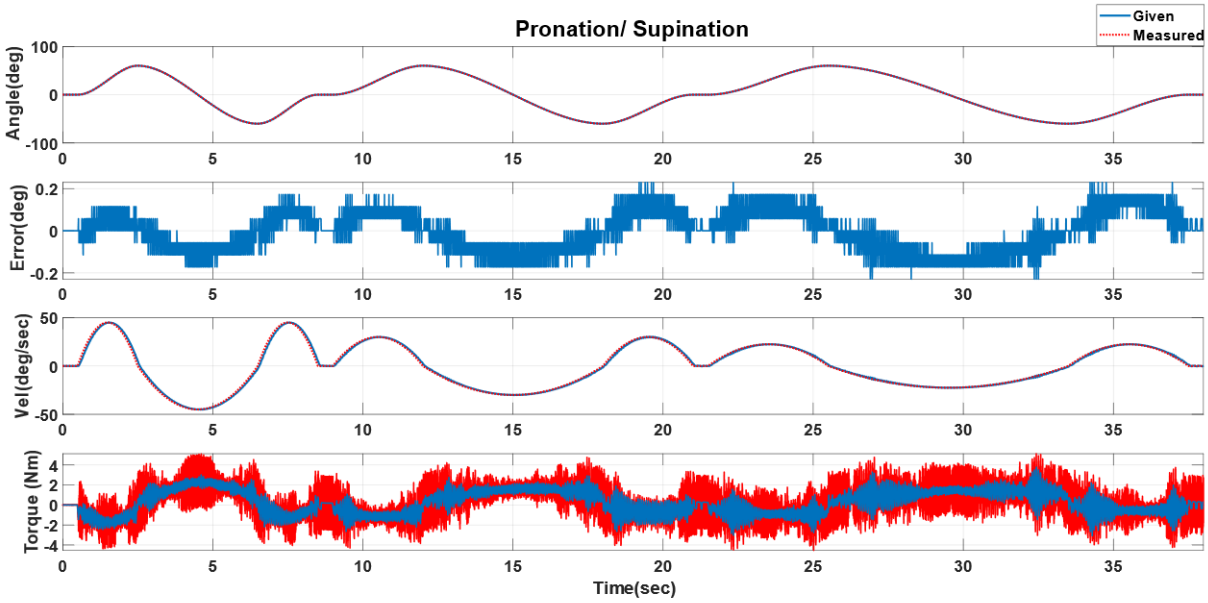

Figure 8.31 All three joints simultaneous movement (detail of Joint-1 movement with velocity comparison (PID) – Subject-C

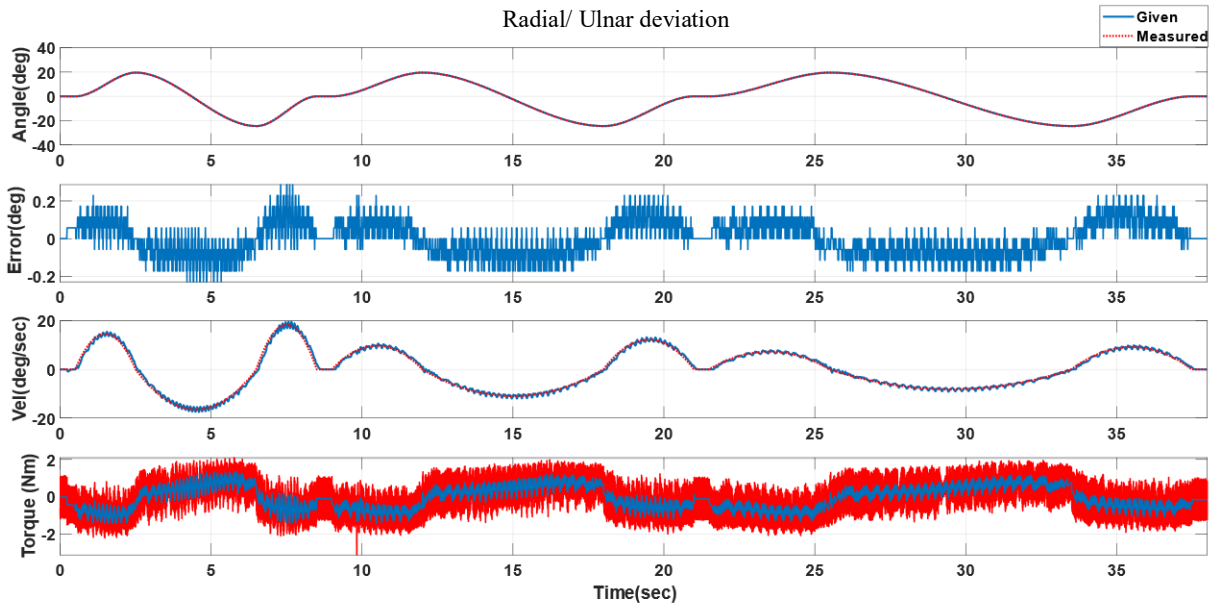

Figure 8.32 All three joints simultaneous movement (detail of Joint-2 movement with velocity comparison) (PID) – Subject-C

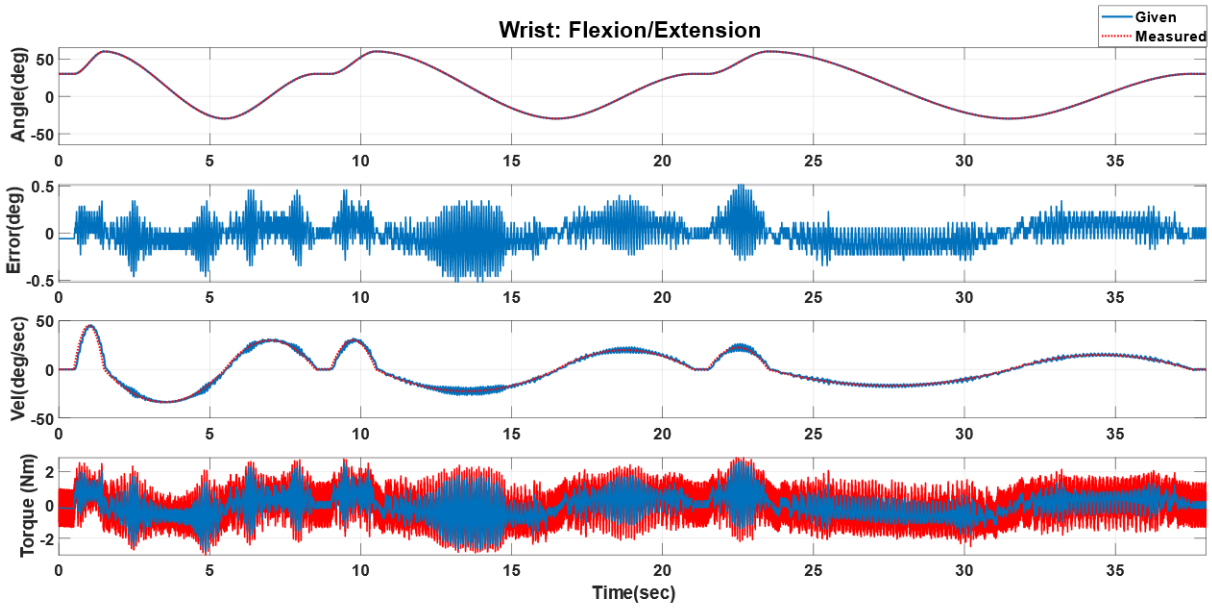

Figure 8.33 All three joints simultaneous movement (detail of Joint-3 movement with velocity comparison) (PID) – Subject-C

8.2.1.10 **Individual Joint-1 (Forearm Pronation/ Supination) movement of Subject-C with PID control**

Only forearm pronation and supination movement (range: +70° -70°) was provided at the period of 38s while Joint-2 (0°) & Joint-3 (+30°) stays at their initial positions. The results can be seen from *Figure 8.34*, and *Figure 8.35*. The tracking performance of all three joints can be seen in

Figure 8.34. *Figure 8.35* shows the reference velocity (solid blue line) during the exercise and measured velocity (red dotted line).

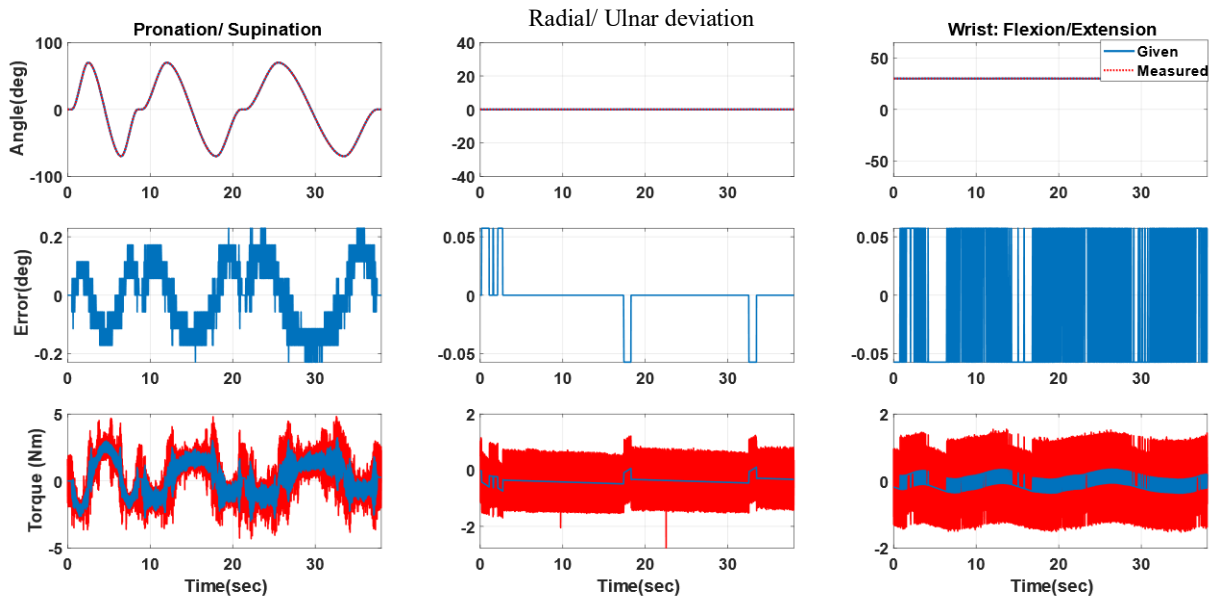

Figure 8.34 Plots of all three joints during Individual Joint-1 movement (PID) – Subject-C

1st column corresponds to Joint-1, and the 2nd and 3rd column corresponds to Joint-2 and Joint-3, respectively. The first row shows the trajectory comparison (given joint angles – red dotted line, Measured joint angles – solid blue line) for three joints. The second row shows the tracking error, and the third row shows the measured torque during the experiments.

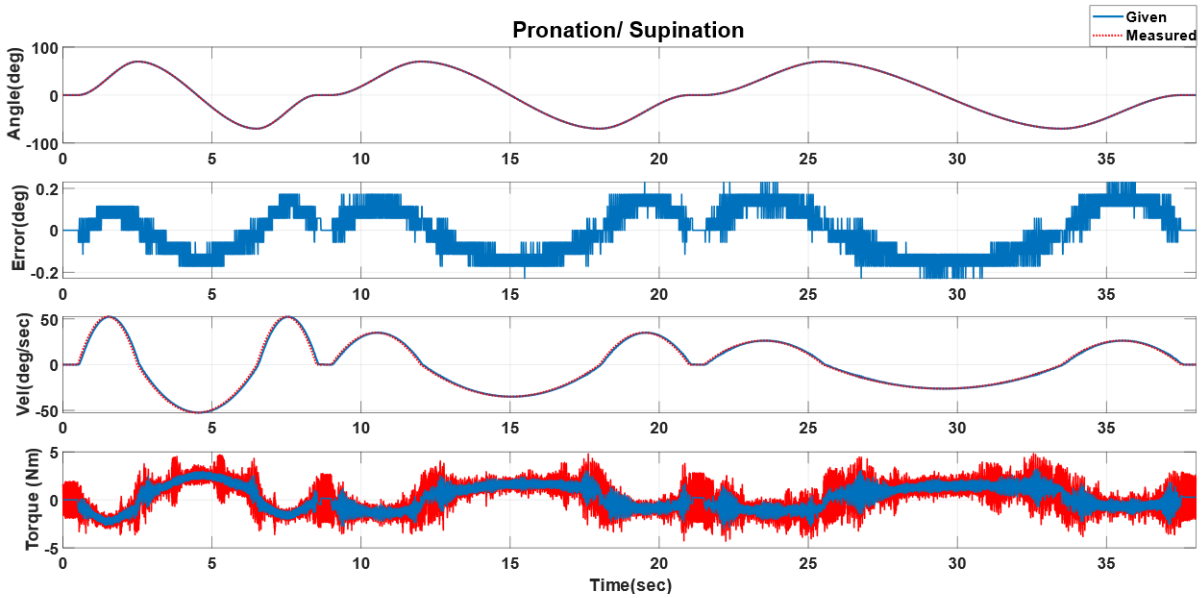

Figure 8.35 Individual Joint-1 movement with velocity comparison (PID) – Subject-C

8.2.1.11 **Individual Joint-2 (Wrist Radial/ Ulnar Deviation) movement of Subject-C with PID control**

Only wrist Radial/ Ulnar deviation movement (range: +20° -25°) was provided over the period of 38s while Joint-1 (0°) & Joint-3 (+30°) stayed at their initial positions. The results can be seen from *Figure 8.36*, and *Figure 8.37*. The tracking performance of all three joints can be seen from

Figure 8.36. *Figure 8.37* shows the reference velocity (solid blue line) during the exercise and measured velocity (red dotted line).

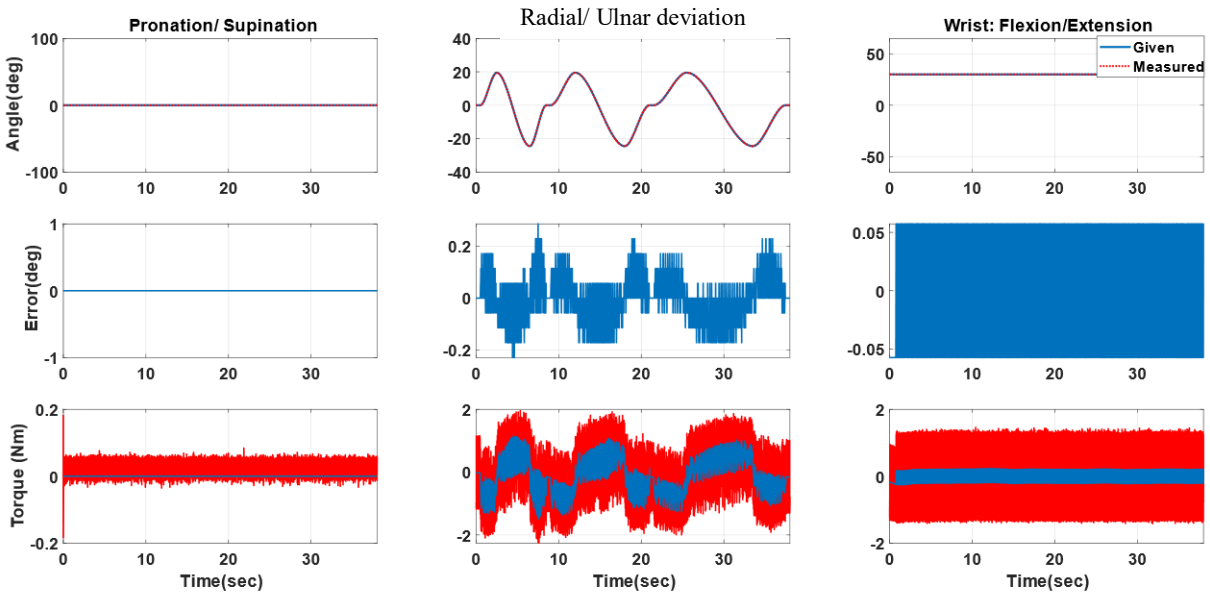

Figure 8.36 Plots of all three joints during Individual Joint-2 movement (PID) – Subject-C

1st column corresponds to Joint-1, and the 2nd and 3rd column corresponds to Joint-2 and Joint-3, respectively. The first row shows the trajectory comparison (given joint angles – red dotted line, Measured joint angles – solid blue line) for three joints. The second row shows the tracking error, and the third row shows the measured torque during the experiments.

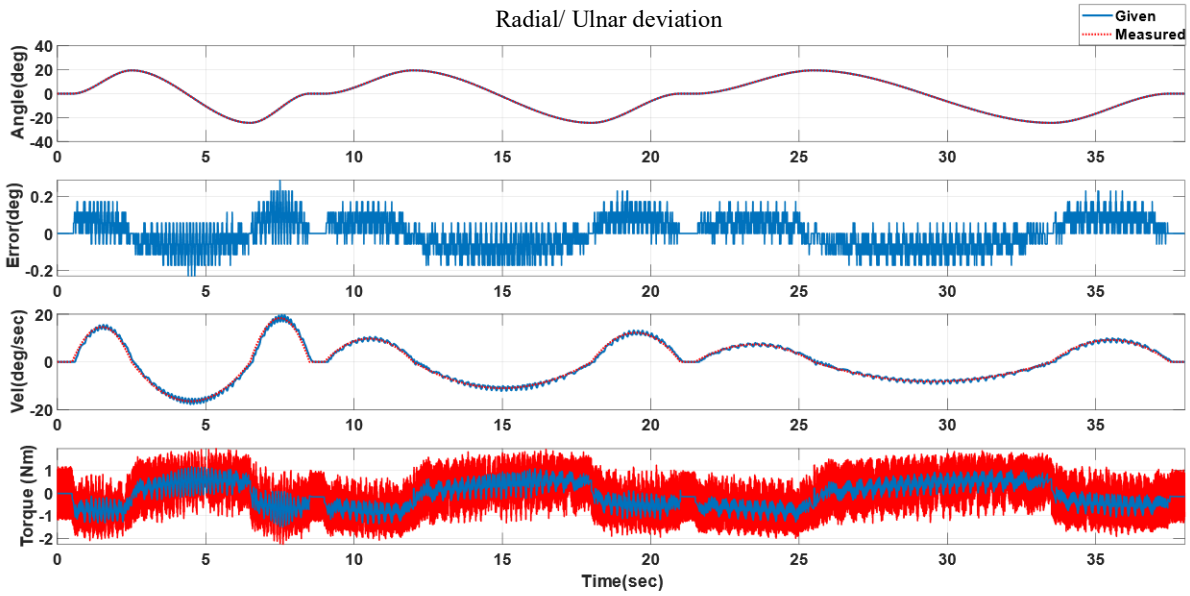

Figure 8.37 Individual Joint-2 movement with velocity comparison (PID) – Subject-C

8.2.1.12 Individual Joint-3 (Wrist Flexion/ Extension) movement of Subject-C with PID control

Only wrist flexion/ Extension movement (range: +60° -30°) was provided from the initial position (+30°) over the period of 38s while Joint-1 (0°) & Joint-2 (0°) stayed at their initial positions. The results can be seen from *Figure 8.38*, and *Figure 8.39*. The tracking performance of all three joints

can be seen from *Figure 8.28*. *Figure 8.39* shows the reference velocity (solid blue line) during the exercise and measured velocity (red dotted line).

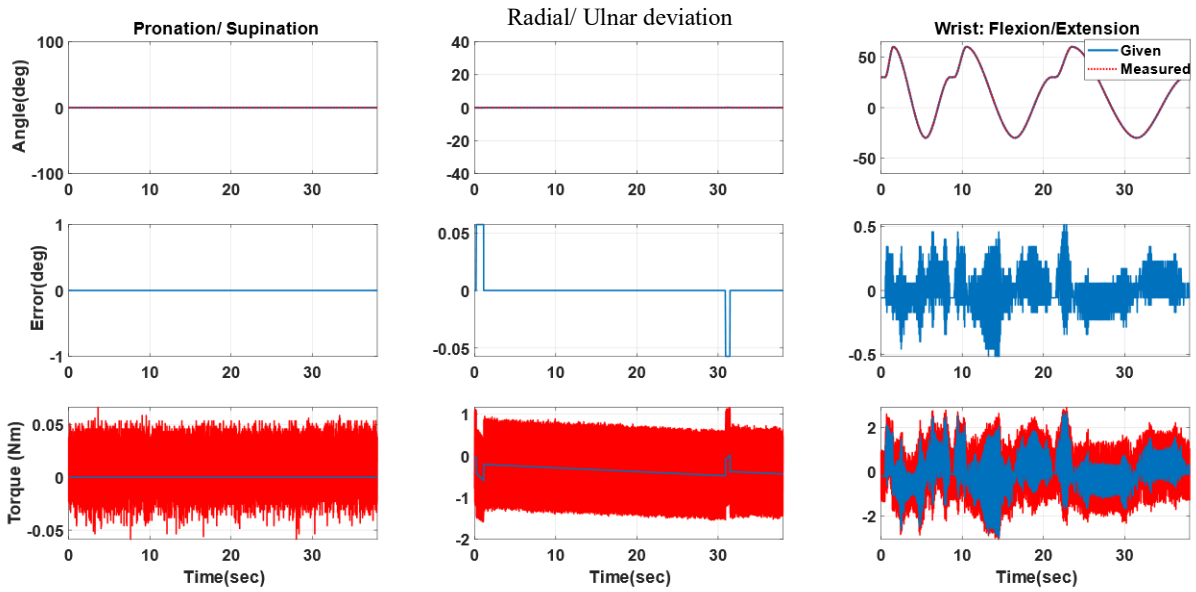

Figure 8.38 Plots of all three joints during Individual Joint-3 movement (PID) – Subject-C

1st column corresponds to Joint-1, and the 2nd and 3rd column corresponds to Joint-2 and Joint-3, respectively. The first row shows the trajectory comparison (given joint angles – red dotted line, Measured joint angles – solid blue line) for three joints. The second row shows the tracking error, and the third row shows the measured torque during the experiments.

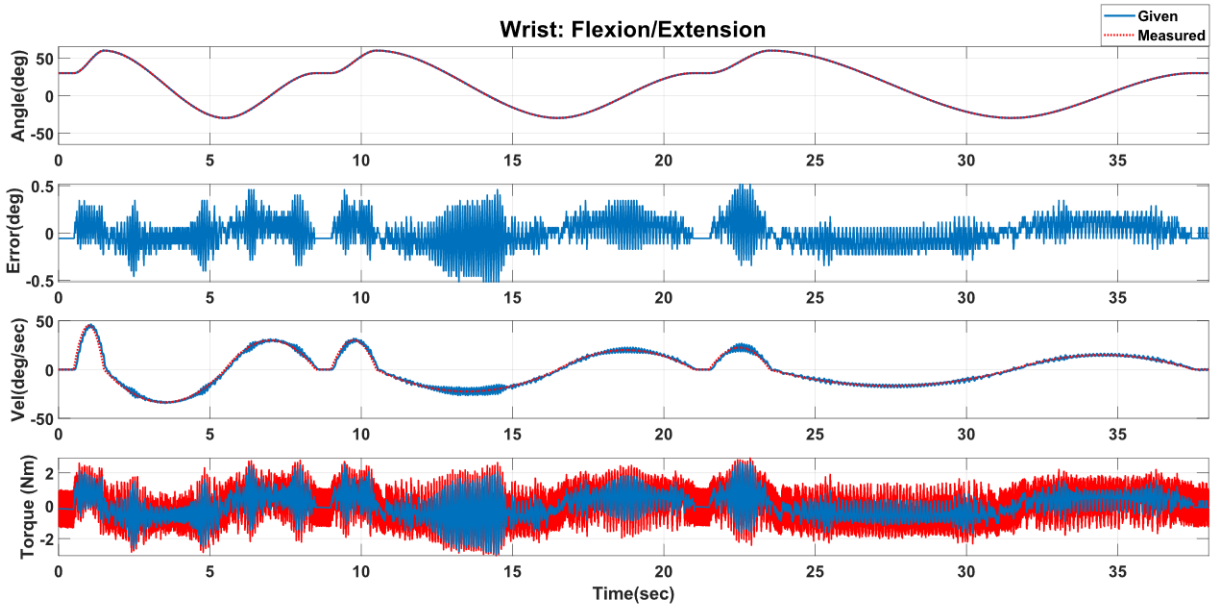

Figure 8.39 Individual Joint-3 movement with velocity comparison (PID) – Subject-C

8.2.2 **Experimental Results with modified Computed Torque Control (mCTC)**

In this section experimental results can be seen for passive exercises of forearm and wrist joints of subjects, provided by UWM-FWRR on Computed Torque Control mode.

8.2.2.1 **Simultaneous Joint movements of Subject-A with the mCTC control**

Subject-A (age: 28 years; height: 5ft 4 in; Weight: 125 lbs.) wore the UWM-FWRR and all three joints (Forearm Pronation/ Supination (Joint-1) – range: +70° -70°, Wrist Radial/ Ulnar Deviation (Joint-2) – range: +20° -25°, & Wrist Flexion/ Extension (Joint-3) – range: +60° -30°) simultaneously move over the same time period (38s) and follows the trajectory mentioned in the section (see 8.2). The experimental results can be seen from *Figure 8.40*, *Figure 8.41*, *Figure 8.42*, and *Figure 8.43*. The tracking performance of all three joints' simultaneous movement can be seen from *Figure 8.40*. Here the maximum tracking error found to be less than 2.1° (8.4%), which

proves that the tracking performance is quite good. *Figure 8.41*, *Figure 8.42*, and *Figure 8.43*, show the plots of the joints separately. Here, the reference velocities (third row) are denoted with a red dotted line, and the measured velocities from the experiment are shown with a solid blue line. Maximum joint torque for Joint-1 found to be -3.34 Nm and +3.1 Nm; for Joint-2, the maximum joint torque is -1.4 Nm and +1.7 Nm, and for Joint-3 it is -1.6 Nm and +1.4 Nm. The positive and negative signs denoted the direction of the joint torques.

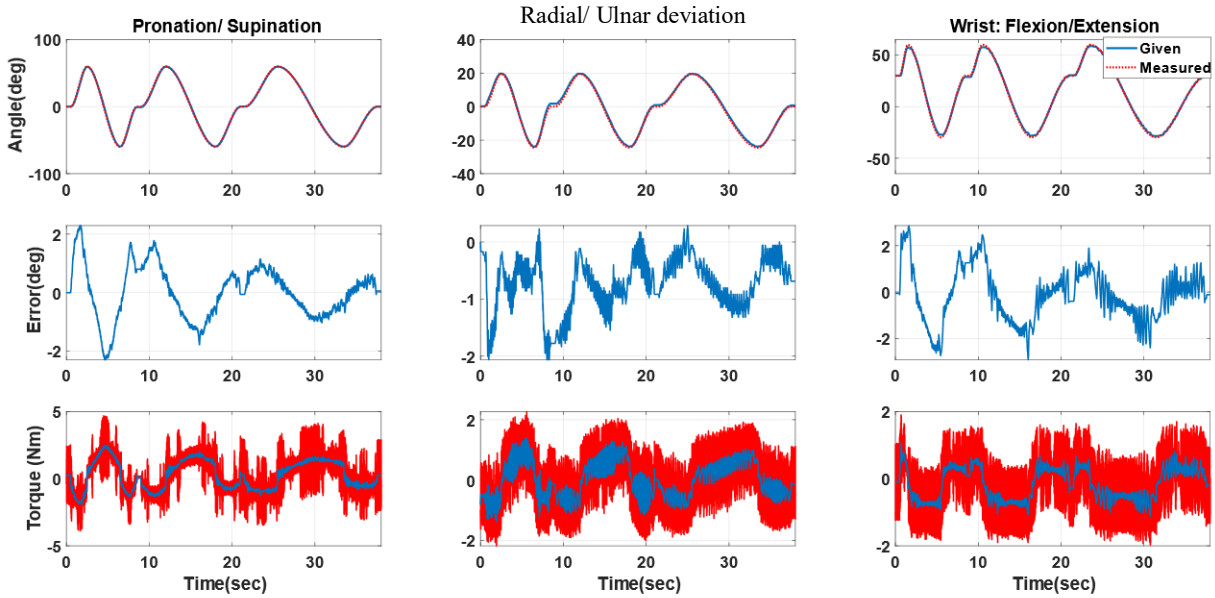

Figure 8.40 All three joints simultaneous motion (mCTC) – Subject-A

1st column corresponds to Joint-1, and the 2nd and 3rd column corresponds to Joint-2 and Joint-3, respectively. The first row shows the trajectory comparison (given joint angles – red dotted line, Measured joint angles – solid blue line) for three joints. The second row shows the tracking error, and the third row shows the measured torque during the experiments.

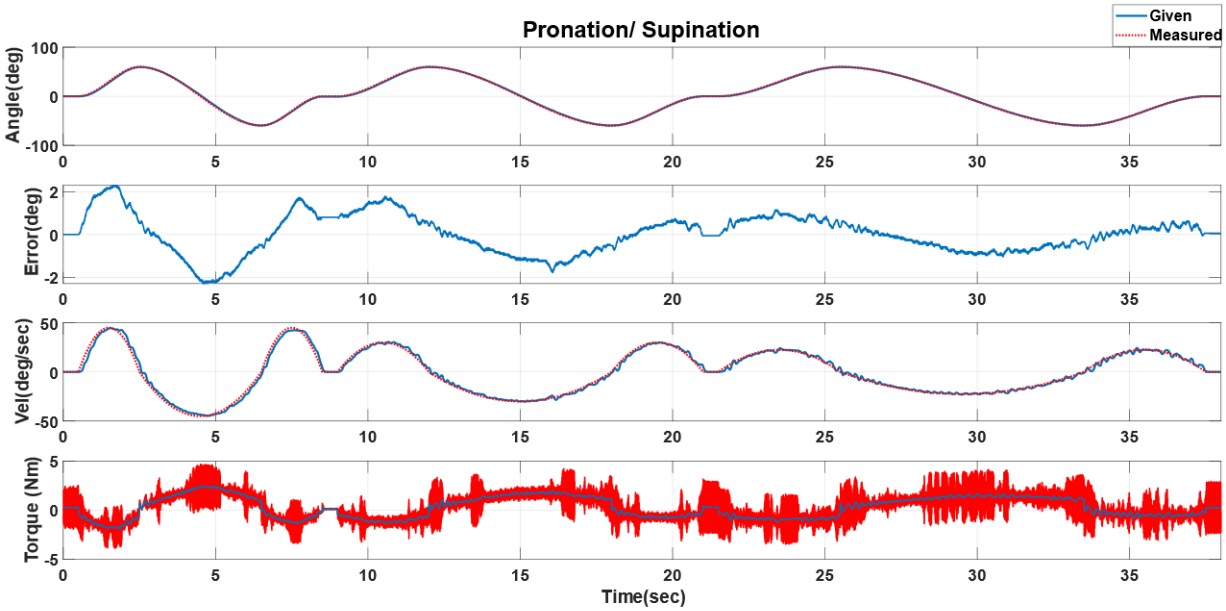

Figure 8.41 All three joints simultaneous movement (detail of Joint-1 movement with velocity comparison (mCTC) – Subject-A

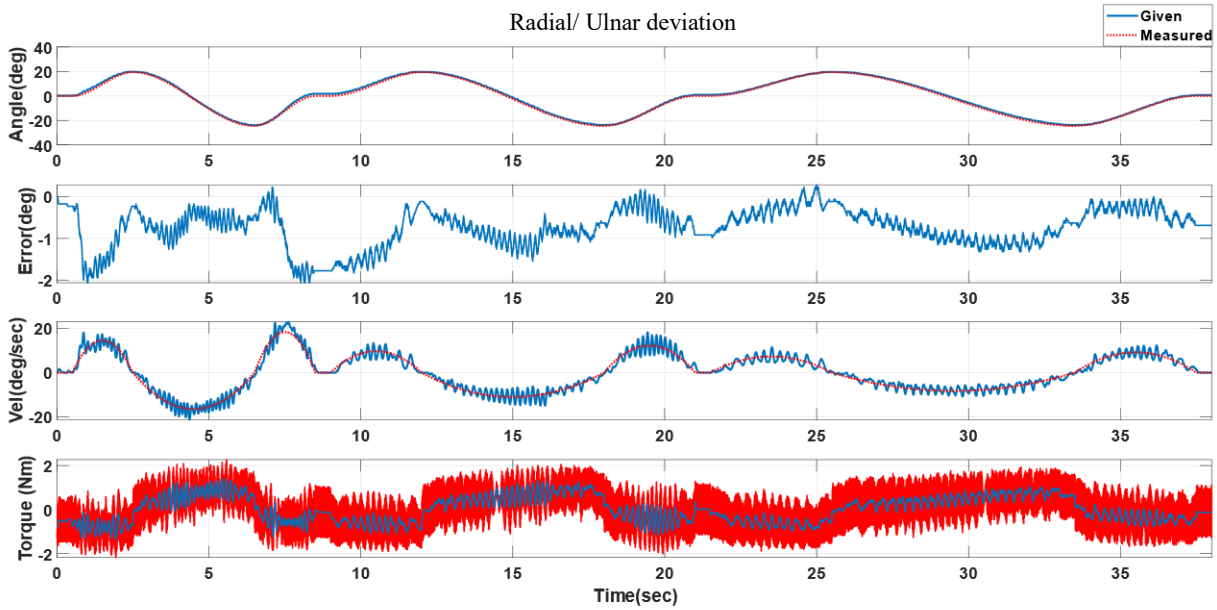

Figure 8.42 All three joints simultaneous movement (detail of Joint-2 movement with velocity comparison) (mCTC) – Subject-A

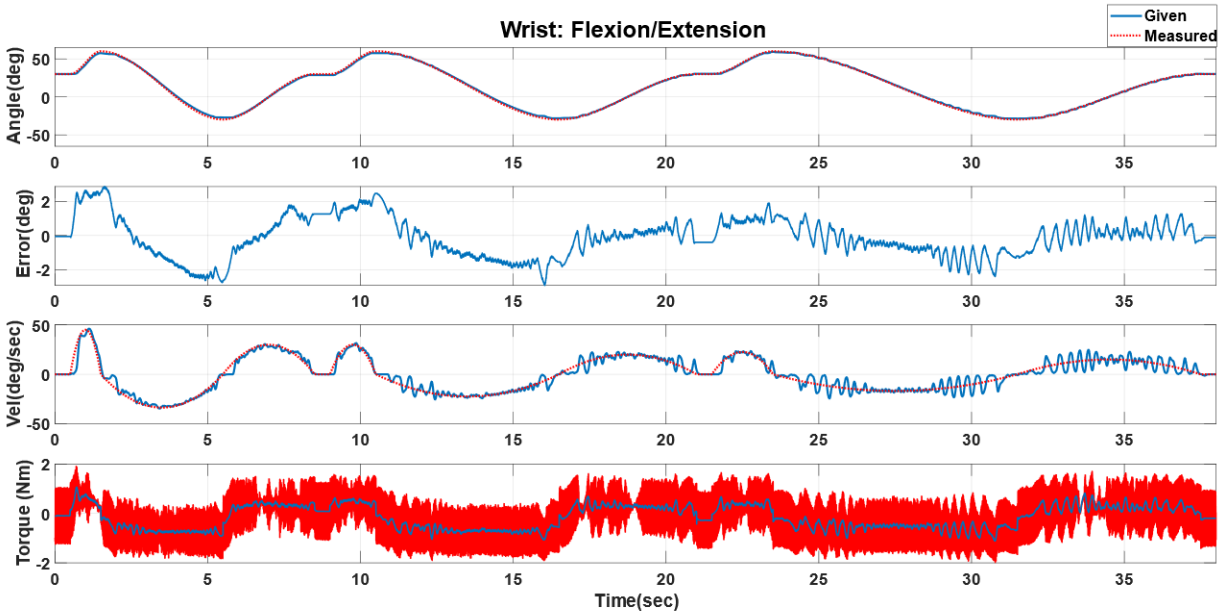

Figure 8.43 All three joints simultaneous movement (detail of Joint-3 movement with velocity comparison) (mCTC) – Subject-A

8.2.2.2 Individual Joint-1 (Forearm Pronation/ Supination) movement of Subject-A with PID control

Only forearm pronation and supination movement (range: +70° -70°) was provided at the period of 38s while Joint-2 (0°) & Joint-3 (+30°) stays at their initial positions. The results can be seen from *Figure 8.44*, and *Figure 8.45*. The tracking performance of all three joints can be seen from *Figure 8.44*. *Figure 8.45* shows the reference velocity (solid blue line) during the exercise and measured velocity (red dotted line).

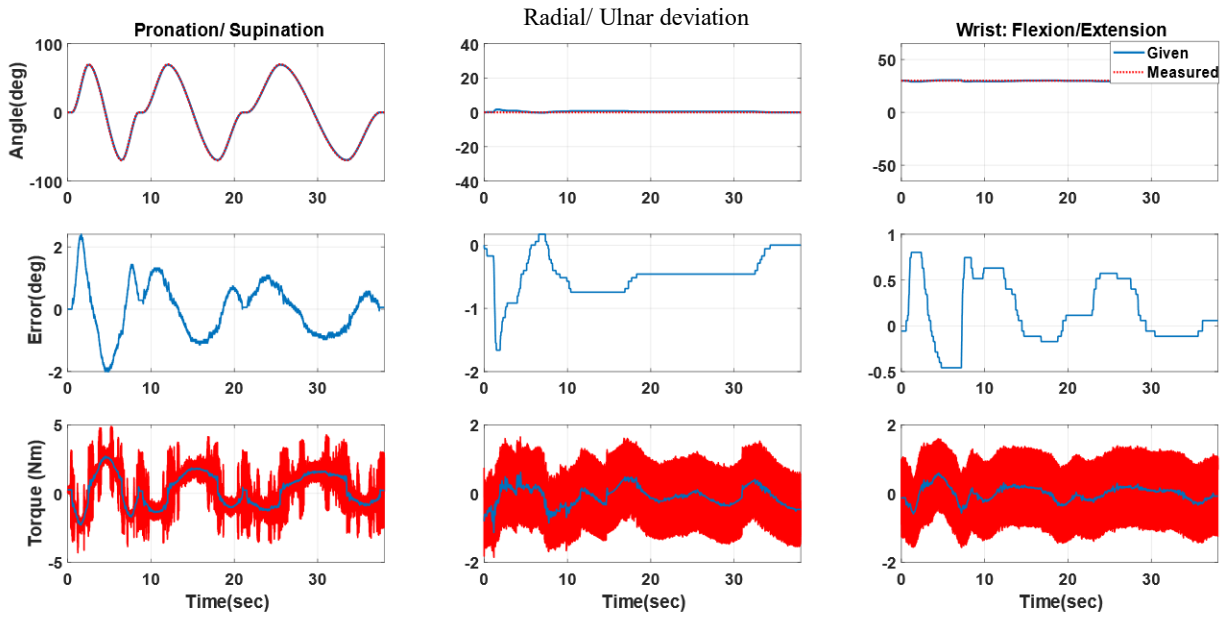

Figure 8.44 Plots of all three joints during Individual Joint-1 movement (mCTC) – Subject-A

1st column corresponds to Joint-1, and the 2nd and 3rd column corresponds to Joint-2 and Joint-3, respectively. The first row shows the trajectory comparison (given joint angles – red dotted line, Measured joint angles – solid blue line) for three joints. The second row shows the tracking error, and the third row shows the measured torque during the experiments.

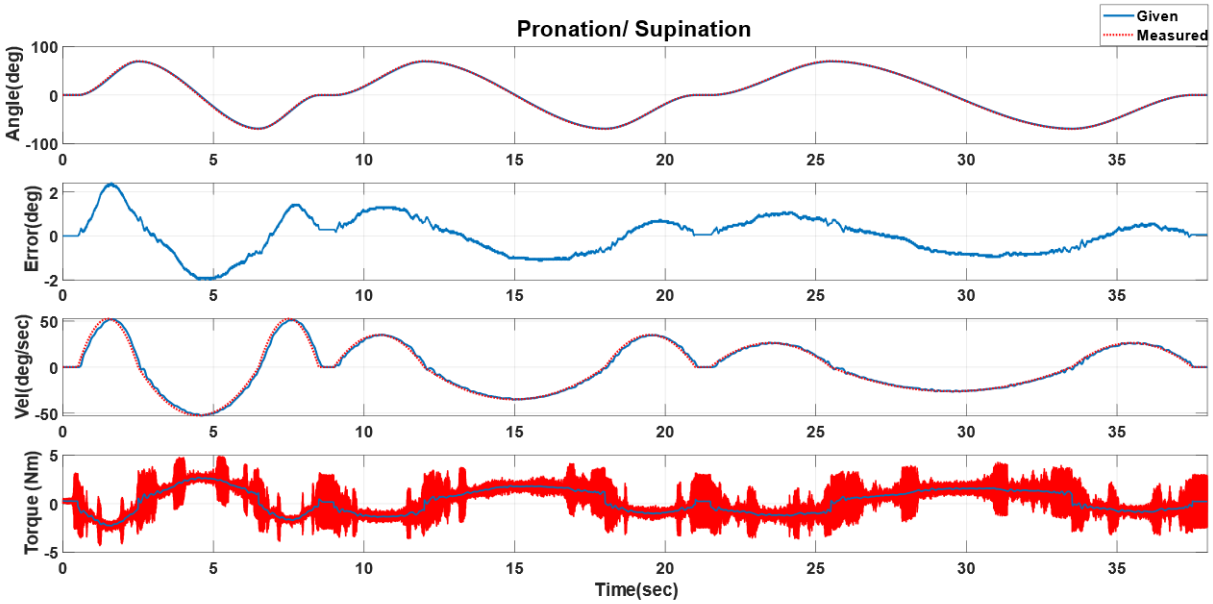

Figure 8.45 Individual Joint-1 movement with velocity comparison (mCTC) – Subject-A

8.2.2.3 **Individual Joint-2 (Wrist Radial/ Ulnar Deviation) movement of Subject-A with PID control**

Only wrist Radial/ Ulnar deviation movement (range: +20° -25°) was provided over the period of 38s while Joint-1 (0°) & Joint-3 (+30°) stayed at their initial positions. The results can be seen from *Figure 8.46*, and *Figure 8.47*. The tracking performance of all three joints can be seen from

Figure 8.46. *Figure 8.47* shows the reference velocity (solid blue line) during the exercise and measured velocity (red dotted line).

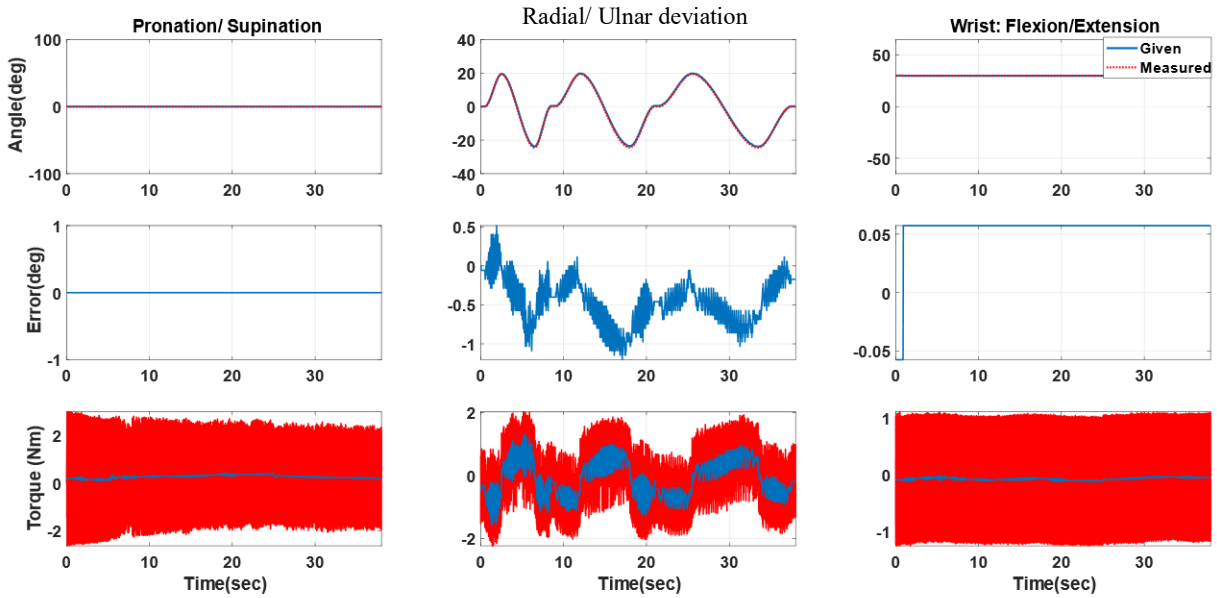

Figure 8.46 Plots of all three joints during Individual Joint-2 movement (mCTC) – Subject-A

1st column corresponds to Joint-1, and the 2nd and 3rd column corresponds to Joint-2 and Joint-3, respectively. The first row shows the trajectory comparison (given joint angles – red dotted line, Measured joint angles – solid blue line) for three joints. The second row shows the tracking error, and the third row shows the measured torque during the experiments.

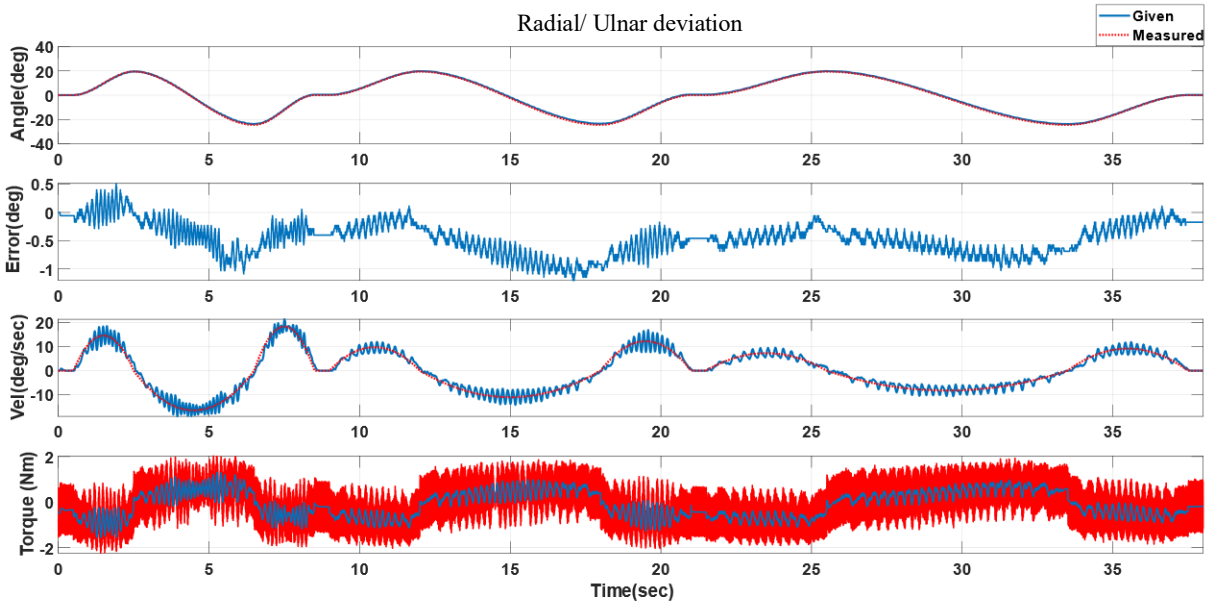

Figure 8.47 Individual Joint-2 movement with velocity comparison (mCTC) – Subject-A

8.2.2.4 Individual Joint-3 (Wrist Flexion/ Extension) movement of Subject-A with PID control

Only wrist flexion/ Extension movement (range: +60° -30°) was provided from the initial position (+30°) over the period of 38s while Joint-1 (0°) & Joint-2 (0°) stayed at their initial positions. The results can be seen in *Figure 8.48* and *Figure 8.49*. The tracking the performance of all three joints

can be seen in *Figure 8.48*. *Figure 8.49* shows the reference velocity (solid blue line) during the exercise and measured velocity (red dotted line).

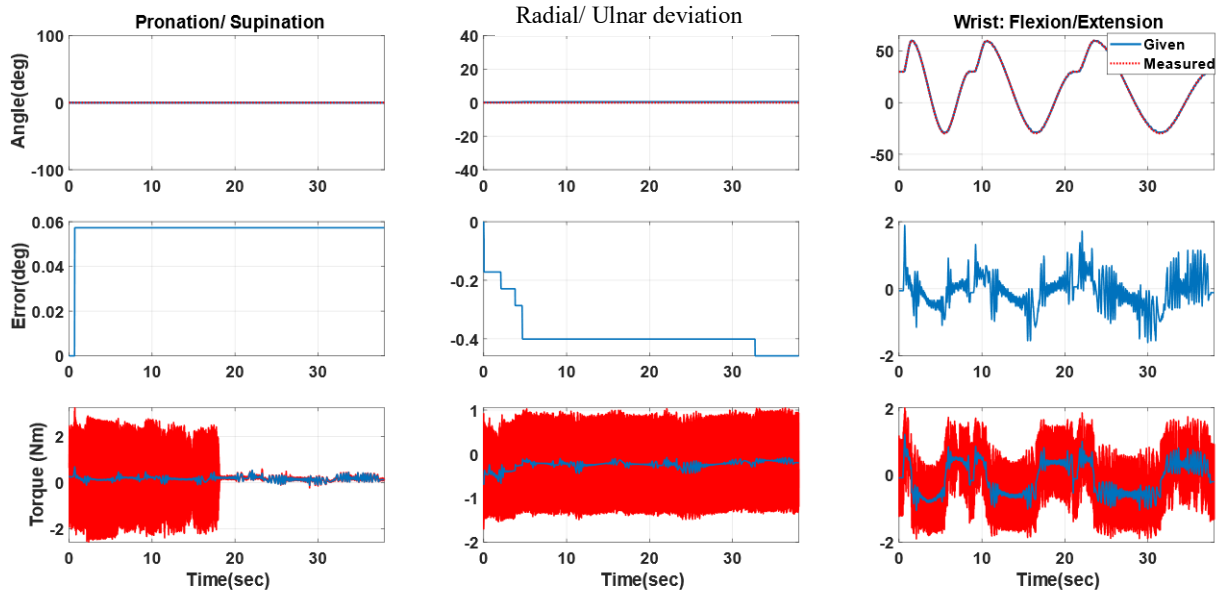

Figure 8.48 Plots of all three joints during Individual Joint-3 movement (mCTC) – Subject-A

1st column corresponds to Joint-1, and the 2nd and 3rd column corresponds to Joint-2 and Joint-3, respectively. The first row shows the trajectory comparison (given joint angles – red dotted line, Measured joint angles – solid blue line) for three joints. The second row shows the tracking error, and the third row shows the measured torque during the experiments.

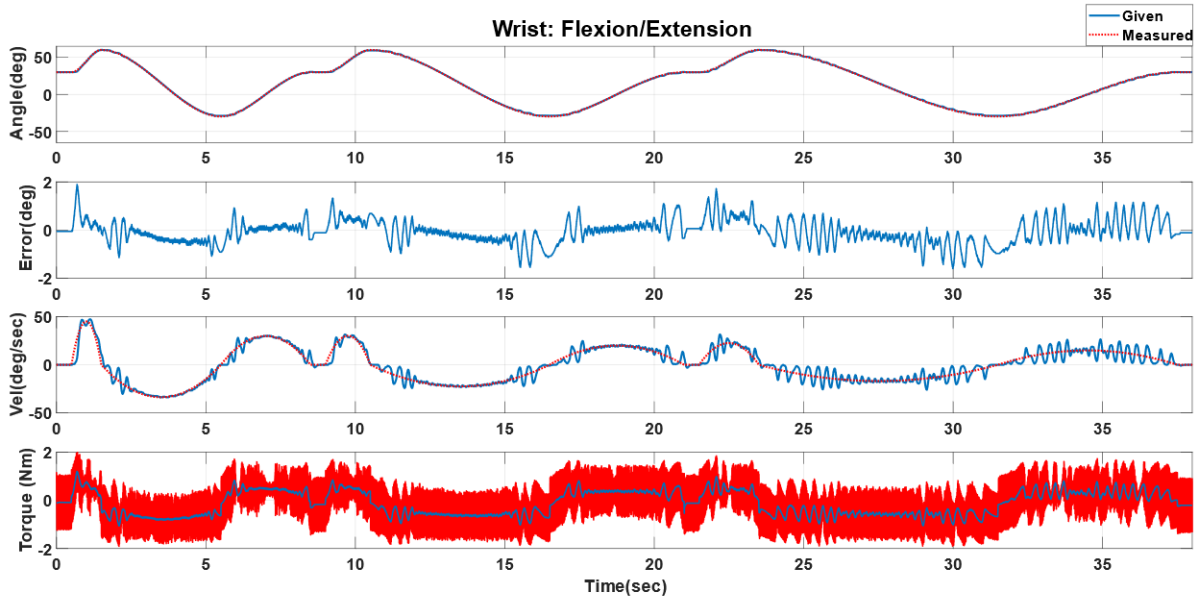

Figure 8.49 Individual Joint-3 movement with velocity comparison (mCTC) – Subject-A

8.2.2.5 **Simultaneous Joint movements of Subject-B with PID control**

Subject-B (age: 29 years; height: 5ft 4 in; Weight: 160 lbs.) wore the UWM-FWRR and all three joints (Forearm Pronation/ Supination (Joint-1) – range: +70° -70°, Wrist Radial/ Ulnar Deviation (Joint-2) – range: +20° -25°, & Wrist Flexion/ Extension (Joint-3) – range: +60° -30°) simultaneously move over the same time period (38s) and follows the trajectory mentioned in the section 8.2). The experimental results can be seen from *Figure 8.50*, *Figure 8.51*, *Figure 8.52*, and *Figure 8.53*. The tracking performance of all three joints' simultaneous movement can be seen from *Figure 8.50*. Here the maximum tracking error found to be less than 0.5° (0.7%), which proves that the tracking performance is quite good. *Figure 8.51*, *Figure 8.52*, and *Figure 8.53*, shows the plots of the joints separately. Here, the reference velocities (third row) are denoted with

a red dotted line, and the measured velocities from the experiment are shown with a solid blue line. Maximum joint torque for Joint-1 found to be -3.36 Nm and +4.34 Nm; for Joint-2, the maximum joint torque is -1.68 Nm and +1.72 Nm, and for Joint-3 it is -1.8 Nm and +1.2 Nm. The positive and negative signs denoted the direction of the joint torques.

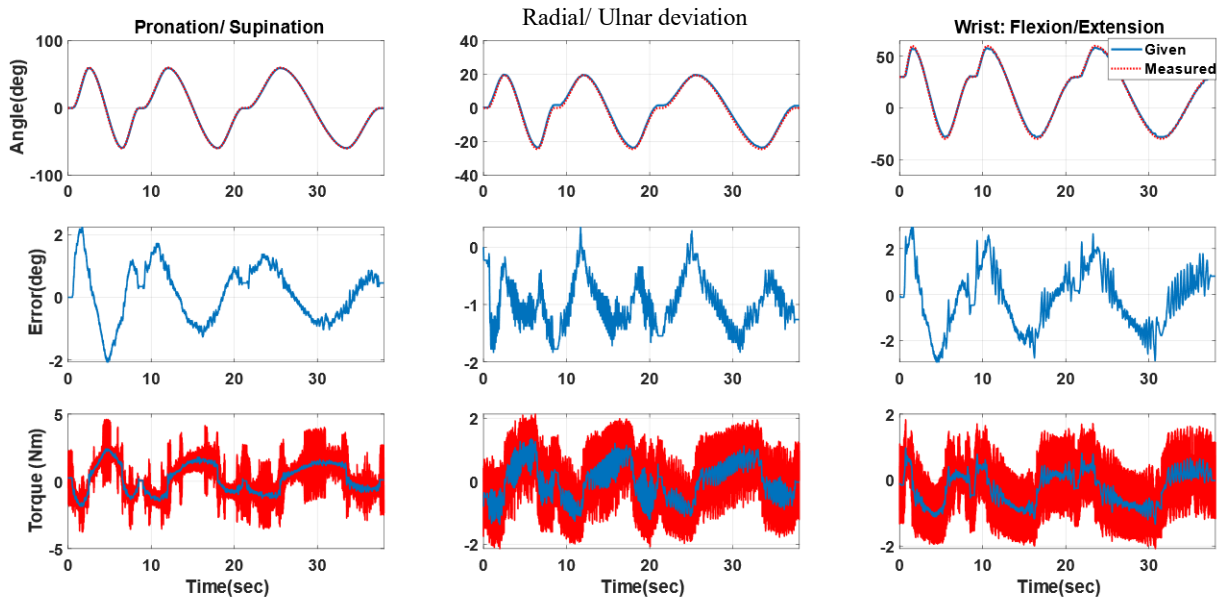

Figure 8.50 All three joints simultaneous motion (mCTC) – Subject-B

1st column corresponds to Joint-1, and the 2nd and 3rd column corresponds to Joint-2 and Joint-3, respectively. The first row shows the trajectory comparison (given joint angles – red dotted line, Measured joint angles – solid blue line) for three joints. The second row shows the tracking error, and the third row shows the measured torque during the experiments.

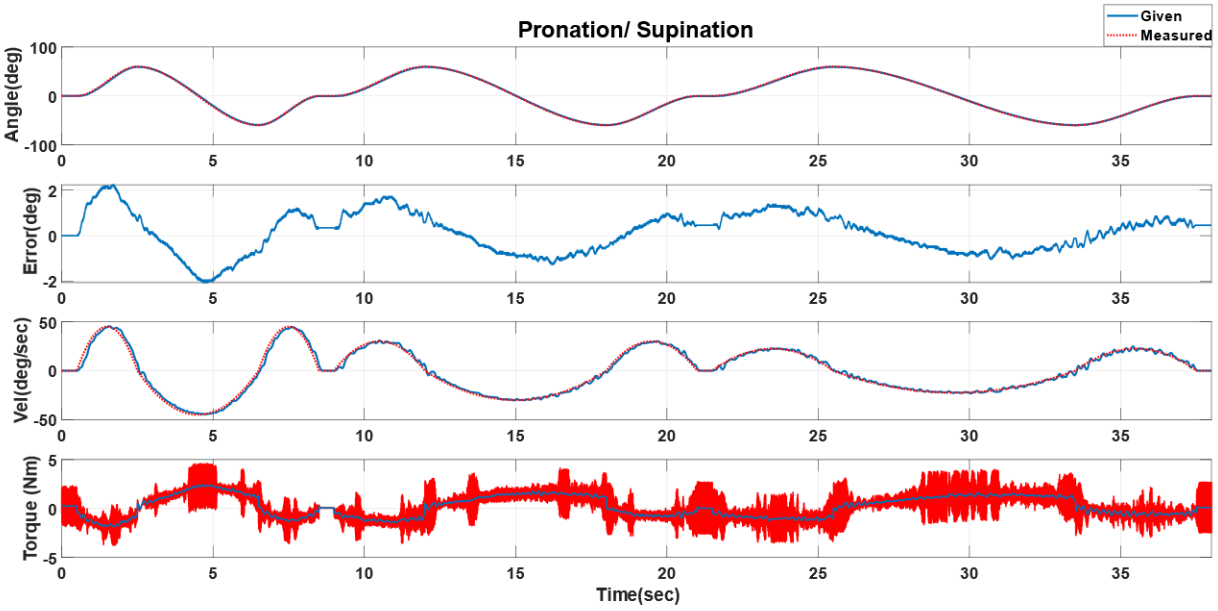

Figure 8.51 All three joints simultaneous movement (detail of Joint-1 movement with velocity comparison (mCTC) – Subject-B

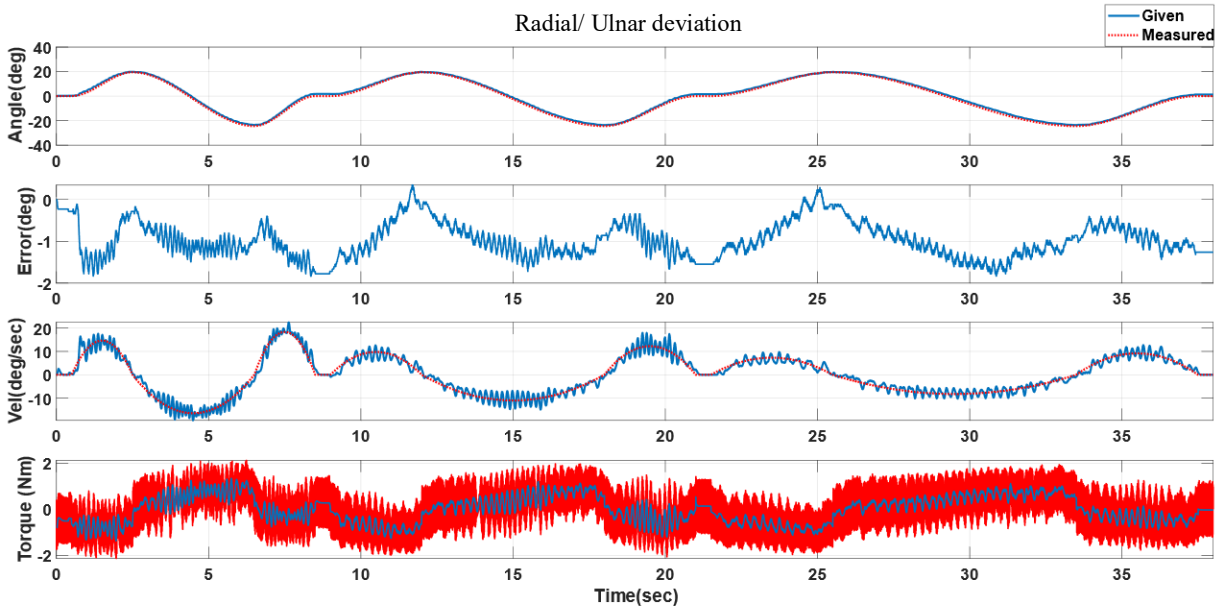

Figure 8.52 All three joints simultaneous movement (detail of Joint-2 movement with velocity comparison) (mCTC) – Subject-B

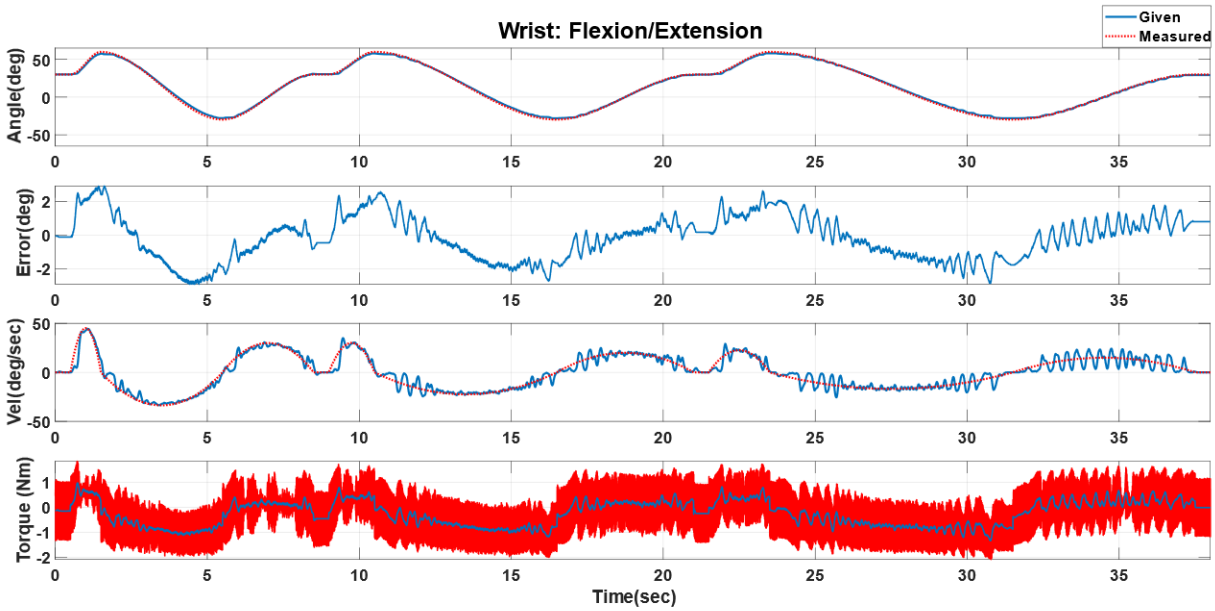

Figure 8.53 All three joints simultaneous movement (detail of Joint-3 movement with velocity comparison) (mCTC) – Subject-B

8.2.2.6 Individual Joint-1 (Forearm Pronation/ Supination) movement of Subject-B with PID control

Only forearm pronation and supination movement (range: +70° -70°) was provided at the period of 38s while Joint-2 (0°) and Joint-3 (+30°) stays at their initial positions. The results can be seen in *Figure 8.54*, and *Figure 8.55*. The tracking performance of all three joints can be seen in *Figure 8.54*. *Figure 8.55* shows the reference velocity (solid blue line) during the exercise and measured velocity (red dotted line).

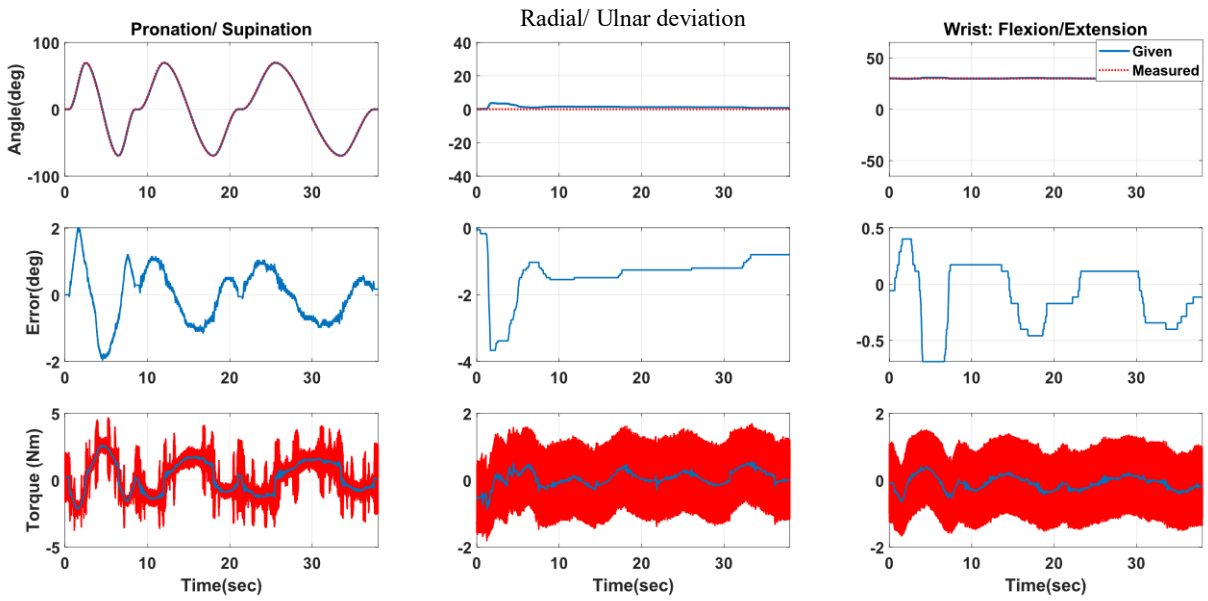

Figure 8.54 Plots of all three joints during Individual Joint-1 movement (mCTC) – Subject-B

1st column corresponds to Joint-1, and the 2nd and 3rd column corresponds to Joint-2 and Joint-3, respectively. The first row shows the trajectory comparison (given joint angles – red dotted line, Measured joint angles – solid blue line) for three joints. The second row shows the tracking error, and the third row shows the measured torque during the experiments.

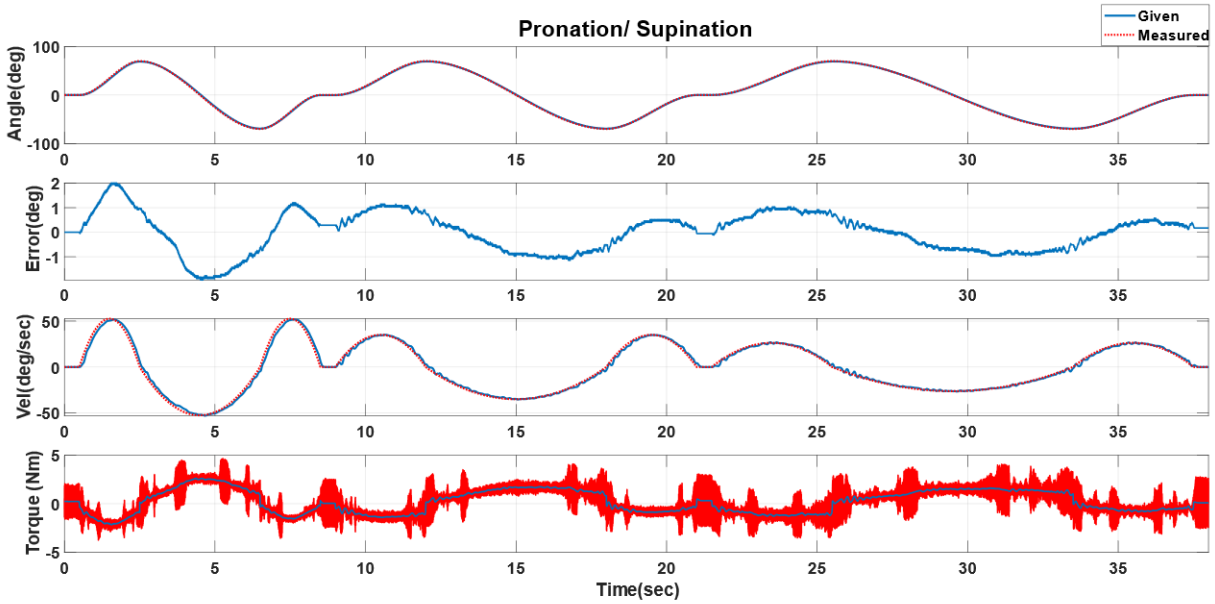

Figure 8.55 Individual Joint-1 movement with velocity comparison (mCTC) – Subject-B

8.2.2.7 **Individual Joint-2 (Wrist Radial/ Ulnar Deviation) movement of Subject-B with PID control**

Only wrist Radial/ Ulnar deviation movement (range: +20° -25°) was provided over the period of 38s while Joint-1 (0°) and Joint-3 (+30°) stayed at their initial positions. The results can be seen from *Figure 8.56*, and *Figure 8.57*. The tracking performance of all three joints can be seen in

Figure 8.56. *Figure 8.57* shows the reference velocity (solid blue line) during the exercise and measured velocity (red dotted line).

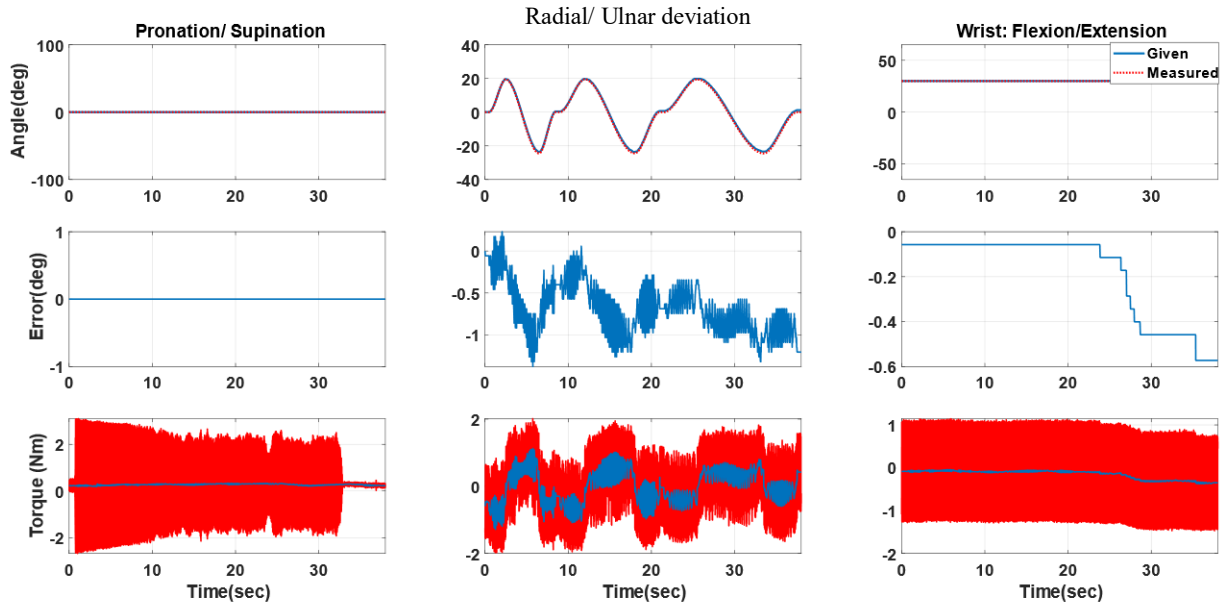

Figure 8.56 Plots of all three joints during Individual Joint-2 movement (mCTC) – Subject-B

1st column corresponds to Joint-1, and the 2nd and 3rd column corresponds to Joint-2 and Joint-3, respectively. The first row shows the trajectory comparison (given joint angles – red dotted line, Measured joint angles – solid blue line) for three joints. The second row shows the tracking error, and the third row shows the measured torque during the experiments.

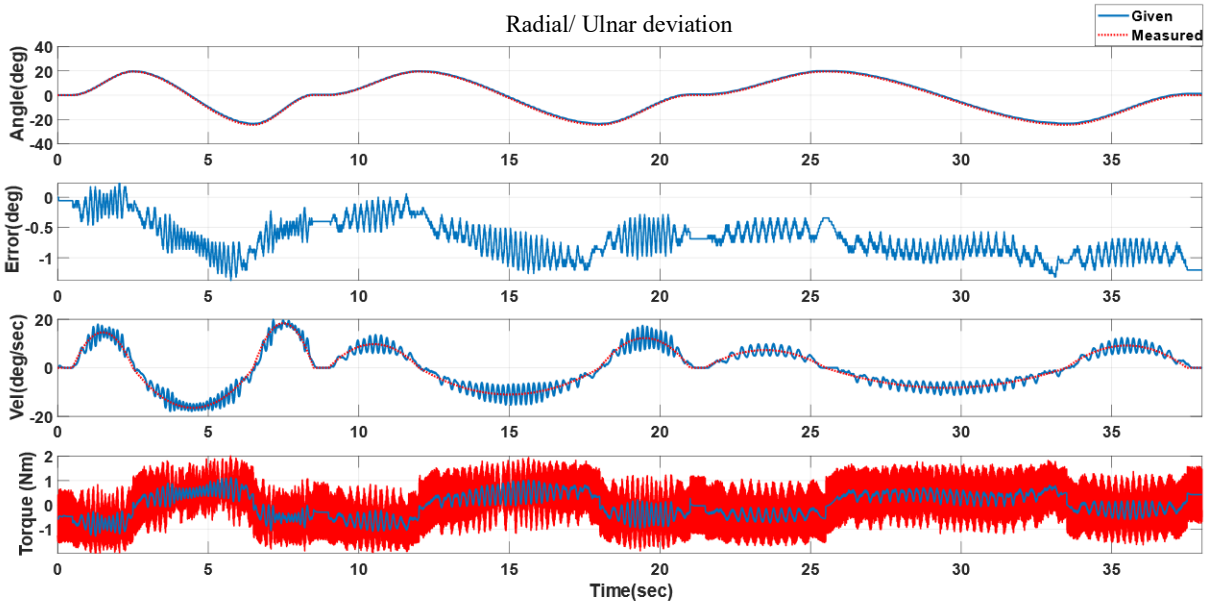

Figure 8.57 Individual Joint-2 movement with velocity comparison (mCTC) – Subject-B

8.2.2.8 **Individual Joint-3 (Wrist Flexion/ Extension) movement of Subject-B with PID control**

Only wrist flexion/ Extension movement (range: +60° -30°) was provided from an initial position (+30°) over the period of 38s while Joint-1 (0°) & Joint-2 (0°) stayed at their initial positions. The results can be seen in *Figure 8.58* and *Figure 8.59*. The tracking performance of all three joints

can be seen in *Figure 8.58*. *Figure 8.59* shows the reference velocity (solid blue line) during the exercise and measured velocity (red dotted line).

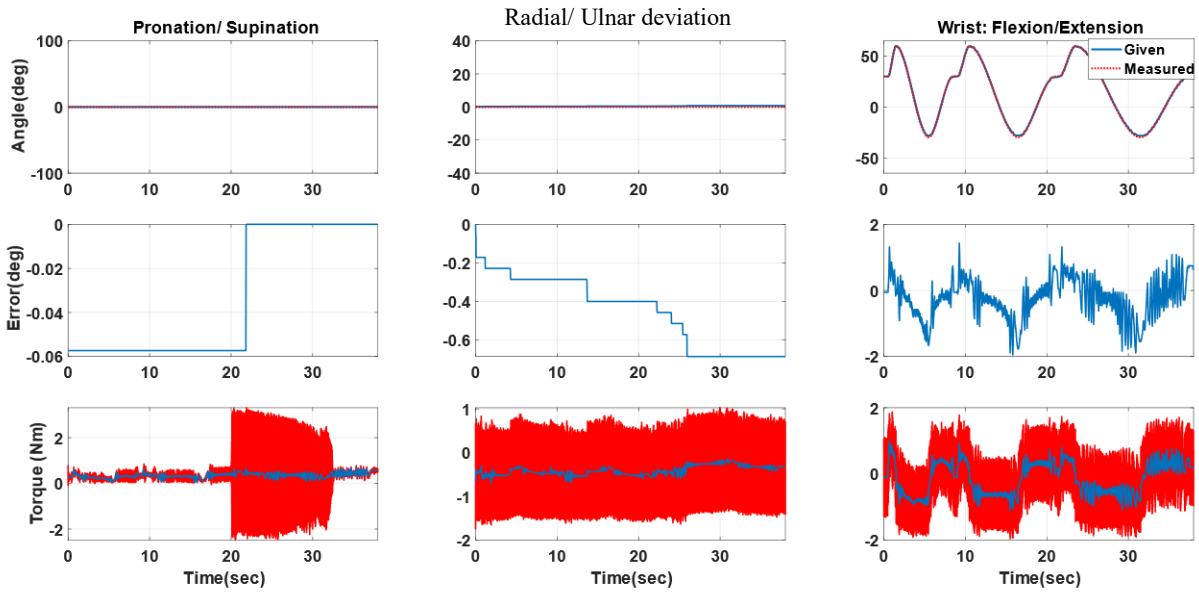

Figure 8.58 Plots of all three joints during Individual Joint-3 movement (mCTC) – Subject-B

1st column corresponds to Joint-1, and the 2nd and 3rd column corresponds to Joint-2 and Joint-3, respectively. The first row shows the trajectory comparison (given joint angles – red dotted line, Measured joint angles – solid blue line) for three joints. The second row shows the tracking error, and the third row shows the measured torque during the experiments.

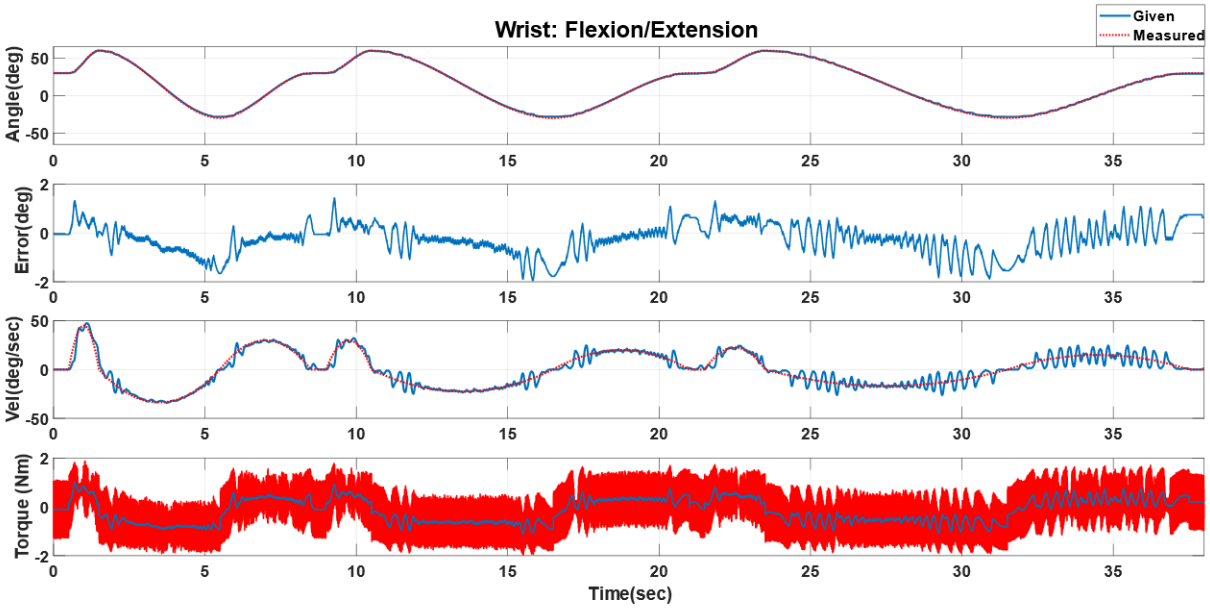

Figure 8.59 Individual Joint-3 movement with velocity comparison (mCTC) – Subject-B

8.2.2.9 **Simultaneous Joint movements of Subject-C with PID control**

Subject-C (age: 29 years; height: 6ft 1 in; Weight: 198 lbs.) wore the UWM-FWRR and all three joints (Forearm Pronation/ Supination (Joint-1) – range: +70° -70°, Wrist Radial/ Ulnar Deviation (Joint-2) – range: +20° -25°, & Wrist Flexion/ Extension (Joint-3) – range: +60° -30°) simultaneously move over the same time period (38s) and follows the trajectory mentioned in the section 8.2). The experimental results can be seen from *Figure 8.60*, *Figure 8.61*, *Figure 8.62*, and *Figure 8.63*. The tracking performance of all three joints' simultaneous movement can be seen from *Figure 8.60*. Here the maximum tracking error found to be less than 0.5° (0.7%), which proves that the tracking performance is quite good. *Figure 8.61*, *Figure 8.62*, and *Figure 8.63* show the plots of the joints separately. Maximum joint torque for Joint-1 found to be -3.37 Nm and +4.17 Nm; for Joint-2, the maximum joint torque is -1.76 Nm and +1.73 Nm, and for Joint-3

it is -1.6 Nm and +1.45 Nm. The positive and negative signs denoted the direction of the joint torques.

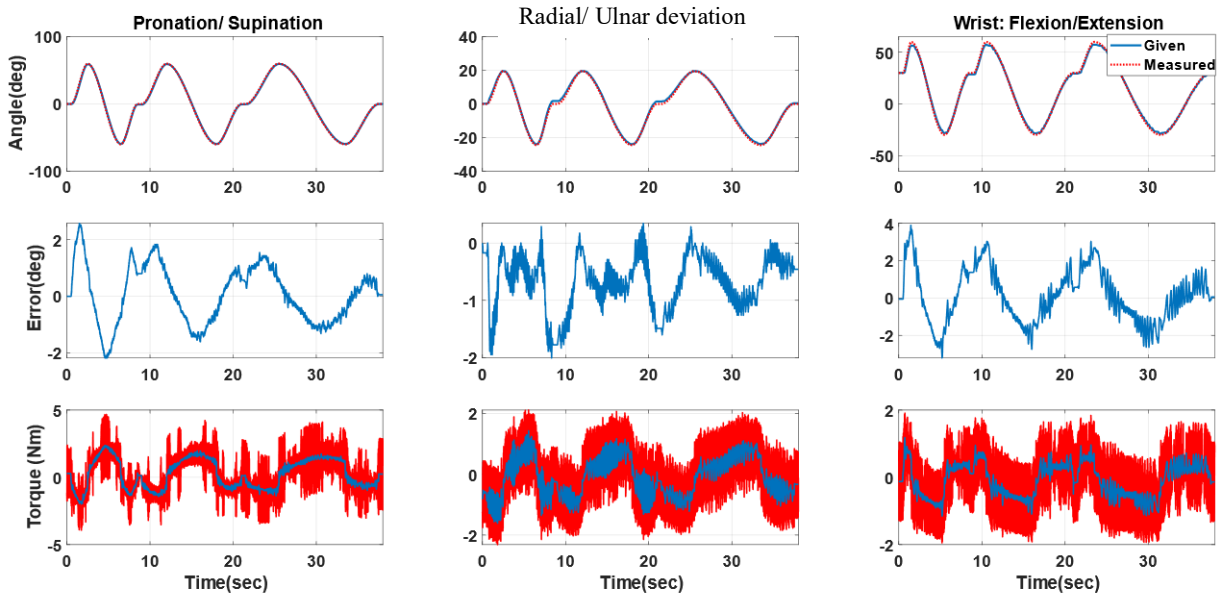

Figure 8.60 All three joints simultaneous motion (mCTC) – Subject-C

1st column corresponds to Joint-1, and the 2nd and 3rd column corresponds to Joint-2 and Joint-3, respectively. The first row shows the trajectory comparison (given joint angles – red dotted line, Measured joint angles – solid blue line) for three joints. The second row shows the tracking error, and the third row shows the measured torque during the experiments.

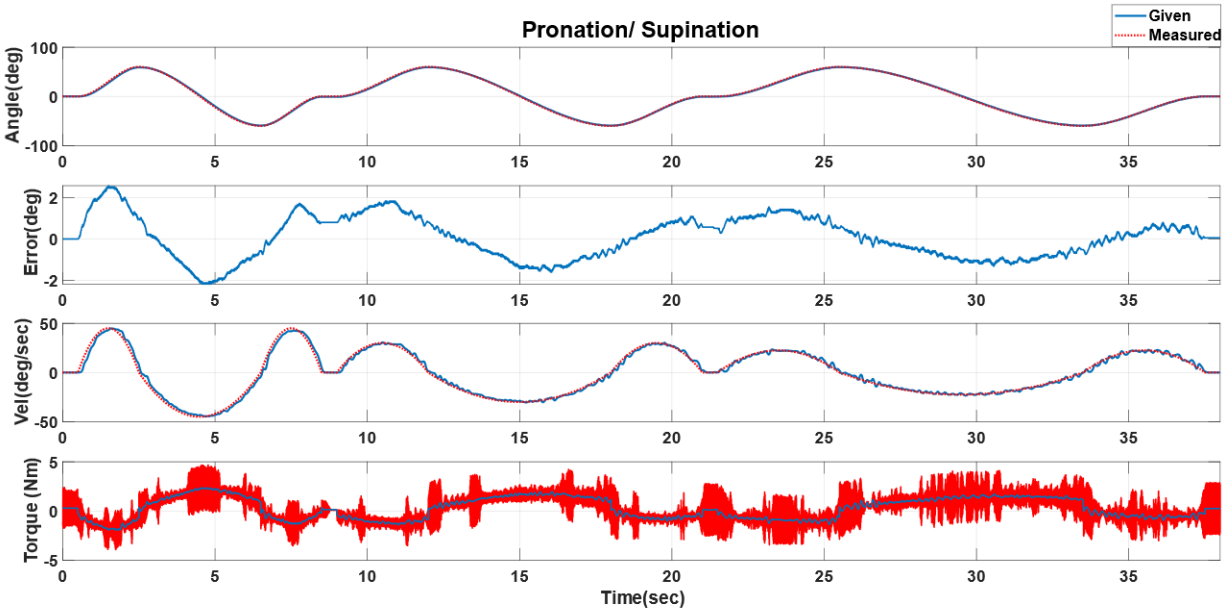

Figure 8.61 All three joints simultaneous movement (detail of Joint-1 movement with velocity comparison (mCTC) – Subject-C

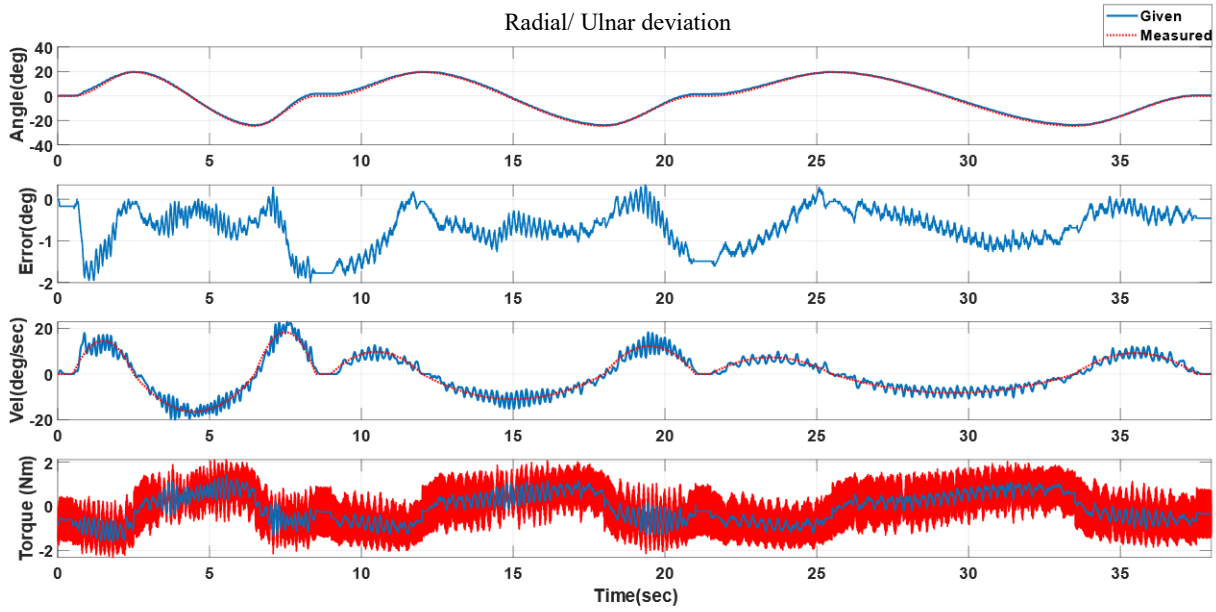

Figure 8.62 All three joints simultaneous movement (detail of Joint-2 movement with velocity comparison) (mCTC) – Subject-C

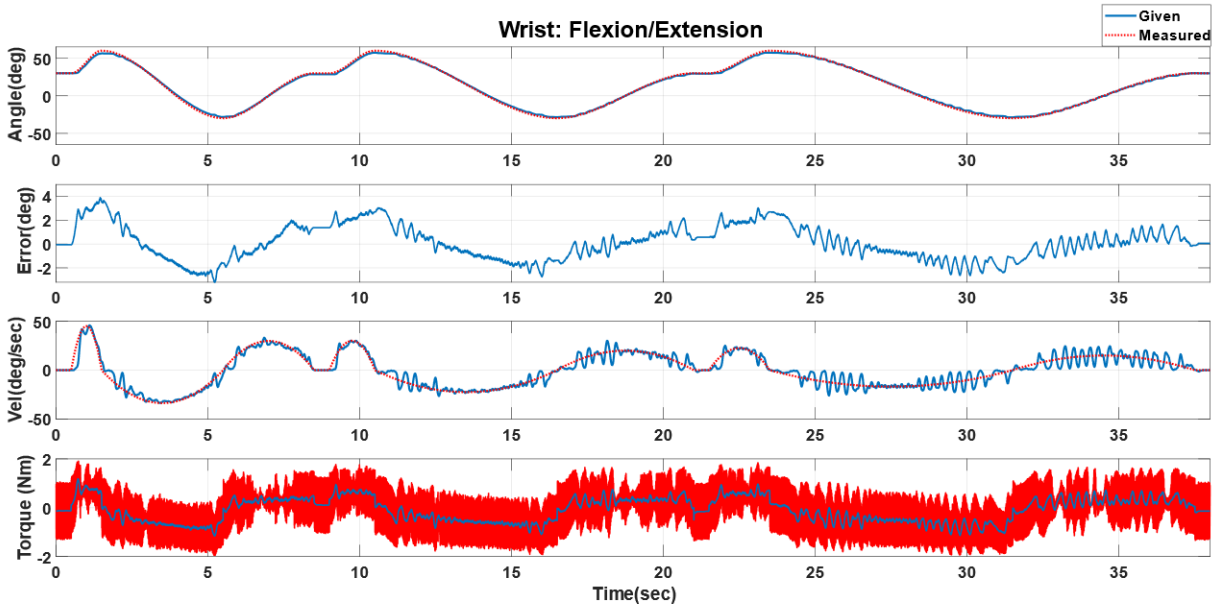

Figure 8.63 All three joints simultaneous movement (detail of Joint-3 movement with velocity comparison) (mCTC) – Subject-C

Here, the computed velocities (third row) are denoted with a red dotted line, and the measured velocities from the experiment are shown with a solid blue line.

8.2.2.10 Individual Joint-1 (Forearm Pronation/ Supination) movement of Subject-C with PID control

Only forearm pronation and supination movement (range: +70° -70°) was provided at the period of 38s while Joint-2 (0°) & Joint-3 (+30°) stays at their initial positions. The results can be seen from *Figure 8.64*, and *Figure 8.65*. The tracking performance of all three joints can be seen from

Figure 8.64. *Figure 8.65* shows the reference velocity (solid blue line) during the exercise and measured velocity (red dotted line).

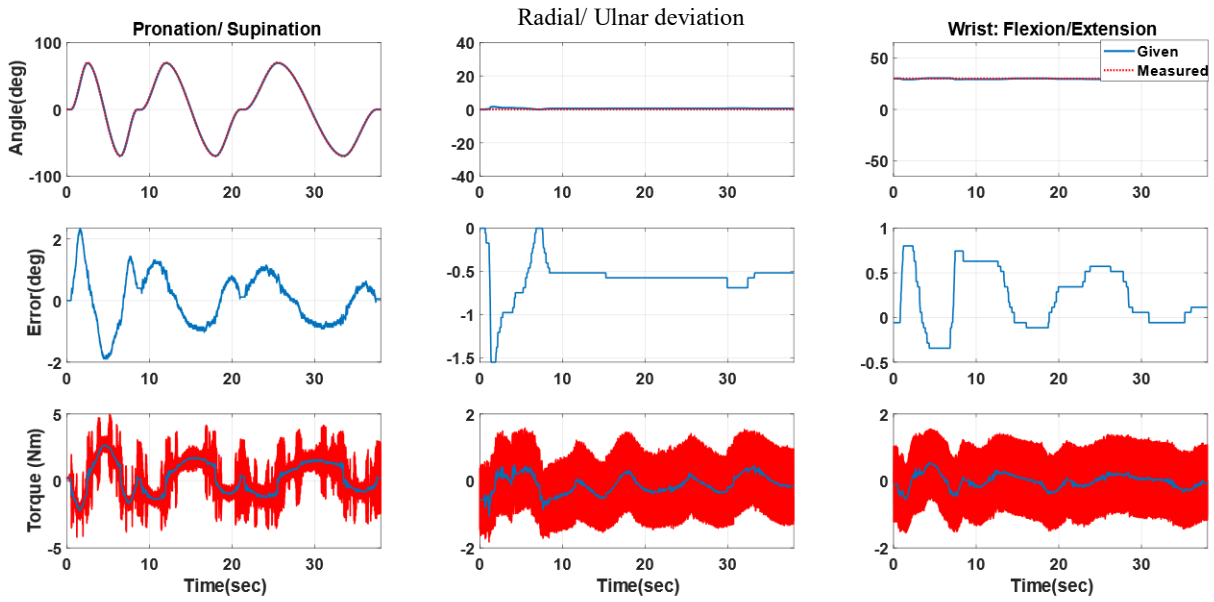

Figure 8.64 Plots of all three joints during Individual Joint-1 movement (mCTC) – Subject-C

1st column corresponds to Joint-1, and the 2nd and 3rd column corresponds to Joint-2 and Joint-3, respectively. The first row shows the trajectory comparison (given joint angles – red dotted line, Measured joint angles – solid blue line) for three joints. The second row shows the tracking error, and the third row shows the measured torque during the experiments.

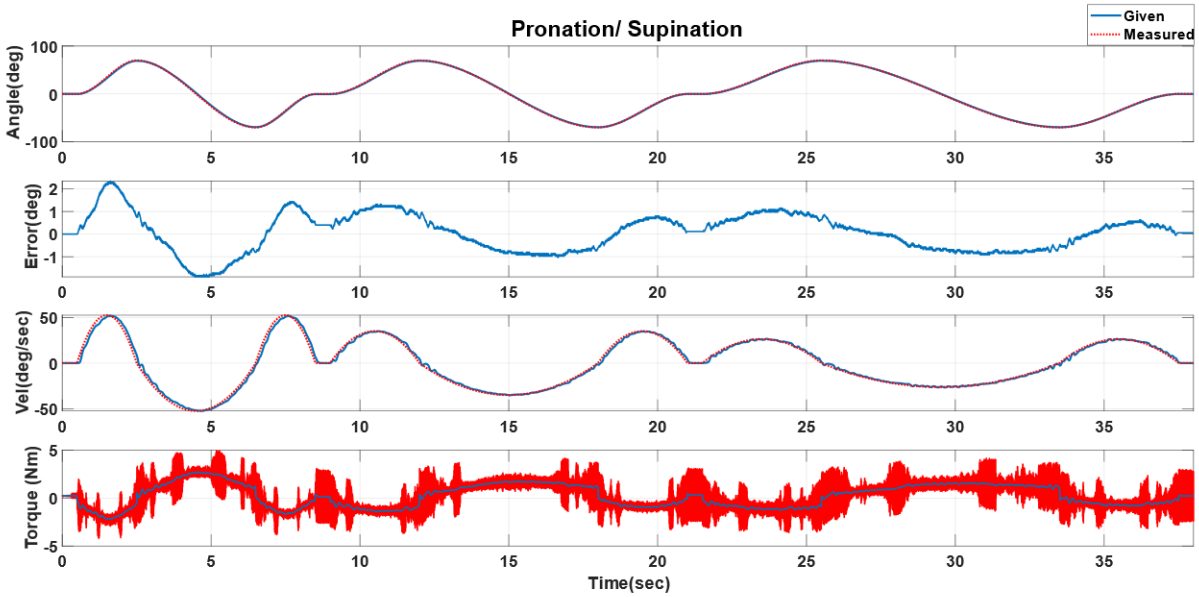

Figure 8.65 Individual Joint-1 movement with velocity comparison (mCTC) – Subject-C

8.2.2.11 **Individual Joint-2 (Wrist Radial/ Ulnar Deviation) movement of Subject-C with PID control**

Only wrist Radial/ Ulnar deviation movement (range: +20° -25°) was provided over the period of 38s while Joint-1 (0°) & Joint-3 (+30°) stayed at their initial positions. The results can be seen from *Figure 8.66*, and *Figure 8.67*. The tracking performance of all three joints can be seen from

Figure 8.66. *Figure 8.67* shows the reference velocity (solid blue line) during the exercise and measured velocity (red dotted line).

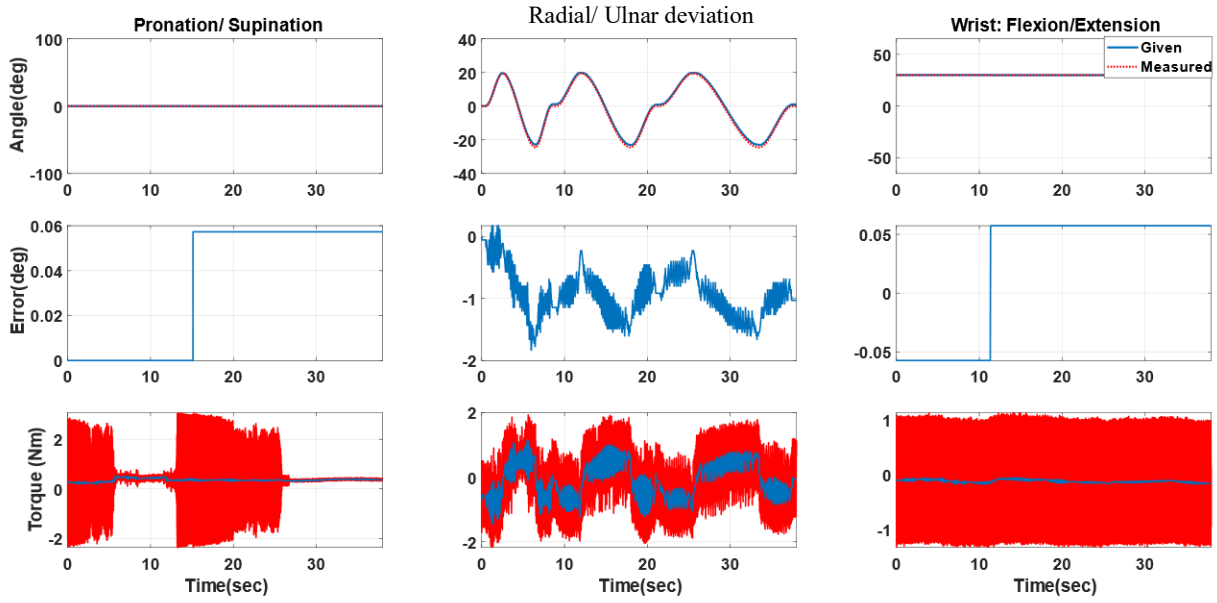

Figure 8.66 Plots of all three joints during Individual Joint-2 movement (mCTC) – Subject-C

1st column corresponds to Joint-1, and the 2nd and 3rd column corresponds to Joint-2 and Joint-3, respectively. The first row shows the trajectory comparison (given joint angles – red dotted line, Measured joint angles – solid blue line) for three joints. The second row shows the tracking error, and the third row shows the measured torque during the experiments.

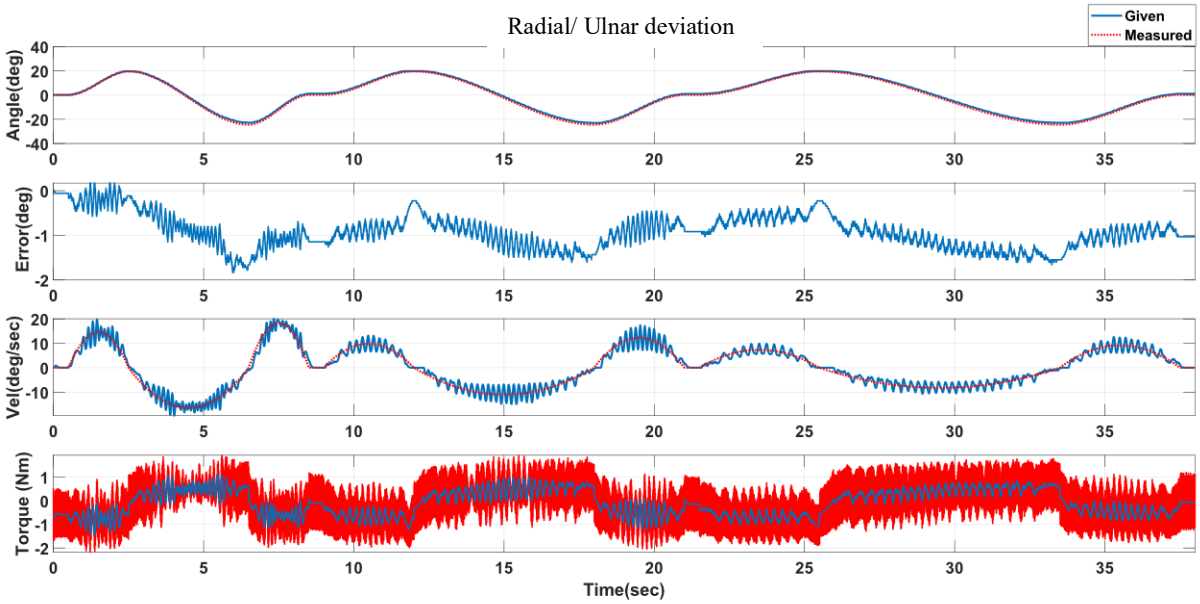

Figure 8.67 Individual Joint-2 movement with velocity comparison (mCTC) – Subject-C

8.2.2.12 **Individual Joint-3 (Wrist Flexion/ Extension) movement of Subject-C with PID control**

Only wrist flexion/ Extension movement (range: +60° -30°) was provided from the initial position (+30°) over the period of 38s while Joint-1 (0°) & Joint-2 (0°) stayed at their initial positions. The results can be seen in *Figure 8.68* and *Figure 8.69*. The tracking performance of all three joints

can be seen in *Figure 8.68*. *Figure 8.69* shows the reference velocity (solid blue line) during the exercise and measured velocity (red dotted line).

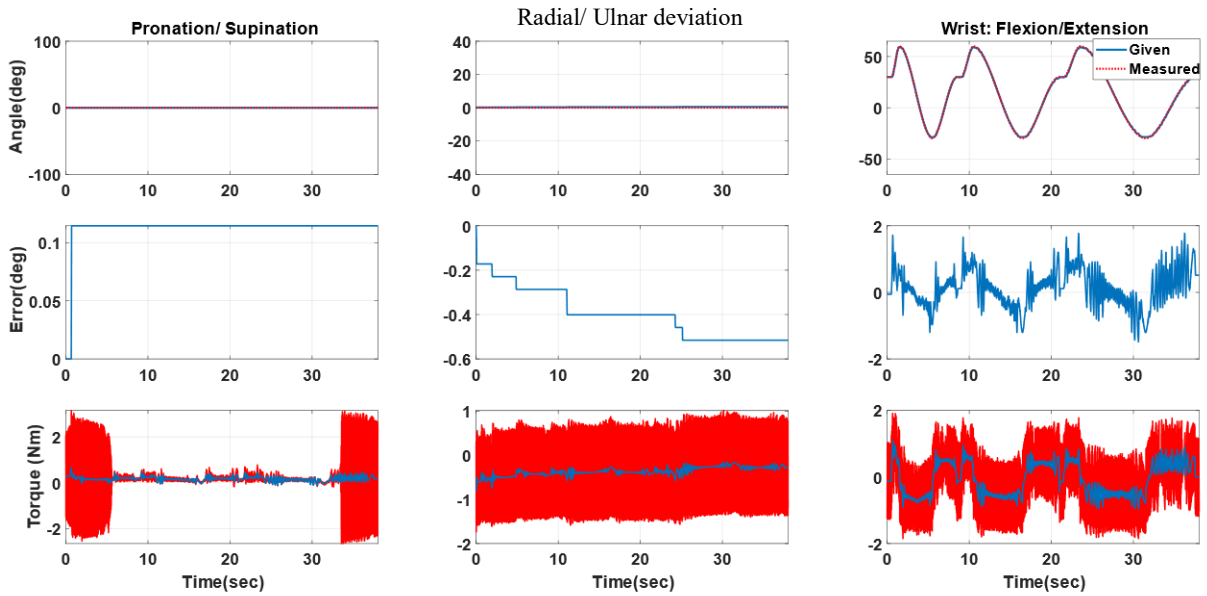

Figure 8.68 Plots of all three joints during Individual Joint-3 movement (mCTC) – Subject-C

1st column corresponds to Joint-1, and the 2nd and 3rd column corresponds to Joint-2 and Joint-3, respectively. The first row shows the trajectory comparison (given joint angles – red dotted line, Measured joint angles – solid blue line) for three joints. The second row shows the tracking error, and the third row shows the measured torque during the experiments.

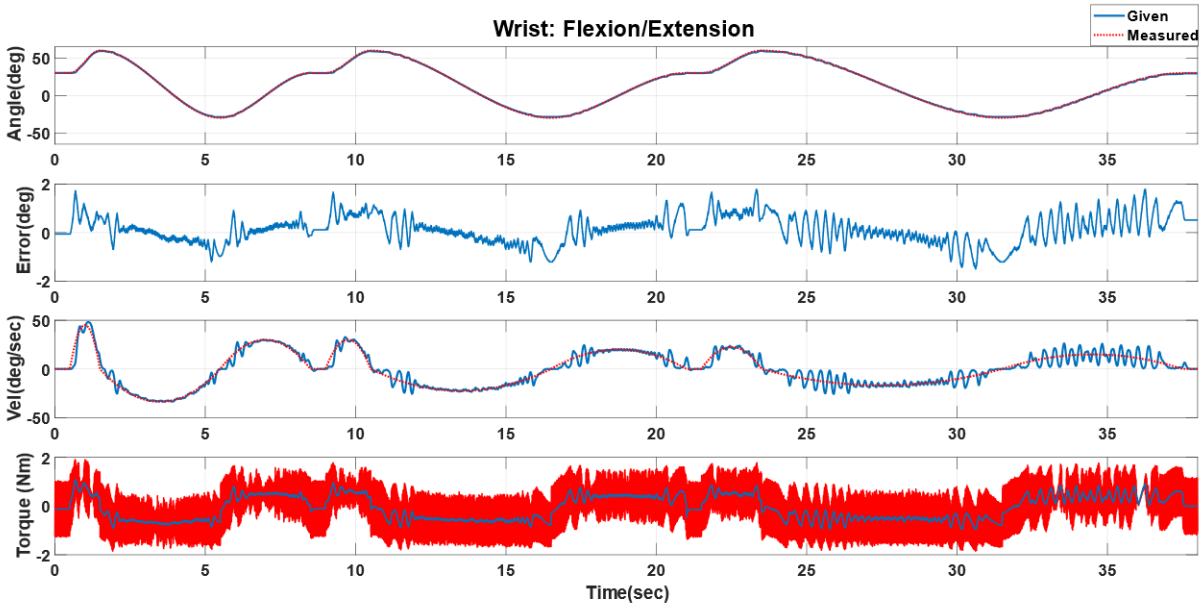

Figure 8.69 Individual Joint-3 movement with velocity comparison (mCTC) – Subject-C

DISCUSSION

The objective of this research was to design, build, and control an exoskeleton robot to provide passive rehabilitation therapy. *UWM-FWWR,* a 3DoFs exoskeleton robot, was developed keeping portability in mind and so that this device can be used at home as well as an extension to existing exoskeleton type robots for shoulder and elbow rehabilitation. To maneuver the *UWM-FWRR,* different control techniques were implemented. Experimental results show that among the implemented PID and mCTC (conventional CTC with the integral term) control techniques, PID control techniques perform better while maneuvering the UWM-FWRR to provide passive arm movement therapy in terms of trajectory tracking although chattering phenomena exists which calls for further tuning of control gain parameters. These control techniques are well established and less complex to design. Theoretically, with perfect dynamic modeling and tuned gains, mCTC should give better tracking performance compared to PID control when the device is maneuvered at higher speeds. However, it is quite complex to estimate or find exact dynamic parameters. Moreover, it is challenging to model the nonlinear frictions terms. Therefore, modeling of the viscous friction term was ignored, considering the exercises are performed at low speeds (passive rehabilitation therapy exercises should be performed slowly because of the subject's arm impairment), and friction coefficients were selected by trial and error. However, viscous friction terms are relevant when the robot is maneuvered at high speeds. Therefore, a viscous friction model should be included in the control law when developing a control strategy to provide active motion assistance.

The robust control strategy discussed in section 6.3, Sliding mode control with Time delay estimation has shown very good result in simulation environment and proven robustness in 2 DoF serial robot manipulator's dynamics even with uncertainties. As UWR-FWRR is a wearable robot and intended to be used by actual patients of different physical condition, spasticity level, weight, and height this robust control (SMC-TDE) should be able to compensate the real world uncertainties during experimentation with UWM-FWRR.

Comparing the natural human forearm and wrist movement [39], and the results from experiments with healthy subjects (*Figure 8.10- Figure 8.69*) we can come to the conclusion that the developed UWM-FWRR can efficiently track the desired trajectories, and should be effective for providing passive rehabilitative therapy to wearers forearm and wrist. Individuals in need of rehabilitative therapy in their forearm and wrist will be able to use this robot to receive therapies at home with further improvements. Moreover, the healthy individuals used as subjects for the experiment were on different height and weight. It is evident from the experiment results for Subject-A, Subject-B & Subject-C that the developed UWM-FWRR can indeed provide rehabilitative movements to the wearers ranging from (5 ft 4 in, 150 lbs.) to (6 ft 1 in, 198 lbs.).

CONCLUSION

A therapeutic exoskeleton type 3DoFs robot, UWM-FWRR (Forearm and Wrist Rehabilitation Robot), corresponding to the human forearm and wrist, has been developed to provide grounds for effective rehabilitation of people with disabilities in forearm and wrist joint movements. In this

thesis, the modeling, design of mechanical and electrical components, development, and control strategies of the *UWM-FWRR* has been produced.

The kinematic model of the *UWM-FWRR* has been developed based on modified Denavit-Hartenberg notations, whereas in dynamic modeling, the iterative Newton-Euler formulation was used. Through simulation, the torque requirements of the actuators for each joint were calculated.

The design of UWM-FWRR is such that it can be made into a portable device that can be used at home and clinical setting. Moreover, this device can effectively be a ground for future research on forearm and wrist rehabilitation devices. UWM-FWRR's design uses a novel approach for donning and doffing in the forearm part (open type bearing made with ball transfer units) to make the device compact and of lesser mass. As the UWM-FWRR is in the research phase, during the design, manufacturability through conventional machines was given utmost priority.

In experiments, typical rehabilitation exercises for single and multi-joint movements were performed with different control techniques such as PID and modified Computed Torque Control. The control architecture was implemented on a field-programmable gate array (FPGA) in conjunction with an RT-PC to run the robot in real-time.

Experiments were carried out with healthy human subjects (n=3) with different body weights and heights through pre-programmed trajectories recommended by a therapist/clinician, and the tracking performance of the robot in the form of passive rehabilitation exercises was carried out.

Experimental results show that the UWM-FWRR can effectively perform passive rehabilitation exercises for forearm and wrist joint movements.

UWM-FWRR can effectively be used in a stationary setting at clinics or even at home due to the nature of its design.

RECOMMENDATIONS & FUTURE SCOPES

UWM-FWRR shows promise in providing rehabilitative therapies to the human forearm and wrist of humans with different body weights and heights. However, through further development of the current version, the potential for this research could be reached to a new level.

Improvements:

- The structure material of UWM-FWRR, which is currently Aluminum-6061, can be replaced with spliced carbon fiber strengthened with continuous carbon fiber filament (additive technology) to further reduce this robot's mass, thus improving portability.
- The robust control strategy discussed in section 7.3, Sliding mode control with Time delay estimation should be implemented to improve UWM-FWRR' performance during experimentation with patients with various level of spasticity.
- A force sensor can be installed with the wrist handle of the UWM-FWRR to get feedback from the patient to enable UWM-FWRR to provide resistive therapies and active assist therapies to the wearer.
- A flexible force sensor can be mounted in the forearm cuff to take force feedback from the wearer's forearm for enhanced feedback.
- UWM-FWRR can be integrated through a smartphone application and cloud server so that the physical therapists' can access and monitor their patients' progress in real-time
- Through the clinical trial of UWM-FWRR and successful commercialization, UWM-FWRR can be introduced in the market, enabling the mass population in need to receive rehabilitative therapies while being at home under the supervision of their physical therapists.

UWM-FWRR′S PATHWAY TOWARDS HOME-BASED REHABILITATION

1. The experimental setup of UWM-FWRR currently uses an external control unit (Desktop PC, PXI with FPGA) for controlling the robot joints. Although for testing purposes current setup is a good choice. However, for commercialization, the control modules are to be made into compact sizes so that the robot, along with motor drivers and control units, can be assembled into a single embodiment.
2. The actuation mechanism of UWM-FWRR relies on the direct drive by electric DC servo motors with Harmonic gear drives. The drive motor along with reducer can be placed in such a way that the patient does not come in contact with the rotating parts, and those rotating parts can be hidden into the robot base compartment.
3. The structure material Al-6061 used for the experimental setup of UWM-FWRR can be replaced with spliced carbon fiber strengthened with continuous carbon fiber filament (additive technology) or other batch manufacturing process so that the commercial version becomes lucrative, aesthetic and has low mass properties.
4. Stress analysis on the robot structural design should be done to optimize the design further for the reduction of mass and required torque delivered by the actuators.
5. The forearm cuff of the UWM-FWRR should be replaced by an elastic material open type cuff (which is currently is a soft strap that wraps around the forearm) that can grab the forearm like the physical therapists during pronation and supination.
6. Force sensor integration with UWM-FWRR will enable active assist, motion assist therapies. Thus, UWM-FWRR will become a complete solution for recovering disabled individuals.

7. The UWM-FWRR should have the ability to integrate itself with smartphone applications through which the main feature of tele-rehabilitation can be achieved.
    a. A smartphone application that can connect with UWM-FWRR and receive all the data relating to force feedback, range of motion, velocities can be sent to the cloud.
    b. Those data should be analyzed through algorithms that can analyze a patient's condition and make a probable therapeutic approach.
    c. Those data will be accessible to authorized personnel (namely, the patient's therapist) so that patient can receive suitable real-time therapy.
8. Finally, anonymous data can be collected from UWM-FWRR's cloud data for machine learning to standardize the physical therapy paradigm.

REFERENCES

[1] Z. AU, R. Islam and M. H. Rahman, "Customer Discovery: Powered Hand Rehab Glove. Vol. $2400. (Milwaukee I-Corps Site: NSF: I Corps #1450386)," Milwaukee, 2018.

[2] M. J and M. G., "Atlas of Heart Disease and Stroke.," UK: World Health Organization, Brighton, 2004.

[3] P. VM, W. DT and L. HR, "Loss of arm function after stroke: measurement, frequency, and recovery," *Int Rehabil Med,* vol. 8, no. 2, p. 69–73, 1986.

[4] M. J, P. B and A. R, "Hand injuries and occupational accidents. Statistics and prevention.," *Ann Chir Main,* vol. 2, no. 4, p. 368–70, 198.

[5] H. &. S. Foundation, "Tracking Heart Disease and Stroke in Canada," 2009. [Online]. Available: http://www.heartandstroke.com. [Accessed 14 February 2019].

[6] D. C. A, "Human and economic burden of stroke.," 15 Januaey 2009. [Online]. Available: http://heartandstroke.com. [Accessed 16 February 2019].

[7] S. Hatem, G. Saussez, M. F. Della and et al., "Rehabilitation of Motor Function after Stroke: A Multiple Systematic Review Focused on Techniques to Stimulate Upper Extremity Recovery," *Front Hum Neurosci,* vol. 10, p. 442, 2016.

[8] D. J. Reinkensmeyer, J. Emken and S. Cramer, "Robotics, motor learning, and neurologic recovery," *Annual Review of Biomedical Engineering,* vol. 6, pp. 497-525, 2004.

[9] J. Denavit and R. S. Hartenberg, "A Kinematic Notation for Lower-Pair Mechanisms Based on Matrices," *Trans ASME J. Appl. Mech. ,* vol. 23, pp. 215-221, 1955.

[10] D. . A. Winter, "ANTHROPOMETRY," in *Biomechanics and Motor Control of Human Movement*, Newyork, Wiley, 2009, p. 86.

[11] N. F. Gordon, M. Gulanick, F. Costa, G. Fletcher and B. A. Franklin, "Physical activity and exercise recommendations for stroke survivors: an American Heart Association scientific statement from the Council on Clinical Cardiology, Subcommittee on Excercise, Cardiac Rehabilitation, and Prevention," *Stroke,* vol. 35, no. 5, pp. 1230-1240, 2004.

[12] J. J. Craig, Introduction to Robotics : Mechanics and Control, NJ: Pearson, 2014.

[13] H. M. Kim, T. K. Hong and G. S. Kim, "Design of a wrist rotation rehabilitation robot," in *International Conference on Cyber Technology in Automation, Control and Intelligent*, Hong Kong, 2014.

[14] N. Kato, D. Shujiro, T. Akagi, T. Morimoto and Y. Soga,, "Development of Wearable Wrist Rehabilitation Device Using Flexible Pneumatic Cylinders," in *MATEC Web of Conferences*, 2016.

[15] L. Sutton, H. Moein, A. Rafiee, J. D. W. Madden and C. Menon, "Design of an assistive wrist orthosis using conductive nylon actuators," in *6th IEEE International Conference on Biomedical Robotics and Biomechatronics (BioRob)*, Singapore, 2016.

[16] N. Omarkulov, K. Telegenov, M. Zeinullin, I. Tursynbek and A. Shintemirov, "Preliminary mechanical design of NU-Wrist: A 3-DOF self-aligning Wrist rehabilitation robot," in *6th IEEE International Conference on Biomedical Robotics and Biomechatronics (BioRob),*, Singapore, 2016.

[17] E. Pezent, C. G. Rose, A. D. Deshpande and M. K. O'Malley, "Design and characterization of the OpenWrist: A robotic wrist exoskeleton for coordinated hand-wrist rehabilitation," in *International Conference on Rehabilitation Robotics (ICORR)*, London, 2017.

[18] A. Pehlivan, S. Fabrizio, E. Andrew, N. Yozbatiran, G. Francisco and M. O'Malley, "Design and validation of the RiceWrist-S exoskeleton for robotic rehabilitation after incomplete spinal cord injury," *Robotica,* 2014.

[19] H. Bian, Z. Chen, H. Wang and T. Zhao, "Mechanical design of EFW Exo II: A hybrid exoskeleton for elbow-forearm-wrist rehabilitation," in *International Conference on Rehabilitation Robotics (ICORR)*, London, 2017.

[20] M. Atlihan, A. Erhan and M. Arslan, "Development of a Therapeutic Exercise Robot for Wrist and Forearm Rehabilitation," in *19th International Conference on Methods and Models in Automation and Robotics*, Poland, 2014.

[21] H. Al-Fahaam, S. Davis and S. Nefti-Meziani, "Wrist rehabilitation exoskeleton robot based on pneumatic soft actuators," in *International Conference for Students on Applied Engineering (ICSAE)*, Newcastle upon Tyne, 2016.

[22] D. Buongiorno, E. Sotgiu, D. Leonardis, S. Marcheschi, M. Solazzi and A. Frisoli, "WRES: A Novel 3 DoF WRist ExoSkeleton With Tendon-Driven Differential Transmission for Neuro-Rehabilitation and Teleoperation," *IEEE Robotics and Automation Letters,* vol. 3, no. 3, pp. 2152-2159, 2018.

[23] Y. Su, Y. Yu and C. Lin, "A compact wrist rehabilitation robot with accurate force/stiffness control and misalignment adaptation," *International Journal of Intelligent Robotics and Applications,* vol. 3, no. 1, pp. 45-58, 2019.

[24] Zion Market Research, "Global Disabled and Elderly Assistive Technology Market Set For Rapid Growth, To Reach Value Around USD 30.82 Billion By 2024," Zion Market Research, August 2018. [Online]. Available: https://www.zionmarketresearch.com/news/disabled-elderly-assistiv. [Accessed 25 February 2019].

[25] "Extremities (Shoulder and Small Joint Implants) Market Analysis, By Product Type (Upper Extremity Devices, Lower Extremity Devices), By Material (Ceramics, Metallic, Polymeric), By End Use (Hospitals, Ambulatory Surgical Centres, Orthopedic Clinics)," Reports and data, May 2019. [Online]. Available: https://www.reportsanddata.com/report-detail/extremities-shoulder-and-small-joint-implants-market. [Accessed 22 August 2019].

[26] Grand View Research, "Rehabilitation Devices/Equipment Market Analysis By Product Type, (Daily Living Aids, Mobility Equipment, Exercise Equipment, Body Support Devices), By Application, By End-use, By Region, And Segment Forecasts, 2018 – 2025," Grand View Research, September 2017. [Online]. Available:

https://www.grandviewresearch.com/industry-analysis/rehabilitation-products-market . [Accessed 15 Fabruary 2019].

[27] J. D. Sanjuan, I. Rulik and T. Ahmed, *Smart Shoulder Rehab,* Milwaukee: NSF: Milwaukee I-Corps Program (#AAH5514), 2019.

[28] Q.Meng and M. Lee, "Design issues for assistive robotics for the elderly," *Advanced Engineering Informatics,* vol. 20, no. 2, pp. 171-186, 2006.

[29] H. J. team, "Pronation and supination," [Online]. Available: https://healthjade.com/pronation-and-supination/. [Accessed 16 1 2020].

[30] CrossFit, "MOVEMENT ABOUT JOINTS, PART 3: THE WRIST," 14 3 2019. [Online]. Available: https://www.crossfit.com/essentials/movement-about-joints-part-3-wrist. [Accessed 16 1 2020].

[31] "Military Disability Made Easy," 2013, [Online]. Available: http://www.militarydisabilitymadeeasy.com/thewrist.html. [Accessed 16 1 2020].

[32] N. Hamilton, M. Manisali and I. Gunal, in *Kinesiology: Scientific basis of human motion*, 11 ed., Boston, McGraw-Hill Higher Education, XV, 2008, p. 627.

[33] M. H. Rahman, T. K. Ouimet, M. Saad, J. P. Kenne and P. S. Archambault, "Dynamic and Evaluation of a Robotic Exoskeleton for Upper-Limb Rehabilitation," *International Journal of Information Acquisition,* vol. 8, no. 1, pp. 83-102, 2011.

[34] A. R. Tilley and H. Dreyfuss , The Measure of Man and Woman: Human Factors in Design, New York: Wiley, 2001.

[35] M. H. Rahman, M. Saad, J. P. Kenne and P. S. Archambault, "Robot assisted rehabilitation for elbow and forearm movements," *Int. J. Biomechatronics and Biomedical Robotics,* vol. 1, no. 4, pp. 206-281, 2011.

[36] R. S. Hartenberg and J. Denavit, in *Kinematic Synthesis of Linkages*, New York, McGraw-Hill, 1965, p. 435.

[37] J. Y. S. Luh, M. W. Walker and R. P. C. Paul, "On-line computational scheme for mechanical manipulators," *ASME J. of Dynamic Systems, Measurement, and Control,* vol. 102, no. 2, pp. 69-76, 1980.

[38] "Physical Therapy Standards," Department of Rehabilitation Services, Brigham and Women's Hospital, [Online]. Available: https://www.brighamandwomens.org/patients-and-families/rehabilitation-services/physical-therapy-standards. [Accessed 25 10 2019].

[39] F. R. Sarlegna and R. L. Sainburg, "The effect of target modality on visual and proprioceptive contributions to the control of movement distance," *Experimental Brain Research,* vol. 176, no. 2, pp. 267-280, 2007.

[40] J. Karges and S. Smallfield, "A description of the outcomes, frequency, duration, and intensity of occupational, physical, and speech therapy in inpatient stroke rehabilitation," *Journal of allied health,* vol. 38, no. 1, pp. E1-10, 2009.

APPENDIX - A-I

The Measure of Man [34]

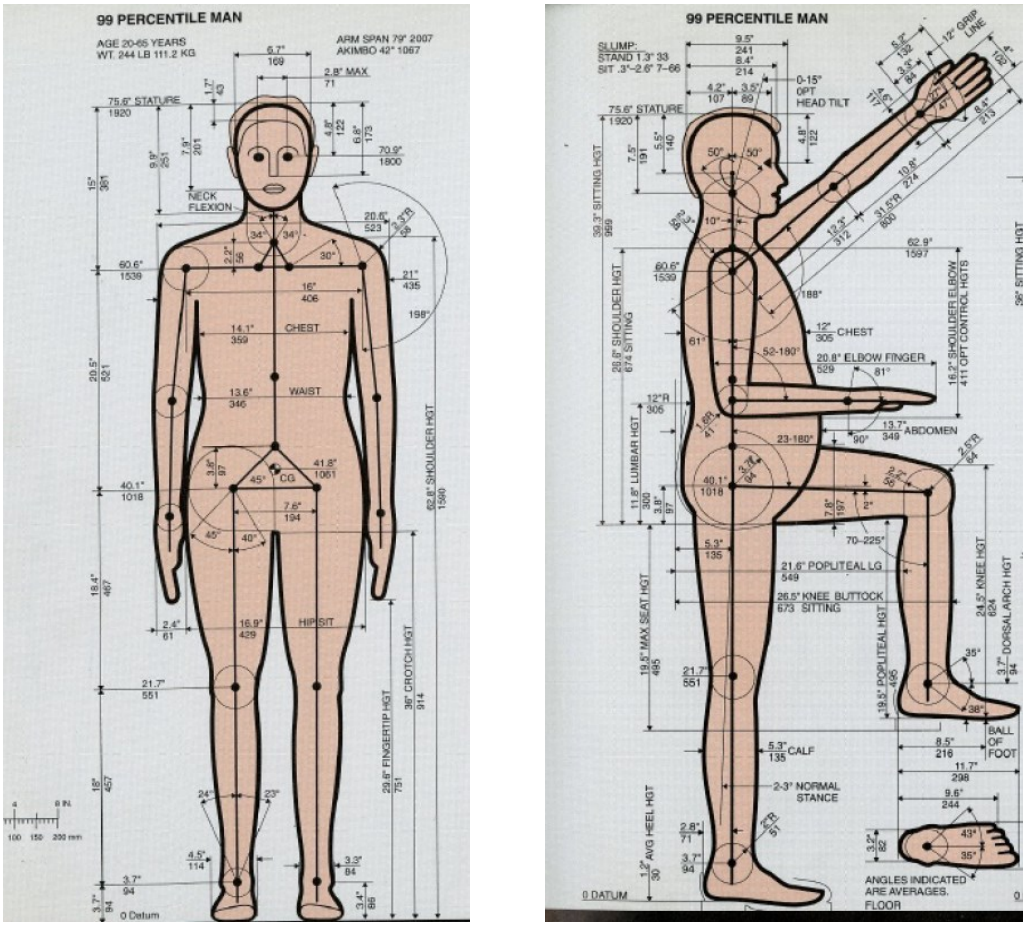

Figure 0.1 The Measure of Man (Front and Side view)

APPENDIX - A-II

The Measure of Women [34]

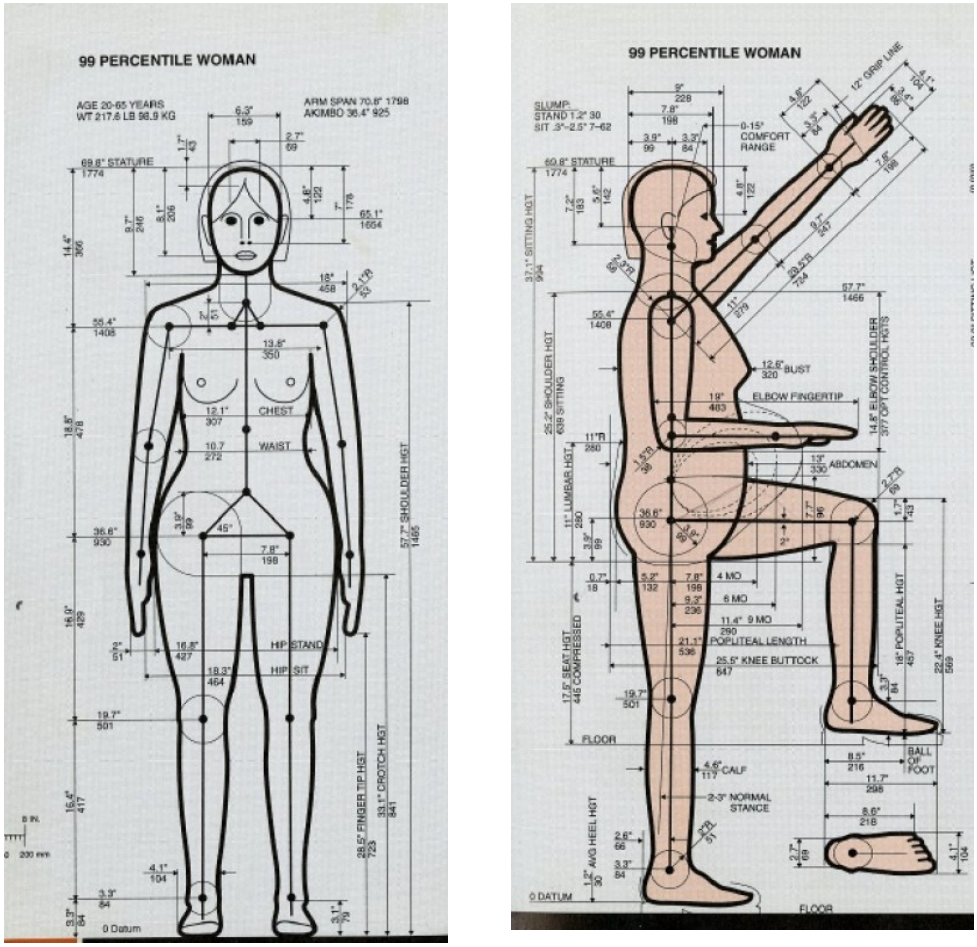

Figure 0.1 The Measure of Women (front and side view)

APPENDIX – B

Mass Characteristics of Upper Limb Segments

Table-A I-1 Mass characteristics of upper limb segments - Adapted from Winter (1990) [10]

Segments & Definition	**Segment Length/ Stature**	**Segment Weight/ Body Weight**	**Centre of Mass / Segment length**		**Radius of Gyration / Segment length**		
			Proximal	***Distal***	***C of G***	***Proximal***	***Distal***
Hand	0.108	0.006	0.506	0.494	0.297	0.587	0.577
Forearm	0.146	0.016	0.430	0.570	0.303	0.526	0.647
Forearm and hand	0.254	0.022	0.682	0.318	0.468	0.827	0.565

APPENDIX – C

Mass and Inertia Properties of MARSE-V2 (Base)

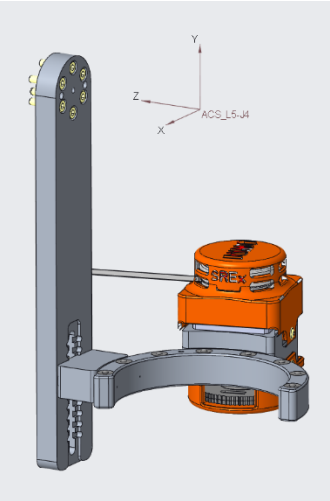


```
VOLUME =  3.0980501e+05  MM^3
SURFACE AREA =  1.4975336e+05  MM^2
AVERAGE DENSITY =  3.1457798e-06 KILOGRAM / MM^3
MASS =  9.7457834e-01 KILOGRAM

CENTER OF GRAVITY with respect to ACS_L5-J4 coordinate frame:
X   Y   Z    -4.4270927e+01 -1.3192314e+02  4.1731477e+01  MM

INERTIA with respect to ACS_L5-J4 coordinate frame:  (KILOGRAM * MM^2)

INERTIA TENSOR:
Ixx Ixy Ixz  2.2344247e+04 -6.3640466e+03  8.3210480e+02
Iyx Iyy Iyz -6.3640466e+03  6.4712956e+03  4.5824326e+03
Izx Izy Izz  8.3210480e+02  4.5824326e+03  2.2781679e+04

INERTIA at CENTER OF GRAVITY with respect to ACS_L5-J4 coordinate frame:  (KILOGRAM * MM^2)

INERTIA TENSOR:
Ixx Ixy Ixz  3.6857197e+03 -6.7215858e+02 -9.6842007e+02
Iyx Iyy Iyz -6.7215858e+02  2.8639610e+03 -7.8295993e+02
Izx Izy Izz -9.6842007e+02 -7.8295993e+02  3.9103041e+03

PRINCIPAL MOMENTS OF INERTIA:  (KILOGRAM * MM^2)
I1  I2  I3   1.8174940e+03  3.8559529e+03  4.7865379e+03

ROTATION MATRIX from ACS_L5-J4 orientation to PRINCIPAL AXES:
       0.51046       -0.59295       -0.62277
       0.70075        0.70659       -0.09837
       0.49837       -0.38620        0.77619

ROTATION ANGLES from ACS_L5-J4 orientation to PRINCIPAL AXES (degrees):
angles about x  y  z   7.223        -38.519         49.275

RADII OF GYRATION with respect to PRINCIPAL AXES:
R1  R2  R3 4.3184522e+01  6.2900990e+01  7.0081336e+01  MM
------------------------------------------------
```

APPENDIX – D

Mass and Inertia Properties of UWM-FWRR (Joint 1 w/o hand)

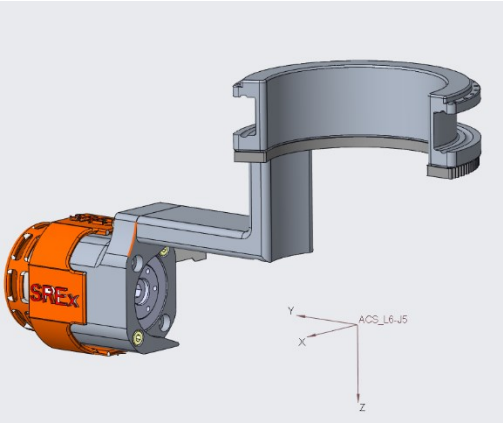


```
VOLUME =  2.5586445e+05  MM^3
SURFACE AREA =  1.2564442e+05  MM^2
AVERAGE DENSITY =  3.2041648e-06 KILOGRAM / MM^3
MASS =  8.1983189e-01 KILOGRAM

CENTER OF GRAVITY with respect to ACS_L6-J5 coordinate frame:
X   Y   Z    -7.3528576e+00  9.4180525e+01 -3.6160842e+01  MM

INERTIA with respect to ACS_L6-J5 coordinate frame:  (KILOGRAM * MM^2)

INERTIA TENSOR:
Ixx Ixy Ixz  1.4055104e+04 -6.0097495e+01 -5.7379439e+02
Iyx Iyy Iyz -6.0097495e+01  2.9228729e+03  6.4754855e+02
Izx Izy Izz -5.7379439e+02  6.4754855e+02  1.1952182e+04

INERTIA at CENTER OF GRAVITY with respect to ACS_L6-J5 coordinate frame:  (KILOGRAM * MM^2)

INERTIA TENSOR:
Ixx Ixy Ixz  5.7112009e+03 -6.2782779e+02 -3.5581296e+02
Iyx Iyy Iyz -6.2782779e+02  1.8065316e+03 -2.1445095e+03
Izx Izy Izz -3.5581296e+02 -2.1445095e+03  4.6359726e+03

PRINCIPAL MOMENTS OF INERTIA:  (KILOGRAM * MM^2)
I1  I2  I3   5.5125774e+02  5.7822453e+03  5.8202019e+03

ROTATION MATRIX from ACS_L6-J5 orientation to PRINCIPAL AXES:
       0.13848        0.45811        0.87804
       0.87185       -0.47695        0.11134
       0.46979        0.75010       -0.46545

ROTATION ANGLES from ACS_L6-J5 orientation to PRINCIPAL AXES (degrees):
angles about x  y  z-166.547         61.407        -73.181

RADII OF GYRATION with respect to PRINCIPAL AXES:
R1  R2  R3 2.5930742e+01  8.3981930e+01  8.4257122e+01  MM
-------------------------------------------
```

APPENDIX – E

Mass and Inertia Properties of UWM-FWRR (Joint 1 with Forearm)

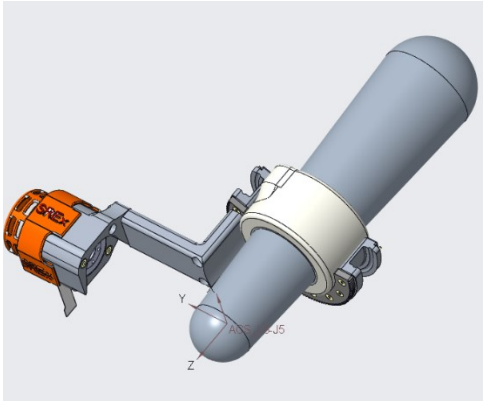


```
VOLUME =  1.3758100e+06  MM^3
SURFACE AREA =  2.1655370e+05  MM^2
AVERAGE DENSITY =  1.4726610e-06 KILOGRAM / MM^3
MASS =  2.0261017e+00 KILOGRAM

CENTER OF GRAVITY with respect to ACS_L6-J5 coordinate frame:
X   Y   Z    -2.9724651e+00  3.8109781e+01 -1.1998256e+02  MM

INERTIA with respect to ACS_L6-J5 coordinate frame:  (KILOGRAM * MM^2)

INERTIA TENSOR:
Ixx Ixy Ixz  5.1522394e+04 -6.0404945e+01 -5.7318292e+02
Iyx Iyy Iyz -6.0404945e+01  4.0389406e+04  6.4777057e+02
Izx Izy Izz -5.7318292e+02  6.4777057e+02  1.2512789e+04

INERTIA at CENTER OF GRAVITY with respect to ACS_L6-J5 coordinate frame:  (KILOGRAM * MM^2)

INERTIA TENSOR:
Ixx Ixy Ixz  1.9412392e+04 -2.8992173e+02  1.4941400e+02
Iyx Iyy Iyz -2.8992173e+02  1.1204122e+04 -8.6165975e+03
Izx Izy Izz  1.4941400e+02 -8.6165975e+03  9.5522676e+03

PRINCIPAL MOMENTS OF INERTIA:  (KILOGRAM * MM^2)
I1  I2  I3   1.7217014e+03  1.8856021e+04  1.9591060e+04

ROTATION MATRIX from ACS_L6-J5 orientation to PRINCIPAL AXES:
       0.00477        0.49246       -0.87032
       0.67258        0.64248        0.36723
       0.74001       -0.58712       -0.32816

ROTATION ANGLES from ACS_L6-J5 orientation to PRINCIPAL AXES (degrees):
angles about x  y  z-131.784        -60.496        -89.445

RADII OF GYRATION with respect to PRINCIPAL AXES:
R1  R2  R3 2.9150654e+01  9.6470474e+01  9.8332786e+01  MM

-------------------------------------------
```

APPENDIX – F

Mass and Inertia Properties of UWM-FWRR (Joint 2)

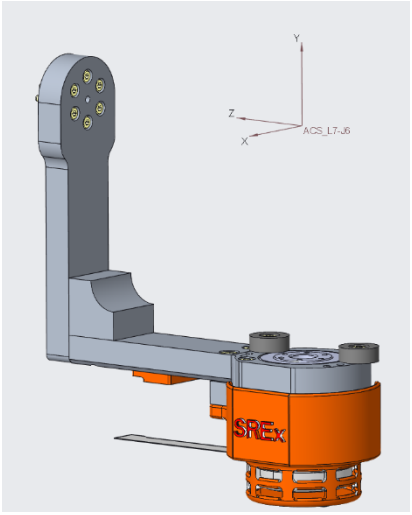


```
VOLUME =  2.2950139e+05  MM^3
SURFACE AREA =  1.0778027e+05  MM^2
AVERAGE DENSITY =  3.0348588e-06 KILOGRAM / MM^3
MASS =  6.9650431e-01 KILOGRAM

CENTER OF GRAVITY with respect to ACS_L7-J6 coordinate frame:
X   Y   Z     2.7081762e-01 -1.0599759e+02  4.6851094e+01  MM

INERTIA with respect to ACS_L7-J6 coordinate frame:  (KILOGRAM * MM^2)

INERTIA TENSOR:
Ixx Ixy Ixz  1.2908592e+04  2.5035556e+01 -3.4395184e+00
Iyx Iyy Iyz  2.5035556e+01  3.9714051e+03  2.2655169e+03
Izx Izy Izz -3.4395184e+00  2.2655169e+03  9.1789133e+03

INERTIA at CENTER OF GRAVITY with respect to ACS_L7-J6 coordinate frame:  (KILOGRAM * MM^2)

INERTIA TENSOR:
Ixx Ixy Ixz  3.5541806e+03  5.0416927e+00  5.3977991e+00
Iyx Iyy Iyz  5.0416927e+00  2.4425097e+03 -1.1933953e+03
Izx Izy Izz  5.3977991e+00 -1.1933953e+03  1.3532952e+03

PRINCIPAL MOMENTS OF INERTIA:  (KILOGRAM * MM^2)
I1  I2  I3   5.8609603e+02  3.2096860e+03  3.5542035e+03

ROTATION MATRIX from ACS_L7-J6 orientation to PRINCIPAL AXES:
      -0.00245       -0.00384       -0.99999
       0.54076        0.84117       -0.00455
       0.84118       -0.54076        0.00002

ROTATION ANGLES from ACS_L7-J6 orientation to PRINCIPAL AXES (degrees):
angles about x  y  z  89.803        -89.739        122.538

RADII OF GYRATION with respect to PRINCIPAL AXES:
R1  R2  R3 2.9008314e+01  6.7884304e+01  7.1434702e+01  MM
-----------------------------------------------
```

APPENDIX – G

Mass and Inertia Properties of UWM-FWRR (Joint 3 w/o Hand)

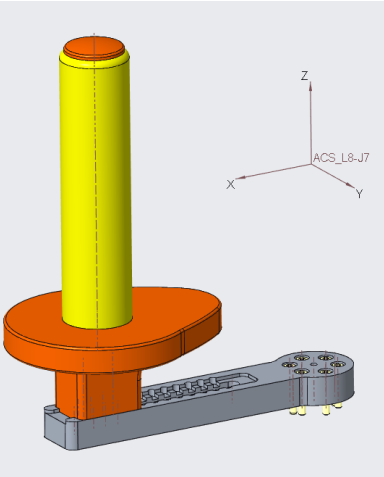


```
VOLUME =  2.0620409e+05  MM^3
SURFACE AREA =  5.8727443e+04  MM^2
AVERAGE DENSITY =  1.5783771e-06 KILOGRAM / MM^3
MASS =  3.2546782e-01 KILOGRAM

CENTER OF GRAVITY with respect to ACS_L8-J7 coordinate frame:
X   Y   Z     8.4654194e+01  3.2961541e-02 -5.2278788e+01  MM

INERTIA with respect to ACS_L8-J7 coordinate frame:  (KILOGRAM * MM^2)

INERTIA TENSOR:
Ixx Ixy Ixz  1.6435881e+03 -1.0976152e+00  1.1543727e+03
Iyx Iyy Iyz -1.0976152e+00  4.4343558e+03  3.1486256e-01
Izx Izy Izz  1.1543727e+03  3.1486256e-01  2.8838979e+03

INERTIA at CENTER OF GRAVITY with respect to ACS_L8-J7 coordinate frame:  (KILOGRAM * MM^2)

INERTIA TENSOR:
Ixx Ixy Ixz  7.5406086e+02 -1.8945166e-01 -2.8602376e+02
Iyx Iyy Iyz -1.8945166e-01  1.2124183e+03 -2.4598015e-01
Izx Izy Izz -2.8602376e+02 -2.4598015e-01  5.5148696e+02

PRINCIPAL MOMENTS OF INERTIA:  (KILOGRAM * MM^2)
I1  I2  I3   3.4934566e+02  9.5620205e+02  1.2124184e+03

ROTATION MATRIX from ACS_L8-J7 orientation to PRINCIPAL AXES:
       0.57714        0.81664       -0.00025
       0.00036        0.00005        1.00000
       0.81664       -0.57714       -0.00026

ROTATION ANGLES from ACS_L8-J7 orientation to PRINCIPAL AXES (degrees):
angles about x  y  z -90.015          0.000        -54.750

RADII OF GYRATION with respect to PRINCIPAL AXES:
R1  R2  R3 3.2762244e+01  5.4202686e+01  6.1034055e+01  MM
-------------------------------------------
```

APPENDIX – H

Mass and Inertia Properties of UWM-FWRR (Joint 3 with hand)

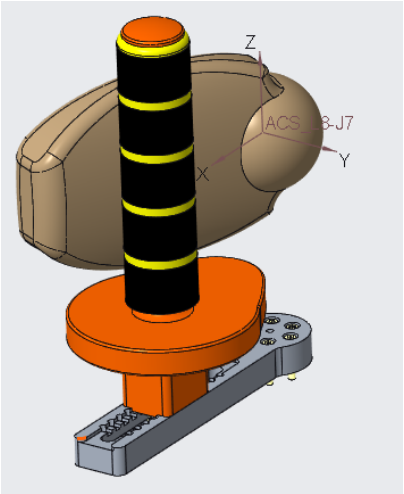


```
VOLUME =  4.6520063e+05  MM^3
SURFACE AREA =  8.5460778e+04  MM^2
AVERAGE DENSITY =  1.6733374e-06 KILOGRAM / MM^3
MASS =  7.7843761e-01 KILOGRAM

CENTER OF GRAVITY with respect to ACS_L8-J7 coordinate frame:
X   Y   Z     5.2513216e+01 -1.1033203e+01 -2.1291129e+01  MM

INERTIA with respect to ACS_L8-J7 coordinate frame:  (KILOGRAM * MM^2)

INERTIA TENSOR:
Ixx Ixy Ixz  1.5966170e+03 -4.4888116e+02  8.9972931e+02
Iyx Iyy Iyz -4.4888116e+02  2.3645285e+03  2.9286218e-01
Izx Izy Izz  8.9972931e+02  2.9286218e-01  5.1833704e+02

INERTIA at CENTER OF GRAVITY with respect to ACS_L8-J7 coordinate frame:  (KILOGRAM * MM^2)

INERTIA TENSOR:
Ixx Ixy Ixz  1.1489813e+03 -8.9989934e+02  2.9384948e+01
Iyx Iyy Iyz -8.9989934e+02 -1.3499583e+02  1.8315514e+02
Izx Izy Izz  2.9384948e+01  1.8315514e+02 -1.7230724e+03

PRINCIPAL MOMENTS OF INERTIA:  (KILOGRAM * MM^2)
I1  I2  I3  -1.7510255e+03 -5.7148406e+02  1.6134226e+03

ROTATION MATRIX from ACS_L8-J7 orientation to PRINCIPAL AXES:
      -0.05413        0.45613       -0.88826
      -0.14216        0.87699        0.45900
       0.98836        0.15112        0.01737

ROTATION ANGLES from ACS_L8-J7 orientation to PRINCIPAL AXES (degrees):
angles about x  y  z -87.832        -62.656        -96.768

RADII OF GYRATION with respect to PRINCIPAL AXES:
R1  R2  R3 4.7427947e+01  2.7095062e+01  4.5526280e+01  MM

-------------------------------------------
```

APPENDIX – I

Motor Specifications, Maxon EC45 30W

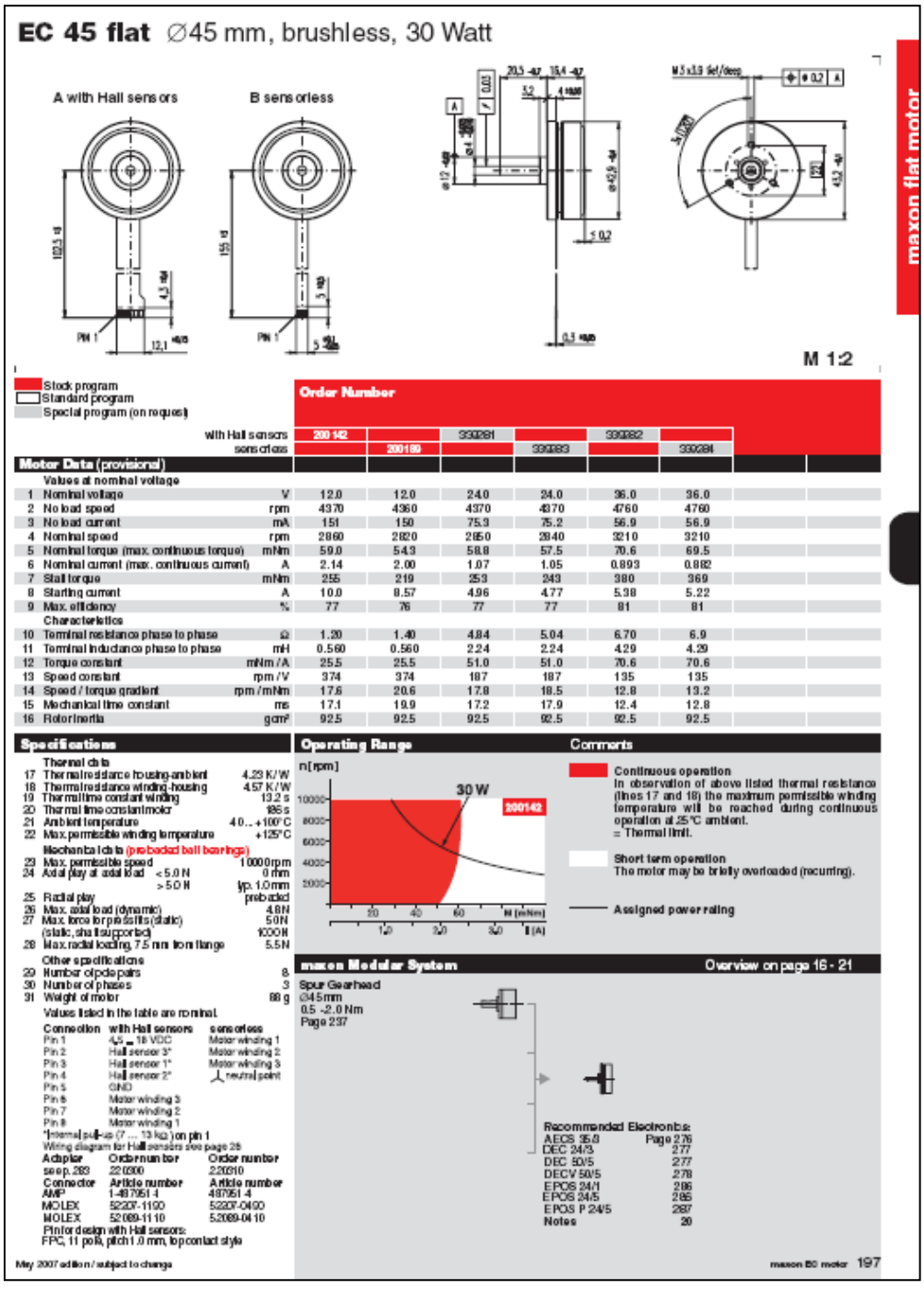

EC 45 flat ∅45 mm, brushless, 30 Watt

maxon flat motor

A with Hall sensors

B sensorless

M 1:2

Stock program
Standard program
Special program (on request)

Order Number						
with Hall sensors	200142		339281		339282	
sensorless		200189		339283		339284

Motor Data (provisional)								
	Values at nominal voltage							
1	Nominal voltage	V	12.0	12.0	24.0	24.0	36.0	36.0
2	No load speed	rpm	4370	4360	4370	4370	4760	4760
3	No load current	mA	151	150	75.3	75.2	56.9	56.9
4	Nominal speed	rpm	2860	2820	2850	2840	3210	3210
5	Nominal torque (max. continuous torque)	mNm	59.0	54.3	58.8	57.5	70.6	69.5
6	Nominal current (max. continuous current)	A	2.14	2.00	1.07	1.05	0.893	0.882
7	Stall torque	mNm	255	219	253	243	380	369
8	Starting current	A	10.0	8.57	4.96	4.77	5.38	5.22
9	Max. efficiency	%	77	76	77	77	81	81
	Characteristics							
10	Terminal resistance phase to phase	Ω	1.20	1.40	4.84	5.04	6.70	6.9
11	Terminal inductance phase to phase	mH	0.560	0.560	2.24	2.24	4.29	4.29
12	Torque constant	mNm / A	25.5	25.5	51.0	51.0	70.6	70.6
13	Speed constant	rpm / V	374	374	187	187	135	135
14	Speed / torque gradient	rpm / mNm	17.6	20.6	17.8	18.5	12.8	13.2
15	Mechanical time constant	ms	17.1	19.9	17.2	17.9	12.4	12.8
16	Rotor inertia	gcm²	92.5	92.5	92.5	92.5	92.5	92.5

Specifications

	Thermal data	
17	Thermal resistance housing-ambient	4.23 K / W
18	Thermal resistance winding-housing	4.57 K / W
19	Thermal time constant winding	13.2 s
20	Thermal time constant motor	186 s
21	Ambient temperature	40...+100°C
22	Max. permissible winding temperature	+125°C
	Mechanical data (preloaded ball bearings)	
23	Max. permissible speed	10000 rpm
24	Axial play at axial load < 5.0 N	0 mm
	> 5.0 N	typ. 1.0 mm
25	Radial play	preloaded
26	Max. axial load (dynamic)	4.8 N
27	Max. force for press fits (static)	50 N
	(static, shaft supported)	1000 N
28	Max. radial loading, 7.5 mm from flange	5.5 N
	Other specifications	
29	Number of pole pairs	8
30	Number of phases	3
31	Weight of motor	88 g

Values listed in the table are nominal.

Connection	with Hall sensors	sensorless
Pin 1	4.5 ... 18 VDC	Motor winding 1
Pin 2	Hall sensor 3*	Motor winding 2
Pin 3	Hall sensor 1*	Motor winding 3
Pin 4	Hall sensor 2*	neutral point
Pin 5	GND	
Pin 6	Motor winding 3	
Pin 7	Motor winding 2	
Pin 8	Motor winding 1	

Thermal switch (7 ... 13 kΩ) on pin 1
Wiring diagram for Hall sensors see page 25

Adaptor	Order number	Order number
see p. 283	220300	220310
Connector	Article number	Article number
AMP	1-487951-4	487951-4
MOLEX	52207-1190	52207-0490
MOLEX	52089-1110	52089-0410

Pin for design with Hall sensors:
FPC, 11 pole, pitch 1.0 mm, top contact style

Operating Range

Comments

Continuous operation
In observation of above listed thermal resistance (lines 17 and 18) the maximum permissible winding temperature will be reached during continuous operation at 25°C ambient.
= Thermal limit.

Short term operation
The motor may be briefly overloaded (recurring).

Assigned power rating

maxon Modular System — Overview on page 16 - 21

Spur Gearhead
∅45 mm
0.5 -2.0 Nm
Page 237

Recommended Electronics:

AECS 35/8	Page 276
DEC 24/3	277
DEC 50/5	277
DECV 50/5	278
EPOS 24/1	286
EPOS 24/5	285
EPOS P 24/5	287
Notes	20

APPENDIX – J

Harmonic Drive Specifications, CSF-11-100-2XH-F

Technical Data

Rating table

Table 170-2

Size	Ratio	Rated Torque at input speed 2000rpm	Limit for Repeated Peak Torque	Limit for Average Torque	Limit for Momentary Peak Torque	Maximum Input Speed	Limit for Average Input Speed	Moment of Inertia ($^1/_4GD^2$)
		Nm	Nm	Nm	Nm	rpm	rpm	$kgcm^2$
5	30	0.25	0.5	0.38	0.9	10000	6500	2.5×10^{-4}
	50	0.4	0.9	0.53	1.8			2.5×10^{-4}
	100	0.6	1.4	0.94	2.7			
8	30	0.9	1.8	1.4	3.3	8500	3500	3.2×10^{-3}
	50	1.8	3.3	2.3	6.6			3.0×10^{-3}
	100	2.4	4.8	3.3	9.0			
11	30	2.2	4.5	3.4	8.5	8500	3500	1.4×10^{-2}
	50	3.5	8.3	5.5	17			1.2×10^{-2}
	100	5.0	11	8.9	25			
14	30	4.0	9.0	6.8	17	8500	3500	3.4×10^{-2}
	50	5.4	18	6.9	35			3.3×10^{-2}
	80	7.8	23	11	47			
	100	7.8	28	11	54			

* The upper value of moment of inertia is for 1U, whereas, the lower value of it is for 2 XH.